ENGINEERED IMPLANTABLE NANOTECHNOLOGY SENSOR AND ELECTRICALLY-CONTROLLED RELEASE OF ANTIBIOTIC AND ANTI-INFLAMMATORY DRUGS USING POLYPYRROLE FILMS ELECTRODEPOSITED ON TITANIUM FOR ORTHOPEDIC IMPLANTS

BY

SIRINRATH SIRIVISOOT

SC.M., BROWN UNIVERSITY, 2007

A DISSERTATION SUBMITTED IN PARTIAL FULFILLMENT OF THE REQUIREMENTS FOR THE DEGREE OF DOCTOR OF PHILOSOPHY IN THE DIVISION OF ENGINEERING AT BROWN UNIVERSITY

PROVIDENCE, RHODE ISLAND

MAY 2010

This dissertation by Sirinrath Sirivisoot is accepted in its present form

by the Division of Engineering as satisfying the

dissertation requirement for the degree of Doctor of Philosophy.

Date_____ _____

Professor Thomas J. Webster, Advisor

Recommended to the Graduate Council

Date_____ _____

Professor Robert H. Hurt, Reader

Date_____ _____

Professor Shouheng Sun, Reader

Date_____ _____

Professor Edith Mathiowitz, Reader

Approved by the Graduate Council

Date_____ _____

Professor Sheila Bonde,
Dean of the Graduate School

CURRICULUM VITA

SIRINRATH SIRIVISOOT

182 Hope Street, Box D, Brown University, Providence, Rhode Island 02912

Tel: (860) 595-9488 · Email: Sirinrath@Brown.edu

EDUCATION:

Brown University, Providence, Rhode Island 02912

Ph.D., Electrical Science and Computer Engineering *Expected 2009*

Sc.M., Engineering *2007*

Mahidol University, Bangkok, Thailand

B.Eng., Computer and Electrical Engineering (First Class Honor) *2003*

RESEARCH EXPERIENCE:

Graduate Research Assistant, Nanomedicine Laboratory under Professor Thomas J. Webster, Division of Engineering, Institute for Molecular and Nanoscale Innovation (IMNI), Brown University, Rhode Island 02912.

1. **Bone Growth Sensors:** Engineered nanotechnology sensors, which are capable to detect and monitor bone growth.

- Anodized titanium (Ti) to create nanopores using wet chemistry.
- Multiwalled carbon nanotubes (MWCNTs) grown out of anodized nanotubular Ti using cobalt-catalyzed chemical vapor deposition *(in collaboration with Professor Brain W. Sheldon)*, characterized using SEM-EDS, TEM, Raman spectroscopy, and ATR-FTIR.
- Determined osteoblast (bone-forming cells) adhesion, proliferation, and differentiation on MWCNT-Ti using total protein, alkaline phosphatase activity, and calcium mineral deposition assays, as well as SEM-EDS, XRD, fluorescent microscopy.
- Investigated electrochemical characteristics of reduction-oxidation (redox) couples of proteins from osteoblast extracelluar matrix and ferri-ferrocyanide using cyclic voltammetry.
- Confirmed type of proteins, which were synthesized by osteoblasts *in vitro*, using gel electrophoresis, in-gel digestion, SDS-PAGE, and mass spectrometry.
- Measured contact angles with various probe liquids, and determined surface energy (Owen-Wendt method) and critical surface tension (Zisman method) of MWCNT-Ti, anodized Ti, and commercial pure Ti.
- Studies the shear stress of MWCNT-Ti, polyethylene glycol, and collagen using Instron.

2. **Electrically-Controlled Drug Release System:** Controlled the releases of antibiotics (penicillin/streptomycin) and anti-inflammatory drug (dexamethasone) from nanostructured conducting polypyrrole (PPy) films.

- Synthesized PPy colloids with wet chemistry and minimized cytotoxicity.
- Electrodeposited nanostructured PPy films on Ti and MWCNT-Ti using cyclic voltammetry.
- Investigated mechanisms of electropolymerization of pyrrole in-situ using UV-vis spectrophotometry.
- Determined Zeta potentials of both drugs in different pH, electrolytes, and

concentrations to obtain good electrodeposition yields.

- Conjugated PPy functionalized amine groups with activated PLGA-COOH via EDC and NHS chemicals.
- Characterized nanostructured PPy-drug films using XPS, AFM, TEM, SEM, and ATR-FTIR.
- Measured resistivity and conductivity of nanostructured PPy-drug films using a four-point probe.
- Evaluated osteoblast and fibroblast (scar tissue-forming cells) functions (adhesion and proliferation) using MTS assays and fluorescent microscopy.
- Controlled drug releases from nanostructured PPy films using electrical stimulation (cyclic voltammetry with potentiostat).
- Determined drug release profiles using UV-vis spectrophotometry and BCA protein assay.
- Investigated bioactivity of antibiotics inside nanostructured PPy films by cultures bacteria (*Stapylococcus Epidermidis*) before and after triggering penicillin/streptomycin releases.
- Assessed inflammatory responses from macrophages (inflammatory cells) on nanostructured PPy-dexamethasone films using nitrite assay and fluorescent microscopy before and after triggering anti-inflammatory drug releases.

3. **Nanofibrous Composites for Vascular Application:** Electrospun polyurethane (PU) and MWCNT nanocomposites *(in collaboration with Professor Robert Hurt)*.

- Designed electrospun scaffolds and controlled the diameter and distribution of nanocomposite fibers by various concentrations of functionalized MWCNTs and PU.
- Studied endothelial and smooth muscle cell adhesion and proliferation on electrospun nanoscaffolds of MWCNT and PU using MTS assays and fluorescent microscopy.

HONORS AND ACHIEVEMENTS:

- Thai Government Scholarship (Nanosensors). *2005*
- Selected research highlights in IEEE Spectrum, Popular Mechanics, MIT Review, Scientific Frontline, Technology Review, Science Daily, and Brown University. *2007-2008*

JOURNAL PUBLICATIONS:

- **S Sirivisoot** and TJ Webster, "Decreased Bacteria Colonies by Electrically-Controlled Antibiotic Releases from Bone Sensing Implant (in preparation).
- **S Sirivisoot**, RA Pareta, TJ Webster, "Electrically-Controlled Release of Antibiotic and Anti-inflammatory Drugs from Nanostructured Polypyrrole Films For Orthopedic Applications (Submitted to *Biomaterials*).
- **S Sirivisoot** and TJ Webster, "Multiwalled Carbon Nanotubes Enhance Electrochemical Properties of Titanium to Determine In Situ Bone Formation", *Nanotechnology*, 19, 295101, 2008.
- **S Sirivisoot**, C Yao, X Xiao, BW Sheldon, and TJ Webster, "Greater Osteoblast Functions on Multiwalled Carbon Nanotubes Grown From Anodized Nanotubular Titanium for Orthopedic Applications", *Nanotechnology*, 18, 365102, 2007.

BOOK CHAPTERS:

- Y Lei, **S Sirivisoot**, and TJ Webster, Understanding and Controlling Protein, Cell, and Tissue Responses, *Biological Interactions on Material Surfaces* (in revising).
- L Zhang, **S Sirivisoot**, G Balasundaram, and TJ Webster, in: B Basu, D Katti, A Kumar (Eds.), *Advanced Biomaterials: Fundamentals, Processing, and Applications*, John Wiley & Sons Inc., in press.
- L Zhang, **S Sirivisoot**, G Balasundaram, and TJ Wesbter, Nanoengineering For Bone Tissue Engineering, in: A Khademhosseini (Eds.), *Micro- and Nano-engineering of The Cell Microenvironment: Technologies and Applications*, Artech House, Norwood (2008), pp. 431-460.

PATENT:

Nanovis Inc., **S Sirivisoot**, C Yao, X Xiao, and TJ Webster, "Method to Enhance Osteoblast Functionality and Measure Electrochemical Properties for A Medical Implant", European Patent: WO2009009666 (A2), UK, Jan 15, 2009.

SELECTED OTHER PUBLICATIONS:

- **S Sirivisoot**, RA Pareta, and TJ Webster, "Electrically-Controlled Penicillin/Streptomycin Release From Nanostructured Polypyrrole Coated on Titanium for Orthopedic Implants", in: E Kny (Eds.), *Nanocomposite Materials*, *Solid State Phenomena*, Vol. 151, pp.197-202, 2009.
- **S Sirivisoot**, RA Pareta, and TJ Webster, "Drug Loaded Polypyrrole Coating on Titanium for Supporting Bone Growth and Inhibiting Fibrosis*", Con. Proc. Biomedical Engineering Society (BMES) 2008 Annual Fall Meeting*, St. Louis, MO, Oct 2008.

- **S Sirivisoot** and TJ Webster, “Multiwalled Carbon Nanotubes Grown from Anodized Titanium for Sensing New Bone Growth”, *Con. Proc. The 34th Northeast Bioengineering Conference*, Brown University, Providence, RI, Mar 2008.
- **S Sirivisoot** and TJ Webster, “Surface Characteristics of Multiwalled Carbon Nanotubes Grown Out of Titanium For Monitoring Bone Formation”, *Con. Proc. Annual Graduate Material Links (GML)*, Northeastern University, Boston, MA, Feb 2008.
- **S Sirivisoot**, C Yao, X Xiao, BW Sheldon, and TJ Webster, “Developing Biosensors for Monitoring Orthopedic Tissue Growth”, *Con. Proc. Materials Research Society (MRS) Annual Fall Meeting*, Boston, MA, Nov 2006.
- **S Sirivisoot**, C Yao, X Xiao, BW Sheldon, and TJ Webster, “Carbon Nanotube-Titanium Electrodes for Detecting Calcium Deposition by Osteoblasts”, *Con. Proc. Annual Graduate Material Links (GML)*, Northeastern University, Boston, MA, Feb 2007.
- **S Sirivisoot**, C Yao, X Xiao, BW Sheldon, and TJ Webster, “Developing Biosensors for Monitoring Orthopedic Tissue Growth”, *Con. Proc. American Institute of Chemical Engineers (AICHE) 2006 Annual Fall Meeting*, T8009: Nanostructured Scaffolds for Tissue Engineering #5 – (22b), San Francisco, CA, Nov 2006.
- **S Sirivisoot** and TJ Webster, “Is My Implant Working: Nanotechnology Sensors For Determining Bone Growth”, *Magazine: BoneZone@Online, Strategic Sourcing for the Orthopaedic Industry*, Fall 2007 Issue.

SELECTED OTHER PRESENTATIONS:

- **S Sirivisoot**, RA Pareta, and TJ Webster, “The Development of Nanotechnology-based In Situ Biosensors to Determine Tissue Growth Next to Implants”, *The 3rd Tissue Engineering Conference, Aegean Conference*, Rhodes, Greece, Sept 2008.

- **S Sirivisoot**, RA Pareta, and TJ Webster, "Design of an Intelligent In Situ Nanotechnology Sensor for Determining Bone Growth", *SBE's 4th International Conference on Bioengineering and Nanotechnology (ICBN), AICHE International Conference*, Dublin, Ireland, July 2008.
- **S Sirivisoot** and TJ Webster, "Controlled Release of Antibiotics From Conductive Polymers For Improving Bone Implants", *MRS International Materials Research Conference (IMRC)*, Chongqing, China, June 2008.
- **S Sirivisoot**, RA Pareta, and TJ Webster, "Biosensing Osteoblast Differentiation In Vitro Through Multiwalled Carbon Nanotubes Grown Out of Titanium", *The 8th World Biomaterials Congress (WBC)*, Amsterdam, Netherlands, May 2008.

PROFESSIONAL SOCIETIES:

Society for Biomaterials (SFB), Materials Research Society (MRS), Biomedical Engineering Society (BMES), Orthopaedic Research Society (ORS), American Institute of Chemical Engineers (AICHE). *2006-Present*

PROFESSIONAL ACTIVITIES:

- Abstract reviewer for SFB 2009 Annual Meeting in an implant pathology special interest group.
- Write-up 'Research/Researcher' Column of MRS Bulletin.
- Teacher Assistant, Mathematics and Sciences, PRIME (GK-12) Program.
- Symposium Assistant (Bioelectronics and Biomaterials), MRS International Materials Research Conference (IMRC) 2008, Chongqing, China.

INDUSTRY EXPERIENCE:

- System Consultant (Programmer), ITOS Consulting Company Limited, on site at Advance Info Service (AIS) Public Company Limited, Bangkok, Thailand, *2005*.
  Experience: C/C++, shell script based on UNIX; implemented and tested mobile applications of AIS Networking (WAP, JAVA, MMS, etc.).

- Software Developer, MFEC Public Co., Ltd, on site at Total Access Communication (DTAC), Public Co., Ltd., Bangkok, Thailand, *2003-2004*.
  Experience: Java, JSP, ASP, HTML, C/C++, ESQL, Korn shell script based on Window and UNIX; managed telephone call formats architectures; monitored servers and supervising a billing system.

- Summer Internship, Exxon Mobil Corp. / Esso (Thailand) Public Co., Ltd, *2002*.
  Experience: Trained the intra/extra-networking architecture, monitored the intra-network of Exxon Mobile Corp., and developed an internal telephone database system with Visual Basic and ASP.

ACKNOWLEDGMENTS

First and foremost, I would like to express my deep gratitude to my advisor Professor Thomas J. Webster for his brilliant advice, support, and direction for my thesis work. Without his guidance, this work would not have happened. I also really appreciate Professors Robert H. Hurt, Shouheng Sun, and Edith Mathiowitz for being my thesis committee and for their helpful suggestions towards my research throughout this time.

I am grateful to the Coulter and Hermann Foundation for financial support. I appreciate Professor Brian W. Sheldon for his PECVD system, Dr. Xingcheng Xiao (Ph.D.), who developed essential techniques in growing MWCNTs, and Dr. Abhishek Kothair (Ph.D.) for his time and assistance in CVD. I would also like to thank Professor Edith Mathiowitz for her ATR-FTIR, Mr. Anthony W. McCormick for his assistance with SEM, AFM, and TEM, Mr. Geoffrey Williams for his assistance in cellular imaging techniques, Mr. Michael Platek (the Thin Film Surface Characterization Laboratory, University of Rhode Island) for his assistance with XPS and his patience to acquire the essential data of my thesis work, and Mr. Gary Lavigne (Institute of Materials Science, University of Connecticut) for his assistance with Raman spectroscopy.

I would like to acknowledge Dr. Chang Yao (Ph.D.) for his patience teaching me cell cultures and assays, Dr. Rajesh A. Pareta (Ph.D.) for his excellent ideas and much help in my research, and Dr. Chenjie Xu (Ph.D.) for his assistance in gel electrophoresis and his essential advice regarding lab techniques, and his friendship. I appreciate Dr. Aihui Yan (Ph.D.) for her zeta potential experiments that assembled important results of my research.

I would like to thank past and present nanomedicine lab mates, with whom I have worked for almost four years. As well, I am grateful to Dr. Wessyl R. Kelly (Ph.D.) for her friendship and advice in my research writing.

Lastly, I am thankful to my family, who is my inspiration and has always supported me through all these years.

Abstract of “Engineered Implantable Nanotechnology Sensor and Electrically-Controlled Release of Antibiotic and Anti-Inflammatory Drugs Using Polypyrrole Films Electrodeposited on Titanium for Orthopedic Implants” by Sirinrath Sirivisoot, Ph.D., Brown University, May 2010.

The development of electrochemical sensors and responsive drug delivery systems are current challenges in the field of orthopedics. Micro and nanotechnology enable the development of dynamic systems that integrate an external signal in response to a biological environment within a living system. This research included the development and examination of: (i) multiwalled carbon nanotubes (MWCNTs) grown out of anodized nanotubular titanium (MWCNT-Ti) to sense bone growth, biofilm formation, or scar tissue growth next to an implant *in situ*, and (ii) a biodegradable and electroactive conductive polymer (polypyrrole, PPy) to deliver antibiotic (penicillin/streptomycin) and anti-inflammatory (dexamethasone) drugs through the application of voltage to increase implant efficacy based on information from (i). Importantly, MWCNT-Ti enhanced the redox reaction of ferri/ferrocyanide and of the proteins synthesized by osteoblasts (bone-forming cells) remaining cytocompatible with osteoblasts and even enhancing osteoblast differentiation (alkaline phosphatase activity and calcium deposition) after 21 days of culture *in vitro* when compared to anodized nanotubular Ti and commercially pure Ti. Penicillin/streptomycin (P/S) and dexamethasone (Dex) were embedded simultaneously during the electrodeposition of PPy films on such materials. The PPy doped drugs enhanced osteoblast adhesion and proliferation*, in vitro,* whereas they inhibited fibroblast (fibrous-tissue forming cells) adhesion and proliferation when compared to conventional Ti. Both drugs (P/S and Dex) were released at about 80% of their initial concentration into PBS buffer after applying 5 cycles of cyclic voltammetry (CV) from -1 V to 1 V with scan rate of 100 mV/s. The bioactivity of P/S and Dex was confirmed by analyzing bacteria (*Staphylococcus epidermidis*) and macrophages (inflammatory and immune-response cells) functions *in vitro*, before and after electrically-

triggered release. After 5 CV cycles, the P/S releases decreased the number of *Staphylococcus epidermidis* after 1 and 12 hours, while the Dex releases decreased the macrophage adhesion after 8 and 13 hours. Results showed that MWCNTs and conductive PPy were cytocompatibility with osteoblasts, and that these conducting bio-nanomaterials can be integrated with electronic devices for the development of an implantable closed-loop sensing and therapeutic system for orthopedic applications.

TABLE OF CONTENTS

TABLE OF FIGURES

TABLE OF TABLES

CHAPTER 1

Introduction

1.1 Bone Tissue Engineering

1.1.1 Bone Histology

In the human body, bone matrices are roughly 90% type-I collagen and a mineral phase consisting of calcium phosphate-based apatite mineral [1]. Collagen fibrils (10-300 nm in diameter) are impregnated with inorganic carbonate apatite nanocrystals (tens of nanometers in length and width, 2-3 nm in thickness), as shown in Figure 1-1 [1]. Bone is distinguished into cortical (compact) and cancellous (trabecular) bone (Figure 1-2 and Figure 1-3). Most long bones are composed of a cortical shell with a cancellous interior, which has a spongelike appearance with numerous large spaces and provides space for bone marrow (medullar cavity). The differences between cortical and cancellous bone are described in Table 1-1. Approximately 80% of the skeletal mass in the adult human skeleton is cortical bone (dense bone), which forms the outer wall of all bones and is largely responsible for the supportive and protective function of the skeleton. The bulk of cortical bone is in the shaft of long bones of the appendicular skeleton. The remaining 20% of the bone mass is cancellous bone, a lattice of large plates and rods known as the trabeculae, which is found in the inner parts of bones [2].

Table 1-1. Differences in cortical and cancellous bone [2].

	Cortical	Cancellous
Skeletal mass	80%	20%
Bone surface	33%	67%
Surface/volume ratio (mm^2/mm^3)	2.5	20
Soft tissue	10%	75%
Adult tissue	Secondary osteon (Haversian systems) Interstial lamellae Circumferential lamellae	Curved plates, rods Bone structural unit Interstitial lamellae
Porosity	Low	High
Marrow	Fatty	Hematopoietic
Main soft tisse	Viscera	Marrow
Developmental	Instramembranous ossification	Endochondral ossification
Turnover	Slow	Rapid
Function	Mainly biomechanical also supportive and protective	Mainly mineral homeostasis, also supportive

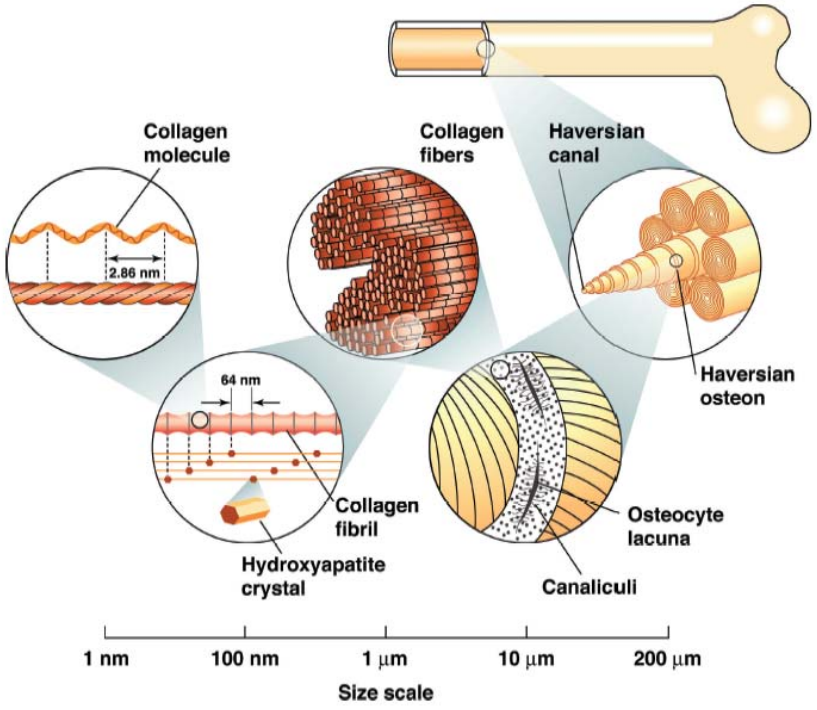

Figure 1-1. Hierarchical nanostructure of cortical bone in the range from tens to hundreds of nanometers (diameter of collagen fibrils) to hundreds of micrometers (osteocyte lacuna and osteons) [1].

Mature compact bone is lamellar, or layered, in structure. It is permeated by an elaborate system of interconnecting vascular canals, the Haversian system, which contains blood supply for osteocytes (Figure 1-2). Bone is arranged in concentric layers around these canals, forming osteons. Immature compact bone does not contain osteons, and has a woven structure. It forms around a framework of collagen fibers and is eventually replaced by mature bone in a remodeling process. Bone adapts its architecture to best carry out its functions, including that of providing skeletal support [3], and it has been determined that it provides piezoelectricity as the underlying physical mechanism to regulate bone growth [4]. The piezoelectric effect is the production of electrical polarization in a material by the application of

mechanical stress, and the converse effect, the application of an electrical field to produce strain [5]. Piezoelectricity in bone relates a shear stress applied along the long axis of the bone to a polarization voltage that appears on a surface at right-angles to the axis. Piezoelectricity in bone may be ascribed to the crystalline micelle of collagen molecules. The piezoelectricity appears only when the shearing forces act on the oriented collagen fibers so that they slip past one another [6]. Consideration of the symmetry of the configuration of collagen fibers in bone shows the existence of effects which can be represented by only two piezoelectric contraints d_{14} and d_{25}, which are the same in magnitude but opposite in sign [4]. As an aside, it is thought that the converse piezoelectric effect is a possible molecular mechanism by which an organism can detect an external electric field [7]. The stress generated potential of bone promoted osteogenesis, which is mediated by electrical current generated by piezoelectric materials through changing pressure [8]. The magnitude of the piezoelectric sensitivity coefficients of bone (values up 0.7 pC N^{-1}) depends on frequency, on the direction of load, and on relative humidity [9, 10]. The piezoelectic properties of bone are of interest in the view of their role in bone remodeling [11].

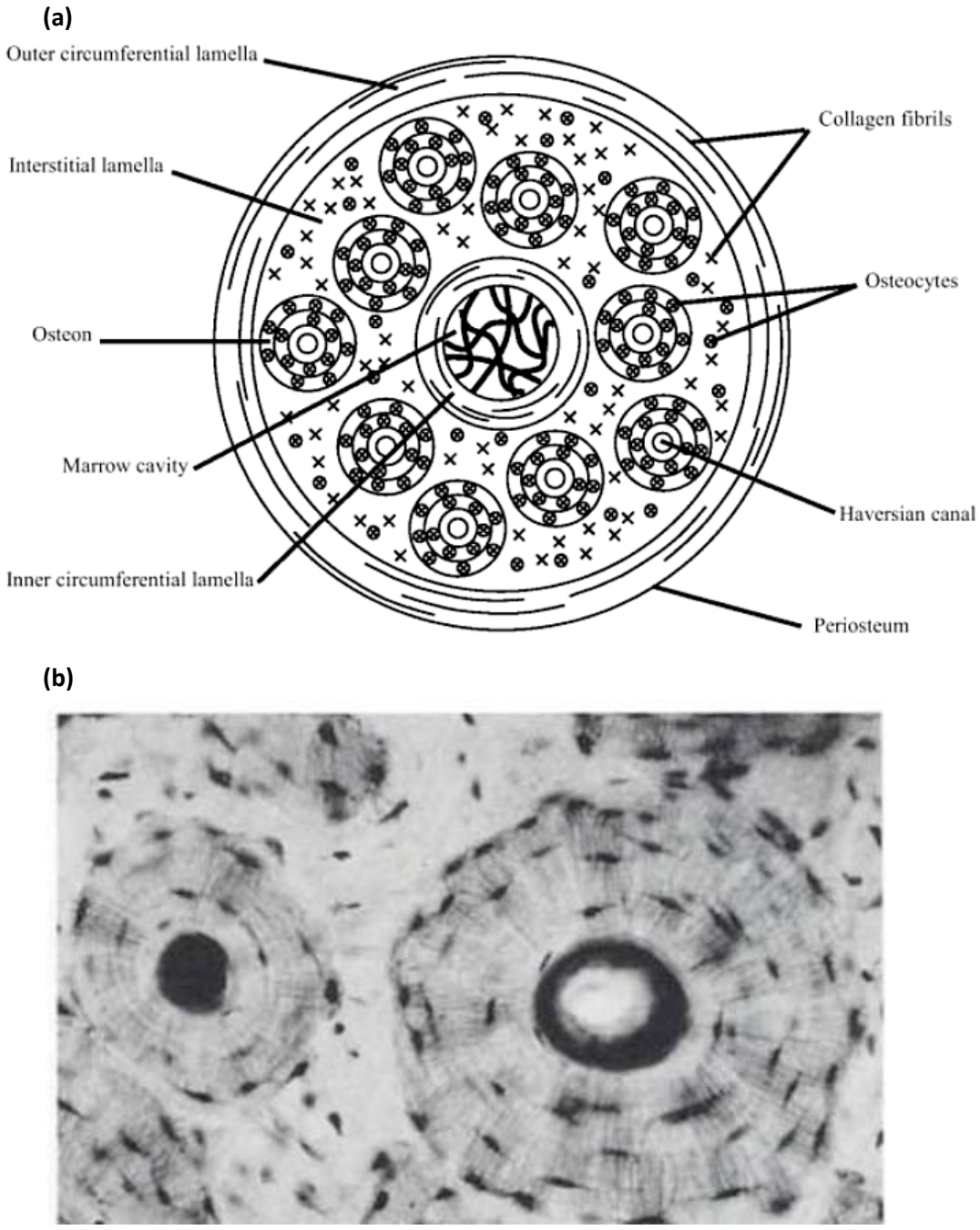

Figure 1-2. (a) Organization of lamellar cortical bone [12] and a (b) cross-section of cortical bone showing osteons with its lacunae, and canaliculi and Haversian canals. Note the intervening interstitial lamella between osteons [2].

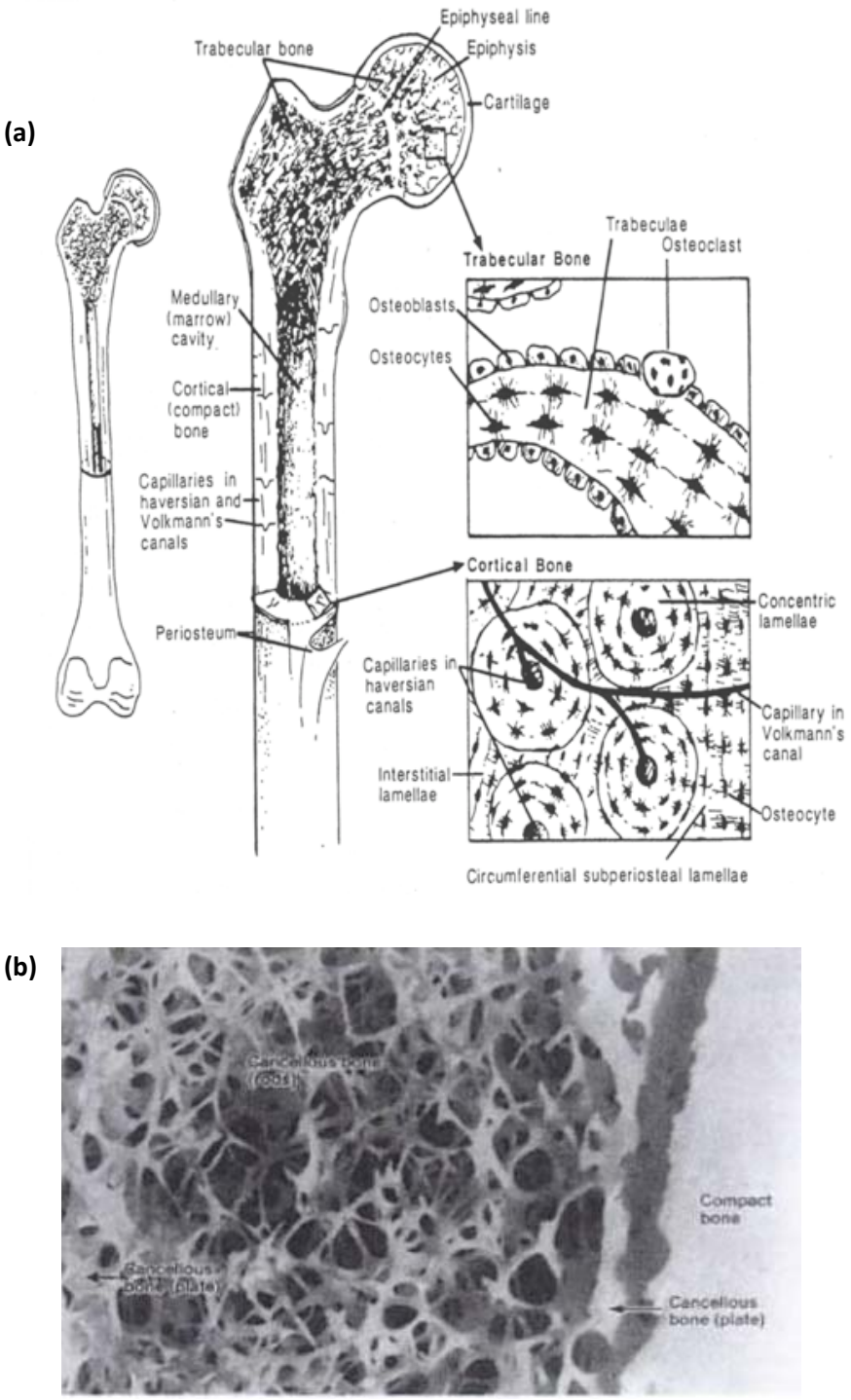

Figure 1-3. (a) Diagram of cortical and cancellous bone [13]**.** (b) Morphology of cancellous bone, composed of a network of trabecular rods and bars, and its adjacent cortical bone, the solid compact part [2].

Bone consists of several living cells, such as osteoblasts, osteocytes, and osteoclasts, which are located in bone's nanostructured mineralized organic matrix (Figure 1-3) [14]. Osteoblasts form the organic matrix of bone, and produce alkaline phosphatase, which plays a critical role in the mineralization of bone. When they are trapped in the bone they formed, osteoblasts differentiate into osteocytes (bone forming, maintaining matrix, homeostatic calcium, and mechano-sensory receptor cells). While osteoblasts make bone, osteoclasts decompose bone by releasing hydrochloric acid that degrades calcium phosphate-based apatite minerals in an aqueous environment [14]. The synthesis, deposition, and mineralization of this organic matrix, in which osteoblasts proliferate and mineralize (that is, deposit calcium), requires the ordered expression of a number of osteoblast genes, such as alkaline phosphatase, type-I collagen, and osteocalcin. The expression of osteocalcin is a marker of late osteoblast differentiation and is induced only after the expression of other osteoblastic markers, such as alkaline phosphatase and type-I collagen [15].

Bone is formed either by direct mineralization of an extracelluar matrix secreted by osteoblasts (called intramembranous ossification) or by the deposition of a bone matrix on a preexisting cartilage matrix (called endochondral ossification) [16]. Osteoblasts produce bone matrix and calcification follows, resulting in a primary ossification center. Primary bone is a temporary tissue and is soon replaced by a definitive lamellar, or secondary, bone. In the secondary ossification zone, osteoblasts ultimately deposit a bone matrix over the 3-dimensional calcified cartilage matrix.

The skeleton contains 99% of the total calcium in the body and acts as a calcium reservoir [16]. Calcification begins by the deposition of calcium salts on collagen fibrils, a process induced by proteoglycans and high-affinity calcium-binding glycoproteins. The deposition of

calcium salts is accelerated by the ability of osteoblasts to concentrate calcium into intracytoplasmic vesicles and release these vesicles, when necessary, to the extracellular medium (via matrix vesicles). This process is aided by alkaline phosphatase secretion by osteoblasts and is present at ossification sites to mediate the mineralization of bone. During bone growth, areas of primary bone formation, areas of bone resorption, and areas of secondary bone formation appear side by side. This combination of bone synthesis and removal (called bone remodeling) occurs not only in growing bones but also throughout the adult life.

Bone has the ability to self-repair or remodel routinely (Figure 1-4). Typically, bone growth is associated with the partial resorption of preformed tissue by osteoclasts and the simultaneous laying down of new bone by osteoblasts (exceeding the rate of bone loss). Bone remodeling in adults is a dynamic physiological process that occurs simultaneously in multiple locations of the skeleton, not related to bone growth [16]. However, osteoporosis (which results from unbalanced bone remodeling) and other joint diseases, such as osteoarthritis (a disease with mechanical abnormalities entailing degradation of joints), rheumatoid arthritis (a chronic system disease primarily in joints), or traumatic arthritis (which maybe caused by trauma that penetrates the joint capsule, introducing infectious agents), frequently occur. The causes of age-related bone loss are believed to be multifactorial. Some of the factors include a decline in hormonal activity (gonadal hormones, growth hormones, thyroxin, etc.), nutritional deficiency, especially of calcium and vitamin D, and inactivity (Figure 1-5) [2]. These disabilities associated with bone all lead to difficulties in performing common activities and may require an orthopedic implant.

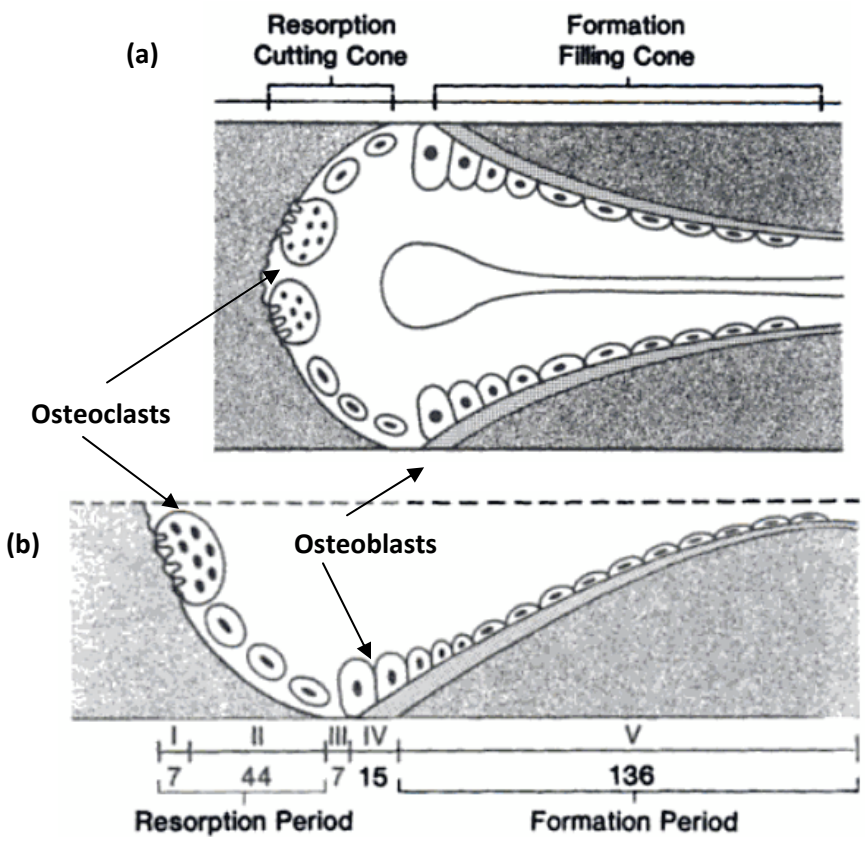

Figure 1-4. (a) Diagram of longitudinal osteonal bone, where remodeling is occurring, showing the basic multicellular unit formed by an osteon and its Haversian system. (b) A cancellous bone remodeling unit, divided into the osteoclastic resorption (I), mononuclear resorption (II), coupling or reversal phase (III), initial mineralization phase (IV), and formation and mineralization (V) phases [2].

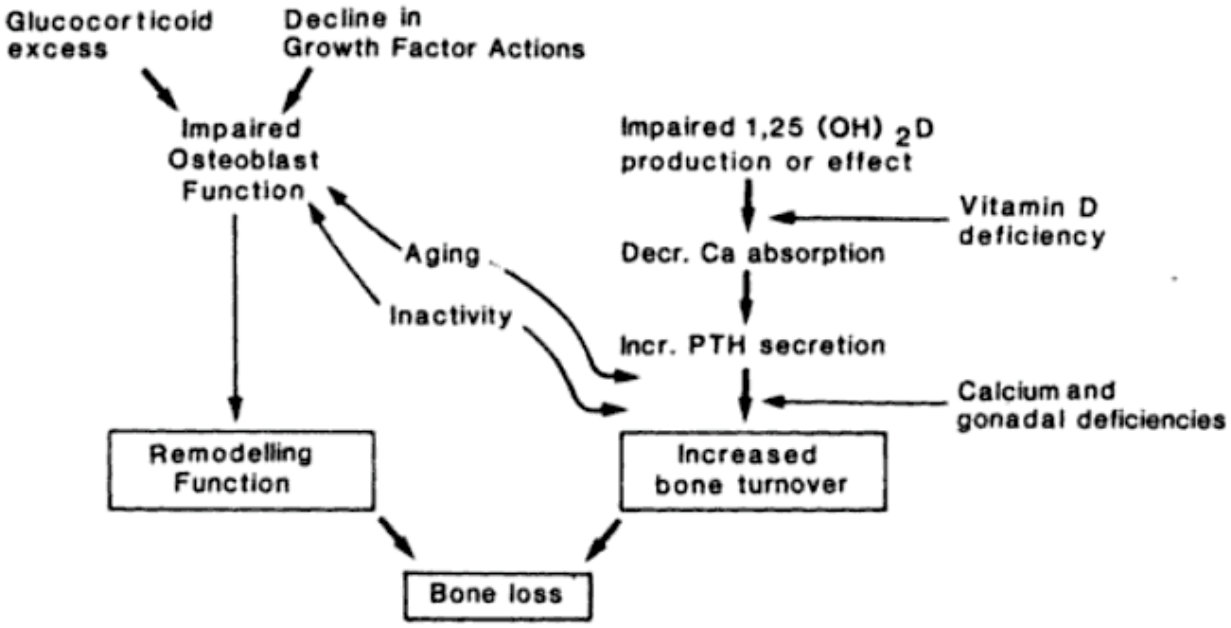

Figure 1-5. Model of age-related bone loss [2]. 'PTH' is parathyroid hormone. PTH is promotes bone synthesis by osteoblasts as well as osteoclast formation and activity, the combination of bone synthesis and degradation generally occurring together in a turnover process.

1.1.2 Titanium Hip Prosthesis

One of the most common orthopedic implants required to restore human function is the hip prosthesis. In orthopedics, many different kinds of materials are used each of which results in varying forms of new bone growth. Orthopedic implants are generally composed of materials that withstand cyclic physiological load-bearing and possess high strength, ductility, fracture toughness, hardness, corrosion resistance, formality, and acceptable biocompatibility properties [17]. It is important that implants are constructed from materials that are biocompatible with low toxicity potential, to not be rejected by the body. Current total hip femoral stem implants are typically constructed from titanium (Ti), Ti-alloys, or cobalt-chromium alloys [cemented with

poly(methyl methacrylate) or press fitted into place] (Figure 1-6), connected to a modular cobalt-chromium alloy or alumina ceramic head that articulates on a ultrahigh-molecular weight polyethylene or alumina ceramic acetabular cup fitted into a Ti or cobalt-chromium cup liner that is cemented, screwed, or press-fit into place. In general, for total hip replacements, patients younger than 50 years old will be outfitted with a press fit stem (which may have a coating of hydroxyapatite on the stem or acetabular cup). However, this system does not utilize any cement due to the theory that there will be some degree of bone regeneration or growth into the hydroxyapatite coating in young patients [18]. Cemented poly(methyl methacrylate) stems are used in patients older than 50 years, because their bodies are usually not able to produce enough bone to hold the stem in place. The hardness of a metal and the smoothness of the bearing surfaces determine its relative wear rate. Ti has high a level of biocompatibility, low level of corrosion, and modulus of elasticity closer to that of bone to allow for its use in numerous porous implants that have yielded excellent long-term results. Ti-based alloys have excellent properties for use in porous forms for biological fixation of prostheses. Fracture fixation components fabricated from Ti-based alloys are also used preferentially when the implant site is known to be infected or when postoperative shadow-free imaging is desired. Because of the fact that Ti is not ferromagnetic, Ti and its alloys can be safely examined with magnetic resonance imaging, which makes them especially useful for long-term implants. Cobalt-chromium alloys are more wear resistant than Ti or Ti-alloys, since cobalt-based alloys have a higher moduli of elasticity than Ti-based alloys. However, there is a technical problem of successfully attaching the coating onto cobalt-chromium alloys while maintaining adequate properties of both the coating and substrate.

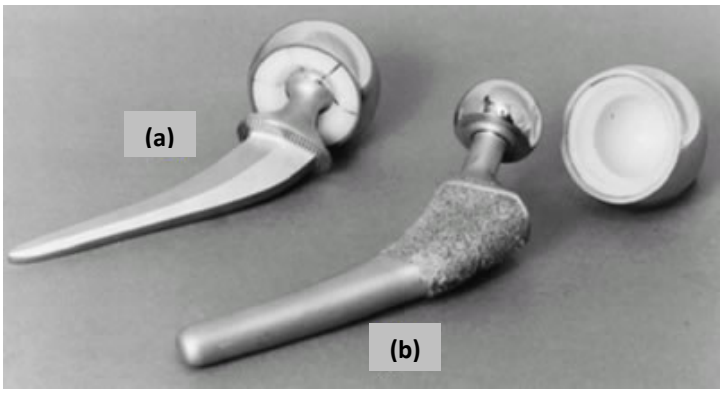

Figure 1-6. Types of stems used in total hip replacements: (a) cemented stems, and (b) press-fitted stem [18].

Commercially pure Ti (American Society for Testing and Materials F183, ASTM F67) and Ti-6Al-4V (ASTM F136) are the dominant Ti alloys used in implants. Commercially pure Ti is 98-99.6% pure Ti [17]. Due to the stability of the oxide layer that forms on commercially pure Ti and its relatively higher ductility compared to Ti-6Al-4V, commercially pure Ti is commonly used for total hip arthroplasties. Various forms of Ti are currently being implanted based on altered surface roughness and the geometry of porous coatings (such as cobalt-chromium beads, pure-fiber metals, plasma sprayed Ti, and hydroxyapatite, and bioactive nonmetallic materials with calcium phosphate composition coatings). The calcium phosphate coatings can enhance biocompatibility and improve bone growth onto and into the implants, which can enhance the short- and long-term performance of orthopedic implants. Whereas porous coatings can increase surface roughness of implants or bone -contact percentage at the interfaces, which can be postulated to be advantageous for stimulating new bone ingrowth and provide enhanced fixation.

After implantation, the body tries to maintain homeostasis by activating host defense mechanisms; clearly, this may lead to implant failure and cause harm or even death to the

patient. The effect of the implant on the host tissue includes excessive inflammation, foreign body interactions, immunological sequences, systemic toxicity, blood-surface interactions, thrombosis, device-related infection, and tumorigenesis. Figure 1-7 shows the sequence of events involved in inflammatory and wound-healing responses. Acute inflammation can take up to a week for traditional materials, while chronic inflammation can last up to a month. The main characteristics in acute inflammation are the exudation of fluid and plasma proteins, along with the emigration of leukocytes (predominantly neutrophils). Neutrophils (polymorphonuclear leukocytes) and other motile white cells emigrate from blood vessels to the perivascular tissue and the implant site. Chronic inflammation is less uniform histologically than acute inflammation, and is characterized by the presence of macrophages, monocytes, and lymphocytes, with the proliferation of blood vessels and connective tissue. After the chronic inflammatory response, granulation tissue can be formed as a normal foreign body reaction. The foreign body reaction comprises foreign body giant cells (such as monocytes and macrophages), and the components of granulation tissue include foreign body giant cells, fibroblasts, capillaries, and epithelial cells. In granulation tissue, there are modified macrophages (resembling epithelial cells) surrounded by lymphocytes, called granuloma, in an attempt to digest materials. In the case of granuloma tissue, macrophages adhere to the biomaterial surface in early inflammation and wound-healing response can recruit foreign body giant cells, which then may persist for the lifetime of the implant. However, if macrophages cannot engulf the large foreign materials, then they can become quiescent or active by releasing lysosomal proteins, which will corrode or degrade the biomaterial slowly. If there is an accumulation of fibroblasts within or around the extracelluar matrix of the granuloma, this process is called “fibrosis”. Fibrosis can isolate the foreign body reaction and the implant from the local tissue environment. Fibrosis occurs at the interfacial foreign body reaction and encapsulates the

biomaterial for the lifetime of the implant. Decreasing the amount of fibroblasts at the implant interface is favorable since the callus formation can ultimately encapsulate implants placed in bone with stratified undesirable connective tissue. Without fibroblasts present in granulation tissue, neovascularization can still occur to generate new blood capillaries by endothelial cells. The brief description of the functions of such cells, involved in the inflammatory and would-healing response, are listed in Table 1-2.

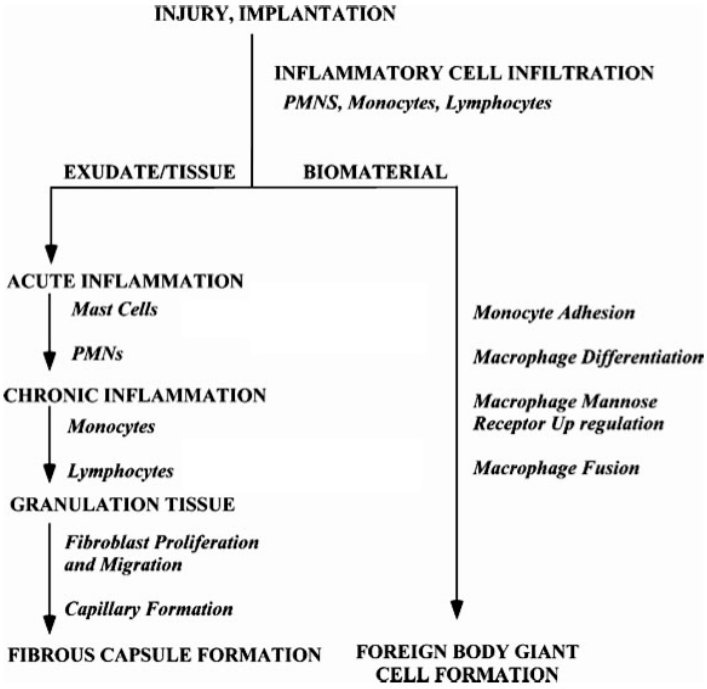

Figure 1-7. Sequence of events involved in the inflammatory and wound-healing response leading to foreign-body giant cell formation [17].

Table 1-2. Types of cells involved in the inflammation and wound-healing response with short descriptions of their major functions.

Cells	Descriptions
Polymorphonuclear leukocytes	A category of white blood cells characterized by the presence of granules in their cytoplasm.
Leukocytes (white blood cells)	Cells of the immune system defending the body against both infection and foreign materials. Leukocytes are grouped into three major classes: lymphocytes, granulocyte, and monocytes.
Lymphocytes	Cells are further divided into B and T cells, which are responsible for specfic recognition of foreign agents and their subsequent removal from the host.
Granulocytes	The most numerous of the leukocytes, rid the body of large pathogenic organisms such as protozoans or helminthes and are also key mediators of allergy and other forms of inflammation.
Monocytes	Cells constitute up to 7 percent of the total number of white blood cells in the blood, move from the blood to sites of infection, where they differentiate further into macrophages.
Macrophages	Any of the large phagocytic cells of the reticuloendothelia system.
Foreign body giant cells	A collection of fused macrophages (giant cels), which are generated in response to the presence of a large foreign body.
Epithelial cells	The closely packed cells forming the epithelium.
Fibroblasts	Cells which develop the connective tissue.
Endothelial cells	Cells form new blood vessels (called angiogenesis).

1.1.3 Bone Implant Failure Modes

Due to above, current implants generally last 10-20 years with an approximate revision rate of 7% after 10 years of service [17, 19]. Although Ti is one of the most biocompatible materials (not adversely recognized by the human immune system), there are many reasons leading to the failure of Ti implants aggressively. During and after bone implantation, bone matrix is destroyed and bone cells adjacent to the implant die. The damaged blood vessels produce a localized hemorrhage to form a blood clot. During orthopedic implant repair, the blood clot, cells, and damaged bone matrix are actively removed by macrophages (Figure 1-8). Primary bone is then formed by endochondral and intramembranous ossification, both processes contributing simultaneously to facture healing. Typically bone tissue heals without forming a scar; however, the implant itself can promote scar tissue formation. A lack of fixation into surrounding bone eventually loosens the implant and is the most common cause of hip replacement failure. Wear particles trigger the invasion of inflammatory responses, which can cause the failure of implants if it is prolonged. Moreover, the internal environment of the body is extremely corrosive (by osteolysis or bone resorption) which generates degradation products by wear and electrochemical corrosion of metallic surfaces leading to the loosening of an implant (Figure 1-9). Importantly, based on clinical data collected by the Canadian Joint Replacement Registry in 2006, the most common reasons for revisions of a total hip replacement were aspetic loosening of the implant (54%), osteolysis (28%), implant wear (24%), instability (16%), bone fracture (7%), implant fracture (4%), and single stage-infection (2%) [20]. For a total knee replacement, the most common reasons for the implant failures were aspetic loosening of the implant (35%), implant wear (30%), osteolysis (17%), two stage-infection (13%), instability (12%), implant fracture (10%), bone fracture (4%), and single stage-infection (2%) [20]. To promote a successful

integration of a biomaterial into host tissue, the physiological chemical bonding of host matrix protein molecules to the synthetic implant surface without an intervening immuno-competent fibro-inflammatory layer must occur.

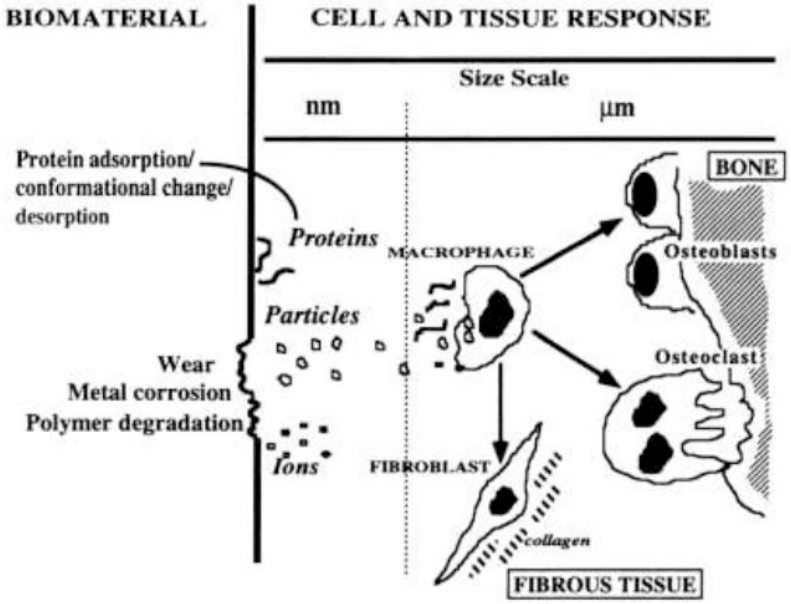

Figure 1-8. Schematic of a few of the molecular and cellular interactions that can comprise a tissue response to biomaterials. Cells are in the micrometer size, while proteins interacting with materials, particles and ions are in the nanometer size. Macrophages can release cellular mediators, such as cytokines and eicosanoids (arrows) that affect cells such as fibroblasts, osteoblasts, and osteoclasts, and thereby, formation of tissue at the millimeter scale [17].

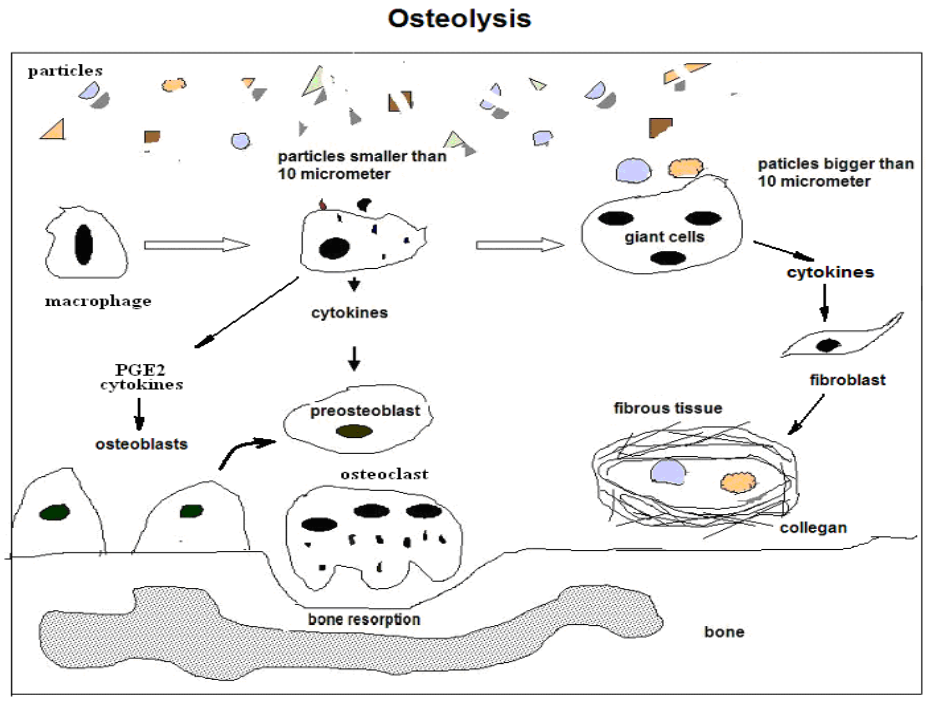

Figure 1-9. Schematic of biomaterial wear debris activating macrophages and inducing osteolysis [17, 21]. Particulate debris is generated from wear of arthroplasty components, metal corrosion or polymer degradation. Particles <10μm are engulfed directly by macrophages but cannot be digested easily. Consequently, macrophages begin to release interleukins (IL-1, IL-6), prostaglandin E_2 (PGE_2), and tumor necrosis factors (TNF) which then mediate bone resorption via osteoclasts [22]. On the other hand, macrophages form giant cells to phagocytose large particles (>10μm) and then secrete cytokines to signal fibroblasts to synthesize collagen which can result in a fibrous tissue capsule around the implant [17].

1.1.4 Biomedical Nanostructured Interfaces

A cell-biomaterial surface interaction is an important factor to regulate cellular activities (such as adhesion, proliferation, migration, differentiation, and cell shape) on surface features. After an implant is introduced into the body, within a few seconds, a biomaterial-blood interface occurs and initial events at the surface of the biomaterials involve adsorption of water, ions, and

proteins from the blood. Many anchorage dependent cells, such as fibroblasts and osteoblasts, require adhesion for survival. There are two main types of cell adhesion: (i) to neighboring cells and (ii) to an extracelluar matrix (ECM) or proteins absorbed onto a substrate. Cell adhesion is mediated by several different types of transmembrane receptor proteins connected to the cytoskeleon of the cell [23]. Critical in the design of successful biomaterials for bone tissue engineering is the ability for such materials to control protein adsorption and bioactivity, since protein adsorption consequently affects cellular responses after biomaterials are implanted (Figure 1-10). The degree to which proteins adsorb on implant surfaces depends on numerous biomaterial properties, such as surface chemistry, charge, wettability, topography, roughness, and energy. Affected by surface roughness, the composition of the protein layers and the orientation of the molecules adsorbed on the implant surfaces have been shown to be an important factor for osseointegration.

Moreover, cell-surface structures (receptors, receptor clusters, lamellopodia, and filopodia) that are used to sense the external environment and interact with biomaterials are on the order of a few tenths of a nanometer [24]. Therefore, nanotopography of biomaterials (with different bond strengths, orientations, and protein folding/unfolding) can regulate cell adhesion and consequently change cell shape, growth, and the regulation of certain gene expression. Relative cell spreading increases on high surface free energy or wettable materials [17]. Focal adhesion contacts from cells (Figure 1-11) occur either via adsorbed proteins or the ECM, and the distance separating the cell membrane and the substrate in the region of the focal adhesion contacts approaches 10-15 nm [25]. Moreover, the basement membrane of the ECM is composed of hierarchically arranged collagen, laminin, other protein fibrils, and proteoglycans in a complex topography at the nanometer range. The specific peptide sequences (such as

arginine-glycine-aspartic acid, RGD) of proteins in the ECM mediate integrin receptor binding for cell attachment. Cell-matrix-biomaterial interactions associated with cell signaling occur at the nanoscale level [26]. This signal regulates cell attachment, spreading, migration, differentiation, and gene expression.

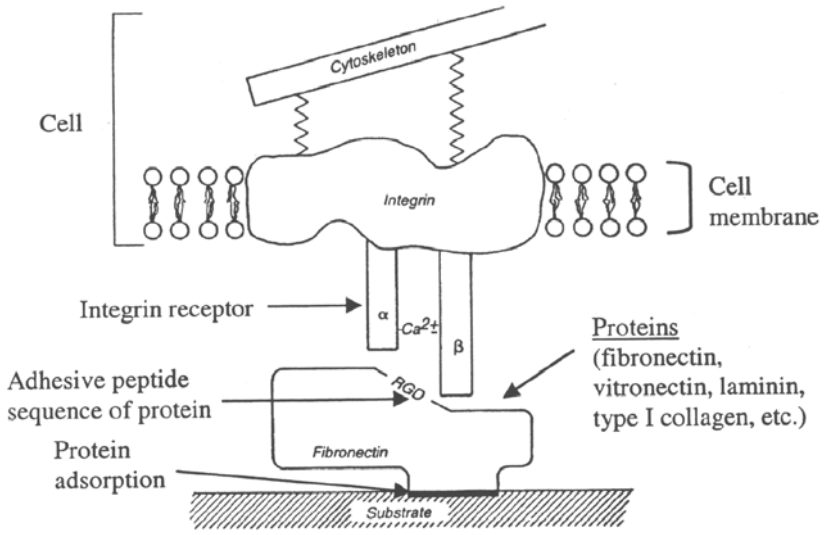

Figure 1-10. Schematic of the interaction of cells to an implanted surface as mediated by proteins [5].

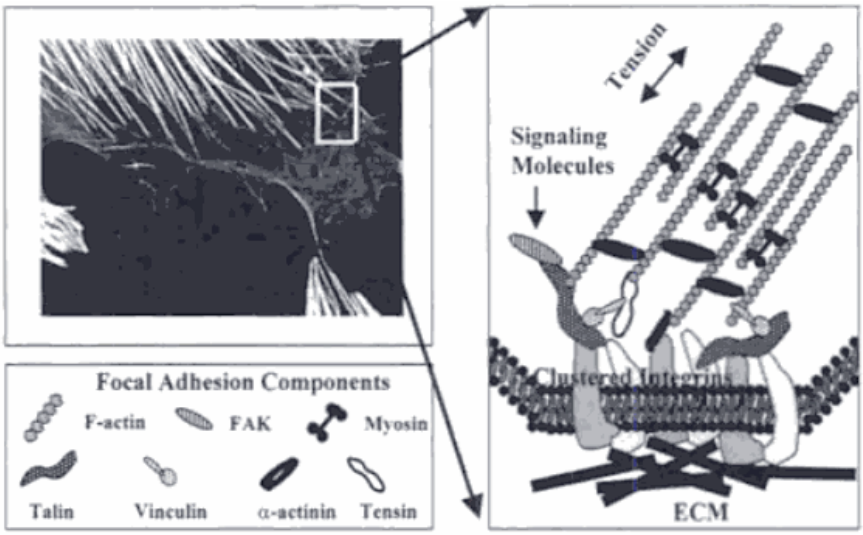

Figure 1-11. Diagram of some of the potential links between actin filaments and integrins in focal adhesion [27].

It has been shown that nanometer surface roughness on implants improves protein (such as vitronectin and fibronectin) adsorption, subsequent osteoblast attachment, and eventual osseointegration [28]. This has been demonstrated for nanophase ceramics [26-29], polymeric-nanoscaffolds [30-31], and carbon nanofibers [32] due to higher surface area, engergy, and wettability of nanoscaled compared to conventional materials. Therefore, a change in biomaterial surface properties can significantly affect cell-biomaterial interfacial characteristics, and influence cellular behavior and functions. ECM nanofeatures (such collagen banding patterns) are the inspiration to design better biomaterials in more favored nanoscaled dimensions to mimic natural tissue and increase surface energy and bioactivity for select protein adsorption for the next generation of tissue engineering and regenerative medicine materials.

Due to thermodynamic equilibrium, protein adsorption on biomaterials occurs under a condition of lowered interfacial surface energy. The chemical end groups, such as –OH, –COOH,

can effect to the chemical and physical adsorption of proteins. Importantly, one needs specific chemistry and curvature of nanomaterials to provide the best cues to specific cells (such as osteoblasts). Osteoblasts naturally favor a porous and calcium-phosphate-rich surface, resulting in enhanced cell functions until bone is deposited. Among bioceramics, calcium phosphate ceramics have excellent osteoconductivity, bioactivity, and an ability to form a strong bone-calcium phosphate interface [24]. Moreover, the surface area of calcium-phosphate coatings is much higher when nanorough surfaces are obtained after coating a metal (such as Ti), leading to more cell adhesion and quicker bone formation/binding to host-surrounded connective tissue.

1.1.5 Implant Diagnosis: Imaging Techniques vs. Electrochemical Sensors

Approximately 200,000 total, 100,000 partial, and 36,000 revised hip replacements were performed in the United States in 2003 [29]. Unfortunately, only limited techniques, such as insensitive imaging (through X-rays or bone scans), exist to determine if sufficient bone growth is occurring next to titanium implants after surgery. Thus, techniques used in diagnosing orthopedic implants need to more accurately identify musculoskeletal injuries and conditions after implantation. Although there have been improvements in implant design to increase bone formation, the clinical diagnosis of new bone growth surrounding implants remains problematic, sometimes significantly increasing hospital stays and decreasing the ability of doctors to quickly prescribe a change in action if new bone growth is insufficient.

Currently, a physical examination (e.g., palpation, or laboratory testing) might be completed before imaging or electrochemical sensing techniques are used to inform a clinician

about a patient's health. Although advanced imaging techniques, such as bone scans, computer tomography scans, and radiographs (X-rays) are important in this diagnosis, each has its own limitations and difficulties. A bone scan is used to identify areas of abnormal active bone formation, such as arthritis, infection, or bone cancer. However, bone scans require an injection of a radioactive substance (e.g., technetium) and a prolonged delay for absorbance before performing the scan. Computer tomography produces a two dimensional cross-sectional image of a body on the computer screen. Although this technique produces more detail than an X-ray, in some cases (e.g., severe trauma to the chest, abdomen, pelvis or spinal cord) a dye (e.g. barium sulfate) must be injected in order to improve the clarity of the image. This often causes pain to the patient. X-rays, on the other hand, may be inadequate for accurate diagnoses, and non-unions of fractures may go clinically undetected until failure. Moreover, X-rays cannot be used to adequately diagnose soft tissue growth (which occurs often times between the implant and newly formed bone). An electrochemical technique, called electromyography, has been used to analyze and diagnose muscle or nerve functions inside body conditions [30]. Thin electrodes are placed in soft tissues to help analyze and record electrical activity in the muscles. However, this electrode technique leads to pain and discomfort for the patient. When the needles are removed, soreness and bruising can occur. Moreover, conventional diagnostic techniques including radiography and magnetic resonance imaging do not allow detailed examination of the implant to the bone interface because of the metallic implant itself. In summary, current methods of assessing the healing process do not provide physicians with sufficient information to adequately assess the progress of healing, particularly in its early stages. They are costly and repeated imaging, in particular, may be detrimental to the patient's health. Surgeons often find it difficult to assess the patient's bone healing status during follow-

up clinic visits. A device that allows doctors to monitor the healing cascade is necessary and such a device can assist in developing care therapies and rehabilitation.

The development of a molecular sensing device, which converts the cell process or biological recognition event into a useful electrical signal, can produce an accurate and sensitive platform for patient diagnosis. *In vivo,* many cellular processes rely on the redox reactions of various biomolecules and ions. The mechanisms of electron transfer reaction and the role of proteins in aiding the electron transfer of redox processes can be examined by electrochemical analysis. In electronic theory, when two different materials come in contact with each other, electron transfer will occur in an attempt to balance the Fermi level[1], causing the formation of a double layer of electrical charge at the interface [28]. Electrochemical biosensors on the implant itself show promise for medical diagnostics *in situ* to possibly determine new bone growth surrounding the implant because of their real-time sensitivities and convenient assessments. Yet, this technology has not been fully explored for sensing bone growth in orthopedic applications. Incorporation of such electrochemical sensors as self-diagnosing devices into or onto current bone implants may be possible through nanotechnology; different types of nanoscaled biomaterials have varying abilities to enhance *in vitro/in vivo* bone formation.

The hip and joint replacements can contain embedded sensors that allow the health care system to detect early problems, proactively treat them, and provide better care for the patient. The data can include such measures as implant positioning, load bearing data, range-of-motion data, dislocation potential, bone ingrowth measurements, particles (such as wear debris) count around an implant (a link to osteolysis), temperature, pH, lactate levels, glucose levels, bacteria levels, other local biochemistry events [32]. These diagnostic sensors or chips in orthopedic implants can remain silent for years until a problem is detected. Patients would not require

going to the hospital but the chips can be activated and send diagnostic data automatically through existing wireless infrastructure or biomedical telemetry to the hospital. In 2006, a wireless microsensor was introduced to monitor the bone healing process (osseointegration) after surgery using nanotechnology for hip replacement [33]. Through such technology, the need for X-rays to monitor bone functionality, and thus costs and exposure to radiation can be reduced. Furthermore, such sensors not only reduce post-operation recovery time, but also the wait time for patients needing artificial hip and joint implants.

1.2 Nanofabrication by Electrochemical and Chemical Methods for Biomedical Applications

Nanofabrication via electrical or chemical processes can create structures at the nanoscale, such as nanoporous templates, nanoroughness, and nanodimensions. This section includes examples of the construction of two- and three-dimensional nanostructures by electrochemical and chemical approaches, including: (i) anodization; (ii) chemical vapor deposition; and (iii) electrochemical polymerization (all techniques used in this thesis). These nanostructures require assistance from conventional top-down micro/nanofabrication processes to integrate into the implantable sensor chip or nanodevice, used throughout biomedical telemetry.

1.2.1 Anodized Nanotubular Titanium

Titanium (Ti) is a highly reactive metal and the Ti oxide layer forms spontaneously in air, water, and other media with a thickness of 2 to 7 nm. The atomic diameter of Ti is 0.29 nm and the

oxide layer is only about 5 to 20 atoms thick [34]. The standard electrode potential is in a range from -1.2 to -2.0 V for Ti to Ti^{3+}, however, due to a strong chemical affinity to oxygen, it easily produces a compact oxide film, ensuring high corrosion resistance of the metal in the body or other envioronments [35]. Although, the stoichiometry of the oxide can be TiO_2, TiO, or Ti_2O_3 which could change at the metal/oxide interface [34], TiO_2 is primary found because it has one of the highest heats of reaction (ΔH = -915 kJ/mol at 298.16 to 2000 K) [36]. TiO_2 is an n-type (metal-excess or donor type) semiconductor, while TiO and Ti_2O_3 are listed as amphoteric conductors. TiO_2 is non-conducting, but electrons can tunnel through the layer, leading to denaturing and conformational changes in proteins [37].

Although TiO_2 has good biocompatibility by means of the appropriate degree of host response and anticorrosion, commercially pure Ti has poor direct bone growth [17]. For example, it has been shown that bone formation is greater on anodized Ti and its alloys than smooth surfaces [38-40]. To improve osteoblast (bone-forming cell) responses and bone tissue growth, surface modification of orthopedic Ti-based implants is an important technique to increase surface roughness and modify chemistry (e.g., by chemical/electrochemical passivation treatments, plasma deposition, ion implantation, and nano-patterning). Osseointegration is the direct structural and functional connection between living bone and the surface of a load bearing artificial implant. Therefore, favorable chemical composition and topography are highly desirable for improving bone tissue responses.

A high-density and high-aspect-ratio nanostructure is the most difficult to fabricate by any conventional top-down nanofabrication technique, but an excellent technique for producing nanostructures is to anodize Ti (Figure 1-12). Anodization (anodic oxidation) is an electrochemical passivation process, which is used to change metal surface texture and to

increase the thickness of the natural oxide layer. The passivated metal often used is an anode and inert materials (such as platinum (Pt) and gold (Au)). When voltage is applied, metal and oxygen ion diffusion occurs leading to the growth of the metal oxide film (Figure 1-13). Specifically, electrons attracted to the anode allow ions at the metal surface to react with water molecules in the electrolyte to form an oxide layer on the metal and hydrogen gas is released from the cathode side. If the diluted electrolyte acid is used, the oxide layer will be partially dissolved and the oxidation surface becomes porous. Various electrolytes have been used in the anodization processes, such as hydrochloric acid (HCl), nitric acid (HNO_3), sulfuric acid (H_2SO_4), and hydrofluoric acid (HF), which produce different size of nanopores and surface roughness of Ti [13, 41]. For example, the 1 N H_2SO_4 anodized Ti (20 V DC for 60 minutes) was non-porous but a few bigger pores were noticed in some regions, whereas, the 1 N H_3PO_4 anodized Ti was rough with a flowery pattern, and the 0.25 N HF anodized surface showed rough granulated debris pattern, with the thickness of the oxide film between 200-400 nm [41].

Anodized Ti has been researched and used in the orthopedic field to increase osseointegration and biocompatibility of implants [38, 42]. In particular, the anodization technique can create uniform nanofeatures of Ti with diameters less than 100 nm [43]. Anodization changes the surface structure of Ti and offers highly interconnected, three-dimensional porosity of the Ti oxide, which is uniform and consistent in order to enhance osteoblast adhesion, proliferation, and differentiation, due to its nanoscaled features which promote protein (such as vitronectin, fibronectin) adsorptions [13, 40, 43]. Huang et al. anodizied Ti in a 5 M NaOH solution at 25 °C with a potentiodynamic anodization treatment, and showed that the number of osteoblast-like U-2 OS cells adhering on TiO_2/Ti_2O_3 increased more than 1.4 times when compared to untreated Ti [44]. Zhu et al. provided evidence that anodized

Ti had higher surface energy and wettability than unanodized Ti [45]. Osteoblast proliferation was increased on anodized Ti (using 0.25 N HF as electrolyte in 20 V DC for 60 minutes) about 37% after 11 days of culture due to its nanoscale surfaces roughness and higher surface energy of anodized Ti [41]. In addition, vinculin aids in the assembly of focal contacts in osteoblast precursor cells by cross-linking and recruiting other proteins to form cell adhesive plagues. Alkaline phosphatase activity by osteoblasts after 7 days and calcium deposited in their extracellular matrix after 3 weeks were 50% higher on nanotubular Ti (anodized in 0.5% HF for 45 min with 20 volts creating nanotubes approximately 80 nm in diameter) compared to non-anodized Ti *in vitro* [46].

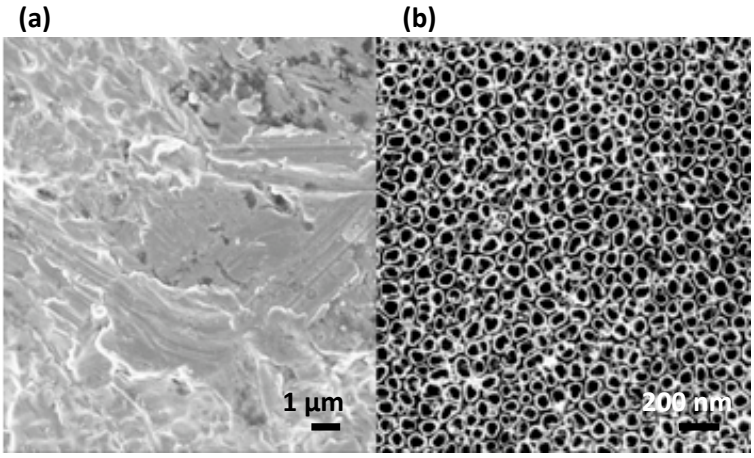

Figure 1-12. Scanning electron microscope images of (a) unanodized Ti and (b) anodized nanotubular Ti [47].

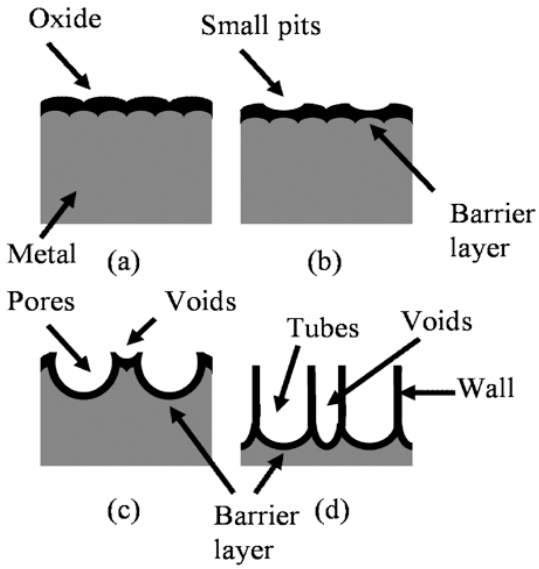

Figure 1-13. Schematic diagram of the evolution of nano-tube-like structures on a Ti surface during anodization in aqueous hydrofluoric acid under constant voltage: (a) oxide formation; (b) pit formation in some concave sites; (c) pore formation and growth under field-enhanced dissolution leading to void formation; and (d) fully developed nanotubes [13].

1.2.2 Carbon Nanotubes

Another nanomaterials used as a composite for tissue engineering is carbon nanotubes (CNTs). Due to their unique electrical, mechanical, chemical, and biological properties, many studies have shown that CNTs are promising materials for bone implantation [48-55]. Iijima discovered CNTs in 1991 [56] which opened up many research efforts in nanotechnology and nanomaterials. The nanosize effect associated with high surface-to-volume ratios of CNTs affect cellular bioactivity, leading to enhanced permeability through the cell membrane with a profound influence on cellular dynamics [57, 58]. CNTs are macromolecules of carbon, classified either as singlewalled carbon nanotubes (SWCNTs) with diameters of 0.4–2 nm or multiwalled

carbon nanotubes (MWCNTs) with diameters of 2-100 nm [56, 59]. However, their length can be up to a few millimeters. CNTs can be produced by a laser furnace, arc, and chemical vapor deposition (CVD). However, CVD is a scalable and controllable method for obtaining high purity CNTs [60]. Moreover, Sato et al. showed the potential for growing MWCNTs by CVD with biometallic particles Ti (and Co as a catalyst), and they revealed that Co combined with Ti, led to a strong mechanical contact between MWCNTs and Ti [61].

CNTs have an electric-current-carrying capacity 1000 times higher than copper and silver [62, 63]. Thus, CNTs have improved electrical properties compared to numerous biomaterials. For instance, CNT-titanium nitride (TiN) nanocomposites, composed of 12% CNTs by volume, exhibited 45% increased electrical conductivity over TiN materials [64]. Since bone regenerates under piezoelectric phenomena, researchers have used CNTs to promote bone growth *in vitro/in vivo* [55, 65, 66]. For example *in vitro*, nanocomposites of polylactic acid and MWCNTs promoted osteoblast differentiation as indicated by 46% increases in calcium deposition in the extracellular matrix and 300% greater the expression of various genes (such as osteopontin, osteonectin mRNA, and osteocalcin) when an alternating current (10 μA at 10 Hz of electrical stimulatin for six hours daily for 21 consective days) was applied to the composite [65, 66].

Moreover, combining MWCNTs with powder precusor materials improves wear resistance and low friction coefficient of laser-surface-alloyed (Ti-6Al-4V) hydroxyapatite composites coatings and have potential applications in the field of coating materials for metal implants under high-load-bearing conditions. [53]. As the amount of CNTs increased in composites, the hardness/strength/fracture toughness of composites increased, while the friction coefficient of as-alloyed CNT reinforced hydroxyapatite composite coatings decreased, suggesting that the hydroxyapatile lubrication effect of these coatings improved. Another study

showed that MWCNTs, reinforced with coatings (Figure 1-14), promoted human osteoblast hFOB 1.19 proliferation *in vitro* compared to hydroxyapatile coatings alone, as osteoblasts were observed near MWCNTs regions (Figure 1-14e and Figure 1-14f) [52]. In addition, SWCNTs, functionalized with phosphates and poly(aminobenzene sulfonic acid), can substitute for collagen to direct the anisotropic crystallization of hydroxyapatite reaching a thickness of 3 mm after 14 days of mineralization, resulting in composites that can be used as a supporting scaffolds for orthopedic applications [67].

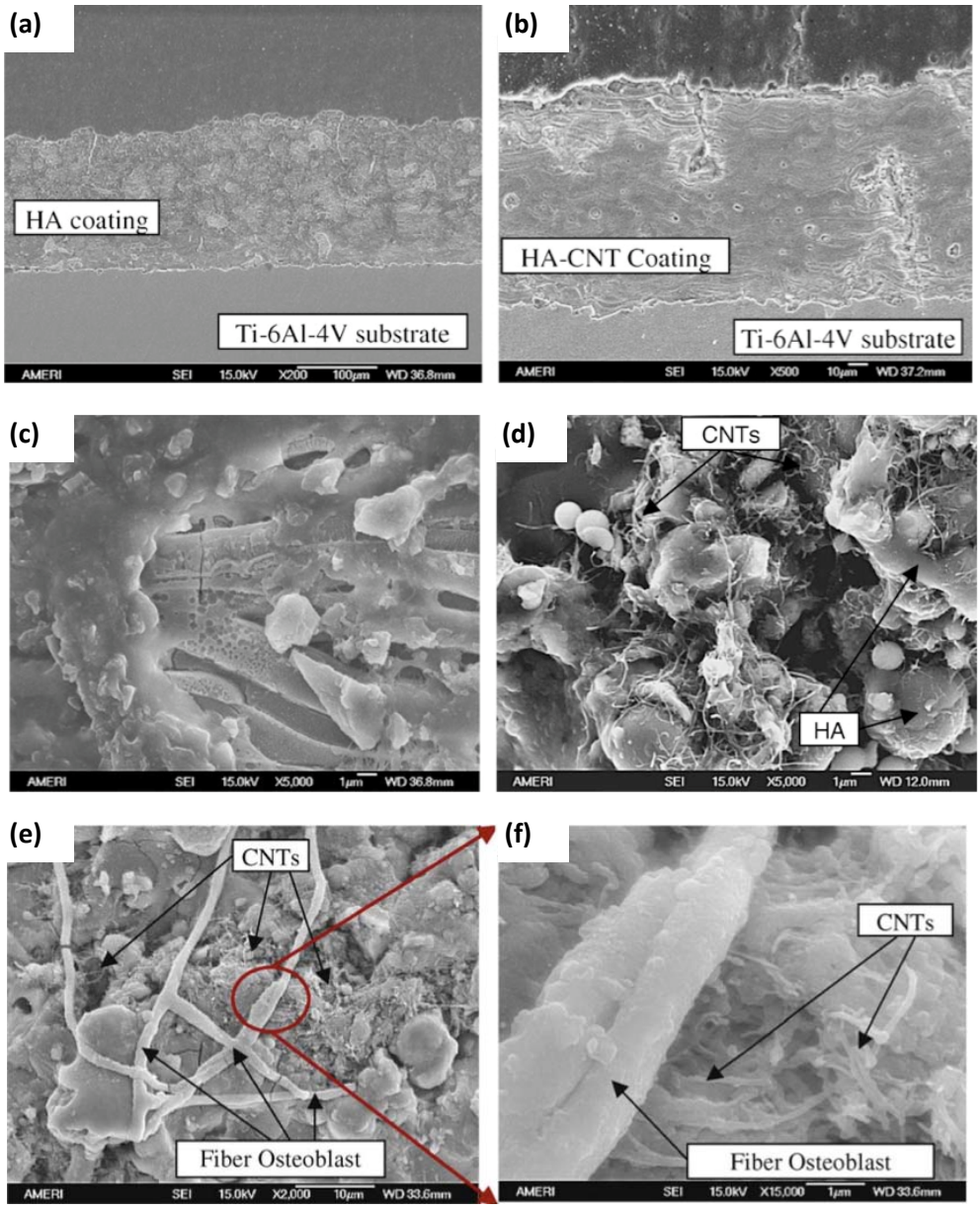

Figure 1-14. SEM cross-sectional images of plasma sprayed (a) hydroxyapatite, and (b) hydroxyapatite-4 wt% CNT coating on Ti alloys; top-surface of plasma sprayed (c) hydroxyapatite coating without CNTs, (d) hydroxyapatite-4 wt% CNT coating (showing the distribution of CNTs), (e) growth of osteoblasts on hydroxyapatite matrix, and (f) cell-growth alongside of CNTs *in vitro* [52].

Not only can CNTs improve hardness and strength of composites, but also they can provide composite nanosurface roughness, improve protein adsorption, which is essential in intial cell adhesion processes, and enhance cell proliferation and differentiation. For example, nanophase PLGA cast of CNF (with diameters = 60 nm) compacts (root-mean-square roughness = 0.265 nm) possessed 50% greater surface roughness when compared with conventional PLGA casts, and promoted osteoblast adhesion after one hour when compared with casts of conventional CNF (with diameters = 200 nm) compacts (root-mean-square roughness = 0.177 nm) due to the higher surface roughness of PLGA casts of nanophase CNFs [68]. Results provided evidence that osteoblast adhesion was more released to carbon fiber diameter than either the presence or absence of the pyrolytic outer layer. In other words, osteoblast adhesion was enhanced as carbon fiber dimensions decreased from conventional to nanophase no matter whether the pyrolytic outer layer was present or not on the CNFs. When carbon fiber groups with and without the pyrolytic outer layer are collectively considered, there was not a consistant difference in the adhesion of fibroblasts to nanophase over conventional dimension fibers. However, when comparing similar diameter fibers from each subsequent surface energy category, the namometer and conventional fiber compacts with a pyrolytic layer had a 16% and 44%, respectively, increase in the fibroblast adhesion over respective formulations without the pyrolytic layer [68]. In addition, the number of osteoblasts adhered more on carbon nanofiber (CNF) micro-patterns than polycarbonate urethane [69].

Decreased macrophage functions were observed by Kim et al. on aligned regions (spacing dimesions varied from 30-100 μm) of CNTs compared to polycarbonate urethane [70]. Osteoblasts mophology extended in all directions within the CNT scaffold that formed on polycarbonate urethane membranes [71]. Specifically, more than 70% of the macrophages

adhered on polycarbonate urethane but less than 30% on the CNT array, and macrophages on CNTs remained low and unchanged from four hours to four days. Khang et al. reported that functions of chondrocytes (cartilage synthesizing cells) were enhanged on electrically stimulated highly dispersed CNTs in polycarbonate urethane compared to stimulated pure PCU [72]. Moreover, chondrocyte adhesion was enhanced more than 50% on CNT/PCU composites compared to PCU alone without electrical stimulation, because CNT/PCU composites have greater nanometer roughness, were more hydrophilic (than pure PCU), and were observed to promote greater amounts of initial fibronectin adsorption. Another study showed that osteoblasts significantly enhanced their adhesion on vertically aligned CNTs arrays possibly sensing nanoscaled surface features [73]. Moreover, Zanello et al. showed that CNTs are suitable for osteoblast proliferation and bone formation by culturing osteosarcoma ROS 17/2.8 cells on single/multiwalled CNT scaffolds with/without surface modification [51]. Human osteoblast-like (Saos2) cells grown on the MWCNT scaffold showed a higher cell density and transforming growth factor-β1 concentration compared with polystyrene and polycarbonate scaffolds [74].

Recent studies have clearly indicated great promise for carbon nanomaterials to be used as advanced drug carriers, imaging probes and biomedical devices where the use of bulk carbon films or fibers was proven to be inadequate [75]. Importantly, MWCNTs are a promising material for electrochemical biosensors because they also possess a relatively well-characterized behavior in terms of electron transport [76-79]. CNTs with properties of excellent conductivity, metal and semiconductors, especially biocompatibility, have become suitable candidates for the promotion of heterogeneous electron transfer [80]. Electrochemical and spectroscopic measurements show that MWCNTs had increased hemoglobin-polyurethane elastomer (PUE),

changed PUE morphology, improved the conductivity of the PUE film, and thus facilitated direct electron transfer between the immobilized hemoglobin and the conductive surface through the conducting tunnels created by the presence of MWCNTs [81]. Specifically, the hemoglobin/PUE/MWCNT/pyrolytic graphite electrode gave stable and well-defined redox peaks at -285 and -386 mV at 100 mV/s in 0.1 M PBS (pH 7.0), while no clearly defined peaks were observed for the bare pyrolytic graphite electrode and PUE/pyrolytic graphite electrode. Moreover, the glucose biosensor based on the aligned CNTs nanoelectrode ensemble was mediator-free and membrane-free displaying ultrasensitivity to glucose [82], while glucose oxidase attached on the individual SWNTs were used as versatile biosensors [83].

Moreover, cells transduced and transmitted a variety of chemical and physical signals to produce specific substances and proteins within specific tissues and organs. *In situ* sensing of proteins from specific cell induction processess can be employed as a signal of specific cellular responses or bone regeneration. Clearly, these studies encourage the use of CNTs as novel *in situ* sensors to measure bone tissue response surrounding orthopedic implants. In summary, this exciting new nanomaterial (CNTs) may become a powerful tool in bone tissue engineering in terms of their biologically-inspired nanofeatures, superior mechanical properties, and high electrical conductivity to stimulate bone growth or to sense cellular behavior. Continuing these careful studies on CNTs may reveal more potential for this novel biomaterial for engineering biocompatible nanomaterials and nanodevices to benefit orthopedic applications.

1.2.3 Conductive Electroactive Polymers

1.2.3.1 Biocompatibility of Polypyrrole

In the development of drug eluting sensors on bone implants, conductive polymers have advantages over non-conductive polymers since they are dynamic and are responsive to a voltage stimulus. Polypyrrole (PPy) is an intrinsically conductive polymer which can be electrochemically synthesized as a thin and soft film on other conductive materials. PPy has been studied for various applications (e.g., corrosion protection, electrochemical biosensors, electrode coatings, bioelectronics, solid-state devices, and patterned circuits) [84-87]. For use in biomedical applications, PPy has been used to develop drug delivery systems, implantable medical devices for electrically stimulating cells, and template neuronal networks [88-90]. PPy has the potential to electrically stimulate tissues, which may manipulate cellular behavior, and enhance various cell growth (e.g., osteoblasts [91], mouse bone marrow cells [92], smooth muscle cells [93], neurons [94-96], endothelial cells, myofibroblasts [97, 98], fibroblasts [86, 99, 100], cardiac myocytes [101], etc.). For example, Shi et al. used a conductive biodegradable composite made from a polylactide matrix and PPy nanoparticles to improve fibroblast growth via an electrical stimulus (DC 100 mV/mm) [86]. They found that electrical current (DC) ranging from 2.5 to 250 μA/mm had no effect on the viability of cells cultured on the gold-coated Petri dish, and fibroblast viability improved approximately 220% after two hours of culture and 400% after 24 hours of culture when compared to non-stimulated films ($p < 0.05$). Lee et al. showed that PPy can be used to promote human umbilical vein endothelial cell spreading after three hours of culture, by grafting PPy-α-COOH with the cell-adhesive arginine-glycine-aspartic acid (RGD) motif to increase cellular bioactivity *in vitro* [102]. The results indicated that human

umbilical vein endothelial cells improved viability at one, two, and three hours of culture on RGD-grafted PPy-α-COOH compared to ungrafted PPy-α-COOH (about 41%, $p < 0.05$) and unmodified PPy (about 88%, $p < 0.05$), as well as about 33% higher on PPy-α-COOH than on PPy. *In vivo*, the hematoxyline-pholoxine-safran stained samples explanted at 7 days from 144 male Sprague-Dawley rats, showed the mild acute phase inflammation which was similar among the polytetrafluoroethylene, rubber, PPy-coated poly(d,l-lactide-co-glycolide), poly(d,l-lactide-co-glycolide), PPy nanoparticle/poly(d,l-lactide) composite, and poly(d,l-lactide) (Table 1-3) [103]. Among the pure biodegradable materials and those containing PPy, the PPy/PDLLA membrane showed a slightly higher tissue response between day 7 and day 30. Importantly, Wang et al. concluded that the presence of PPy, whether in the form of surface coating or as nanoparticles induced no abnormal inflammation, when compare with those containing no PPy [103].

Table 1-3. Histological observations of the tissue reactions surrounding implants [103]. Week 1 constituted the acute phase, characterized by the presence of the greatest number of total inflammatory cells, including a large amount of PMN cells and lymphocytes. The transition phase began at week 3 and featured a decline in the number of total inflammatory cells and the appearance of foreign body giant cells. The chronic phase began at 4 weeks, along with the increasing number of non-inflammatory cells such as fibroblasts. The capsules began forming from day 7 and the quantity of collagenous tissue increased with implantaion time.

Implants	Phase of inflammation	Time of implantation	Intensity of the reaction	Fibrin or collagen generation	Thickness of capsule at 4 months (μm)
Polytetrafluoroethylene	Acute	Day 3 and 7	Mild	Fibrin + to +++	50 ± 2
	Transition	Day 14	Minimal	Fibrin + Collagen +	
	Chronic	Day 30 to 4 months	Severe	Collagen ++	
			Severe		
Rubber	Acute	Day 3 and 7	Severe	Fibrin ++++	251 ± 3
	Transition	Day 14	Severe	Fibrin +++ Collagen +	
	Chronic	Day 30 to 4 months	Moderate to Severe	Collagen ++	
PPy-coated poly(d,l-lactide-co-glycolide),	Acute	Day 3 and 7	Mild	Fibrin ++	71 ± 2
	Transition	Day 14	Mild	Fibrin ++ Collagen +	
			Mild		
	Chronic	Day 30 to 4 months		Collagen ++	

Implants	Phase of inflammation	Time of implantation	Intensity of the reaction	Fibrin or collagen generation	Thickness of capsule at 4 month (μm)
Poly(d,l-lactide-co-glycolide),	Acute	Day 3 and 7	Mild	Fibrin + to +++	Specimen degraded completely
	Transition	Day 14	Mild	Fibrin ++ Collagen +	
	Chronic	Day 30 to 4 months	Minimal to mild	Collagen ++	
PPy Nanoparticle/poly(d,l-lactide) composite	Acute	Day 3 and 7	Mild to moderate	Fibrin +++	79 ± 3
	Transition	Day 14	Moderate	Fibrin ++ Collagen +	
	Chronic	Day 30 to 4 months	Mild	Collagen +++	
Poly(d,l-lactide)	Acute	Day 3 and 7	Mild	Fibrin + to +++	73 ± 3
	Transition	Day 14	Mild	Fibrin ++ Collagen +	
	Chronic	Day 30 to 4 months	Minimal to mild	Collagen +++	

For drug delivery, Wadhwa et al. investigated the release profiles of Dex from PPy films developed by electrodeposition and the effect of Dex embedded within PPy films on astrocyte and neuron density *in vitro* [88]. Dex was released at 0.5 μg/cm^2 concentration during one CV cycle and a total of almost 16 μg/cm^2 Dex was released after 30 CV cycles. The results showed that the number of astrocytes decreased significantly on PPy embedded Dex when compared to the PPy films without Dex, and there was no significant difference between before and after

electrical stimulation on PPy films embedded with Dex. The final concentration after electrical stimulation of Dex was about 1 μM. For neurons, they observed 35% higher neurite outgrowth when neurons were exposed to released Dex from PPy films than without electrical stimulation. Although PPy has emerged as a promising candidate material with substantial potential for biomedical applications and drug delivery [88], few studies have investigated its possible role in decreasing infection and inflammation using PPy in orthopedic applications.

1.2.3.2 Electrochemical Polymerization

Specifically, polymerization of pyrrole can be initiated by electrochemical or chemical oxidation of an adsorbed pyrrole monomer [104]. These three to five pyrrole residual constructs function as a single radical cation and react with neutral monomers to extend the polymer chain in a nucleophilic environment of solvent molecules and anions [96]. To preserve local electrical neutrality, the positive charge of PPy (of three to five monomers) is compensated by coexisting anions, leading to electrostatic interactions which entrap electrolyte anions positioned interstitially in the growing structure of the polymer chains [105, 106]. Common non-bioactive dopants used include poly(styrenesulfonate) (PSS), poly(l-glutamin acid) (PGlu) [96], dodecylbenzenesulfonic acid sodium salt (DBS) [100], and sodium dodecyl sulfate (SDS) [86]. *In situ* electropolymerization is also advantageous for immobilizing a wide range of biological agents (e.g. laminin peptide sequences, hyaluronic acid, enzymes (oxidase and dehydrogenases), red blood cells, human serum albumin, neurothrophins, etc.) in PPy on implant surfaces [107] [108]. For example, Stauffer et al. combined the laminin fragment with PPy to promote neuronal attachment and growth but reduce astrocyte (glial scar tissue-forming cells) adherence [94].

Although PPy in the doped state is chemically very stable, the transport properties of PPy films can be altered reversibly due to its reduction-oxidation (redox) properties, which involve the charging and discharging of the polymer and the movement of charged molecules in and out of the film [107, 109]. Based on the redox and actuating properties (expansion and contraction) of PPy films, drugs can be electrically induced and controlled to be released in a programmed manner. For example, Wadhwa et al. electrodeposited a PPy film (at a thickness of 50 nm) on gold-coated plastic coverslips (0.77 cm^2), and released an anti-inflammatory drug (dexamethasone) at about a 0.5 $\mu g/cm^2$ concentration after one cycle of cyclic voltammetry and a total of almost 16 $\mu g/cm^2$ after 30 cycles [88]. In other words, nanostructured bioengineered conducting polypyrrole coatings created through electrodeposition can also be used as an electrically-controlled drug delivery vehicle on command for biomedical applications.

1.3 Pharmaceutical Administration

Drug delivery is the method of administering a pharmaceutical compound to achieve a therapeutic effect in humans or animals. The use of nanotechnology can modify drug release profiles, distribution, and improve drug efficacy and safety. There are two main points for this section: (i) the use of antibiotic and anti-inflammatory drugs in orthopedic applications, (ii) the current therapeutic and release platforms for the treatment of infection and inflammation, and (iii) the bioactivity of drugs (such as dexamethasone) to promote bone growth.

1.3.1 Infection and Antibiotics

The failure of osseointegration around orthopedic implants may result from bacterial adhesion, colonization of biomaterial surfaces, and adjacent tissue damaged by microorganisms. Moreover, once a biofilm forms on an orthopedic implant, bacteria become resistant to antimicrobial treatment, thus, requiring the removal of the device before continued infection occurs. During the first two years after the surgery, infection has been reported as one of main causes for revision surgery [110]. Despite modern advances in surgical technique, including careful procedures with laminar airflow operating suites and standardized antibiotic protocols, at least 0.5-1.0% of all hip implants need to be replaced because of infection [111]. On average, about 5% of initially inserted internal fixation devices become infected and the average cost of combined medical and surgical treatment is estimated at US$ 15,000 [112]. The interstitial milieu surrounding a prosthetic implant is known to represent a region of local immune depression, or as an immuno-incompetent, fibro-inflammatory, integration-deficient zone. Bacteria can amplify the wear phenomenon because they have a significant effect on the degradation of implant materials and the exposed surface may act as catalytic surfaces and interact with cellular activities, therefore enhancing the inflammatory process [113]. Moreover, the presence of persistent, although relatively dormant, bacteria can enhance local bone resorption and osteolysis induced by wear debris, which is considered the main factor for aseptic loosening [114].

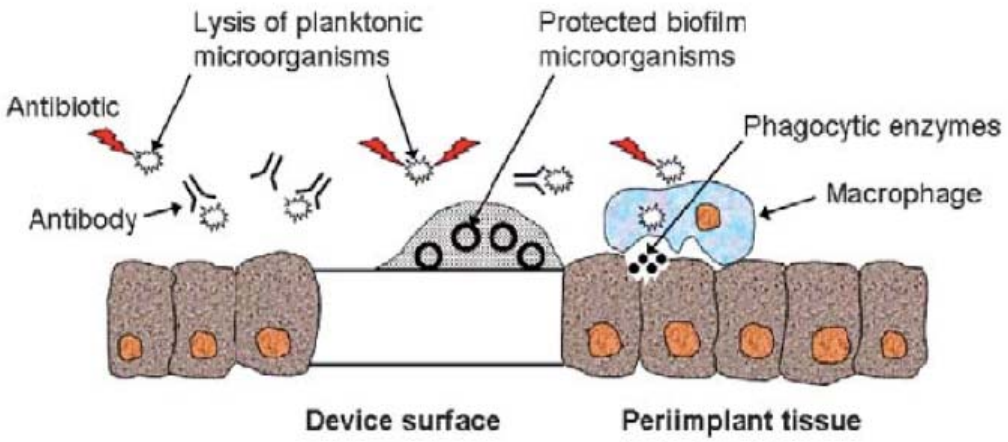

Figure 1-15. Representation of planktonic microorganisms, killed by antibiotics and the immune system, and biofilm microorganisms, attached to a surface and protected in an extracelluar matrix [112].

The pathogenesis of infection around orthopedic implants is related to microorganisms growing in a biofilm, and reducing these infections has proven difficult [112]. Bacteria form a permanent, irreversible, non-diffusible biofilm on orthopedic implants which protects them against antibiotic treatments (Figure 1-15) [115]. Septic loosening of implants is also a contributor to implant failure after orthopedic implant surgery, requiring implant replacement if a biofilm forms. The risk for orthopedic device-related infection is estimated at 1-2%, whereas it may be expected that the real number is markedly higher since detection of infection is not always feasible [116]. Moreover, implant infection may exceed 30% after fixation of open fractures [112]. Four out of five implant related infections are due to *Staphylococci* and two out of three are due to periprosthetic infections, principally caused by *Staphylococcus aureus* and *Staphylococcus epidermidis* [115]. Adherence of *Staphylococcus aureus* to bone implants is mediated by numerous proteins including fibronectin, fibrinogen, fibrin, collagen, laminin,

thrombospondin, and bone sialoprotein [117]. No single routinely used test is sufficiently accurate to diagnose infection. Therefore, a combination of clinical, laboratory, histopathology, microbiology, and imaging studies is usually required [112]. The most commonly used preoperative tests include hematologic screening tests (such as determining white blood cell count, erythrocyte sedimentation rate, C-reactive protein presence, and amounts of plasma fibrinogen), plain radiographs, and radionuclide imaging [111]. Moreover, cultures and histological examination of periprosthetic tissues can be performed.

Treatment problems for infection include extended antibiotic therapy, multiple surgical procedures, and long-term disability for the patient. The treatment goals of infection associated with fracture-fixation devices are bone consolidation and prevention of chronic osteomyelitis. If no antibiotic with efficacy on adherent bacteria is available, treatment with implant retention is generally only suppressive, operating until the implants can be definitively removed. Suggested antimicrobial treatment according to the pathogen and its antimicrobial susceptibility is summarized in Table 1-4. The suggested treatment duration is three months in cases of device retention and six weeks after removal of the infected fixation device [118]. Intravenous treatment should be administered for the first 2-4 weeks, followed by oral therapy to complete the treatment course [112].

Antimicrobial treatment requires a combination of an adequate surgical procedure combined with prolonged antimicrobial therapy treatment, however, local drug delivery (such as antibiotics loaded into bone allografts, polymerized bone cement, hydroxyapatite, and nanoporous titanium) has also been studied to treat an infected bone implants [46, 116, 119-124]. Treating infection can be made more efficient by embedding drugs onto the surface of the implant and controlling the release of antibiotics (e.g., aminoglycosides, penicillins, vancomycin,

gentamicin, cephaloridine, etc.) by external electrical control from under the biofilm or for local antibiotic delivery to the interface of implants. Yet, few orthopedic implants release antibiotics via this process.

Table 1-4. Treatment of implant-associated infection [112]. PO = orally; IV = intravenously; IM = intramuscularly, forte tablet: trimethoprim 160 mg plus sulfamethoxazole 800 mg.

Microorganism	Antimicrobial Agent[1]	Dose	Route
S. aureus or coagulase-negative staphylococci			
• Methicillin-susceptible	Rifampin plus	450 mg every 12 h	PO/IV
	(flu)Cloxacillin[2]	2 g every 6 h IV	IV
		for 2 weeks, followed by	
	Rifampin plus	450 mg every 12 h	PO
	Ciprofloxacin or	750 mg every 12 h	PO
	Levofloxacin	750 mg every 24 h to 500 mg every 12 h	
• Methicillin-resistant	Rifampin plus	450 mg every 12 h	PO/IV
	Vancomycin	1 g every 12 h	IV
		for 2 weeks, followed by	
	Rifampin plus	450 mg every 12 h	PO
	Ciprofloxacin[3] or	750 mg every 12 h	PO
	Levofloxacin[3] or	750 mg every 24 h to 500 mg every 12 h	PO
		400 mg every 24 h	
	Teicoplanin[4] or	500 mg every 8 h	PO
	Fusidic acid or	1 forte tablet every 8 h	IV/IM
	Cotrimoxazole or	100 mg every 12 h	PO
	Minocycline		PO
Streptococcus spp.	Penicillin G[2] or	5 million U every 6 h	IV
	Ceftriaxone	2 g every 24 h	IV
		for 4 weeks, followed by	
	Amoxicillin	750-1000 mg every 8 h	PO

Microorganism	Antimicrobial Agent[1]	Dose	Route
Enterococcus spp.	Penicillin G or	5 million U every 6 h	IV
(Penicillin-susceptible)	Ampicillin or Amoxicillin	2 g every 4−6 h	IV
	plus Aminoglycoside[5]		IV
		for 2-4 weeks, followed by	
	Amoxicillin	750−1000 mg every 8 h	PO
Enterobacteriaceae	Ciprofloxacin	750 mg every 12 h	PO
(quinolone-susceptible)			
Nonfermenters (eg,	Cefepime or Ceftazidime	2 g every 8 h	IV
Pseudomonas aeruginosa)	plus Aminoglycoside[5]		IV
		for 2-4 weeks, followed by	
	Ciprofloxacin	750 mg every 12 h	PO
Anaerobes6	Clindamycin	600 mg every 6−8 h	IV
		for 2-4 weeks, followed by	
	Clindamycin	300 mg every 6 h	PO
Mixed infections	Amoxicillin/Clavulanic acid	2.2 g every 8 h	IV
(without Methicillin-resistant	or Piperacillin/Tazobactam	4.5 g every 8 h	IV
Staphylococci)	or Imipenem	500 mg every 6 h	IV
	or Meropenem	1 g every 8 h	IV
		for 2−4 weeks, followed by individual regimens according to antimicrobial susceptibility	

[1] For total duration of antimicrobial treatment see text. [2] In patients with delayed hypersensitivity, cefazolin (2 g every 8 h IV) can be administered. In patients with immediate hypersensitivity, penicillin should be replaced by vancomycin (1 g every 12 h IV). [3] Methicillin-resistant *S. aureus* (MRSA) should not be treated with quinolones since antimicrobial resistance may emerge during treatment. [4] First 1−3 days of treatment, Teicoplanin dose should be increased to 800 mg IV. [5] Aminoglycosides can be administered in a single daily dose. [6] Alternatively, Penicillin G (5 million U every 6 h IV) or Ceftriaxone (2 g every 24 h IV) can be used for Gram-positive anaerobes (e.g., *Propionibacterium acnes*), and Metronidazole (500 mg every 8 h IV or PO) for Gram-negative anaerobes (e.g., *Bacteroidesspp*).

1.3.2 Foreign Body Inflammatory Responses and Anti-inflammatory Drugs

There is an enormous population of patients with orthopedic implants, for example in the United States alone, total hip and knee arthroplasties account for over half a million interventions each year [125]. The loosening of an implant over time can be caused by erosion of metallic surfaces through wear leading to the need for revision surgery. Wear particles trigger the invasion of inflammatory cells (e.g., polymorphonuclear leukocytes, lymphocytes, monocytes, and macrophages) and eventually fibroblasts (fibrous-forming cells) to the implant-tissue interface, which causes acute-chronic inflammation and fibrosis, respectively [126]. A reduction in the chronic phase of inflammation may adequately reduce foreign body reactions and scar tissue formation, which can cause fibrous (not bone) formation and loosening of implants. Moreover, destructive erosion of bone (bone loss or osteolysis) is a serious complication of several chronic inflammatory diseases. There are three examples, including rheumatoid arthritis, periodontal disease and peri-implant osteolysis, where inflammation and osteolysis are seen closely associated with a local chronic inflammatory reaction. Rheumatoid arthritis affects approximately 2% of the world's population [127]. Additional surgery to removal the inflammatory soft tissue is an effective way to stop these diseases, but increases the time of rehabilitation. Immune activation by an implant can have a key role in the development of arthritis. Implants usually have been implicated in the development of allergic dermatitis, urticaria and vasculitis [128]. Immune-system activation after implantation was seen either in response to the metallic implant itself or to particulate debris generated by the implant [129]. The degradation products of metallic biomaterials include particulate wear debris, colloidal organometallic complexes, free metallic ions, inorganic metal salts or oxides, and precipitated

organometallic storage forms [130]. Microbial colonization of implants and infection of the peri-implant tissues can cause peri-implant bone destruction and may lead to implant failure. The peri-implantitis (an inflammatory process affecting the tissues around an osseointegrated implant, resulting in loss of supporting bone) lesion can be diagnosed on a radiograph by detecting bone loss around the implant [131]. Implant mobility indicated the final stage of the peri-implant disease, characterized by complete loss of the direct bone to implant interface. Importantly, the peri-implant disease should be recognized earlier to allow intervention before a substantial portion of the supporting bone is lost. Therefore, diagnostic procedures used around implants should include sensitive parameters to detect early signs and symptoms of infection.

Various pharmaceuticals have also been used to combat these problems. A synthetic glucocorticoid, such as dexamethasone (Dex), is used clinically in the treatment of rheumatoid arthritis, inflammatory bowel diseases, post-transplantation immunotherapy, and other inflammatory diseases [132]. It suppresses the immune response (by reducing lymphatic activity), stimulates osteogenic differentiation, and promotes protein, fat, and carbohydrate metabolism [133, 134]. Additionally, as an anti-inflammatory substance, Dex reduces numerous pro-inflammatory cytokines, including IL-1β, IL-6, INF-γ and TNF-α [88]. However, some serious side effects have been observed in the clinic through the systemic administration of Dex, such as glucocorticoid-induced osteoporosis (bone loss) observed through orally taking Dex due to high systemic exposure [132]. Therefore, drug administration by local delivery can decrease system toxicity and improve drug efficiency.

1.3.3 The Use of Glucocorticoids and Osteoblast Functions

Glucocorticoids can be influence osteoblast differentiation, density, and function. Since glucocorticoid receptors are found in osteoblasts, growth plate chondrocytes, osteocytes, and at several locations within the bone marrow, synthetic glucocorticoids (such as Dex) affects cell functions [135]. The effects of Dex on osteoprogenitor cell proliferation and phenotypic development also depends on dosage and timing of treatment [136]. Dex has been shown to be a potent stimulator of osteoblastic differentiation of bone marrow osteogenic stromal cells after 2-3 days of treatment reaching a maximum at 7-14 days [137]. Another study suggested that the addition of Dex to marrow-derived cells early in the culture period did not inhibit proliferation greatly enhanced the presence of the osteoblastic phenotype in a rat model [138]. Ryan et al. showed that the withdrawal of Dex at 3 and 10 days enhanced the proliferation of bone marrow stromal cells [139]. Beloti et al. concluded that Dex must be used in culture after first passage of human bone marrow cells to allow osteoblast differentiation demonstrated by reduced cell proliferation and increased alkaline phosphatase activity and bone-like formation [140]. In addition, Dex enhanced *in vitro* bovine vascular smooth muscle cell calcification, which is associated with atherosclerotic lesions, several phenotypic markers for osteoblastic differentiation and increased gene expression of a key transcription factor in osteoblastic differentiation [141]. Since Dex has a significant effect on osteoblast functions (proliferation and differentiation) *in vitro*, the proper concentration and time of treatment can be used as positive control in the drug studies to enhance osteoblast functions to treat osteoporosis (or bone loss).

1.3.4 Drug Delivery Strategies

The most common drug administration routes are oral, transdermal, and nasal delivery methods. However, therapeutic proteins have some disadvantages, limiting their clinical use, including: their short half-lives *in vivo*, low oral bioavailability, and frequent injections leading to oscillating drug concentrations in the patients' blood. These problems can be overcome through controlled release system in order to improve drug effectiveness. However, to further circumvent these problems are drug adsorption and metabolism in order to control proper release dosage. Oral administration and targeted and local drug deliveries can take advantage of controlled drug delivery technology. Ideally, if the drug is released independently with time, the drug concentration can be controlled in the body perfectly through other system parameters.

Micro/nano-encapsulation techniques embeds proteins within micro/nanopores of polymers, releasing them through diffusion or channels. This method protects the drug from degrading and promotes delivery to specific sites. Moreover, they can be designed that the dose and release rates are changed by altering parameters of the polymeric controlled drug release system. This depends on what kind of polymers are used. In non-biodegradable polymer systems, the drug is mainly released by diffusion through polymer membranes. In contrast, the drug is released by both desorption and diffusion through the polymer in biodegradable polymer systems. In order to obtain release kinetics more closely to that of the zero-order, as shown in Figure 1-16 (constant release rate with time to obtain an optimal drug bioactivity), hybrid systems with rate controlling barriers (called reservoir systems) may be an alternative. They consist of outer membrane layers and bioactive drugs in a biodegradable polymer matrix. In the reservoir system, the release experiment is completed under perfect sink conditions to provide zero-order release kinetics. In designing the system, the (later) release kinetics should

be expected to be time-dependent and the initial release kinetics (normally drops exponentially as $t^{|1/2|}$) should be controlled by time-lag and burst effects [142]. The sudden fast release of the drugs and induction period for the release of drugs are important parameters for initial release kinetics; both can be controlled by a matrix-degraded-controlled system.

Importantly, the properties/chemistry of biodegradable polymers are imperative in designing matrix-controlled release systems (such as reservoir systems through their degradation). The degradation mainly occurs by hydrolysis. Thus, the composition of monomers, types of each monomer, polymerization, cross-linking, and functional/additional groups of the polymer backbone vary according to their chemistry. As such, poly(lactic-co-glycolic acid) (PLGA) are bioerodible polymers, widely used as bone scaffolds for bone tissue engineering, and embedded or cross-linked with drugs for drug delivery devices. However, the ratio between two monomers can be varied. The hydrophobicity of PLA limits water uptake of thin films to about 2% and reduces the backbone hydrolysis as compared to PGA [17]. Several implantable, controlled release formulations based on copolymers (PLGA) have already become available. Encapsulating the drug within a biodegradable copolymer can release the drug as desired and in a predictable manner when the particles reach the targeted site, however, a polymeric-drug delivery system with external energy (such as using voltages or magnetic fields) can also improve drug efficacy and safety. Systemic injections have the obvious disadvantage of exposing the whole body to high dosages of the drug and its potential toxicity. These passive drug-eluting systems cannot last as long as needed in applications nor can they release appropriate doses in response to the dynamic change of the local biochemical environment. Local delivery of drugs at the implant-tissue interface can be most effective.

For example, the anionic drugs saliclaten (a phenolic phytohormone) and naproxen (a non-steroidal anti-inflammatory drug) and cationic drug dopamine (used as a neurotransmitter and be used as a medication that acts on the sympathetic nervous system) have been incorporated into conducing polymer films and released by an electrical potential stimulus in a controlled way [143]. Adenosine triphosphate (a multifunctional nucleotide, ATP) was released from PPy upon sensing bioactive molecules in the solution [144]. Ghassabian et al. suggested that magnetic albumin microspheres, containing 13% w/w Dex, can be retained at their target site *in vivo*, following the application of a magnetic field, and are capable of releasing drugs for an extended period of time [145]. Results showed that the presence of a 8000 G magnetic field in a flow rate (0.5 cm/s) equal to that of the blood flow rate in capillaries for 15 min significantly ($p < 0.05$) released more Dex than those in the absence of the magnetic field. Therefore, externally-controlled implantable drug delivery devices can reduce the chance for underdosing, overdosing, and increase patient compliance significantly.

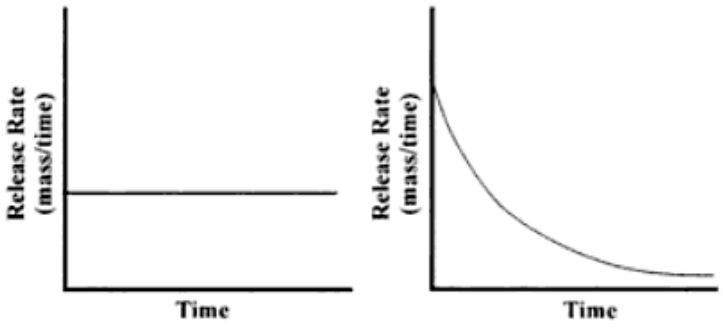

Figure 1-16. Comparion between zero-order mass release and first-order mass release with time showing constant release in zero-order systems compared with decreasing release in first-order systems [146].

To develop a polymeric-drug delivery system in a controlled manner by means of electrical or magnetic fields, the polymer has to respond to such an external force, so that it can be administrated or altered. Drug release profiles influenced by diffusion are hard to control and synthesize. The biodegradable implantable drug delivery system cannot release appropriate doses in response to the dynamic change of the local biochemical environment. Electroactive polymers can be further integrated on a chip for micromanipulation and drug delivery [147]. Thus, to improve drug release in a controllable manner, utilizing the actuating properties of PPy can control drug release by applying electrical potentials. Indeed, release potentials are consistent with the redox and actuating properties of PPy, this leads to a controlled manner of drug release by the application of a voltage. There is a significant challenge in the design and manufacturing of a drug eluting system that possesses the ability to control release kinetics in response to electrical stimulation for a specific biological response from implantation (such to infection or inflammation). Drugs embedded on a bone implant surface can enhance the platform of drug deliver systems for orthopedic implants. The external controlled-release drug delivery system with applied potentials allows one to tailor drug release to match the needs of the physiological system. The PPy delivery system allows for on-command, precise, and local release of drugs from the Ti surface. Moreover, there are the preexisting circuits that can be designed with a microcontroller release on demand using applied voltages, and such circuitry can be integrated with a conducting PPy coated Ti to be used clinically.

1.4 Biomedical Telemetry

A telemetric device for orthopedic implants has been used since 1966 by Rydell as a strain-gauge hip prosthesis, cable-connected to an external measuring equipment [148]. Then, *in vivo* load measurements with hip joints started in 1988. Typically, the telemetry system with a small implantable transmitter used wireless communication with an external computer system. The data was transmitted at high frequency or radio-frequency (RF) pulses (Figure 1-17). Two hip-joint implants with 4-channel transmitters [149] and five hip-joint implants with 8-channgel transmitters [150] were implanted in seven patients for the measurement of forces [148].

Recently, Graichen et al. developed an implantable 9-channel telemetry system for *in vivo* load measurements for orthopedic implants [151]. The semiconductor strain gauges (KSP-1–350-E4, KYOWA, Tokyo, Japan) were placed at the inner circumference of the neck of orthopedic implant cavity. A small loop antenna outside the implant (the pacemaker feedthrough forms a single loop antenna outside of the Ti at one end of the implant) is used to transmit the RF pulses to the external receiving antenna (Figure 1-17). The RF receiver of the external device (TELEPORT, as shown in Figure 1-17) was connected to a microcontroller to analyze the measured voltages. Finally, computer software interpreted the data sent from the microcontroller to display the real-time load components. Graichen et al. used a Ti alloy (Ti4Al6V) for the neck and stem, cobalt-chromium-molybdenum (CoCrMo) for the tightly fitted head, and polyether ether ketone (PEEK) for the cap at the lower end of the stem (Figure 1-18). The six strain gauges and the transmitter circuit were arranged inside the neck cavity with an inner diameter of 9.5 mm. The secondary power coil (30-mm length, 6-mm diameter) was combined with the AC-DC circuit and fixed in a second cavity at the lower end of the stem. The rectified power supply voltages were connected to the transmitter circuit by two cables through

a drill. Another pair of cables connected the two-lead feedthrough at the center of the lower end plate to the transmitter. The antenna loop for RF transmission consisted of a niobium wire. The wire was electron-beam welded and protected against mechanical damage by a PEEK cap, and the upper and lower endplates of the implant were also welded. These instrumented prototypes were used in laboratory tests to investigate the measurement accuracy for all six load components [151].

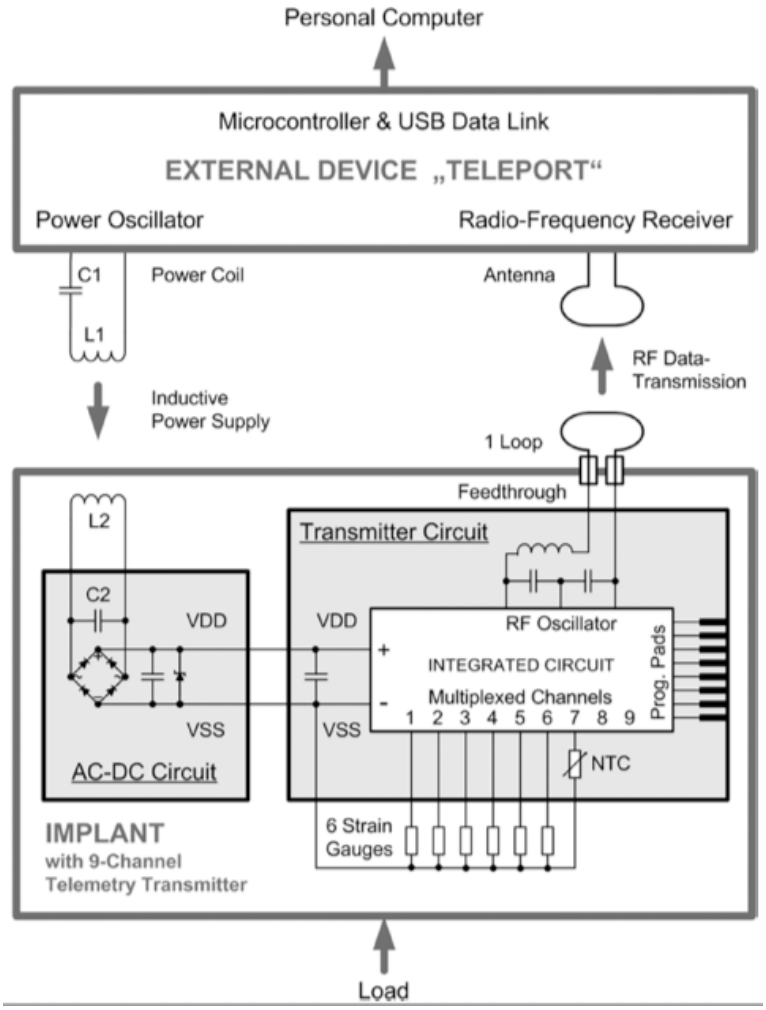

Figure 1-17. Block diagram of the implantable telemetry system for measuring the implant load [151]. Coupled coils are used as an inductive power supply (alternating magnetic field) and near-field RF data transmission.

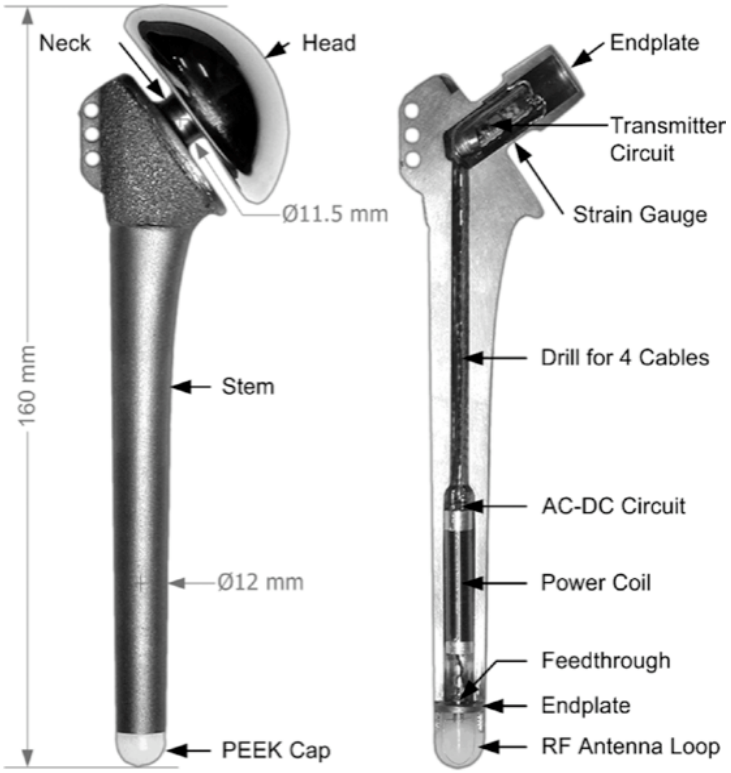

Figure 1-18. Instrumented shoulder endoprosthesis (left) and a cut model with measurement electronics (right) [151].

Biomedical telemetry is a special area of biomedical instrumentation that permits transmission of physiological information from an often inaccessible location to a remote monitoring computer. By using biomedical telemetry, the physiological data (such as biopotentials, temperature, mechanical events, pH, pressure, etc.) of humans and animals can be monitored, supporting future remote-biomedical diagnosis. Its implementation will be necessary to the eventual integration of the current results to clinical applications.

1.5 Objectives of the Present Work

The objective of this research is to develop sensing bio-nanomaterials to improve orthopedic diagnostics rather than the current-medical imaging techniques (such as X-rays or bone scans), and to create local drug delivery systems to enhance bone implant success throughout the patient's lifetime. This dissertation includes the development and examination of the following: (i) multiwalled carbon nanotubes (MWCNTs) grown out of nanotubular anodized Ti used to sense bone growth, infection, or scar tissue growth next to an implant *in situ*; and (ii) biodegradable and conducting electroactive polymeric systems (polypyrrole-polyD,L-lactic-*co*-glycolic acid, PPy-PLGA) to deliver antibiotic (penicillin/streptomycin) and anti-inflammatory drugs (dexamethasone) through diffusion and electrical stimulation to obtain a desired dose and maintain the bioactivity of the therapeutic agent. Moreover, the cytocompatibility of these materials with osteoblasts and fibroblasts were also extensively investigated.

1.5.1 Multiwalled Carbon Nanotubes in Electrochemical Sensors

Firstly, MWCNTs were grown out of anodized Ti nanotubes as a template in order to form a stronger interconnection between MWCNTs and Ti by using a cobalt-catalyzed CVD technique. Then, the adhesion, proliferation, and differentiation of osteoblasts (bone-forming cells) were determined using biologically quantitative assays and osteoblast morphology/number analysis. Moreover, MWCNT-Ti were characterized by high-resolution transmission electron microscopy, Raman spectroscopy, and contact angle measurements. Importantly, the role of MWCNTs in enhancing the sensor performance was studied. Specifically, the redox reactions of iron (II/III)

and the osteoblast extracellular components at the surface of Ti, anodized Ti, and MWCNT-Ti were investigated.

1.5.2 Polypyrrole in Voltage-Controlled Drug Release Systems

To couple advantages of PPy (a conducting polymer) with bone implants, it is possible to embed antibiotics and anti-inflammatory drugs inside a conductive polymer for their local, electrically-controlled, delivery-upon-demand, and sustained release, in order to improve implant lifetime (Figure 1-19). Both antibiotic and anti-inflammatory drugs are desirable for orthopedic applications in order to lyse bacteria under a biofilm formed around a bone implant, and to suppress the inflammatory response. Therefore, the electrically-controlled drug release system from PPy could deploy drugs intact to bone implants to reduce the prevalence of both the septic and aseptic complications.

This thesis work sought to demonstrate on command PPy delivery of penicillin/streptomycin (P/S) (the antibiotics used to treat gram-positive and negative bacteria) and dexamethasone (Dex) (a glucocorticoid used clinically as an anti-inflammatory and immunosuppressive agent and as a supportive agent for osteoblast differentiation). Pyrrole was oxidized with anionic antibiotics (penicillin/streptomycin, P/S) (termed PPy[P/S]) and an anti-inflammatory drug (termed dexamethasone, Dex) (PPy[Dex]) separately and electrodeposited as films onto MWCNT-Ti and gold-palladium coated Ti (AuPd-Ti). PPy-drug films were analyzed for surface topography and roughness using atomic force microscopy (AFM). The mechanism of *in situ* electropolymerization, which affects surface chemistry, was determined by ultraviolet-visible (UV-vis) spectroscopy. X-ray photoelectron spectroscopy (XPS) analyzed surface

composition, compared electropolymerization yield, and confirmed the presences of P/S and Dex within the PPy films. Furthermore, the adhesion of osteoblasts (bone-forming cells) and fibroblasts (fibrous tissue-forming cells) were determined on the PPy[P/S]-Ti, PPy[Dex]-Ti, PLGA-PPy[Dex]-Ti, and commercially pure Ti. Lastly, the bioactivity of P/S was tested with bacteria colonies (*Staphylococcus epidermidis*), while those with Dex were evaluated with macrophages before and after electrical stimulation.

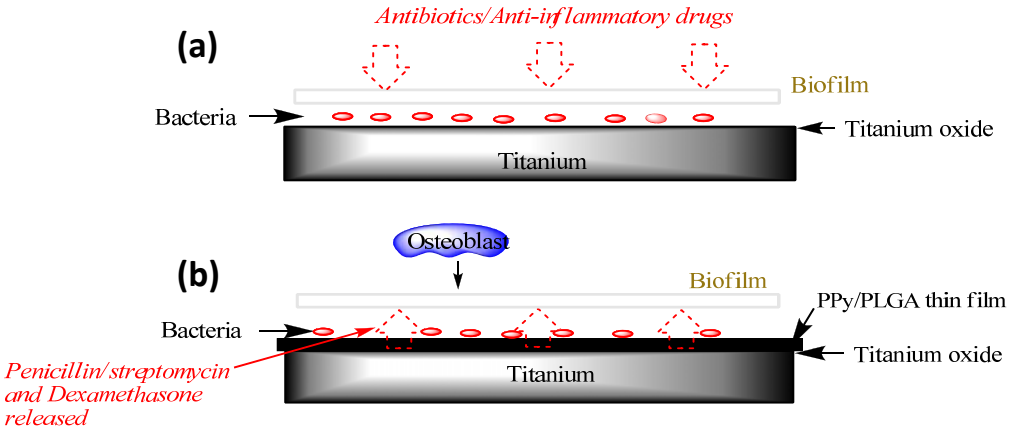

Figure 1-19. (a) The schematic of current antibiotic treatments to a Ti implant after a biofilm is formed by bacteria. (b) The proposed schematic of the voltage-controlled release of drugs *in situ* to reduce bacteria colonization and minimize biofilm formation or inflammation on an implant.

In summary, this dissertation sought to develop nanostructured sensors using MWCNTs grown out of anodized Ti, and electrically-control drug release of antibiotic and anti-inflammatory drugs using polypyrrole films electrodeposited onto Ti. The study also aimed to characterize the cytocompatibility of MWCNTs and PPy films with osteoblasts, fibroblasts, bacteria, and macrophages. This work is advantageous for further sensor device developments,

which will require the evolution of semiconductor and micro/nanocircuit technologies for closed-loop sensing and therapeutic delivery of drugs on demand, in order to improve the success and lifetime of orthopedic implants.

References

1. Ager III JW, Balooch G., R.O. R. Fracture, aging, and disease in bone. J Materi Res 2006 2 March 2006;21(8):1878-1892.

2. Bronner F, Worrell RV. Orthopaedics: Principles of Basic and Clinical Science: Informa Health Care, 1999.

3. Epker BN, Frost HM. Correlation of bone resorption and formation with the physical behavior of loaded bone. J Dent Res 1965;44:33-41.

4. Marino AA, Becker RO. Piezoelectric effect and growth control in bone. Nature 1970;228(5270):473-474.

5. Reinish GB, Nowick AS. Piezoelectric properties of bone as functions of moisture content. Nature 1975;253:626-627.

6. Silva CC, Thomazini D, Pinheiro AG, Aranha N, Figueiró SD, Góes JC, et al. Collagen-hydroxyapatite films: piezoelectric properties. Materials Science and Engineering B 2001;86(3):210-218.

7. McElhaney JH, Stalnaker R, Bullard R. Electric fields and bone loss of disuse. J Biomechnics 1968;1(1):47-52.

8. Hastings GW, Mahmud FA. Electrical effects in bone. Journal of Biomedical Engineering 1988 Nov;10(6):515-521.

9. Jianqing F, Huipin Y, Xingdong Z. Promotion of osteogenesis by a piezoelectric biological ceramic. Biomaterials 1997;18(23):1531-1534.

10. Park JB, Lakes RS. Biomaterials: an Introduction. New York: Plenum, 1992.

11. Nalwa HSe. Ferroelectric polymers. Marcel Dekker INC 1995:393-439.

12. Fisher N, Fisher JP, Verschuur GL. Tissue Engineering: Springer, 2006.

13. Yao C. Surface Modification of Titanium by Anodization for Orthopedic Applications: Purdue University; 2005.

14. Frost HM. In: Anonymous, editor. Bone remodeling dynamics: Charles C Thomas Publisher, 1963.

15. Owen TA, Shalhoub V, Barone LM, Wilming L, Tassinari MS, Kennedy MB, et al. Progressive development of the rat osteoblast phenotype in vitro: reciprocal relationships in expression of genes associated with osteoblast proliferation and differentiation during formation of the bone extracellular matrix. J Cell Physiol;143(3):420-430.

16. Junqueira LC, Carneiro J, Kelley RO. Basic histology. 10 ed. Stamford, Conn.: Appleton & Lange, 2003.

17. Ratner BD. Biomaterials science : an introduction to materials in medicine. Amsterdam; Boston: Elsevier Academic Press, 2004.

18. Paczocha P, Indacochea JE. Effect of Preheating on Implant-Cement Interface Strength for Hip Replacement. Journal of Materials Online 2005;1:1-16.

19. Zhang L, Webster TJ. Nanotechnology and nanomaterials: Promises for improved tissue regeneration. Nano Today 2009;4(1):66-80.

20. Hip and Knee Replacements in Canada: Canadian joint Replacement Registry, Canadian Institute for Health Information; 2006.

21. Zhang L, Sirivisoot S, Balasundaram G, Webster TJ. In: Khademhosseini A, Borenstein J, Toner M, Takayama S, editors. Micro and Nanoengineering of the Cell Microenvironment: Technologies and Applications: Artech House, Norwood, 2008. p. 431-460.

22. Bronson JG. Breakthrough technology: searing for artificial articular cartilage. Orthopedic Technology Review 1999;1(1).

23. Baxter LC, Frauchiger V, Textor M, Gwynn Ia, Richards RG. Fibroblast and osteoblast adhesion and morphology on calcium phosphate surfaces. European Cells and Materials 2002;4:1-17.

24. Lipski AM, Jaquiery C, Choi H, Eberli D, Stevens M, Martin I, et al. Nanoscale Engineering of Biomaterial Surfaces. Advanced Materials 2007;19(4):553-557.

25. Cornell R. The substate adhesion during cell culture. Experimental Cell Research 1969;58:289-295.

26. de Oliveira PT, Nanci A. Nanotexturing of titanium-based surfaces upregulates expression of bone sialoprotein and osteopontin by cultured osteogenic cells. Biomaterials 2004 Feb;25(3):403-413.

27. Beckerle MC. Cell adhesion. New York Oxford University Press 2001.

28. Liu H, Webster TJ. Nanomedicine for implants: A review of studies and necessary experimental tools. Cellular and Molecular Biology Techniques for Biomaterials Evaluation 2007 1;28(2):354-369.

29. Zhan C, Kaczmarek R, Loyo-Berrios N, Sangl J, Bright RA. Incidence and Short-Term Outcomes of Primary and Revision Hip Replacement in the United States. J Bone Joint Surg Am 2007;89(3):526-533.

30. Electromyography. Meidcal Encyclopedia, 2008.

31. Fermi level. Encyclopedia Britannica: Encyclopedia Britannica.

32. Get ready for Smart Implants. 2009 [cited; Available from: http://tigerbuford.wordpress.com/2009/03/28/get-ready-for-smart-implants/

33. New Biomedical Device to Monitor Hip Implant Healing. 2006 [cited; Available from: http://www.bio-medicine.org/medicine-news/New-Biomedical-Device-to-Monitor-Hip-Implant-Healing-15183-1/

34. Lautenschlager E, Monaghan P. Titanium and titanium alloys as dental materials. Int Dent J 1993;43(3):245-253.

35. Tomashov ND. Theory of corrosion and protection of metals: the science of corrosion. New York The Macmillan Co, 1966.

36. West JM. Basic corrosion and oxidation. New York: Chichester E. Horwood, 1986.

37. Tummler H, Thull R. Model of the metal/tissue connection of implant made of titanium or tantalum. In: Christel P, Meunier A, Lee AJC, editors. Biological and biomedical performance of biomaterials. Amsterdam: Elsevier, 1986. p. 403-408.

38. Webster TJ, Ejiofor JU. Increased osteoblast adhesion on nanophase metals: Ti, Ti6Al4V, and CoCrMo. Biomaterials 2004 8;25(19):4731-4739.

39. Webster TJ, Siegel RW, Bizios R. Osteoblast adhesion on nanophase ceramics. Biomaterials 1999;20(13):1221-1227.

40. Yao C, Perla V, McKenzie JL, Slamovich EB, Webster TJ. Anodized Ti and Ti6Al4V Possessing Nanometer Surface Features Enhances Osteoblast Adhesion. Journal of Biomedical Nanotechnology 2005;1:68-73(66).

41. Das K, Bose S, Bandyopadhyay A. Surface modifications and cell-materials interactions with anodized Ti. Acta Biomaterialia 2007;3(4):573-585.

42. Huang H-H, Pan S-J, Lu F-H. Surface electrochemical impedance in situ monitoring of cell-cultured titanium with a nano-network surface layer. Scripta Materialia 2005 11;53(9):1037-1042.

43. Yao C, Webster TJ. Anodization: A Promising Nano-Modification Technique of Titanium Implants for Orthopedic Applications. Journal of Nanoscience and Nanotechnology 2006 October 2006;6:2682-2692(2611).

44. Huang H-H, Pan S-J, Lai Y-L, Lee T-H, Chen C-C, Lu F-H. Osteoblast-like cell initial adhesion onto a network-structured titanium oxide layer. Scripta Materialia 2004 11;51(11):1017-1021.

45. Zhu X, Chen J, Scheideler L, Reichl R, Geis-Gerstorfer J. Effects of topography and composition of titanium surface oxides on osteoblast responses. Biomaterials 2004 Aug;25(18):4087-4103.

46. Popat KC, Eltgroth M, LaTempa TJ, Grimes CA, Desai TA. Decreased Staphylococcus epidermis adhesion and increased osteoblast functionality on antibiotic-loaded titania nanotubes. Biomaterials 2007;28(32):4880-4888.

47. Eaninwene Gn, Yao C, Webster TJ. Enhanced osteoblast adhesion to drug-coated anodized nanotubular titanium surfaces. Int J Nanomedicine 2008;3(2):257-264.

48. Webster TJ, Waid MC, McKenzie JL, Price RL, Ejiofor JU. Nano-biotechnology: carbon nanofibres as improved neural and orthopaedic implants. Nanotechnology 2004;15(1):48-54.

49. Smart SK, Cassady AI, Lu GQ, Martin DJ. The biocompatibility of carbon nanotubes. Toxicology of Carbon Nanomaterials 2006 5;44(6):1034-1047.

50. Zanello LP. Electrical properties of osteoblasts cultured on carbon nanotubes. Micro & Nano Letters 2006 July 2006;1(1):19-22.

51. Zanello LP, Zhao B, Hu H, Haddon RC. Bone Cell Proliferation on Carbon Nanotubes. Nano Letters 2006;6(3):562-567.

52. Balani K, Anderson R, Laha T, Andara M, Tercero J, Crumpler E, et al. Plasma-sprayed carbon nanotube reinforced hydroxyapatite coatings and their interaction with human osteoblasts in vitro. Biomaterials 2007 2;28(4):618-624.

53. Chen Y, Zhang TH, Gan CH, Yu G. Wear studies of hydroxyapatite composite coating reinforced by carbon nanotubes. Carbon 2007 4;45(5):998-1004.

54. Wei W, Sethuraman A, Jin C, Monteiro-Riviere NA, Narayan RJ. Biological Properties of Carbon Nanotubes. Journal of Nanoscience and Nanotechnology 2007 May 2007;7:1284-1297(1214).

55. Harrison BS, Atala A. Carbon nanotube applications for tissue engineering. Cellular and Molecular Biology Techniques for Biomaterials Evaluation 2007 1;28(2):344-353.

56. Iijima S. Helical microtubules of graphitic carbon. Nature 1991 11/07;354(6348):56-58.

57. Dai L. Carbon nanotechnology : recent developments in chemistry, physics, materials science and device applications. Amsterdam; Boston: Elsevier, 2006.

58. Hurt RH, Monthioux M, Kane A. Toxicology of carbon nanomaterials: Status, trends, and perspectives on the special issue. Toxicology of Carbon Nanomaterials 2006 5;44(6):1028-1033.

59. Lin Y, Taylor S, Li H, Fernando KAS, Qu L, Wang W, et al. Advances toward bioapplications of carbon nanotubes. Journal of Materials Chemistry 2004;14(4):527-541.

60. Robertson J. Realistic applications of CNTs. Materials Today 2004 10;7(10):46-52.

61. Sato S, Kawabata A, Kondo D, Nihei M, Awano Y. Carbon nanotube growth from titanium-cobalt bimetallic particles as a catalyst. Chemical Physics Letters 2005 1/24;402(1-3):149-154.

62. Avouris P, Appenzeller J, Martel R, Wind SJ. Carbon nanotube electronics. Proceedings of the IEEE 2003;91(11):1772-1784.

63. Cui Z. Nanofabrication : principles, capabilities and limits. Berlin: Springer, 2008.

64. Jiang L, Gao L. Carbon nanotubes-metal nitride composites: a new class of nanocomposites with enhanced electrical properties. Journal of Materials Chemistry 2005;15(2):260-266.

65. Supronowicz PR, Ajayan PM, Ullmann KR, Arulanandam BP, Metzger DW, Bizios R. Novel current-conducting composite substrates for exposing osteoblasts to alternating current stimulation. Journal of Biomedical Materials Research 2002 Mar 5;59(3):499-506.

66. Ciombor DM, Aaron RK. The Role of Electrical Stimulation in Bone Repair. Orthobiologics 2005 12;10(4):579-593.

67. Zhao B, Hu H, Mandal SK, Haddon RC. A Bone Mimic Based on the Self-Assembly of Hydroxyapatite on Chemically Functionalized Single-Walled Carbon Nanotubes. Chemistry of Materials 2005;17(12):3235-3241.

68. Price RL, Ellison K, Haberstroh KM, Webster TJ. Nanometer surface roughness increases select osteoblast adhesion on carbon nanofiber compacts. Journal of biomedical materials researchPart A 2004 Jul 1;70(1):129-138.

69. Dongwoo K, Michiko S, Rachel LP, Alexander ER, Thomas JW. Selective adhesion and mineral deposition by osteoblasts on carbon nanofiber patterns. 2006;1(1):65-72.

70. Kim JY, Khang D, Lee JE, Webster TJ. Decreased macrophage density on carbon nanotube patterns on polycarbonate urethane. Journal of Biomedical Materials Research Part A 2009;88A(2):419-426.

71. Aoki N, Yokoyama A, Nodasaka Y, Akasaka T, Uo M, Sato Y, et al. Cell Culture on a Carbon Nanotube Scaffold. Journal of Biomedical Nanotechnology 2005;1:402-405(404).

72. Khang D, Park GE, Webster TJ. Enhanced chondrocyte densities on carbon nanotube composites: The combined role of nanosurface roughness and electrical stimulation. J Biomed Mater Res A 2008:18186050.

73. Giannona S, Firkowska I, Rojas-Chapana J, Giersig M. Vertically Aligned Carbon Nanotubes as Cytocompatible Material for Enhanced Adhesion and Proliferation of Osteoblast-Like Cells. Journal of Nanoscience and Nanotechnology 2007 May 2007;7:1679-1683(1675).

74. Tsuchiya N, Sato Y, Aoki N, Yokoyama A, Watari F, Motomiya K, et al. Evaluation of Multi-Walled Carbon Nanotube Scaffolds for Osteoblast Growth. In: Tohji K, Tsuchiya N, Jeyadevan B, editors.; 2007 2007: AIP; 2007. p. 166-169.

75. Webster TJ. Safety of nanoparticles from manufacturing to medical applications. New York: Springer, 2009.

76. Padigi SK, Reddy RKK, Prasad S. Carbon nanotube based aliphatic hydrocarbon sensor. Biosensors and Bioelectronics 2007 1/15;22(6):829-837.

77. Tang H, Chen JH, Huang ZP, Wang DZ, Ren ZF, Nie LH, et al. High dispersion and electrocatalytic properties of platinum on well-aligned carbon nanotube arrays. Carbon 2004;42(1):191-197.

78. Kurusu F, Koide S, Karube I, Gotoh M. Electrocatalytic Activity of Bamboo-Structured Carbon Nanotubes Paste Electrode Toward Hydrogen Peroxide. Analytical Letters 2006 05/01;39:903-911.

79. Roy S, Vedala H, Choi W. Vertically aligned carbon nanotube probes for monitoring blood cholesterol. Nanotechnology 2006;17(4):S14-S18.

80. Liu Y, Wang M, Zhao F, Xu Z, Dong S. The direct electron transfer of glucose oxidase and glucose biosensor based on carbon nanotubes/chitosan matrix. Biosensors and Bioelectronics 2005 12/15;21(6):984-988.

81. Liu S, Lin B, Yang X, Zhang Q. Carbon-Nanotube-Enhanced Direct Electron-Transfer Reactivity of Hemoglobin Immobilized on Polyurethane Elastomer Film. Journal of Physical Chemistry B 2007;111(5):1182-1188.

82. Lin Y, Lu F, Tu Y, Ren Z. Glucose Biosensors Based on Carbon Nanotube Nanoelectrode Ensembles. Nano Letters 2004;4(2):191-195.

83. Besteman K, Lee J-O, Wiertz FGM, Heering HA, Dekker C. Enzyme-Coated Carbon Nanotubes as Single-Molecule Biosensors. Nano Letters 2003;3(6):727-730.

84. Sung WJ, Bae YH. A glucose oxidase electrode based on polypyrrole with polyanion/PEG/enzyme conjugate dopant. Biosensors and Bioelectronics 2003;18(10):1231-1239.

85. Yuan W-L, O'Rear EA, Cho G, Funkhouser GP, Glatzhofer DT. Thin polypyrrole films formed on mica and alumina with and without surfactant present: characterization by scanning probe and optical microscopy. Thin Solid Films 2001 4/2;385(1-2):96-108.

86. Shi G, Rouabhia M, Wang Z, Dao LH, Zhang Z. A novel electrically conductive and biodegradable composite made of polypyrrole nanoparticles and polylactide. Biomaterials 2004;25(13):2477-2488.

87. Skotheim TA, Elsenbaumer RL, Reynolds JR, Corp Author: NetLibrary I. Handbook of conducting polymers: New York : M. Dekker, Edition: 2nd ed., rev; 1998.

88. Wadhwa R, Lagenaur CF, Cui XT. Electrochemically controlled release of dexamethasone from conducting polymer polypyrrole coated electrode. Journal of Controlled Release 2006;110(3):531-541.

89. Guimard NK, Gomez N, Schmidt CE. Conducting polymers in biomedical engineering. Progress in Polymer Science 2007;32(8-9):876-921.

90. Zhang J, Venkataramani S, Xu H, Song Y-K, Song H-K, Palmore GTR, et al. Combined topographical and chemical micropatterns for templating neuronal networks. Biomaterials 2006;27(33):5734-5739.

91. De Giglio E, Sabbatini L, Colucci S, Zambonin G. Synthesis, analytical characterization, and osteoblast adhesion properties on RGD-grafted polypyrrole coatings on titanium substrates. Journal of Biomaterials Science, Polymer Edition 2000;11(10):1073-1083.

92. De Giglio E, Cometa S, Calvano C-D, Sabbatini L, Zambonin P, Colucci S, et al. A new titanium biofunctionalized interface based on poly(pyrrole-3-acetic acid) coating: proliferation of osteoblast-like cells and future perspectives. Journal of Materials Science: Materials in Medicine 2007;18(9):1781-1789.

93. Rowlands AS, Cooper-White JJ. Directing phenotype of vascular smooth muscle cells using electrically stimulated conducting polymer. Biomaterials 2008;29(34):4510-4520.

94. Stauffer WR, Cui XT. Polypyrrole doped with 2 peptide sequences from laminin. Biomaterials 2006;27(11):2405-2413.

95. George PM, Lyckman AW, LaVan DA, Hegde A, Leung Y, Avasare R, et al. Fabrication and biocompatibility of polypyrrole implants suitable for neural prosthetics. Biomaterials 2005;26(17):3511-3519.

96. Song HK, Toste B, Ahmann K, Hoffman-Kim D, Palmore GTR. Micropatterns of positive guidance cues anchored to polypyrrole doped with polyglutamic acid: A new platform for characterizing neurite extension in complex environments. Biomaterials 2006;27(3):473-484.

97. Mihardja SS, Sievers RE, Lee RJ. The effect of polypyrrole on arteriogenesis in an acute rat infarct model. Biomaterials 2008;29(31):4205-4210.

98. Garner B, Georgevich A, Hodgson AJ, Liu L, Wallace GG. Polypyrrole-heparin composites as stimulus-responsive substrates for endothelial cell growth. Journal of Biomedical Materials Research 1999;44(2):121-129.

99. Shi G, Rouabhia M, Meng S, Zhang Z. Electrical stimulation enhances viability of human cutaneous fibroblasts on conductive biodegradable substrates. J Biomed Mater Res A 2008 Mar 15;84(4):1026-1037.

100. Shi G, Zhang Z, Rouabhia M. The regulation of cell functions electrically using biodegradable polypyrrole-polylactide conductors. Biomaterials 2008;29(28):3792-3798.

101. Nishizawa M, Nozaki H, Kaji H, Kitazume T, Kobayashi N, Ishibashi T, et al. Electrodeposition of anchored polypyrrole film on microelectrodes and stimulation of cultured cardiac myocytes. Biomaterials 2007;28(8):1480-1485.

102. Lee JW, Serna F, Schmidt CE. Carboxy-endcapped conductive polypyrrole: biomimetic conducting polymer for cell scaffolds and electrodes. Langmuir 2006 Nov 21;22(24):9816-9819.

103. Wang Z, Roberge C, Dao LH, Wan Y, Shi G, Rouabhia M, et al. In vivo evaluation of a novel electrically conductive polypyrrole/poly(D,L-lactide) composite and polypyrrole-coated poly(D,L-lactide-co-glycolide) membranes. Journal of Biomedical Materials Research Part A 2004;70A(1):28-38.

104. Thompson BC, Moulton SE, Ding J, Richardson R, Cameron A, O'Leary S, et al. Optimising the incorporation and release of a neurotrophic factor using conducting polypyrrole. Journal of Controlled Release 2006;116(3):285-294.

105. Joo J, Lee JK, Baeck JS, Kim KH, Oh EJ, Epstein J. Electrical, magnetic, and structural properties of chemically and electrochemically synthesized polypyrroles. Synthetic Metals 2001;117(1-3):45-51.

106. Atanasoska L, Naoi K, Smyrl WH. XPS studies on conducting polymers: polypyrrole films doped with perchlorate and polymeric anions. Chem Mater 1992;4(5):988-994.

107. Wallace GG, Spinks GM, Teasdale PR. Conductive electroactive polymers intelligent materials systems. Lancaster, Pa.: Technomic Pub. Co., 1997.

108. Geetha S, Rao CRK, Vijayan M, Trivedi DC. Biosensing and drug delivery by polypyrrole. Analytica Chimica Acta 2006;568(1-2):119-125.

109. Green RA, Lovell NH, Wallace GG, Poole-Warren LA. Conducting polymers for neural interfaces: Challenges in developing an effective long-term implant. Biomaterials 2008;29(24-25):3393-3399.

110. Gioe TJ, Killeen KK, Grimm KM, Mehle S, Scheltema K. Why Are Total Knee Replacements Revised?: Analysis of Early Revision in a Community Knee Implant Registry. Clinical Orthopaedics & Related Research November 2004;428:100-106.

111. Savarino L, Baldini N, Tarabusi C, Pellacani A, Giunti A. Diagnosis of infection after total hip replacement. Journal of Biomedical Materials Research Part B: Applied Biomaterials 2004;70B(1):139-145.

112. Trampuz A, Zimmerli W. Diagnosis and treatment of infections associated with fracture-fixation devices. Injury 2006;37(2, Supplement 1):S59-S66.

113. L. Savarino NB, C. Tarabusi, A. Pellacani, A. Giunti,. Diagnosis of infection after total hip replacement. Journal of Biomedical Materials Research Part B: Applied Biomaterials 2004;70B(1):139-145.

114. Pandey R, Quinn J, Joyner C, Murray DW, Triffitt JT, Athanasou NA. Arthroplasty implant biomaterial particle associated macrophages differentiate into lacunar bone resorbing cells. Annals of the Rheumatic Diseases 1996;55(6):388-395.

115. Campoccia D, Montanaro L, Arciola CR. The significance of infection related to orthopedic devices and issues of antibiotic resistance. Biomaterials 2006;27(11):2331-2339.

116. Winkler H, Kaudela K, Stoiber A, Menschik F. Bone grafts impregnated with antibiotics as a tool for treating infected implants in orthopedic surgery – one stage revision results. Cell and Tissue Banking 2006;7(4):319-323.

117. Widmer AF. New developments in diagnosis and treatment of infection in orthopedic implants. Clin Infect Dis 2001 Sep 1;33 Suppl 2(33):S94-106.

118. Trebse R, Pisot V, Trampuz A. Treatment of infected retained implants. Journal of Bone and Joint Surgery 2005;87(2):249-256.

119. Gerhart TN, Roux RD, Horowitz G, Miller RL, Hanff P, Hayes WC. Antibiotic release from an experimental biodegradable bone cement. Journal of Orthopaedic Research 1988;6(4):585-592.

120. Picknell B, Mizen L, Sutherland R. Antibacterial activity of antibiotics in acrylic bone cement. J Bone Joint Surg Br 1977 August 1, 1977;59-B(3):302-307.

121. Buranapanitkit B, Oungbho K, Ingviya N. The efficacy of hydroxyapatite composite impregnated with amphotericin B. Clin Orthop Relat Res 2005 Aug(437):236-241.

122. Baleani M, Persson C, Zolezzi C, Andollina A, Borrelli AM, Tigani D. Biological and biomechanical effects of vancomycin and meropenem in acrylic bone cement. J Arthroplasty 2008 Dec;23(8):1232-1238.

123. Massimiliano B, Cecilia P, Carola Z, Agnese A, Anna Maria B, Domenico T. Biological and Biomechanical Effects of Vancomycin and Meropenem in Acrylic Bone Cement. The Journal of Arthroplasty 2008;23(8):1232-1238.

124. Squire MW, Ludwig BJ, Thompson JR, Jagodzinski J, Hall D, Andes D. Premixed antibiotic bone cement: an in vitro comparison of antimicrobial efficacy. J Arthroplasty 2008 Sep;23(6 Suppl 1):110-114.

125. Widmer AF. New Developments in Diagnosis and Treatment of Infection in Orthopedic Implants. Clinical Infectious Diseases 2001;33(s2):S94-S106.

126. Kalfas IH. Principles of bone healing. Neurosurgical Focus 2001;10(4):1-4.

127. Haynes DR. Bone lysis and inflammation. Inflammation Research 2004;53(11):596-600.

128. Hallab N, Merritt K, Jacobs JJ. Metal sensitivity in patients with orthopaedic implants. The Journal of Bone and Joint Surgerty 2001;83:428-436.

129. Matthew iR, Frame JW. Ultrastructural analysis of metal particles released from stainless steel and titanium miniplate components in an animal model. Journal of Oral and Maxillofacial Surgery 2004;56(1):45-50.

130. Dörner T, Haas J, Loddenkemper C, Baehr Vv, Salama A. Implant-related inflammatory arthritis. Nature Clinical Practice Rheumatology 2006;2:53-56.

131. Mombelli A, Lang NP. The diagnosis and treatment of peri-implantitis. Periodontology 2000 1998;17(1):63-76.

132. McLaughlin F, Mackintosh J, Hayes BP, McLaren A, Uings IJ, Salmon P, et al. Glucocorticoid-induced osteopenia in the mouse as assessed by histomorphometry, microcomputed tomography, and biochemical markers. Bone 2002;30(6):924-930.

133. Wershil BK, Furuta GT, Lavigne JA, Choudhury AR, Wang ZS, Galli SJ. Dexamethasone or cyclosporin A suppress mast cell-leukocyte cytokine cascades. Multiple mechanisms of inhibition of IgE- and mast cell- dependent cutaneous inflammation in the mouse. J Immunol 1995 February 1, 1995;154(3):1391-1398.

134. Yoon JJ, Kim JH, Park TG. Dexamethasone-releasing biodegradable polymer scaffolds fabricated by a gas-foaming/salt-leaching method. Biomaterials 2003;24(13):2323-2329.

135. Abu EO, Horner A, Kusec V, Triffitt JT, Compston JE. The localization of the functional glucocorticoid receptor alpha in human bone. J Clin Endocrinol Metab 2000 Feb;85(2):883-889.

136. Atmani H, Audrain C, Mercier L, Chappard D, Basle MF. Phenotypic effects of continuous or discontinuous treatment with dexamethasone and/or calcitriol on osteoblasts differentiated from rat bone marrow stromal cells. Journal of Cellular Biochemistry 2002;85(3):640-650.

137. Cheng SL, Yang JW, Rifas L, Zhang SF, Avioli LV. Differentiation of human bone marrow osteogenic stromal cells in vitro: induction of the osteoblast phenotype by dexamethasone. Endocrinology 1994 January 1, 1994;134(1):277-286.

138. Peter SJ, Liang CR, Kim DJ, Widmer MS, Mikos AG. Osteoblastic phenotype of rat marrow stromal cells cultured in the presence of dexamethasone, glycerolphosphate, and L-ascorbic acid. Journal of Cellular Biochemistry 1998;71(1):55-62.

139. Ryan PM, William HR, Aaron GS. Effect of dexamethasone withdrawal on osteoblastic differentiation of bone marrow stromal cells. Journal of Cellular Biochemistry 2003;90(1):13-22.

140. Beloti MM, Rosa AL. Osteoblast differentiation of human bone marrow cells under continuous and discontinuous treatment with dexamethasone. Brazilian Dental Journal 2005;16:156-161.

141. Mori K, Shioi A, Jono S, Nishizawa Y, Morii H. Dexamethasone Enhances In Vitro Vascular Calcification by Promoting Osteoblastic Differentiation of Vascular Smooth Muscle Cells. Arterioscler Thromb Vasc Biol 1999 September 1, 1999;19(9):2112-2118.

142. Mathiowitz E. Encyclopedia of Controlled Drug Delivery: John Wiley & Sons, 1999.

143. Kontturi K, Pentti P, Sundholm G. Polypyrrole as a model membrane for drug delivery. Journal of Electroanalytical Chemistry 1998;453:231-238.

144. Pernaut JM, Reynolds JR. Use of conducting electroactive polymers for drug delivery and sensing of bioactive molecules. A redox chemistry approach. Journal of Physical Chemistry B 2000;104(17):4080-4090.

145. Ghassabian S, Ehtezazi T, Forutan SM, Mortazavi SA. Dexamethasone-loaded magnific albumin micropheres: preparation and in vitro release. international journal of Pharmaceutics 1996;130(1):49-55.

146. Wnek GE, Bowlin GL. Encyclopedia of Biomaterials and Biomedical Engineering. 2 ed: Informa Health Care, 2008.

147. Prakash SB, Urdaneta M, Christophersen M, Smela E, Abshire P. In situ electrochemical control of electroactive polymer films on a CMOS chip. Sensors and Actuators B: Chemical 2008;129(2):699-704.

148. Durr HR, Maier M, Jansson V, Baur A, Refior HJ. Phenol as an adjuvant for local control in the treatment ofgiant cell tumour of the bone. European Journal of Surgical Oncology 1999;25(6):610-618.

149. Graichen F, Bergmann G. Four-channel telemetry system for in vivo measurement of hip joint forces. Journal of Biomedical Engineering 1991 9;13(5):370-374.

150. Graichen F, Bergmann G, Rohlmann A. Hip endoprosthesis for in vivo measurement of joint force and temperature. Journal of Biomechanics 1999 10;32(10):1113-1117.

151. Graichen F, Arnold R, Rohlmann A, Bergmann G. Implantable 9-channel telemetry system for in vivo load measurements with orthopedic implants. IEEE transactions on bio-medical engineering 2007 Feb;54(2):253-261.

CHAPTER 2

Materials and Methods

2.1 Material Fabrication

2.1.1 Anodization

In order to create nanotubes on Ti for subsequent MWCNTs growth, an anodization technique was adapted from Yao et al. [1]. Briefly, 99.2% pure Ti sheets (Alfa Aesar; Ward Hill, MA, USA) were cut into 1 cm squares and cleaned with acetone, and 70% ethanol sonicating for 10 minutes each, followed by deionized water rinsing. Then, these samples were etched for 10 seconds in a solution of 1.5% by weight nitric acid and 0.5% by weight hydrofluoric acid to remove the oxidized layer on Ti surfaces. Cleaned Ti samples were used as an anode, while a high purity platinum sheet (Alfa Aesar; Ward Hill, MA, USA) served as a cathode. Both were immersed in an electrolyte solution consisting of 1.5% by weight hydrofluoric acid, diluted with deionized water, in a Teflon beaker (Figure 2-20). The surface of the etched Ti was placed next to the platinum sheet at a distance of around one centimeter. In this configuration, 20 DC volts (3645A; Circuit Specialists, Mesa, AZ) were applied for 10 minutes to create nanotubes on the surfaces of commercially pure Ti used as orthopedic implants.

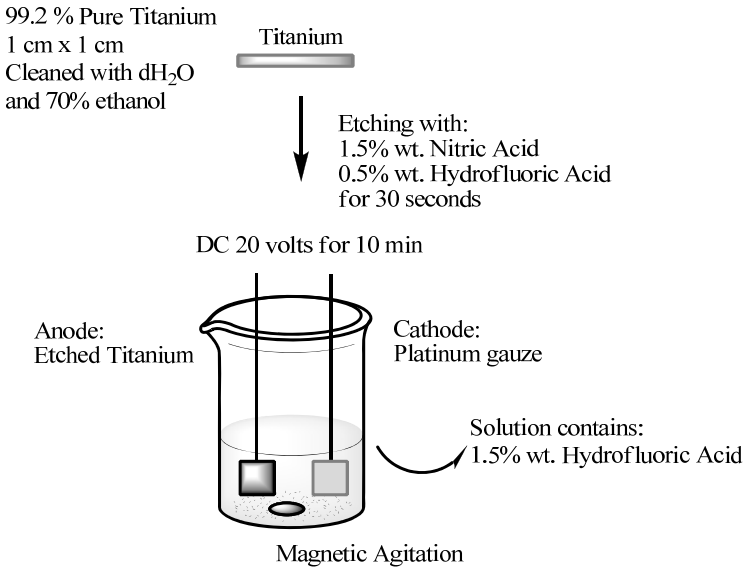

Figure 2-20. Anodization diagram. 20 volts of DC were applied for 10 minutes in 1.5% by weight hydrofluoric acid diluted with deionized water to the modify Ti surfaces to possess nanotubes. Magnetic bar was agitated at the medium speed.

2.1.2 Chemical Vapor Deposition

A plasma-enhanced chemical vapor deposition (PECVD) system (ASTEX by Applied Science & Technology; Grand Rapids, MI, USA) was used to grow MWCNTs in Ti nanotubes, which were created during the aforementioned anodization process. However, in this thesis, plasma was not used to grow MWCNTs. The catalyst for CNT growth was 5 M cobaltous nitrate (Allied Chemical; Brighton, UK), diluted with methanol (Mallinckrodt; Hazelwood, MO, USA). The nanoporous anodized Ti samples were dipped in this solution for five minutes, prior to CVD. Next, the samples were rinsed with distilled water and dried with compressed air. The samples were then placed in the CVD chamber (Figure 2-21) and air was pumped out to a base pressure below 10 mTorr. The samples were then heated to 700 ^{o}C in a flow of 100 standard cubic centimeters per

minute (sccm) hydrogen gas to reduce the cobaltous nitrate to cobalt. To grow MWCNTs, gas composition was changed to 40 sccm H_2 and 160 sccm C_2H_2 (acetylene) for 20 and 30 minutes, respectively. Finally, the samples were cooled in a 100 sccm Ar flow. The dense and entangled MWCNTs formed a three-dimensional structure on the Ti surface with exceptional electrical conductivity.

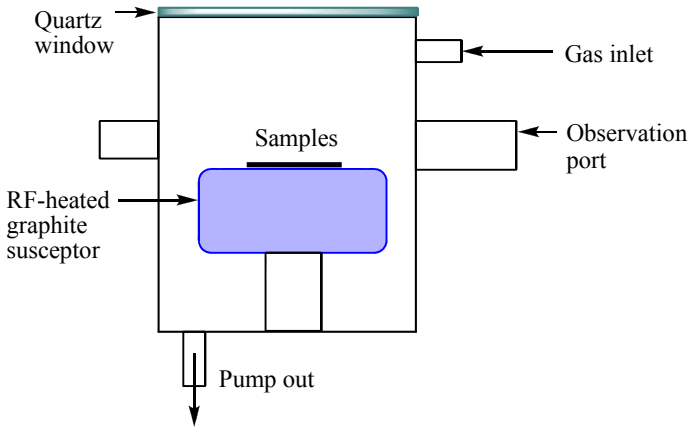

Figure 2-21. The chemical vapor deposition (CVD) system used to grow MWCNTs on Ti surfaces which were anodized to possess nanotubes using cobaltous nitrate as a catalyst, and acetylene gas as a carbon source.

2.1.3 Drug-Eluting Electrically Conducting Polymer

2.1.3.1 Electrochemical Polymerization (Electrodeposition)

MWCNT-Ti and commercially pure Ti (Alfa Aesar; Ward Hill, MA, USA) were used as templates to electrodeposit PPy membranes. Before the electropolymerization of pyrrole, Ti was coated with gold-palladium (AuPd; Ted Pella; Redding, CA, USA) by a PS-2 sputter coating unit (ISI

International Scientific Instruments, Inc.; Pleasanton, CA, USA) for 4.5 minutes using a 20 mTorr vacuum argon environment at 20 mA. All chemicals were reagent grade, and were used as received without any purification. All solutions were prepared in double deionized water. Pyrrole monomers (0.1M; Sigma-Aldrich; St. Louis, MO, USA), as shown in Figure 2-22a, were either oxidized with 6.82 mM penicillin/streptomycin (P/S; $C_{37}H_{57}N_9O_{16}S$; Hyclone; Logan, UT, USA), as shown in Figure 2-22c, or 0.125 mM dexamethasone (Dex; $C_{22}H_{29}FO_5$; Sigma-Aldrich; St. Louis, MO, USA), as shown in Figure 2-22b, onto 1 cm^2 of either MWCNT-Ti or AuPd-Ti in a 1 M phosphate buffer saline (PBS; Gibco; Grand Island, NY, USA) at a pH of 7.2. Electrochemical polymerization was carried out by cyclic voltammetry (Epsilon EC; Bioanalytical Systems; West Lafayette, IN, USA) using a three-electrode system (Figure 2-23). The working electrode was either MWCNT-Ti or AuPd-Ti, the counter electrode was platinum gauze (Alfa Aesar; Ward Hill, MA, USA), and the reference electrode was silver/silver chloride (Ag/AgCl in 3 M NaCl; Bioanalytical Systems; West Lafayette, IN, USA), as shown in Figure 2-22d. Potentials of 0 V to 1.1 V (a scan rate of 100 mV/s and 10 repeat scans) were used for electrodepositing.

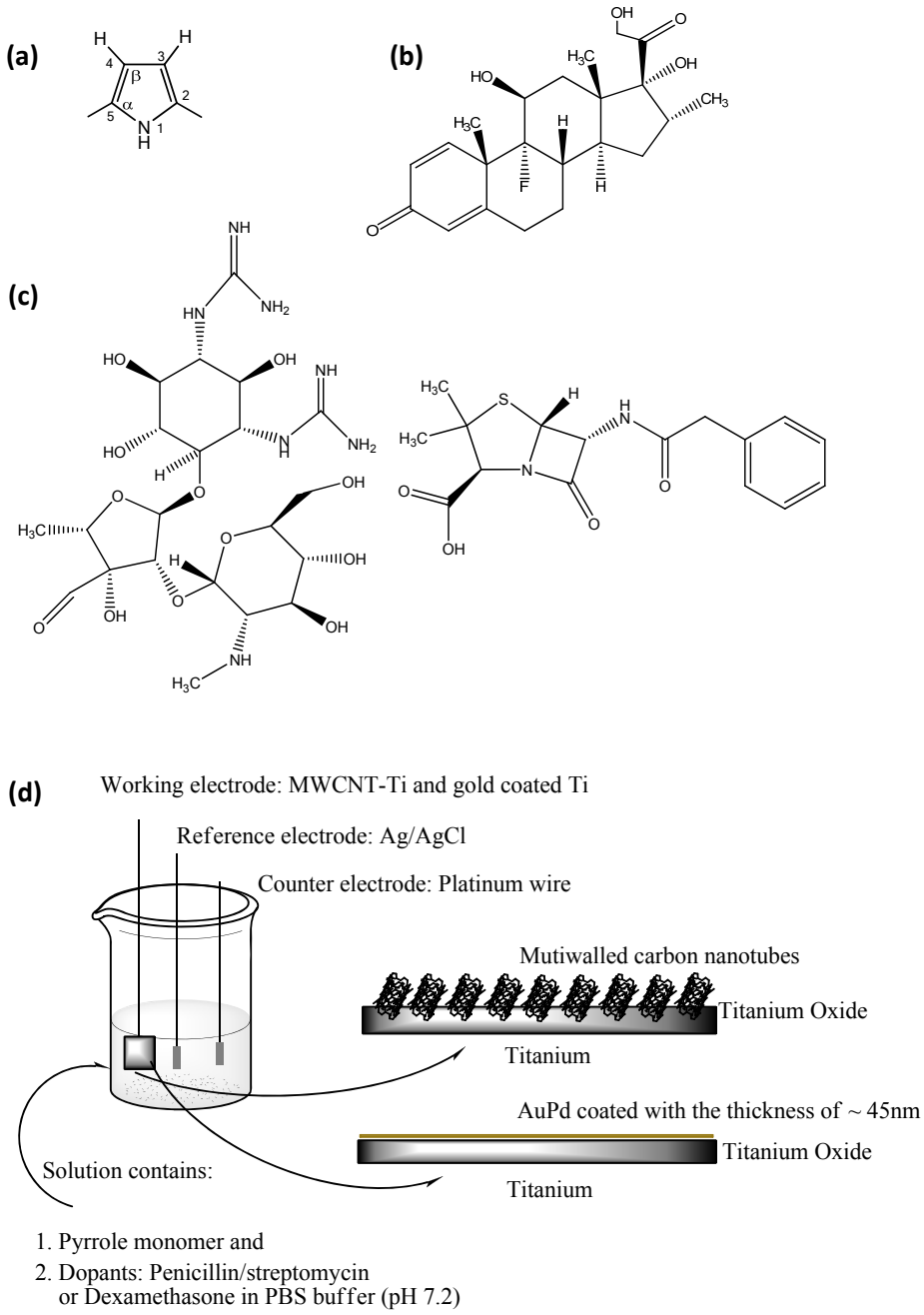

Figure 2-22. The structures of: (a) pyrrole monomer, (b) dexamethasone, and (c) penicillin/streptomycin. (d) Electrodeposition diagram using an EC epsilon electrochemical instrument (Bioanalytical System, Inc.; West Lafayette, IN, USA) with three electrodes (cyclic voltammetry).

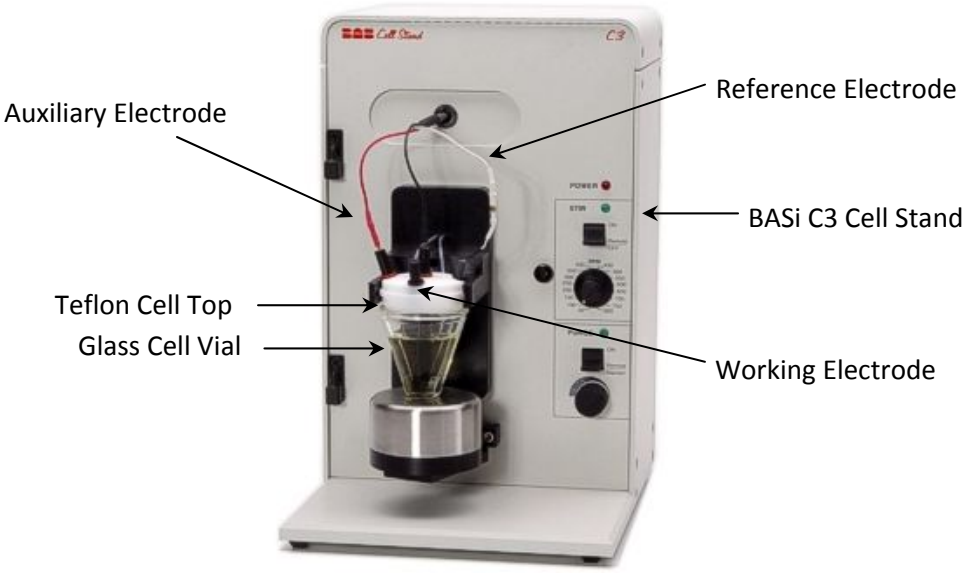

Figure 2-23. BASi C3 Cell Stand Equipment (Bioanalytic Systems, Inc.; West Lafayette, IN, USA) for electroanalytical experiments with three electrodes (red: auxiliary electrode, white: reference electrode, and black: working electrode), all functions are controlled by an EC epsilon electrochemical instrument (Bioanalytic System, Inc.).

2.1.3.2 Mechanisms of Pyrrole Electropolymerization

Zeta potentials of P/S and Dex were recorded on a Malvern Zetasizer Nano S (Malvern Instruments; U.K.) using eight runs using via two-beam mode to measure the zero potential of P/S and Dex in PBS buffer (pH 7.2; 1X; Gibco; Grand Island, NY, USA) and deionized water. The dispersant dielectric constant and viscosity were taken as 79.0 and 1.02 cP for PBS buffer and as 78.5 and 0.8872 cP for deionized water, respectively. The mechanism of pyrrole polymerization and the influence of doping were monitored by recording the UV-vis absorption spectra of the

stock solution (pyrrole monomers; either P/S or Dex, and PBS buffer) at room temperature on a SpectraMax V5 spectrophotometer (Molecular Devices; Chicago, IL, USA) from 340 nm to 850 nm immediately after electropolymerization. Self-polymerization was developed further by allowing the stock solution after applying the sweep voltages to sit first for four hours, and then again for 30 hours, and measuring absorbance changes. 1X PBS buffer (pH 7.2; Gibco; Grand Island, NY, USA) was used as a blank and was subtracted from the stock solution absorbance.

2.1.3.3 Electrochemical Measurements (Cyclic Voltammetry)

An Epsilon EC electrochemical workstation and Digisim software (Bioanalytical Systems; West Lafayette, IN, USA) were used to perform the cyclic voltammetry experiments in this study. The substrates of interest were used as the working electrodes. A silver/silver chloride (Ag/AgCl in 3M NaCl; MW-2052; Bioanalytical Systems; West Lafayette, IN, USA) and a platinum wire (MW-1032; Bioanalytical Systems; West Lafayette, IN, USA) were used as reference and counter electrodes, respectively. Before the measurements, all electrodes were cleaned with deionized water. All electrodes were connected to the electrochemical workstation and immersed in an electrolyte solution. The electrolytes were a 10 mM $K_3Fe(CN)_6$ (potassium ferricyanide; Sigma-Aldrich; St. Louis, MO, USA) solution with 1 M KNO_3 (Sigma-Aldrich; St. Louis, MO, USA), and a solution of 0.6 N HCl was used to dissolve the extracellular components deposited by osteoblasts cultured on commercially pure Ti for 7, 14, and 21 days. The cyclic voltammograms (CV) were generated by applying a linear sweep potential at several scan rates. The electrochemical responses at the three types of working electrodes were compared with CV in

both electrolyte solutions. All measurements were carried out at room temperature in oxygen and non-oxygen (under nitrogen degassing) containing electrolyte solutions.

2.1.3.4 Poly(d,l,lactic-co-glycolic acid) Conjugation

Poly(d,l-lactic-*co*-glycolic acid) with acidic end groups (50:50 PLGA functionalized COOH; MW=96.7 kDa; Absorbable Polymers; Pelham, AL, USA) were activated at the carboxylic acid groups with 1-ethyl-3-[3-dimethylamiopropyl] carbodiimide (EDC; Pierce; Rockford, IL, USA) and thereby changed at room temperature into a stable intermediate form with N-hydroxysuccinimide (NHS; Pierce; Rockford, IL, USA), termed PLGA-NHS here. PLGA-COOH (3.45 M) in chloroform was added with EDC (80 mM) and was converted to PLGA-NHS with NHS (78.2 mM). The solution was well stirred during each addition. PLGA-NHS was precipitated with ethyl ether (3 ml; Mallinckrodt; Hazelwood, MO, USA) and washed three times in a cold mixture of ethyl ether and methanol (Mallinckrodt; Hazelwood, MO, USA) 1:1 (v/v) to remove residual NHS. PLGA-NHS was dried under vacuum for 48 hours before conjugation with an amine group of PPy. To prepare $PPyNH_2$[Dex], 40 mM 3-Amino-2-ethoxycarbonylpyrrole hydrochloride ($C_7H_{11}ClN_2O_2$; Combi-Blocks; San Diego, CA, USA) was added to a solution of pyrrole monomers, Dex, and PBS buffer. The conjugation of $PPyNH_2$[Dex] and PLGA-NHS was achieved by vertically soaking the $PPyNH_2$[Dex]-Ti in a solution of PLGA-NHS (1g) and chloroform (30 ml) while vigorously stirring and maintaining the reaction for 15 hours at room temperature. Then, the PLGA-PPy[Dex]-Ti samples were precipitated in cold methanol and washed three times to remove unreacted PLGA-NHS. The PLGA-PPy[Dex]-Ti samples were dried under vacuum for three hours. Prior to

cell experiments, all samples were cleaned with double deionized water and sterilized using ultraviolet exposure for four hours on each side of the samples.

2.1.3.5 Electrically-Controlled Drug Release

Cyclic voltammetry was used to stimulate and evaluate the cumulative drug release through redox activity. P/S and Dex were released from PPy into PBS buffer (pH 7.2) by applying sweep voltages from -1 V to 1 V for up to 25 cycles with a scan rate of 100 mV/s. The cumulative release of P/S and Dex were determined in PBS buffer (pH 7.2) during electrical stimulation. The P/S release into PBS was determined quantitatively by using a BCA protein assay kit (Thermo Scientific; Rockford, IL, USA) at an absorbance of 542 nm with a SpectraMax V5 spectrophotometer (Molecular Devices; Chicago, IL, USA) during the reduction of the electroactive PPy[P/S]. The amine groups of P/S reacted with a BCA protein assay and changed into a purple color [6]. Dex was measured at an absorbance of 245 nm under a Lambda 35 UV-vis spectrophotometer (PerkinElmer; Waltham, MA, USA). The absorbance of PPy was subtracted from the light absorbance at 562 nm and 245 nm. Five samples of each drug were analyzed and then used to determine the average cumulative release profile with a standard curve for each drug.

Pierce® BCA Protein Assay Kit (Cat# 23225; Thermo Scientific, Rockford, IL, USA) were used in this study to detect P/S releases from PPy films after electrical stimulations [6]. Working reagent was prepared by mixing a equal volume of BCA Reagent A and BCA Reagent B. P/S (Hyclone) were series-diluted with PBS to obtain the standard curve. 25 μl of each standard or unknown sample were added into a microplate well, then added 200 μl of the working reagent

to each well and mix plate thoroughly on a plate shaker for 30 seconds. 96-well plate were covered and incubated at 37°C for 30 minutes. Before measuring the absorbance at 562 nm on a plate reader, the plate should be cool down at room temperature first.

2.2 Material Characterization

2.2.1 Surface Composition Characterization Using X-ray Diffraction (XRD)

The commercially pure Ti and MWCNT-Ti were characterized with X-ray diffraction (XRD) to verify the calcium-phosphate or hydroxyapatite presence using Cu Kα radiation (Siemens Diffractometer D5000 Kristalloflex; Bruker AXS Inc; Chicago, IL, USA). 2θ angles were varied from 20° to 70° min^{-1}. Diffraction signal intensity was recorded and processed using DiffracPlus: TexEval (Bruker AXS, Inc; Palo Alto, CA, USA) software.

2.2.2 Solid State Characterization (SEM, TEM, and Raman Spectroscopy)

Substrates were examined by scanning electron microscopy (SEM; Zeiss/Leo 1530VP FE-4800; Peabody, MA, USA) without AuPd sputter coating at a 3 kV acceleration voltage with an in-lens secondary electron detector and a high-resolution transmission electron microscope (HRTEM) with a 200 kV JEOL (Tokyo, Japan) HRTEM 2010 equipped with an ER-B high efficiency CCD camera (Advanced Microscopy Techniques; Danvers, MA, USA). Samples for HRTEM analysis were prepared by sonication of the MWCNTs in 70% ethanol for 10 minutes and then by drying a drop of the suspension on a carbon TEM grid. Raman spectra of MWCNT-Ti were acquired with

a Raman Spectroscope (Ramascope System 2000; Renishaw; UK). A standard argon ion laser had an excitation source with a wavelength of 488 nm (50 mW). A helium neon laser had an excitation source with a wavelength of 633 nm (35 mW). Each laser beam at the sample was focused by a 50X objective lens and measured approximately 0.1 mm in diameter with a scan time of approximately 10 seconds and the number of co-added scans equalled four.

2.2.3 Wettability and Surface Energy (Contact Angle Measurements and Fourier Transform Infrared Spectroscopy)

The surface energy of the substrates of interest was measured by contact angles. Contact angle measurements were made using the sessile drop method, which was analyzed using the easy drop model system (DSA-10; Krüss; Germany). One drop each (10 μl) of double deionized water, glycerol (Sigma-Aldrich; St. Louis, MO, USA), and polyethylene glycol 200 (Sigma-Aldrich; St. Louis, MO, USA) was placed on top of one centimeter squares of the substrates of interest. The contact angle was immediately measured within 10 sec after placing the drop on each sample. Measurements were performed three times, the average contact angle was determined, and results were used to calculate the solid surface energy according to the Owen-Wendt method and the critical surface tension by the Zisman method with computer analysis software (DSA 1 v 1.80; Krüss; Germany). Solid surfaces of the substrates were analyzed by Fourier transform infrared (FTIR) spectroscopy (Spectrum One FTIR; PerkinElmer; Waltham, MA, USA) by applying pressure to solid samples on the Universal ZnSe Attenuated Total Reflectance (ATR) top-plate. Data was recorded in transmittance mode in the range of 650-4000 cm^{-1} after 8 scans with a resolution of 2 cm^{-1}.

2.2.4 Conductive Polymer Characterization (SEM, AFM, and XPS)

A scanning electron microscope (SEM; Zeiss/Leo 1530VP FE-4800; Peabody, MA, USA) was used to assess the electropolymerization of pyrrole around the MWCNTs without a AuPd sputter coating. SEM captured images of PPy-deposited MWCNT-Ti at a 5 kV accelerating voltage with an in-lens secondary electron detector. The surface roughness and topography of the PPy-drugs on AuPd-Ti were analyzed with an atomic force microscope (AFM; Park Scientific Instrument, Sunnyvale, CA, USA). The AFM in non-contact mode evaluated five μm square surfaces at a scan rate of 1 Hz. PSI ProScan Image Processing Software was used to determine the root mean square roughness (R_{rms}) and the peak-to-valley roughness (R_{pv}) of the samples. The root mean square roughness is given by the standard deviation of data, determined using the standard definition [2]:

$$R_{rms} = \sqrt{\frac{\sum_{n=1}^{N} \left(Z_n - \overline{Z}\right)^2}{N-1}} \qquad \textbf{[2-1]}$$

where $\overline{Z}$ is the mean Z height. The peak-to-valley roughness is given by the highest data point in an area minus the lowest point, determined using the standard definition [2]:

$$R_{p-v} = Z_{\max} - Z_{\min} \qquad \textbf{[2-2]}$$

where $Z_{\max}$ is the maximum height and $Z_{\min}$ is the minimal height. The film thickness was measured using a profilometer (Dextak 3; Veeco; Lowell, MA, USA). To measure the thickness of the PPy film electrodeposited on AuPd-Ti, a diamond stylus profilometer was positioned vertically in contact with the sample, and then moved laterally across the edge of the AuPd-Ti substrate and PPy films for a length of 10 μm. Data were collected three different times and the average thickness of the PPy films electrodeposited on AuPd-Ti were calculated.

X-ray photoelectron spectroscopy (XPS) was used to determine PPy surface chemistry. XPS studies were performed using a PerkinElmer (Waltham, MA, USA) 5500 Multitechnique Surface Analyzer (Al Kα X-ray source with 1486.6 eV photons; survey 0.8 eV/step; multiplex 0.125 ev/step). The surface composition of the PPy-drug samples was calculated from high-resolution XPS at the C 1*s* and N 1*s* core spectra. The PLGA-PPy[Dex] was additionally scanned at the O 1*s* core spectrum to confirm the presence of PLGA conjugated with PPy functionalized amine groups. A standard line shape based on Gaussian functions was used to decompose the core-level spectra.

2.2.5 Shear Stress Testing

Tensile tests between samples of interest (PPy-Ti, PPy-MWCNT grown out of anodized Ti, PPy-MWCNT grown on commercially pure Ti, MWCNT-Ti, and commercially pure Ti) and collagen paper (Nippi Collagen Casings; Nippi, Inc.; Tokyo, Japan) were investigated to characterize relative shear stress before failure. Collagen papers were cleaned with 70% ethanol and dried in room temperature. Then, samples were attached to the collagen papers, which were cut into 10 cm height x 1 cm width, using 0.25 M polyethylene glycol (PEG; MW=1000; Sigma; St. Louis, MO, USA). Tensile tests were performed by an Instron 5882 elecrtro-mechanical testing system (Norwood, MA, USA) using 5.8kN load cells, and data sampling was performed at 0.001 kHz. The sample attached with collagen paper was clamped in the testing machine and extended at a rate of 1 mm/min until sample failure. The tensile force and displacement were collected using Instron DAX software (version 9.3; Norwood, MA, USA). The tensile was force divided by the

area of contact (1 cm x 1 cm). The experiments were repeated two different times at an n=3. The average shear stress was calculated for each sample and data plotted versus displacement.

2.3 Cell Assays

2.3.1 Cell Manipulations

2.3.1.1 Bringing Up Frozen Cells

Osteoblast, fibroblast, or macrophage vials was brought up to 37 °C quickly and wiped outside with 70% ethanol. Cells were aliquoted into 10 ml of media. After six hours, media was replaced for first time and again every other day.

2.3.1.2 Freezing Down Cells

Osteoblast, fibroblast, or macrophage culture plates was rinsed with sterilized PBS three times, then added 0.5 ml of Trypsin-EDTA Solution (1X; T3924; Sigma) for osteoblasts or 0.5 ml of 0.25% Typsin-EDTA solution (T4049; Sigma) for fibroblasts and macrophages, and incubating until cells are removed from the cell culture plate. New fresh cell media (1 ml) were added into cell culture plate, mixed it well, and placed 1.5 ml of cell suspension into each 2 ml tube. Finally, dimethyl sulphoxide (DMSO; D2438; Sigma) for 75 μl (or 5% DMSO) were added into the 2 ml tube, kept in -80°C for one day, and finally put vials into liquid nitrogen for full storage.

2.3.2 Osteoblast Assays

2.3.2.1 Sample Preparation

Anodized Ti, MWCNT-Ti, carbon nanopaper (CNP; Buckypaper), as shown in Figure 2-24, PPy[Dex]-Ti, PPy[P/S]-Ti, PPy-Ti, and commercial pure Ti were sterilized by UV light exposure for four hours on each side and were rinsed with PBS three times before osteoblast cultures. Substrates were then immediately rinsed with 0.1M phosphate buffered saline (PBS; 8 g NaCl, 0.2 g KCl, 1.5 g Na_2PO_4, and 0.2 g KH_2PO_4 in 1000 ml deionized water adjusted to a pH of 7.4; Sigma-Aldrich; St. Louis, MO, USA) three times and placed in 12 well plates. Carbon nanopaper (CNP; Buckypaper; NanoLab, Inc; Newton, MA, USA) is MWCNT compacts, which were purified with hydrochloric acid (HCl) to dissolve residual catalyst Iron (Fe) particles before compaction. Specifically, MWCNTs were sonicated and pressurized into the filter surface and were formed the sheet. The diameter of MWCNTs was 15 nm and the length was 5-15 μm. Raman spectrum (I_D/I_G) ratio of MWCNT compacts as CNP was 1.65.

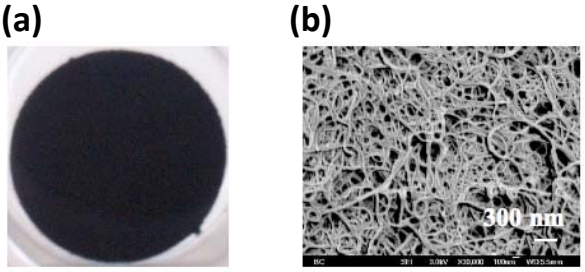

Figure 2-24. Carbon nanopaper used in cell experiments (CNP; Buckypaper; NanoLab, Inc; Newton, MA, USA): (a) top view of CNP (diameter of 40 mm) and (b) an SEM micrograph of CNP (scale bar = 300 nm).

2.3.2.2 Osteoblast Adhesion and Morphology

In vitro osteoblast cytocompatibility assays were determined on four types of samples in the present study including pure Ti, anodized nanotubular Ti, CNTs grown from anodized nanotubular Ti, and CNP. For the CNTs grown from anodized Ti, all substrates used in the cell assays employed the cobaltous nitrate catalyst. Human osteoblasts (CRL-11372; population numbers 5-12; ATCC; Manassas, VA, USA) adhesion and differentiation from non-calcium to calcium depositing cells were determined on each substrate. For adhesion, 3,500 osteoblasts/cm^2 were seeded in Dulbecco's Modified Eagle Medium (DMEM; Gibco; Grand Island, NY, USA) supplemented with 10% fetal bovine serum (FBS; Hyclone; Logan, UT, USA) and 1% penicillin/streptomycin (P/S; Hyclone; Logan, UT, USA) onto the substrates under standard incubator conditions (a humidified, 5% CO_2, and 95% air environment at 37° C) for four hours, and then were washed with PBS three times to remove nonadherent cells. Afterward, remaining osteoblasts were fixed with acetate buffer containing 10% formalin (Fisher-Scientific; USA) for 10 minutes, stained with a fluorescent stain (4',6-diamidino-2-phenylindole (DAPI; Invitrogen; USA), diluted to 300 nM) and counted under a fluorescence microscope (Zeiss Axiovert 200M; Peabody, MA, USA). Five random fields were counted per substrate. Cell adhesion testing was repeated three different times. Initial osteoblast adhesion after four hours on the anodized Ti surfaces with and without MWCNTs was also evaluated by scanning electron microscopy (SEM; Hitachi 2700). Before SEM analysis, all samples were fixed with acetate buffer containing 10% formalin (Fisher-Scientific; USA) for 10 minutes, dehydrated with a series of ethanol (30%, 50%, 70%, 90%, and 100%; 20 minutes each), critically point dried (CPD) by LADD Research (Williston, VT, USA), and finally coated with a thin layer of gold-palladium (AuPd; Ted Pella, Inc; Redding, CA, USA).

2.3.2.3 Osteoblast Proliferation

Cell proliferation was assessed using an MTS (3-(4,5-dimethylthiazol-2-yl)-5-(3-carboxymethoxyphenyl)-2-(4-sulfophenyl)-2H-tetrazolium, inner salt tetrazolium/formazan) assay (Promega, Boston, MA) after osteoblasts (3,500 cells/cm^2) were allowed to grow on the PPy-drug membranes for 1, 3, and 5 days in DMEM supplemented with 10% FBS, 1% P/S, 50 nM β-glycerophosphate (Sigma; St. Louis, MO, USA), and 50 μg/ml ascorbic acid (Sigma; St. Louis, MO, USA) under standard cell culture conditions. During osteoblast proliferation experiments, the media was replaced every other day. All samples were transferred to a new cell culture plate, containing fresh culture media, 10% v/v of the MTS assay was added, and were incubated for two hours under standard cell culture conditions [3]. 100 μl of each sample was transferred to a 96-well plate (Corning; Lowell, MA, USA) and absorbance was read at 490 nm with a SpectraMax V5 Spectrophotometer (Molecular Devices; Chicago, IL, USA). Corrected absorbance was calculated by subtracting the average absorbance from the cell culture media (without cells) as controls.

2.3.2.4 Osteoblast Differentiation

In order to evaluate the osteoblast differentiation, 40,000 cells/cm^2 were seeded onto the substrates of interest and were cultured in DMEM supplemented with 10% FBS, 1% P/S, 50 nM β-glycerophosphate (Sigma; St. Louis, MO, USA), and 50 μg/ml ascorbic acid (Sigma; St. Louis, MO, USA) under standard incubator conditions for 7, 14, and 21 days. The culture medium was changed every other day. At the end of the prescribed time period, an alkaline/acid phosphatase assay kit (Upstate) was used to determine the concentration of alkaline phosphatase in cell

lysates. Cell lysates were prepared by first rinsing all samples with Tris-buffered saline (TBS; 42 mM Tris-HCl, 8 mM Tris Base and 0.15 M NaCl; pH of 7.4; Sigma-Aldrich; St. Louis, MO, USA) three times and then subjecting the cells to three freeze-thaw cycles using distilled water. A calcium quantification kit (Pointe Scientific; Canton MI, USA) was also used to determine the amount of calcium deposited by osteoblasts cultured on each substrate. An acidic supernatant solution for this assay was prepared by incubating all the samples with 0.6 N HCl (Sigma; St. Louis, MO, USA) overnight. The light absorbance was measured by a spectrophotometer (SpectraMAX 340PC^{384}; Molecular Devices; Chicago, IL, USA) at 650 nm for alkaline phosphatase activity [4] and 570 nm for calcium deposition [5].

The commercially pure Ti and MWCNT-Ti after osteoblast culture for 21 days were also fixed with acetate buffer containing 10% formalin (Fisher-Scientific; USA) for 10 minutes, dehydrated with a series of ethanol (30%, 50%, 70%, 90%, and 100%; 20 minutes each), and were critically point dried by LADD Research CPD. The chemical composition on the surfaces of the commercially pure Ti and MWCNT-Ti after osteoblast culture for 21 days were evaluated by energy dispersive spectroscopy (SEM-EDS; Zeiss/Leo 1530VP FE-4800; Peabody, MA, USA). The energy-disperive spectroscope (EDS) was an Oxford INCA 250 detector with associated software (Oxford Instrument America, Inc; Concord, MA, USA). Long-term cytocompatible testing was conducted in triplicate and was repeated three different times. Numerical data was analyzed using the standard student t-test.

2.3.2.4.1 Alkaline Phosphatase Assay

Alkaline/Acid Phosphatase Assay Kit (R-R-A-pS-V-A) (Cat# 17-128, Lake Placid Upstate, NY, USA) were used in this study [4]. Firstly, Malachite Green Phosphate Detection solution were prepared by adding 10 μl of Malachite Green Additive (Solution B; Cat# 20-104) to each 1 ml of Malachite Green (Solution A; Cat# 20-105) and mixing only enough reagent as required for use that day. The solution may be kept at room temperature during use. Then, phosphate standard curve was prepared by diluting 150 μl of Phosphate Standard (Solution C; Cat# 20-103) with 1350 μl of TBS to make a 0.1 mM working solution. The standard curve should range between 200 and 2000 pmloes per well. After that, 25 μl of each phosphate standard were transferred to wells of a 96-well microtiter plate, added 100 μl of Malachite Green Solution prepared in the beginning, and mixing carefully without creating bubbles (bubbles interfere with measurement of absorbance). Finally, allowing color development proceed for 15 minutes at room temperature and measure absorbance at a wavelength at 650 nm in a microtiter plate reader. Subtract the absorbance of blank solution from standards. Lastly, graph was plotted pmoles phosphate vs. absorbance for the standard curve. Alkaline phosphatase assay was mixed in one microtiter well with 5 μl $NiCl_2$ (40 mM; Cat# 20-178), 5 μl BSA (5mg/ml), 5 μl phosphopeptide stock solution (Serine Phosphopeotide, RRApSVA; Cat# 12-220), and 0.1-0.5 units of cell lystate. Then, it was adjusted volume to 80 μl with pNNP Ser/Thr Assay Buffer (Cat# 20-179), and was transferred for 25 μl aliquots to new microtiter wells (test in triplicate). A blank was prepared the same as the sample, but without cell lystate (replace cell lystate with an equal volume of pNPP Ser/Thr Assay Buffer (Cat# 20-179)). After that, alkaline phosphate assay was incubated with cell lystate for 10-15 minutes at 37°C. Then, to detect alkaline phosphatase activity, 100 μl

Malachite Green solution was added, incubated more for 15-20 minutes at room temperature, and read at 650 nm.

2.3.2.4.2 Calcium Deposition Assay

Calcium (Arsenazo III) (C7529-500, Pointe Scientific, Inc., Canton MI, USA) was used to measure calcium mineral deposition in this study [5]. Reagent was prepared by combining equal volumes of color (o-Cresolphthalein Complexone, 0.11 mM; 8-Hydroxyquinoline 17 mM, surfactant) and buffer (2-Amio-2Methyl-1-Propanol 976 mM; Potassium Cyanide, 2 mM) reagent, mixed it well, and kept at room temperature for 20 minutes before use. Reagents should be combined in clean plastic vessels. Water and glassware containing calcium will react with the reagent. All glassware should be rinsed in dilute hydrochloric acid before use. An aqueous Calcium Standard (10 mg/dl) was mize with 200 μl of reagent, and series diluted to obtain standard curve. The absorbance of blank solution was subtracted from standards. To test the calcium concentration, 200 μl of reagent was mixing with 10 μl of cell lystate, then keep it for at least one minute at room temperature, and finally read and record absorbance at 570 nm.

2.3.2.5 Gel Electrophoresis

The extracellular components deposited by osteoblasts were extracted from osteoblasts cultured on commercially pure Ti. After 21 days of culture, samples were cleaned with TBS buffer three times, and then three freeze-thaw cycles with distilled water were performed to lyse the extracellular components from osteoblasts. Then, samples were soaked in 0.6 N HCl

(Sigma-Aldrich; St. Louis, MO, USA) for 24 hours in 37°C to dissolve calcium and other extracellular components secreted by osteoblasts. The solution of extracellular components was purified by centrifuge for three times to eliminate cell debris, and then freeze-dried into a protein power.

The protein powder was dissolved in PBS and the protein concentration was characterized through Bradford protein assay. 20μg protein was loaded in each well for sodium dodecyl sulfate (SDS) polyacrylamide gel electrophoresis (SDS-PAGE). Gel electrophoresis was carried out at room temperature in 1X Tris-HEPES-SDS Running Buffer (Pierce; Rockford, IL) at a pH of 8.0 with precast SDS polyacrylamine gradient gel 8% (Pierce; Rockford, IL) at 100 V for 120 min. BenchMark™ Protein Ladder (Invitrogen) was used as a marker. Finally, the stacking gel was stained with Coomassie Brilliant Blue R®-250 (B-6529; Sigma; St. Louis, MO).

2.3.3 Fibroblast Assays

2.3.3.1 Sample Preparation

PPy[Dex]-Ti, PPy[P/S]-Ti, PPy-Ti, and commercial pure Ti were sterilized using UV exposure for four hours on each side and were rinsed with 0.1 M PBS buffer three times before fibroblast cultures.

2.3.3.2 Fibroblast Adhesion

Mouse fibroblasts (NIH/3T3; passage number 4-7; ATCC CRL-1658; Manassas, VA, USA) in DMEM (30-2002; ATCC; Manassas, VA, USA) with 10% bovine calf serum (30-2031; ATCC; Manassas, VA,

USA) were seeded at a density of 3,500 cells/cm^2. After four hours of adhesion, samples were rinsed with 0.1M PBS buffer for three times. Fibroblasts were then fixed with 10% formalin buffered acetate (Fisher-Scientific; USA) for 10 minutes and stained with DAPI (Invitrogen; USA). A Leica (Bannockburn, IL, USA) D5500 B fluorescence microscope at 20X magnification captured the fluorescent images and 10 random fields per sample were used to determine cell density by counting DAPI-stained nuclei. The fibroblast adhesion experiments were repeated at three different times.

2.3.3.3 Fibroblast Proliferation

Cell proliferation was assessed using an MTS (3-(4,5-dimethylthiazol-2-yl)-5-(3-carboxymethoxyphenyl)-2-(4-sulfophenyl)-2H-tetrazolium, inner salt tetrazolium/formazan) assay (Promega, Boston, MA) after fibroblasts (3,500 cells/cm^2) were allowed to grow on the PPy-drug membranes for 1, 3, and 5 days in DMEM (30-2002; ATCC; Manassas, VA, USA) with 10% bovine calf serum (30-2031; ATCC; Manassas, VA, USA). During fibroblast proliferation, the media was replaced every other day. All samples were transferred to a new cell culture plate, containing fresh culture media, while 10% v/v of the MTS assay was added, and were incubated for two hours under standard cell culture conditions [3]. 100 μl of each sample was transferred to a 96-well plate (Corning; Lowell, MA, USA) and absorbance was read at 490 nm with a SpectraMax V5 Spectrophotometer (Molecular Devices; Chicago, IL, USA) [3]. Corrected absorbance was calculated by subtracting the average absorbance from the cell culture media (without cells) used as controls.

2.3.4 Macrophage Assays

2.3.4.1 Sample Preparation

PPy[Dex]-Ti, PLGA-PPy[Dex]-Ti, PLGA-NHS, glass, and commercial pure Ti were sterilized using UV exposure for four hours on each side and were rinsed with 0.1 M PBS buffer for three times before macrophage cultures.

2.3.4.2 Macrophage Adhesion

Mouse macrophages (TIB-186; passage number 12-16; ATCC; Manassas, VA, USA) were seeded on substrates of interest to this study in RPMI 1640 media (Hyclone; Logan, UT, USA) supplemented with 10% FBS (Hyclone) and 1% P/S (Hyclone) in a standard cell culture environment (at 37°C and 5% CO_2 in humidified air) at 3,500 cell/cm^2. After four hours, samples were rinsed with 0.1 M PBS buffer for three times and were fixed with 10% formalin buffered acetate (Fisher-Scientific; USA) for 10 min. Then, the samples were rinsed with 0.1 M PBS buffer for three times and stained with 4',6-diamidino-2-phenylindole (DAPI; Invitrogen; USA), diluted to 300 nM, in order to count cell-nuclei in 10 random fields per sample under a fluorescence microscope (D5500 B; Leica; Bannockburn, IL, USA). The macrophage adhesion experiments were repeated three different times.

2.3.4.3 Macrophage Adhesion After Electrical Stimulation

Mouse macrophages (TIB-186; passage number 12-16; ATCC; Manassas, VA, USA) were seeded onto PPy-Ti and PPy[Dex]-Ti in RPMI 1640 media (Hyclone; Logan, UT, USA) supplemented with

10% FBS (Hyclone) and 1% P/S (Hyclone) in a standard cell cultured environment (at 37°C and 5% CO_2 in humidified air) at 10 million cells/cm^2. Macrophages were cultured onto PPy-Ti and PPy[Dex]-Ti for four hours before the application of voltage using cyclic voltammetry (scan rate of 100 mV/s from -1 V to 1V for 5 cycles). After cyclic voltammetry was applied, macrophages on PPy-Ti and PPy[Dex]-Ti were allowed to incubate further for either four or nine hours. The experiments were repeated three different times. Afterward, samples were cleaned with 0.1 M PBS buffer for three times and the remaining macrophages were fixed with acetate buffer containing 10% formalin (Fisher-Scientific; USA) for 10 minutes. Then, samples were cleaned with PBS three times, and stained with a fluorescent stain (4',6-diamidino-2-phenylindole (DAPI; Invitrogen; USA), diluted to 300 nM) and were counted the number of cell adhesion under a fluorescence microscope (D5500 B; Leica; Bannockburn, IL, USA) at 20X magnification. Eight random fields were counted per substrate.

2.3.4.4 Macrophage Assays After Anti-inflammatory Drug Release

After macrophages (TIB-186; passage number 12-16; ATCC; Manassas, VA, USA) were cultured at 3,500 cell/cm^2 for four hours in RPMI 1640 (Hyclone; Logan, UT, USA) supplemented 10% FBS (Hyclone) and 1% P/S (Hyclone) under a standard cell culture environment (at 37°C and 5% CO_2 in humidified air), electrical stimulation was performed on PPy[Dex]-Ti and PPy-Ti by using cyclic voltammetry (from -1 V to 1V) with a scan rate of 100 mV/s up for 5 cycles. Both samples were incubated again for four and nine hours. At each time point, samples with and without electrical stimulation were cleaned with 0.1 M PBS buffer for three times, and macrophages were fixed with acetate buffer containing 10% formalin (Fisher-Scientific; USA) for 10 minutes, stained with

fluorescent stain, 4',6-diamidino-2-phenylindole (DAPI; Invitrogen; USA), diluted as 300 nM, and counted the number of macrophage adhesion under fluorescence microscope (D5500 B; Leica; Bannockburn, IL, USA).

2.3.5 Bacteria Colony Assays

2.3.5.1 Sample Preparation

PPy[P/S]-Ti, PPy-Ti, glass, and commercial pure Ti were sterilized using UV exposure for four hours for each side, and were rinsed with TBS buffer for three times before bacteria cultures.

2.3.5.2 Bacteria Culture

A bacteria cell line (Staphylococcus epidermis; ATCC 35984; Manassas, VA, USA) was obtained in freeze-dried form. The pellet was rehydrated in Luria broth. Cells were used at the 2^{nd} passage and then frozen in glycerol and Luria broth (1:1). A sterile 10 μl loop was used to withdraw bacteria from the 2^{nd} bacteria passage and were inoculated in a polystyrene centrifuge tube with 3 ml of Luria broth. The tube of bacteria was agitated with a shaker (250 rpm) at 37°C for 16 hours before bacteria seeding. Bacteria concentration was assessed at an optical density of 562 nm at 30% transmittance (McFarlan Scale estimated 900 million bacteria/ml). This bacteria concentration was dilute to 10 million cells/ml in DMEM (Gibco; Grand Island, NY, USA) supplemented with 10% FBS (Hyclone; Logan, UT, USA), 50 nM β-glycerophosphate (Sigma; St. Louis, MO, USA) and 50μg/ml ascorbate (Sigma; St. Louis, MO, USA). Bacteria adhesion was investigated on PPy[P/S]-Ti, PPy, and commercially pure Ti after one and 12 hours. All samples

were washed twice with Tris-buffered saline before culture. Bacteria were seeded at 10 million cells/sample and were allowed to adhere in a standard incubator (at 37°C and 5% CO_2 in humidified air). After one and 12 hours of culture, samples were rinsed with TBS buffer three times. Then, all samples were stained with the Live/Dead BacLight bacteria viability kit (Molecular Probes), and images were captured by a Leica (Bannockburn, IL, USA) D5500 B fluorescence microscope at 20X magnification. Ten random fields per samples were used to determine bacteria density. The experiments were repeated three different times.

2.3.5.3 Bacteria Colony Assays After Antibotic Release

Bacteria (*Staphylococcus epidermis*; ATCC 35984; Manassas, VA, USA) at 10 million/ml were incubated for one hour and 12 hours on PPy[P/S]-Ti, PPy-Ti, Glass, and Ti in DMEM (Gibco; Grand Island, NY, USA) supplemented with 10% FBS (Hyclone; Logan, UT, USA), 50 nM β-glycerophosphate (Sigma; St. Louis, MO, USA) and 50μg/ml ascorbate (Sigma; St. Louis, MO, USA) in a standard incubator (at 37°C and 5% CO_2 in humidified air). Electrical stimulations triggered P/S releases from PPy[P/S]-Ti using cyclic voltammetry with a scan rate of 100 mV/s (from -1 V to 1 V) up to 40 cycles. The Live/Dead BacLight bacteria viability kit (Molecular Probes) was used to stain bacteria after electrical stimulations. A fluorescence microscope (D5500 B; Leica; Bannockburn, IL, USA) was used to capture live/dead bacteria at 20X magnification. P/S were also released by cyclic voltammetry after bacteria were cultured for 12 hours, and the fluorescent pictures of stained bacteria were taken at 10X magnification. The experiments were repeated two different times.

2.4 Statistical Analyses

Numerical data was analyzed using Microsoft Excel (Seattle, WA, USA) and KaleidaGraph (Reading, PA, USA). All data were expressed as mean $\pm$ standard error of the mean (S.E.M.). A student t-test and analysis of variance (ANOVA) were used for hypothesis testing in this thesis. Data found to be significant after ANOVA were tested post hoc by the Tukey's honest significant difference (HSD) test.

References

1. Yao C, Perla V, McKenzie JL, Slamovich EB, Webster TJ. Anodized Ti and Ti6Al4V Possessing Nanometer Surface Features Enhances Osteoblast Adhesion. Journal of Biomedical Nanotechnology 2005;1:68-73(66).

2. Park Scientific Instrument. User's Guide to Autoprobe CP and M5. Part III: Software Reference for PSI ProScan Software. Sunnyvale, CA, USA, 1998.

3. Promega. CellTiter 96® AQ_{ueous} One Solution Cell Proliferation Assay, Technical Bulletin. Medison, WI, USA, 2005.

4. Upstate. Certificate of Analysis, Alkaline/Acid Phospatase Assay Kit. Cat# 17-128. Lake Placid, NY, USA.

5. Pointe Scientific. Instruction Calcium Reagent Set, Calcium (Arsenazo III). Canton, MI, USA.

6. Thermo Scientific. Instructions Pierce® BCA Protein Assay Kit (Pierce Biotechnology). 23225 23227. Rockford, IL, USA.

CHAPTER 3

RESULTS

3.1 Fabrication of Materials

3.1.1 Anodized Titanium

Results of this study showed that the commercially pure Ti exhibited a smooth surface at the nanometer scale (Figure 3-25a). After anodization, nanotubes were formed on commercially pure Ti uniformly with diameters of about 50-60 nm and depths of 200 nm [1, 2], as shown in Figure 3-25b.

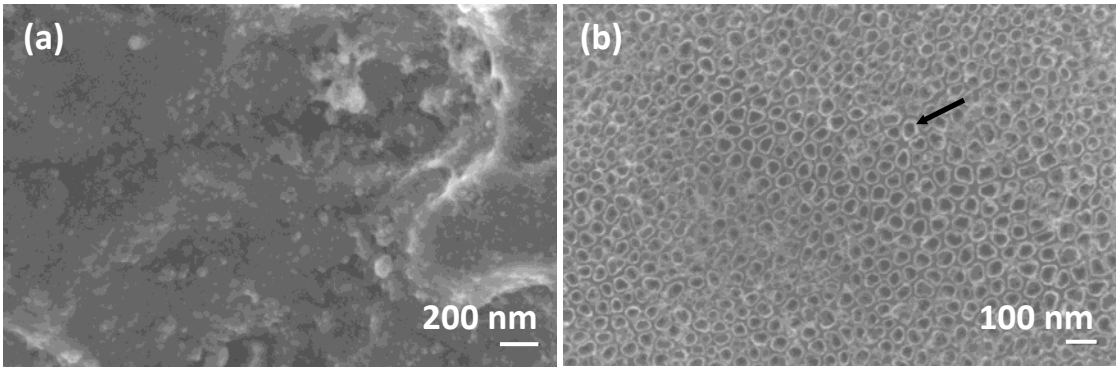

Figure 3-25. SEM micrographs of (a) commercially pure Ti and (b) anodized nanotubular Ti. The arrow indicates the nanotubes formed on Ti after anodization.

3.1.2 Multiwalled Carbon Nanotubes Grown Out of Anodized Nanotubular Titanium

After CVD treatment, MWCNTs covered the anodized nanotubular Ti (Figure 3-26 and Figure 3-27). When the cobalt catalyst pretreatment was not used, carbon from acetylene (C_2H_2) gas did not reduce to form MWCNT structures (Figure 3-26a and Figure 3-26b). Figure 3-26c, Figure 3-26d, Figure 3-26e, and Figure 3-26f illustrate that when anodized Ti was pretreated with the catalyst solution (5% wt. cobaltous nitrate in methanol) and subjected to CVD MWCNT-Ti formed. MWCNTs were also grown on unanodized Ti by cobalt-catalyzed CVD for 30 minutes and were observed under SEM as shown in Figure 3-27c and Figure 3-26d. The MWCNT growth time in the C_2H_2 gas also influenced the MWCNT with more substantial MWCNT coverage observed with an increase from 20 (Figure 3-26c and Figure 3-26d) to 30 (Figure 3-26e, Figure 3-26f, Figure 3-27a and Figure 3-27b) minutes; similar diameter MWCNTs were observed when MWCNTs were grown out of anodized nanotubular Ti using cobalt-catalyzed CVD method as shown in Figure 3-27e and Figure 3-27f. Using more than 5% wt. cobaltous nitrate increased non-MWCNT formation (Figure 3-26g and Figure 3-26h), due to apparent cobalt poisoning effects [3]. Generally, the catalyst poisoning effect is attributed to a progressive blocking of the active surfaced by excess amorphous carbon [4]. Thus, in Figure 3-26g and Figure 3-26h, amorphous carbons were formed when anodized Ti was treated with 10% wt. cobaltous nitrate before the CVD process. Although the topography of MWCNT-Ti was non-uniform and oriented in the random direction, greater roughness of MWCNT-Ti was observed at the nanometer scale under SEM than commercially pure Ti (Figure 3-26 and Figure 3-27). The MWCNTs grown in this study were 50-60 nm (matching the diameter of the anodized Ti nanotubes) in diameter, as determined by HRTEM (Figure 3-28) and possessed lengths in micrometers (Figure 3-27). Cobalt

particles were found on MWCNT-Ti under HRTEM (Figure 3-28) and were confirmed by elemental analysis (or SEM-EDS, see the osteoblast extracelluar component analysis section). Cobalt was found on MWCNT-Ti even after osteoblasts were cultured for 21 days.

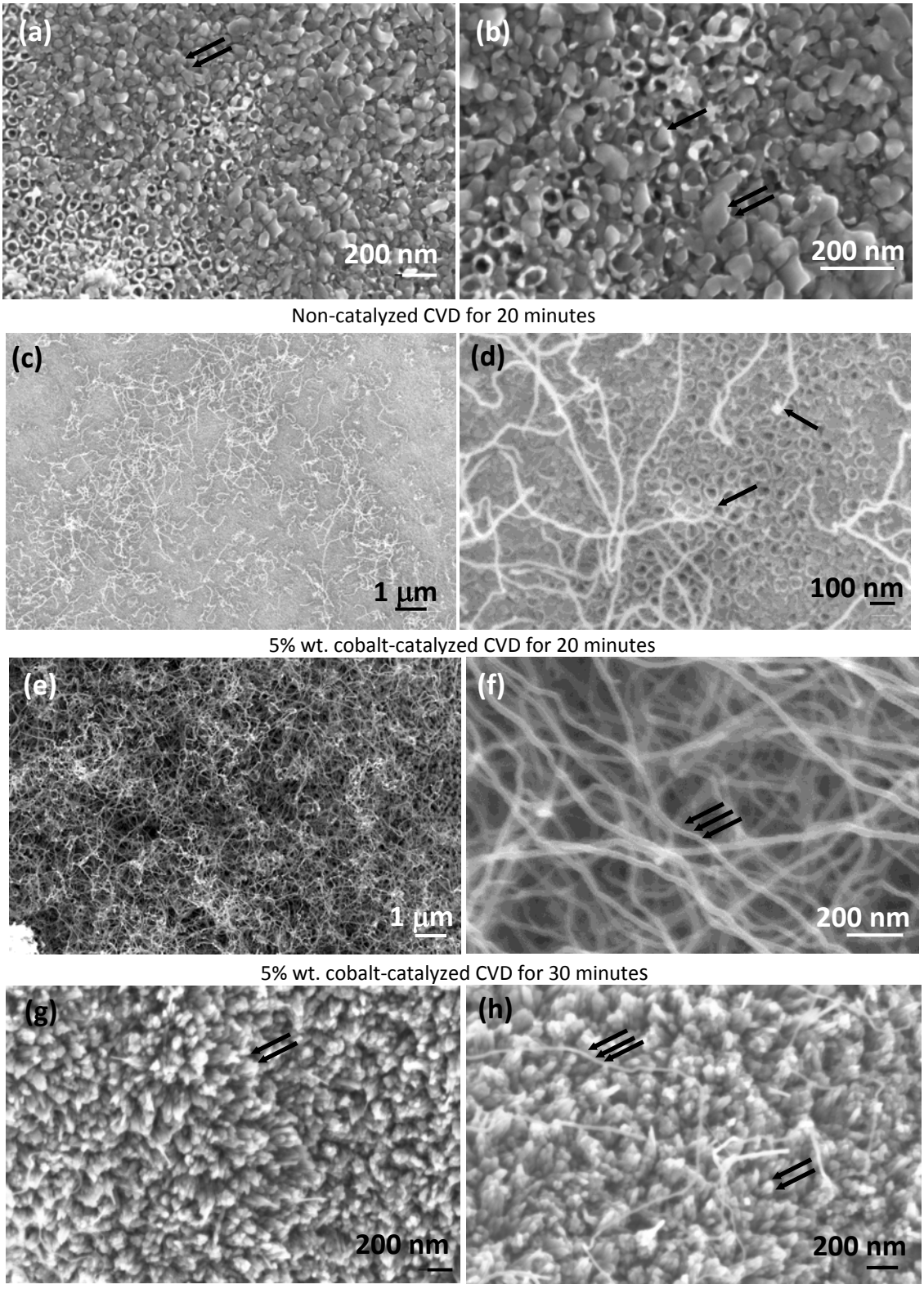

Figure 3-26. SEM micrographs of: (a), (b) MWCNT-Ti without a Co catalyst in CVD for 20 minutes; (c), (d) with a Co catalyst in CVD for 20 minutes; and (e), (f) MWCNT-Ti with a Co catalyst in CVD for 30 minutes. The single arrows show MWCNTs coming out of the Ti nanotubes. The double arrows indicate amorphous carbon and the triple arrows indicate MWCNTs.

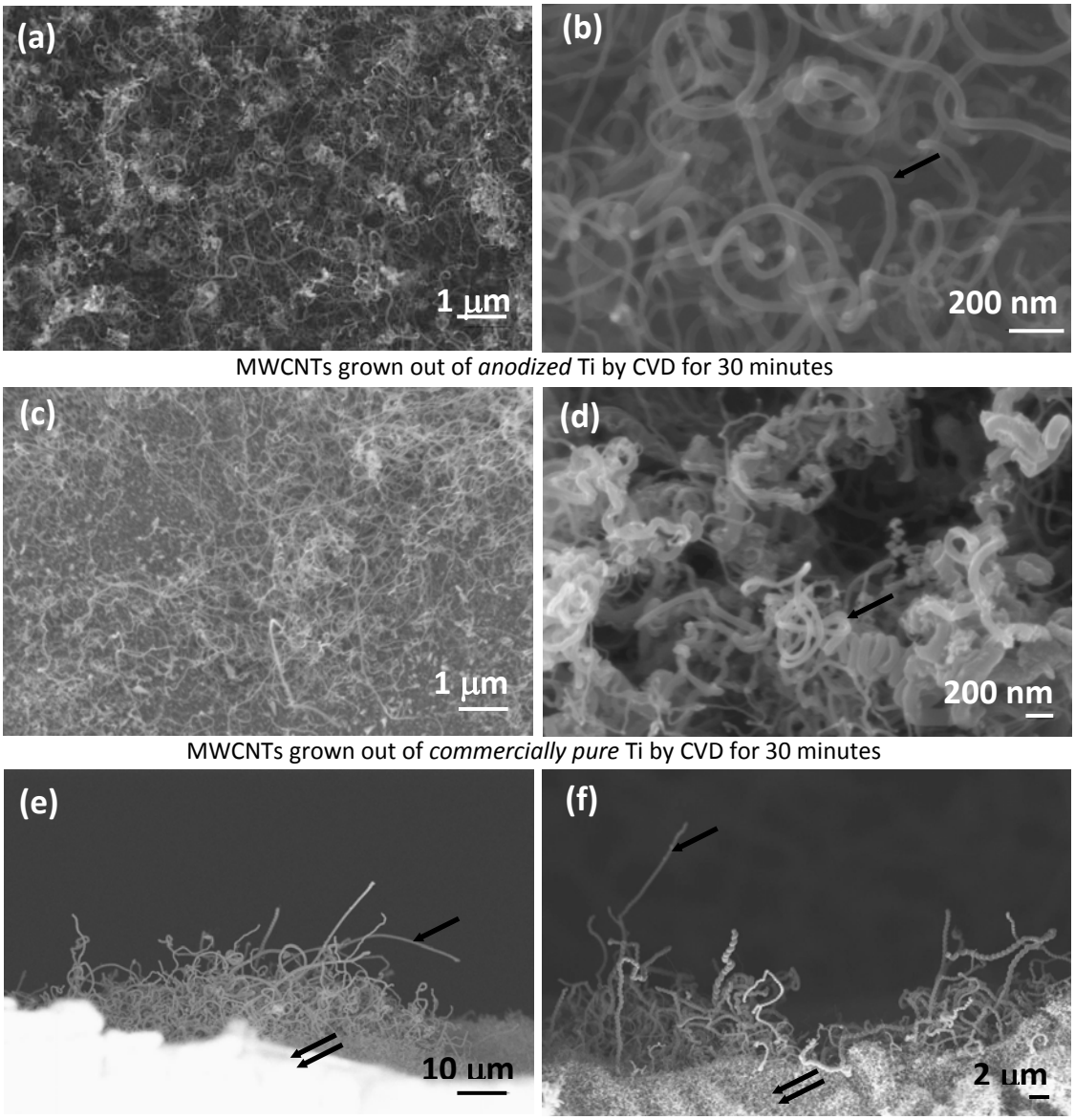

Figure 3-27. SEM micrographs of MWCNTs grown out of: (a), (b) anodized nanotubular Ti for 30 minutes (top view); (c), (d) commercially pure Ti for 30 minutes (top view); and (e), (f) anodized nanotubular Ti for one hour (side view), by cobalt-catalyzed CVD. The single arrows show MWCNT and double arrows indicate anodized Ti templates.

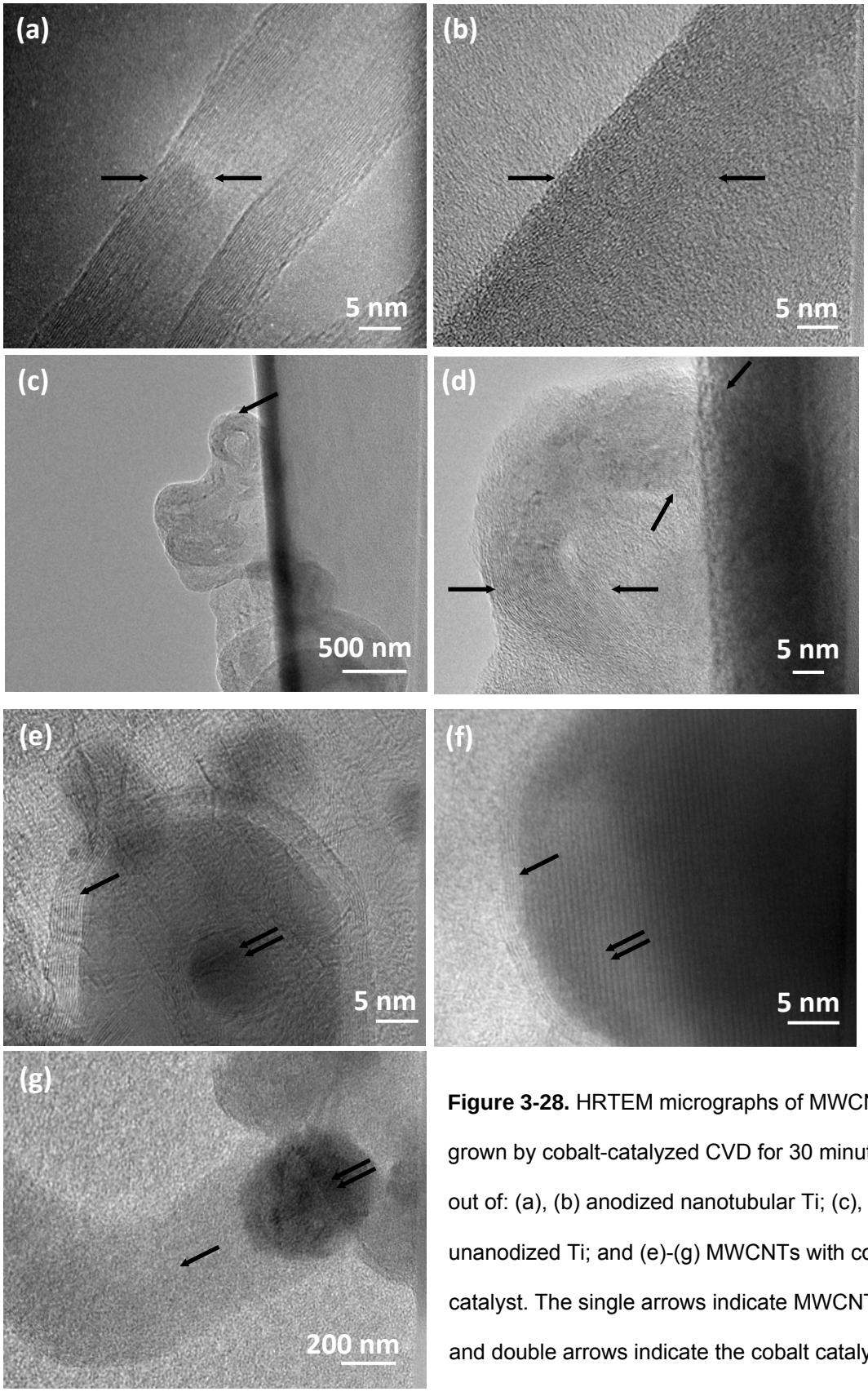

Figure 3-28. HRTEM micrographs of MWCNTs grown by cobalt-catalyzed CVD for 30 minutes out of: (a), (b) anodized nanotubular Ti; (c), (d) unanodized Ti; and (e)-(g) MWCNTs with cobalt catalyst. The single arrows indicate MWCNTs and double arrows indicate the cobalt catalyst.

3.1.3 Electrodeposition of Polyprrole

Electrodeposition was performed through oxidation with an applied sweep voltage in positive range of 0 to 1.1 V. The PPy films were electrodeposited onto AuPd-Ti or MWCNT-Ti in a positively charged state. After this electrochemical deposition, a homogeneous black fillm was observed on the AuPd-Ti around 0.8 cm^2. Moreover, adding dopants (either P/S or Dex) into PBS increased the electropolymerization reaction of pyrrole to balance the charge of PPy (approximately four monomers representing one cation). Both P/S and Dex (containing carboxylic groups) are anions, which were entrapped electrostatically into the PPy film during the electrodeposition. Adding amine-containing pyrrole monomers and Dex made the reaction more robust and superior than pyrrole monomers with Dex (as demonstrated by higher current in CV presented in Figure 3-29). The PPy film thickness on Ti increased corresponding to the number of sweep voltage cycles. Specifically, profilometer analysis revealed that PPy-Ti had a thickness of 4.66$\pm$0.83 µm, PPy[P/S]-Ti had a thickness of 5.97$\pm$0.69 µm, PPy[Dex]-Ti had a thickness of 4.97$\pm$0.75 µm, and $PPyNH_2$[Dex]-Ti had a thickness of 5.76$\pm$1.3 µm (Table 3-5).

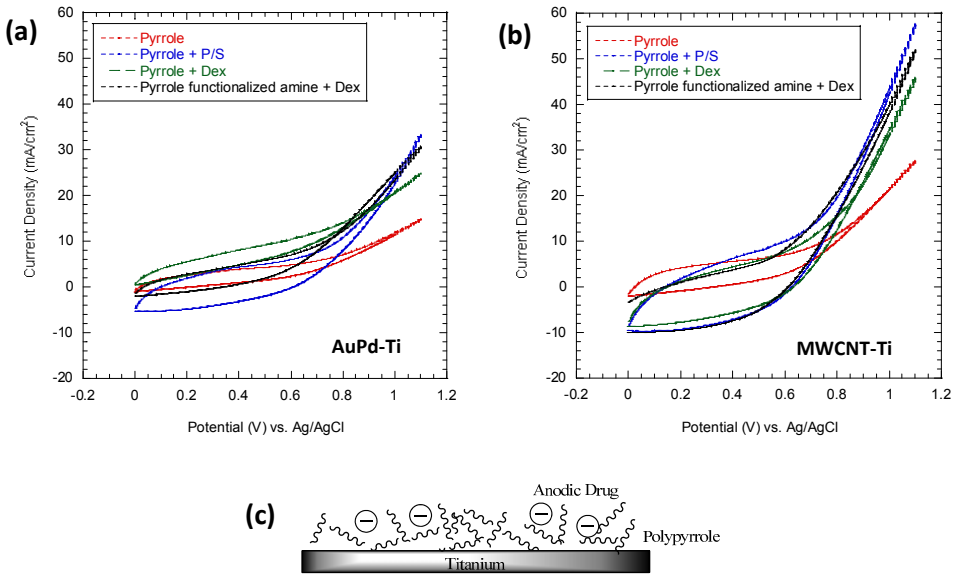

Figure 3-29. Cyclic voltammetry of potentiodynamic electropolymerization of pyrrole in solution of 0.1M pyrrole monomers in 1M phosphate buffer saline at pH 7.2 with penicillin/streptomycin (P/S) or dexamethasone (Dex) as anionic dopants on: (a) AuPd-Ti and (b) MWCNT-Ti. (c) The diagram of anodic drugs embedded within PPy film, which were electrodeposited on AuPd-Ti.

Table 3-5. Thickness of PPy films electrodeposited on AuPd-Ti analyzed using a profilometer (Dektax 3, Vecco, Lowell, MA, USA).

PPy Films	Thickness (μm)
PPy-Ti	4.66 ± 0.83
PPy[P/S]-Ti	5.97 ± 0.69
PPu[Dex]-Ti	4.97 ± 0.75
$PPyNH_2$[Dex]-Ti	5.76 ± 1.30

3.1.4 Zeta Potential Measurements of Drugs (Penicillin/Streptomycin and Dexamethasone) to be Embedded in Polypyrrole Films

Results of this study also showed that both P/S and Dex possessed negative zeta potentials and thus, were overall anionic charges (Table 3-6). Thus, P/S and Dex can be used as dopant molecules for oxidative polymerization with PPy. For Dex, increased dilution in a buffer led to a decrease in zeta potential (Table 3-6). At that point, Dex became more stable. For P/S, the zeta potential did not change after dilution with the PBS buffer. The combination of pyrrole monomers with P/S or Dex was also measured using the Zeta potential. The results showed that the pyrrole functionalized NH_2 with Dex had a consistent zeta potential at $+16.8 \pm 1.4$ mV, however, pyrrole with and without P/S or Dex did not.

Table 3-6. Zeta potential measurements before electropolymerization of P/S and Dex molecules in PBS buffer at pH 7.2 and deionized water.

Sample	Concentrations (mM)	Medium	Zeta potential (mV)
Dexamethasone (D1756; Sigma)	0.1250	PBS buffer at 7.2	-23.1 ± 1.2
	0.0625	PBS buffer at 7.2	-24.1 ± 2.2
	0.0156	PBS buffer at 7.2	-33.9 ± 2.0
	1.00	Deionized water	-21.2 ± 1.0
As-received Penicillin/Streptomycin (Hyclone)	6.82	PBS buffer at 7.2	-14.2 ± 2.9
	6.82	PBS buffer at 7.2	-16.5 ± 3.0
	3.64	PBS buffer at 7.2	-14.4 ± 2.6
	2.18	Deionized water	-1.26 ± 0.4

3.1.5 Mechanism of Electropolymerization

Since colloidal particles formed and precipitated in PBS buffer after completion of electropolymerization, the self-polymerization of pyrrole and dopants (P/S, Dex, or Cl^-) in PBS was investigated further by retaining the stock solution and measuring its absorbance after 4 and 30 hours. *In situ* electropolymerization of pyrrole monomers and P/S was accompanied by progressive changes in the UV-vis spectra, with the appearance first of polarons and subsequently bipolarons in Figure 3-30b, but it took sometime for the appearance of polarons and bipolarons in the stock solution of pyrrole monomers and Dex, and pyrrole monomer functionalized with NH_2 and Dex, as shown in Figure 3-30c and Figure 3-30d. Lastly, polarons and bipolarons were slightly observed when electrodepositing the PPy without any drugs on AuPd-Ti (Figure 3-30a).

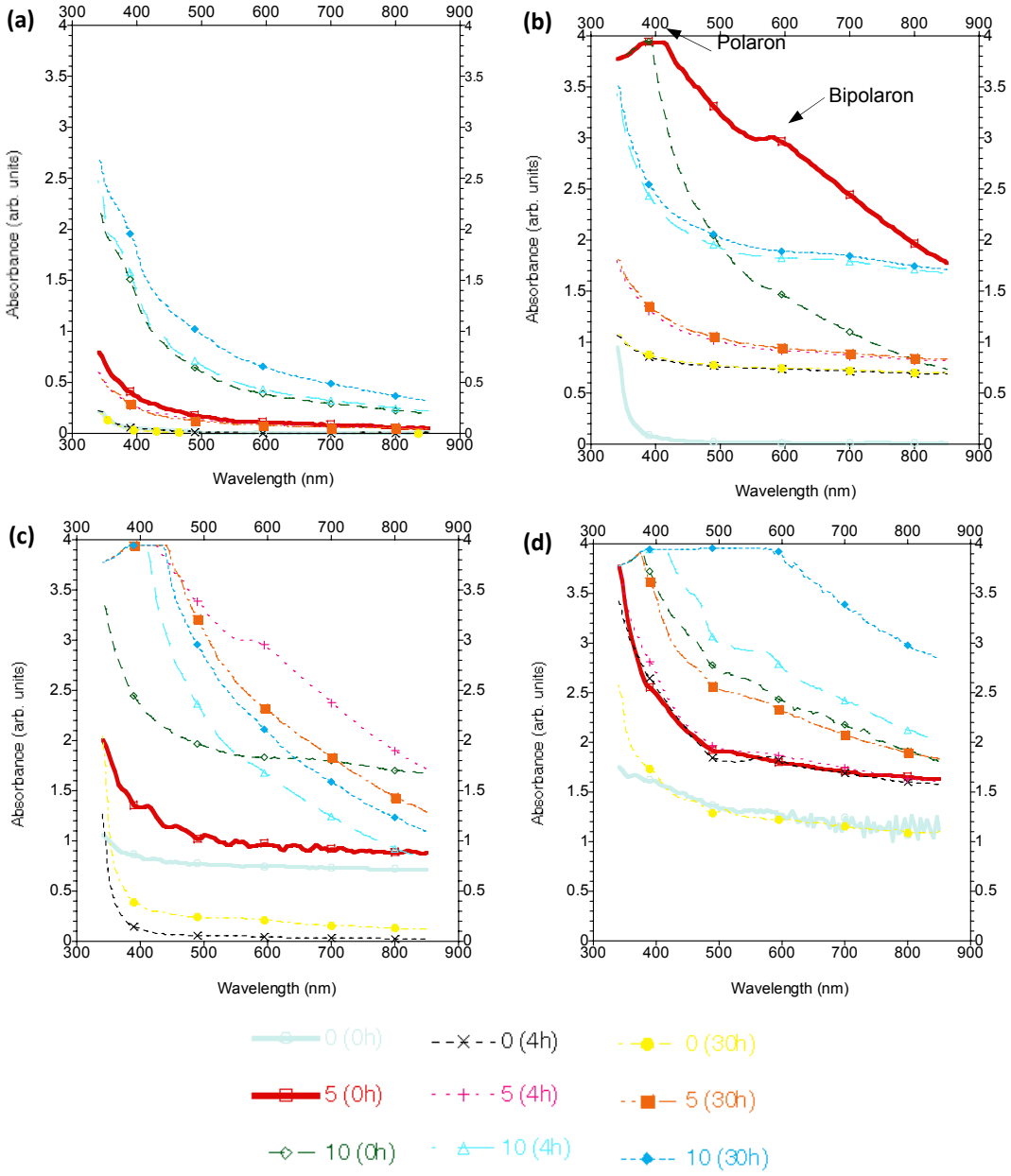

Figure 3-30. UV-vis spectra *in situ* of the self-electropolymerization after electrodeposition of: (a) PPyCl-Ti, (b) PPy[P/S]-Ti, (c) PPy[Dex]-Ti, and (d) PPy functionalized with NH_2 [Dex]-Ti.

3.2 Characterization of Materials

3.2.1 Raman Spectrophotometry

Raman spectra provided data of the quality, electronic structure, and diameter of the MWCNTs. First-order bands present in the spectra were a result of the C sp^2 vibration modes (1200-1700 cm^{-1}) of the MWCNTs. The G band (1500-1600 cm^{-1}) was attributed to the in-plane vibration while the D band (1200-1500 cm^{-1}) originated from the double resonant Raman scattering from defects [5]. The D band of the MWCNTs were observed at 1355.5 cm^{-1} and the G band at 1595.29 cm^{-1} for a wavelength of 488 nm, and the D band was observed at 1333.19 $cm^{-1}$and the G band at 1601.69 cm^{-1} for a wavelength of 633 nm (Figure 3-31). The radial breathing mode (RBM) resulted from out-of-the-plane atomic vibrations [6]. Sharp RBM peaks were present at 1293.16 cm^{-1} and 1751.4 cm^{-1} (Figure 3-31), which originated from the innermost nanotubes [7].

Typically, G bands are present due to tangential stretch modes of the nanotubes, and D bands are due to disordered graphite or amorphous carbons [5, 7]. The Raman intensity ratio (intensity of D band/intensity of G band; I_D/I_G) reflects the degree of this structural disorder in MWCNTs (low I_D/I_G represents low defect concentrations) [8, 9]. Raman intensity ratio (I_D/I_G) in Figure 3-31 is 0.8236 for 488 nm and 1.0815 for 633 nm. The diameter of the innermost nanotube can be identified using the relation [7]:

$$\omega_{(n,m)} = \frac{C}{d_{(n,m)}^{\ 2}} \qquad \textbf{[3-1]}$$

where ω is the RBM frequency separation in the wavelength number and C = 47.7 cm^{-1} for semiconducting nanotubes, and 79.5 cm^{-1} for metallic nanotubes [7]. Here, $d_{(n,m)}$ is the diameter of the nanotube in nanometers with its structure specified by a pair of indices *(n,m).*

Measurements showed that the average RBM peak separation of 4 cm^{-1} represents an approximate innermost diameter of 3.35 nm.

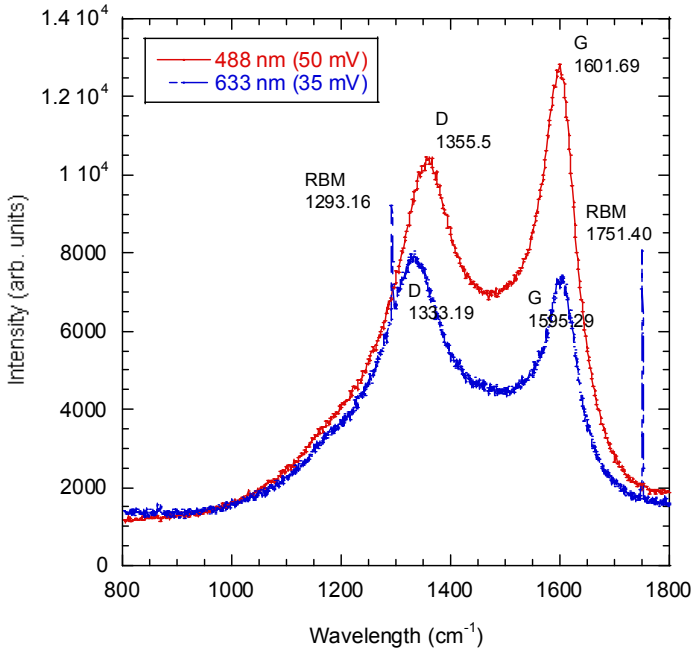

Figure 3-31. Raman spectra of MWCNTs grown out of anodized nanotubular Ti: for 488 nm, D band at 1355.5 $cm^{-1}$and G band at 1595.29 cm^{-1} and for 633 nm, D band at 1333.19 cm^{-1} and G band at 1601.69 cm^{-1}.

3.2.2 Contact Angle Measurements and Surface Energy

The results of this study showed that anodized nanotubular Ti had the lowest double deionized water contact angles (Figure 3-32) whereas MWCNT-Ti had the highest double deionized water contact angles. When using glycerol, the contact angles on commercially pure Ti was significantly higher than anodized Ti, but had comparable contact angles to those of MWCNT-Ti. Lastly, polyethylene glycol (MW=1000) contact angles for commercially pure Ti, anodized Ti, and MWCNT-Ti were not significantly different as shown in Figure 3-32.

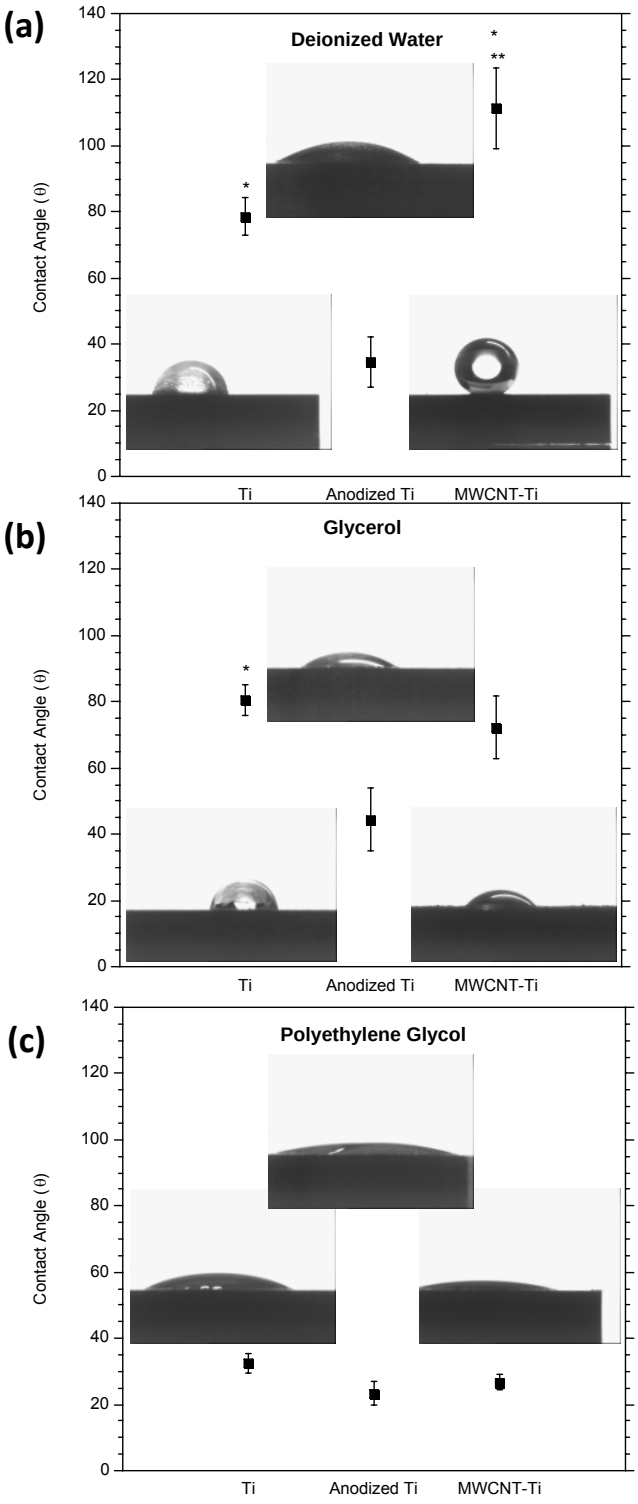

Figure 3-32. Contact angle measurements using the easy drop model system (Krüss) with (a) double deionized water, (b) glycerol, and (c) polyethylene glycol (PEG), all on commercially pure Ti, anodized Ti, and MWCNT-Ti. Values are mean ± S.E.M.; N=3; * $p<0.01$ compared to anodized Ti and ** $p< 0.01$ compared to Ti.

The surface energy of commercially pure Ti, anodized Ti, and MWCNT-Ti, which were calculated from double deionized water, glycerol, and polyethylene glycol, were compared in Table 3-7. Table 3-7 was calculated based on the Zisman and Owens-Wendt methods. σ_{crit} from the Zisman model is critical surface tension of biomaterial surfaces related to biological interactiveness [10]. σ_{tot} from the Owens-Wendt model is the total surface energy which is composed of polar and dispersive (non-polar) components. The dispersive component is associated with London dispersive forces (an induced dipole-induced dipole attraction) of interaction, and the polar component is associated with acid-base interactions [11]. Typically, σ_{tot} is related via an interaction parameter, such as adhesion energy from polarizabilities, dipole moments, and ionization potential.

By combining the contact angle results from three different liquids, it was found that the critical surface tension of MWCNT-Ti was approximately 42.23 dynes/cm, while the critical surface tension of commercially pure Ti and anodized nanotubular Ti was 36.92 dynes/cm and 18.06 dynes/cm, respectively (Table 3-7). Regarding the Zisman method, the higher biological response should occur on MWCNT-Ti than anodized Ti and commercially pure Ti due to its highest critical surface tension [10] (this was confirmed by results from this study (in the section of osteoblast responses). According to the Owens-Wendt method, the total surface energy of anodized Ti and MWCNT-Ti were similar. However, the total surface energy of the anodized Ti contributed more to the polar part, while that of the MWCNT-Ti contributed to the dispersive component.

Water tends to adsorb on hydrophilic high-energy surfaces. Results showed that anodized Ti had the lowest double deionized water contact angles (the boundary of the water layer was closer to the surface), thus, anodized Ti was more hydrophilic than commercially pure

Ti and MWCNT-Ti (Figure 3-32). Hydroxyl groups are normally found on commercially pure Ti, however, anodized Ti was more hydrophilic than commercially pure Ti due to increased surface roughness of anodized Ti [12], and thus more hydroxyl groups were present on anodized Ti. Hydroxyl groups are very important in the donor or acceptor character of a surface, and contribute to the polar part of total surface energy [13]. The results confirmed that anodized Ti was hydrophilic with a high polar component of total surface energy (Table 3-7).

The hydrophobicity of MWCNTs did not depend on the total surface energy (Table 3-7). Instead, MWCNT-Ti had high total surface energy but had highest double deionized water contact angles (Figure 3-32). The results from the FTIR spectra showed that the dispersive surface energy of MWCNT-Ti contributed from the C-O and C-H groups (Figure 3-33). The peak from 1050 to 1250 cm^{-1} are typically assigned to C-O stretching and from 3400 to 3900 cm^{-1} are assigned to C-H stretching [14]. Thus, the polar surface energy of anodized Ti was mainly attributed to the hydroxyl groups on anodized Ti and the dispersive component was attributed to the non-polar molecules of carbon.

Table 3-7. Solid-vapor surface energy.

Substrates	Type of Surface energy (σ_{SV}; dynes/cm) Calculation			
	Zisman	Owens-Wendt		
	σ_{crit}	σ^{tot}	σ^{D}	σ^{P}
Ti	36.92	44.34	42.7	1.64
Anodized Ti	18.06	64.08	44.73	19.65
MWCNT-Ti	42.23	64.38	61.37	3.00

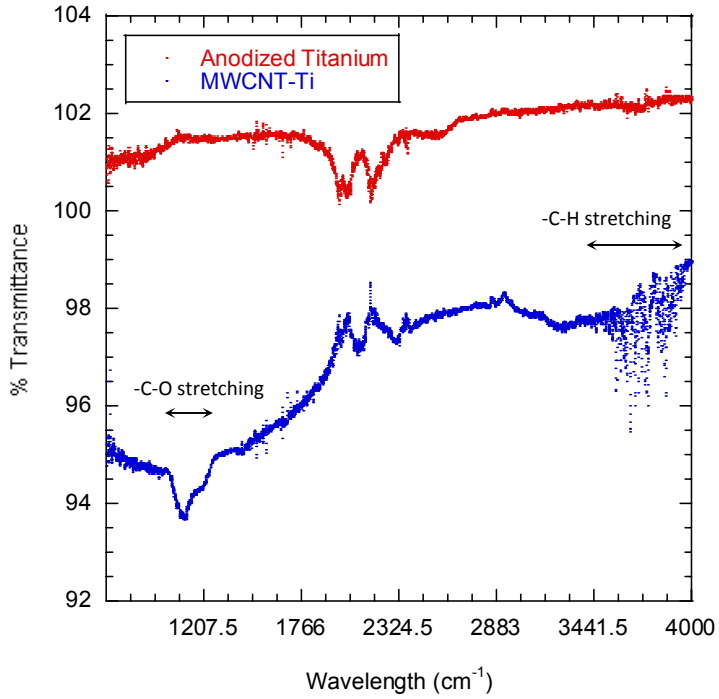

Figure 3-33. FTIR spectra of MWCN-Ti and anodized Ti in comparison.

3.2.3 Electrochemical Behavior (Cyclic Voltammetry)

3.2.3.1 Aerobic Electrolyte Solution (Non Nitrogen-Degassing)

3.2.3.1.1 Electrochemical Behavior of the $Fe^{2+/3+}$ Redox Couple on Ti, Anodized Ti, and MWCNT-Ti

Cyclic voltammetry experiments of the $Fe^{2+/3+}$ redox couple were performed by placing electrodes in an electrolyte solution of 10 mM $K_3Fe(CN)_6$ and 1 M KNO_3. In potassium ferricyanide ($K_3Fe(CN)_6$), the reduction process is Fe^{3+} ($Fe(CN)_6^{3-} + e^- \rightarrow Fe(CN)_6^{4-}$) followed by the oxidation of Fe^{2+} ($Fe(CN)_6^{4-} \rightarrow Fe(CN)_6^{3-} + e^-$) under a sweeping voltage. The iron (II/III) redox couple did not exhibit any observable peaks for bare Ti and anodized Ti electrodes, as

shown in Figure 3-34a and Figure 3-34b, but for the MWCNT-Ti electrode, the well-defined redox peaks were observed in varied scan rates, as shown in Figure 3-34c. This simply implies that the electrochemical reaction was slow using both of these electrodes. However, the highly directed electron transfer at the MWCNT-Ti electrode were observed as redox peaks, as shown in Figure 3-34c. At a scan rate of 100 mV/s in Figure 3-34c, a well-defined redox peak appeared with the anodic (E_{pa}) and cathodic (E_{pc}) potentials at 175 mV and 345 mV, respectively. Moreover, on the inner set of Figure 3-34c, the relationship between the anodic and cathodic peak currents versus the square root of the scan rate was linear, while the ratio of I_{pa}/I_{pc} was about 1, corresponding to the Randles-Seveik equation. Because the root scan rate had this linear relation with peak currents, the mass transport in this process must be by diffusion. Zhang et al. found that the heterogeneous charge-transfer rate constant (k) of the $\mathrm{Fe(CN)}_6^{4-/3-}$ complex with water as a solvent was 0.05 cm/s [15]. Since the k value is in the range of 10^{-4} to 10^{-1} cm/s and $\Delta E_p > 59/n$ mV (in this case n=1 and ΔE_p~170 mV), this process was quasi-reversible.

To analyze the electrochemical behavior at the surface of the MWCNT-Ti electrode, the Randles-Seveik equation was used for quasi-reversible processes, as shown in [3-2]. Hence, the peak current (I_p) is given by:

$$I_p = 2.99 \times 10^5 A D^{1/2} n (n_a \gamma)^{1/2} C \qquad \textbf{[3-2]}$$

Where n is the number of electrons participating in the redox process, n_a is the number of electrons participating in the charge-transfer step, A is the area of the working electrode (cm^2), D is the diffusion coefficient of the molecules in the electrolyte solution (cm^2/s), C is the concentration of the probe molecule in the bulk solution (molar), and γ is the scan rate of the

sweep potential (V/s). When the $Fe(CN)_6^{4-/3-}$ redox system exhibits a heterogeneous one-electron transfer (n=n_a=1) and the concentration C is equal to 10 mM, the diffusion coefficient D is equal to $6.7 \pm 0.02 \times 10^{-6}$ cm^2/s [16, 17]. Hence, indeed, the quasi-reversible redox of iron (II/III) is enhanced by using MWCNTs grown out of anodized nanotubular Ti.

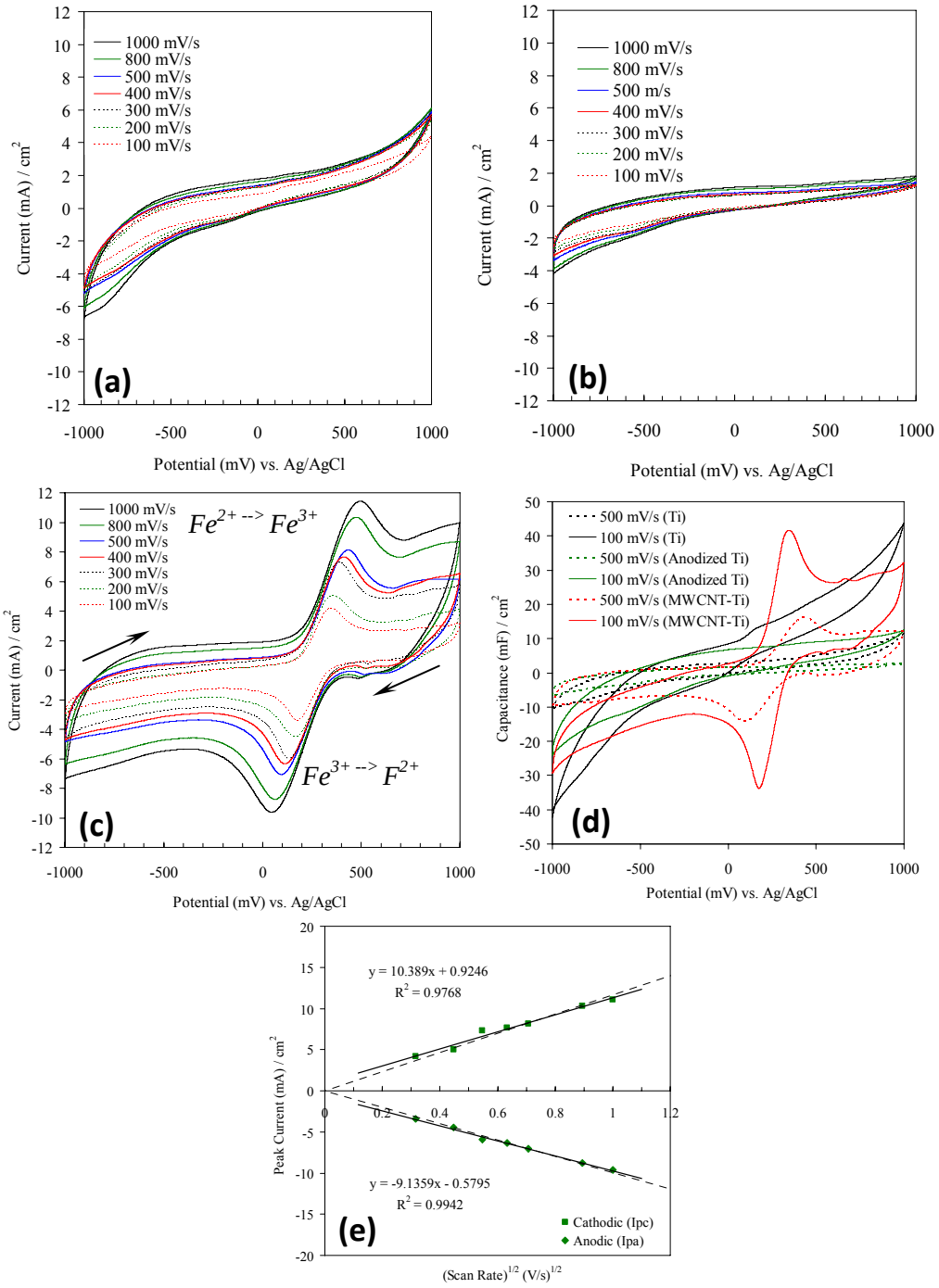

Figure 3-34. Cyclic voltammograms with an electrolyte solution of 10 mM $K_3Fe(CN)_6$ in 1 M KNO_3 using: (a) commercially pure Ti; (b) anodized Ti; and (c) MWCNT-Ti. (d) The capacitance of all the electrodes in comparison. (e) The plot of the square root of scan rates with anodic peak currents (I_{pa}) and cathodic peak currents (I_{pc}). The arrows in (b) represent that cyclic voltammetry was performed from -1 V to 1V.

3.2.3.1.2 Electrochemical Behavior using Ti, Anodized Ti, and MWCNT-Ti to Determine Bone Growth

Results from this study showed that MWCNT-Ti has the potential to detect the redox reaction in the extracellular components deposited by osteoblasts to indicate new bone formation, as shown in Figure 3-35 and Figure 3-36. While with commercially pure Ti and anodized Ti, the redox process was not detected, as shown in Figure 3-35a and Figure 3-36b, the results in Figure 3-35c confirmed that MWCNTs grown out of anodized nanotubular Ti enhanced the direct electron transfer, increasing the electrical conductivity of MWCNT-Ti. The excellent electrochemical behavior observed here makes MWCNT-Ti a superior candidate for biosensor applications. After the surface area of the MWCNT-Ti electrode was reduced from 1 cm^2 to 1 mm^2, the redox potentials also decreased as shown in Figure 3-35c and Figure 3-36b. The faradic current of the oxidation process dropped approximately 10 times with respect to this decrease in surface area (A), corresponding to equation [3-2]. Regarding the Randles-Sevcik equation, the peak current was linearly proportional to the area. The current in Figure 3-35 was 10 times greater and the area was 100 times greater than that in Figure 3-36. When plotting the anodic (I_{pa}) and cathodic peak (I_{pc}) current for MWCNT-Ti, a linear relationship to the square root of the scan rates was observed, as shown in Figure 3-36c. The redox peaks detected in the solution at calcium concentrations of 1.481 $\mu g/cm^2$ (after 7 days of culture) and 1.597 $\mu g/cm^2$ (after 14 days of culture) had less faradic current and I-V graph area than a calcium concentration of 2.48 $\mu g/cm^2$ (after 21 days of culture), as shown in Figure 3-37c and Figure 3-37b.

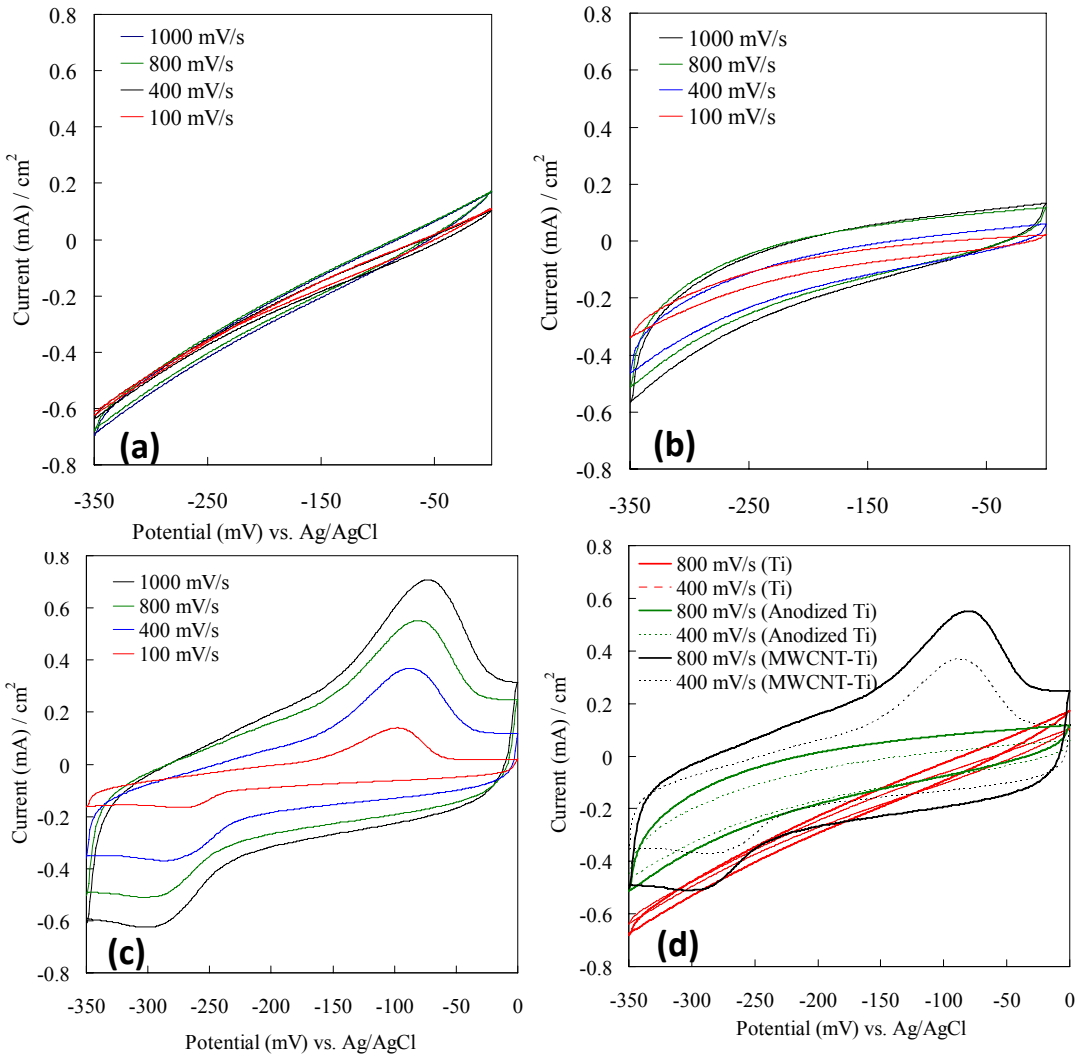

Figure 3-35. Cyclic voltammmograms with an electrolyte solution of 0.6 N HCl (calcium, concentration of 2.48 μg/cm^2, from the extracellular components deposited by osteoblasts cultured on commercially pure Ti after 21 days) using: (a) commercially pure Ti; (b) anodized Ti; and (c) MWCNT-Ti with a working area of 1 cm^2. (d) CV of all three electrodes in comparison. Only MWCNT-Ti possessed the quasi-reversible redox potential, while commercially pure Ti and anodized Ti did not.

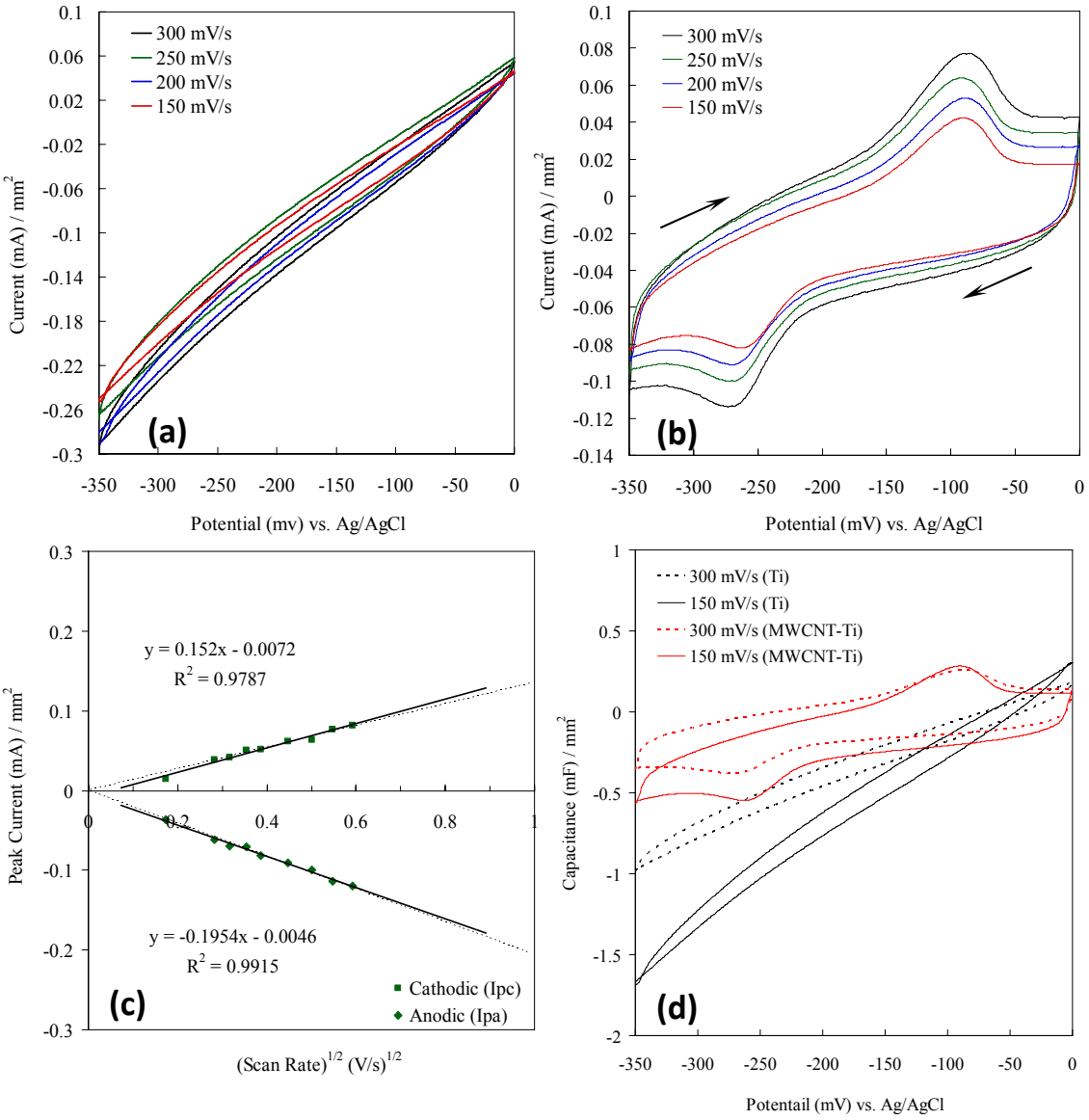

Figure 3-36. Cyclic voltammograms with an electrolyte solution of 0.6 N HCl (calcium concentration of 2.48 μg/cm^2, from the extracellular components deposited by osteoblasts cultured on Ti after 21 days) using: (a) commercially pure Ti and (b) MWCNT-Ti with a working area of 1 mm^2. (c) Plot of the experimental cathodic and anodic peak currents, obtained from (b), versus the square root of the scan rates; and (d) the compared capacitance of MWCNT-Ti and Ti. The arrows in (b) represent that cyclic voltammetry was performed from -1 V to 1V.

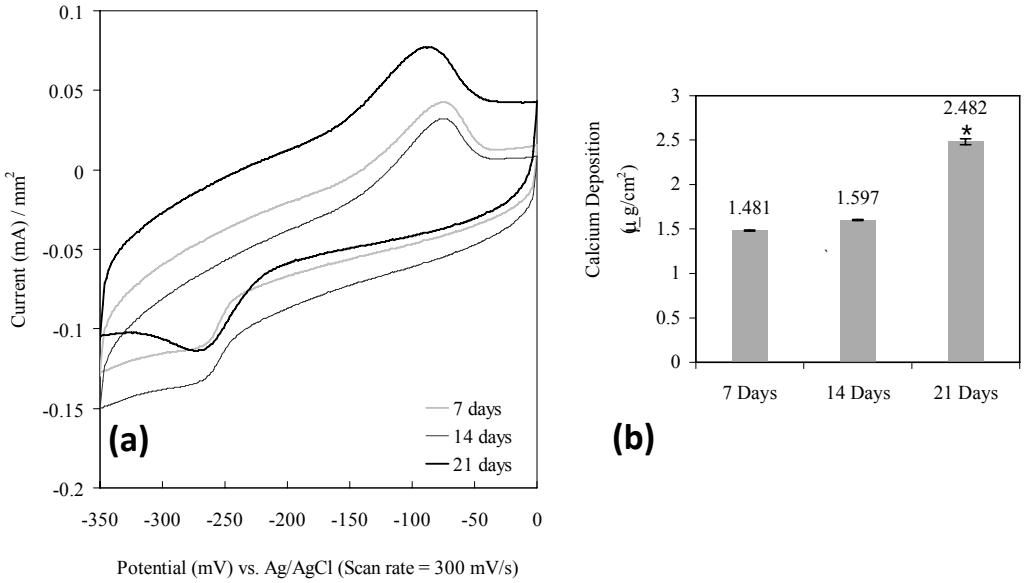

Figure 3-37. (a) Cyclic voltammograms of MWCNT-Ti electrodes in an electrolyte solution of calcium deposited by osteoblasts after they were cultured on commercially pure Ti for 7, 14, and 21 days. (b) Results from the calcium deposition assay determined the calcium concentrations in electrolyte solutions from osteoblasts cultured on Ti for 7, 14, and 21 days. Data = mean ± S.E.M.; N=3; *p<0.01 when compared with 7 and 14 days.

3.2.3.2 Anaerobic Electrolyte Solution (Nitrogen-Degassing)

This section provides results which compared the electrochemical behavior between commercial electrodes, specifically a glassy carbon electrode (GCE) and a platinum electrode (PTE), and the presently prepared MWCNT-Ti electrodes. Both electrolytes (specifically, the solution of 10 mM $K_3Fe(CN)_6$ in 1 M KNO_3 at pH 6.9, and extracellular components secreted by osteoblasts cultured on commercially pure Ti for 21 days) were degassed with nitrogen gas in order to reduce oxygen in the electrolytes. The degassing with nitrogen gas was carried out in order to optimize the potential peak separation (ΔE_p) to be closer to the reversible redox reaction (ΔE_p< 59 mV). Figure 3-38 shows the results from using 10 mM $K_3Fe(CN)_6$ in 1 M KNO_3 (at pH 6.9) as the electrolyte. After degassing, the results showed all the peak potential separations decreased significantly, which were obtained by using GCE, PTE, and MWCNT-Ti electrodes in both electrolytes. Importantly, ΔE_p from the MWCNT-Ti electrode was less than those obtained from GCE and PTE at the same scan rate, as shown in Figure 3-38. In addition, at the scan rate of 25 mV/s, ΔE_p obtained from the MWCNT-Ti was only 70 mV (closer to be reversible process). Thus, the use of MWCNT-Ti electrode was sensitive to the environment (with or without oxygen-containing elcetrolytes), which enhanced the direct electrode transfer (smaller ΔE_p) providing a distinct redox reaction curve (current-voltage curve).

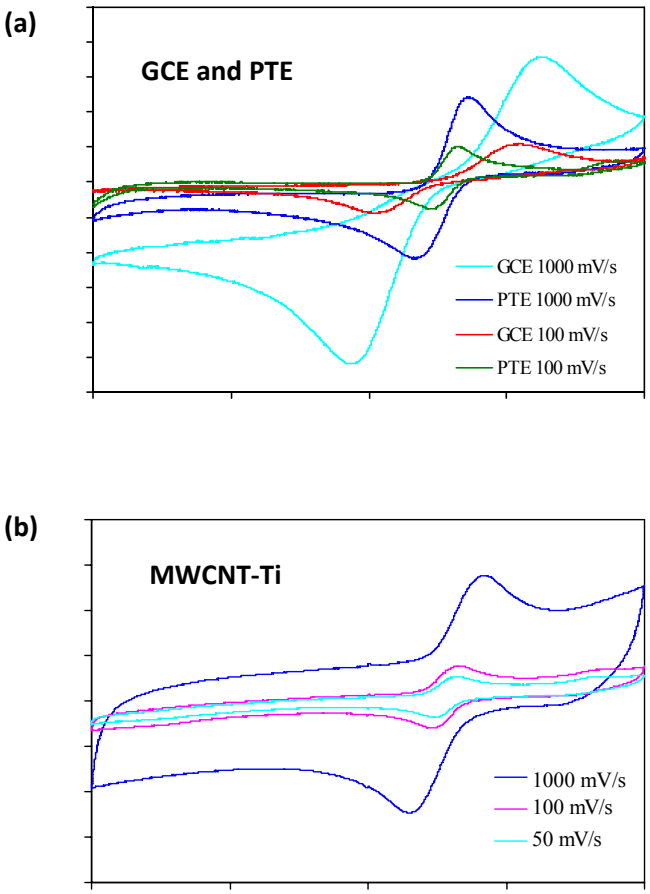

Scan Rate	ΔE_p (mV)		
(mV/s)	GCE	PTE	MWCNT-Ti
1000	718	232	296
100	370	136	106
50	-	-	76

Figure 3-38. Cyclic voltammograms from: (a) a glassy carbon electrode (GCE) and a platinum electrode (PTE), and (b) a MWCNT-Ti electrode with an electrolyte solution of 10 mM $K_3Fe(CN)_6$ in 1 M KNO_3 at various scan rates. The peak potential separations (ΔE_p) are shown in the accompanying table.

Similarly, when the degassed extracellular components secreted by osteoblasts cultured on commercially pure Ti for 21 days were used as the electrolyte, there was only one redox couple detected using GCE and PTE, but more than one redox reaction detected when using MWCNT-Ti, as shown in Figure 3-39. A redox peak was not observed on MWCNT-Ti using degassed osteoblast extracellular matrix components, but the hydrogen reduction (below -0.6 V) still occurred, as shown Figure 3-39. Moreover, the hydrogen reduction from using GCE and PTE was observed below -0.6 V but not through the use of MWCNT-Ti. Indeed, the MWCNT-Ti enhanced the direct electron transfer and improved electrode sensitivity.

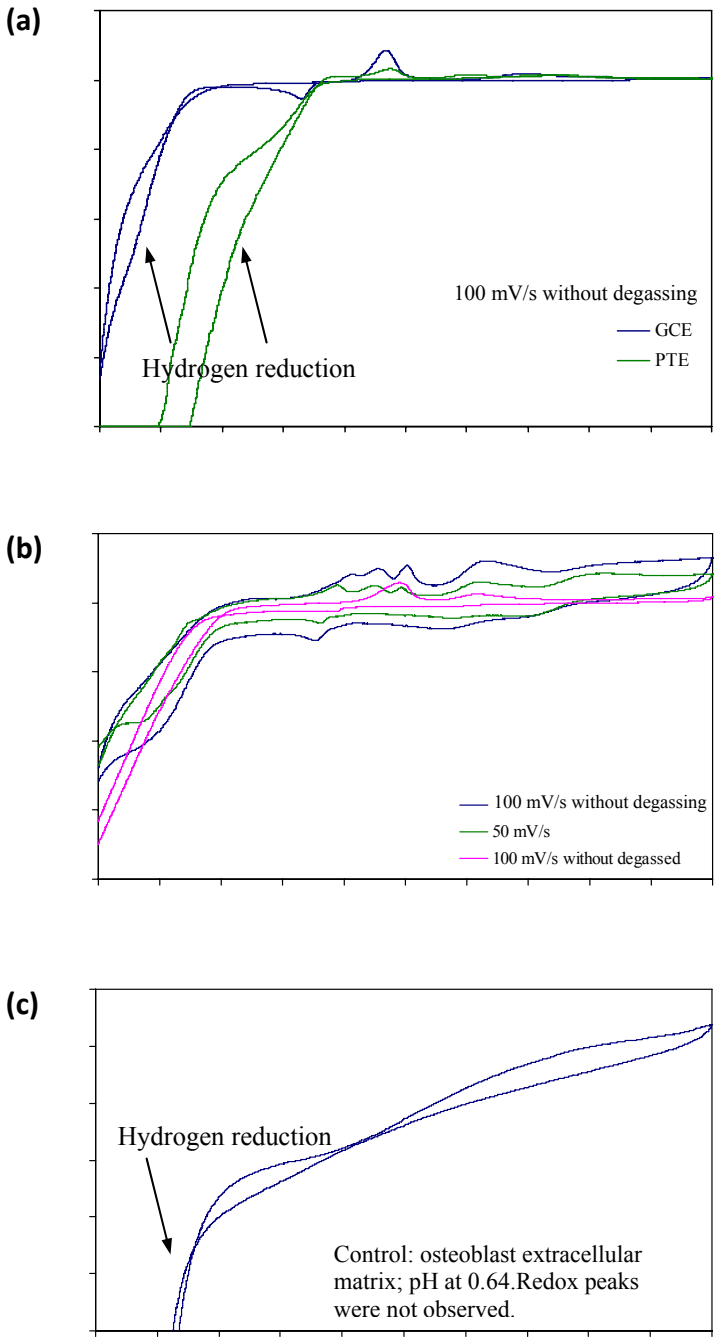

Figure 3-39. Cyclic voltammograms with an electrolyte solution of osteoblast extracellular matrix (pH at 1) on: (a) a glassy carbon electrode (GCE) and a platinum electrode (PTE) at 100 mV/s with degassing and (b) a MWCNT-Ti electrode at 50 and 100 mV/s with and without degassing. (c) A MWCNT-Ti electrode was used as a control osteoblast extracellular matrix (pH 0.64).

3.2.4 Identification of Protein in Extracellular Matrix

The extracellular matrix deposited by osteoblasts after 21 days was dissolved with 0.6 N HCl (details can be found in section 3.3.1.1.2). The proteins remaining in the extracellular matrix were identified by sodium dodecyl sulfate polyacrylamide gel electrophoresis (SDS-PAGE). Specifically, purified tubulin gel electrophoresis was performed with 8% SDS-PAGE. The resulting gel diagram indicated that the mass of the protein in the first band was between 70-80 kDa and the second band was around 60 kDa.

Thus, results from gel electrophoresis showed two major protein bands. The hypothesis is that the proteins are acidi-resistant since they retained activity and tranfered electrons with GCE, PTE, and MWCNT-Ti electrodes as observed redox peaks. This proteins could be bone sialoprotein (BSP; 70-80 kDa), containing Arg-Gly-Asp (RGD), which improves the attachment of osteoblasts and pre-osteoclasts to biomaterial surfaces [18]. Bone sialoprotein (a non-collagenous protein) can be isolated and purified from the mineral compartment of natural bone. It comprises 10-15% of the non-collageneous proteins in the mineral component of bone. Another possibility is osteocalcin, calcium-binding protein (a bone-carboxylated glutamic acid (Gla) protein with MW= 58.42 kDa) [18]. After osteoblasts synthesized bone, about 50% osteocalcin is released into the circulation, but the remaining 50% is incorporated into hydroxyapatite in bone. However, the role of these hypothesized proteins in the aforementioned redox reactions as detected by the novel MWCNT-Ti sensor have not confirmed and it is still a question which proteins from the osteoblast extracelluar components played a role in redox reactions for MWCNT-Ti and the other commercial electrodes tested here.

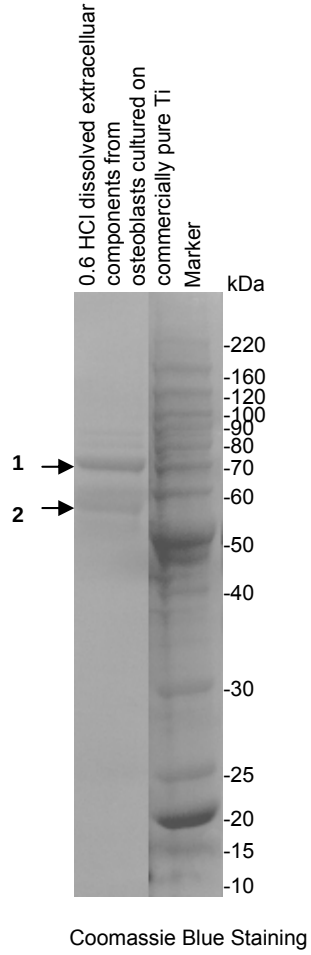

Figure 3-40. 10% SDS-PAGE (stack gel), stained with Coomassie Blue, of the extracellular protein components deposited by osteoblasts along with marker proteins. The first band is around 70-80 kDa, which could be bone sialoprotein (BSP; MW=70-80 kDa). The second band is around 50-60 kDa, which could be osteocalcin (MW=58.2 kDa).

3.2.5 SEM-EDS Analysis of MWCNT-Ti After Sensing Bone Growth

The MWCNT-Ti sensor was further analyzed after detecting the presence an osteoblast secreted extracelluar matrices using SEM-EDS. For this, the MWCNT-Ti electrode was cleaned with double deionized water before analysis. Results revealed calcium (Ca) and sodium (Na) crystals on top of the MWCNT-Ti sensor as shown in Figure 3-41 which confirmed that calcium was present in the osteoblast extracelluar matrix.

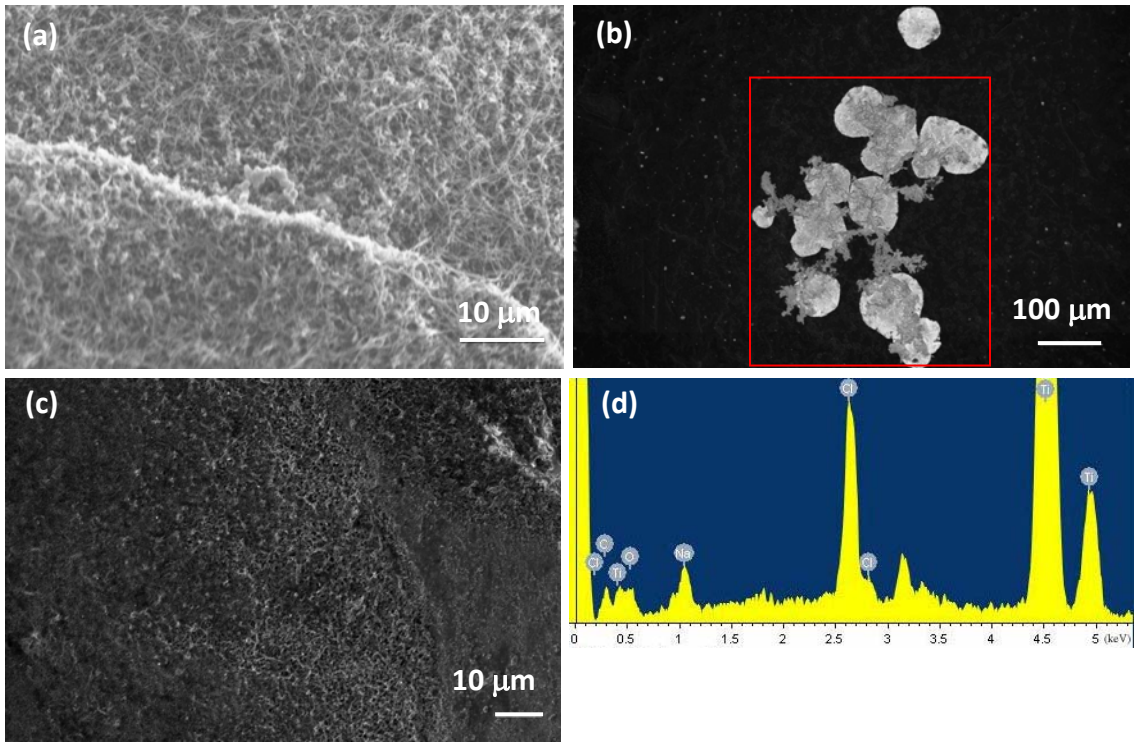

Figure 3-41. SEM-EDS analysis of: (a), (c) a MWCNT-Ti electrode after it measured the redox of an osteoblast secreted extracellular matrix was measured; (b) the remaining crystals on MWCNT-Ti after washing with double deionized water as analyzed by SEM-EDS. (d) The EDS spectrum of (b) revealed sodium (Na) and chloride (Cl) crystals on MWCNT-Ti on MWCNT-Ti after the electrochemical measurements.

3.2.6 SEM and TEM Analyses of Electrodeposited Polypyrrole on MWCNT-Ti

SEM and HRTEM analyses confirmed that PPy electrodeposited around MWCNTs as shown in Figure 3-42 (SEM micrographs) and Figure 3-43 (HRTEM micrographs). PPy electrodeposited non-uniformly around MWCNTs grown out of anodized nanotubular Ti. At the MWCNT-Ti surface, a thick coating of PPy was observed, but not on the inner side of the MWCNT-Ti (Figure 3-42). As observed under HRTEM, MWCNTs had a different degree of electrodeposited PPy. The thinner coating of PPy electrodeposited on MWCNT is shown in Figure 3-43a and the thicker coating is shown in Figure 3-43b.

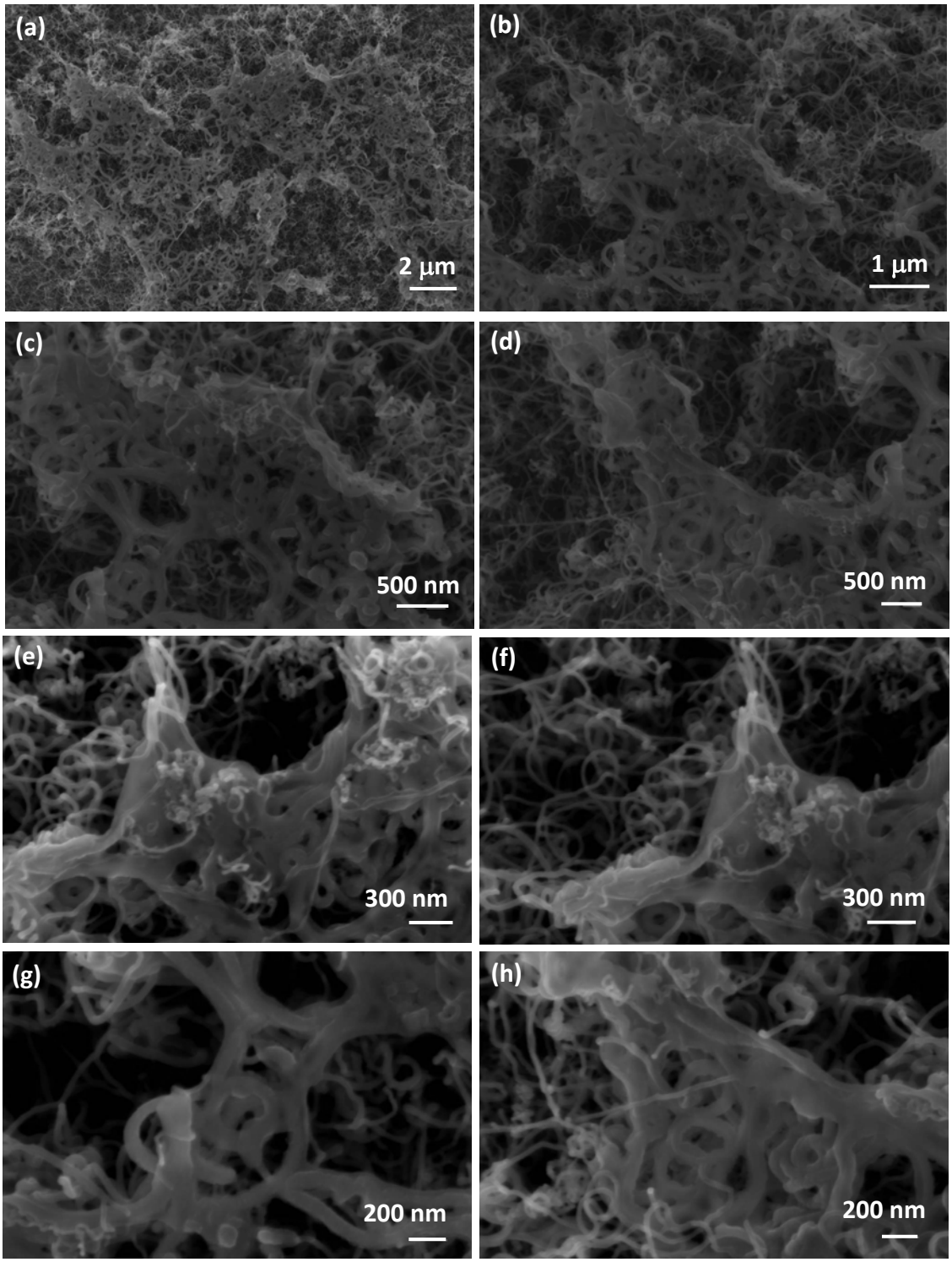

Figure 3-42. SEM micrographs of PPy electrodepostied on MWCNT-Ti with scar bars of: (a) 2 μm; (b) 1 μm; (c) and (d) 500 nm; (e) and (f) 300 nm; and (g) and (h) 200 nm.

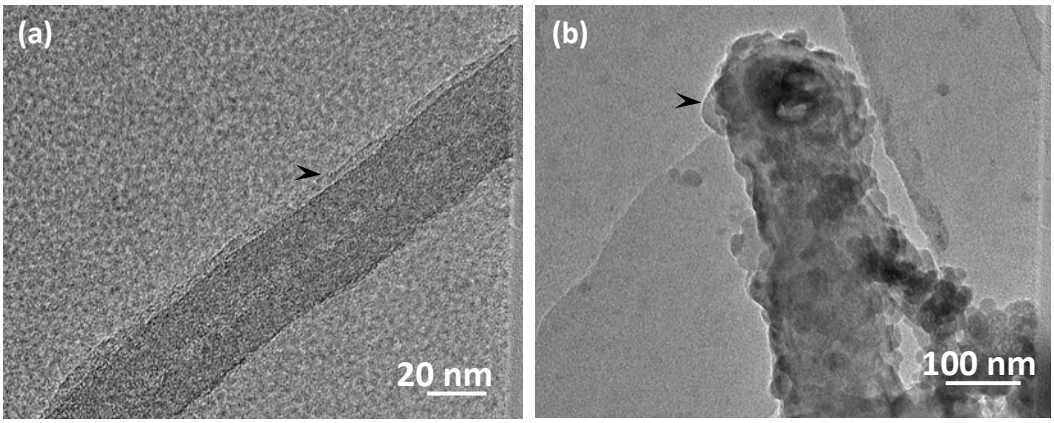

Figure 3-43. HRTEM micrographs of PPy electrodepostied on MWCNT-Ti. The arrow represents the PPy layer coating around the MWCNTs.

3.2.7 Characterization of Electrodeposited Polypyrrole Films on AuPd-Ti

3.2.7.1 Roughness Analysis

The surface topography of PPy drug-containing films were analyzed using AFM measurements for the average root-mean-square roughness (R_{rms}) and average peak-to-valley roughness (R_{pv}) as shown in Figure 3-44. R_{rms} is the estimate of the standard deviation of the bidimensional Gaussian-type distribution of heights around the mean value of the collected points. R_{pv} is determined by the difference between the highest peak and the lowest valley within multiple samples in the evaluation area. The results showed that PPy-Ti had a R_{rms} value of 35.87 nm and a R_{pv} value of 349.0 nm, PPy[P/S]-Ti had a R_{rms} value of 57.58 nm and a R_{pv} value of 200.5 nm, and PPy[Dex]-Ti had a R_{rms} value of 100.04 nm and a R_{pv} value of 495.5 nm. Importantly, the surface of the PLGA-PPy[Dex]-Ti possessed the highest R_{rms} value of 198.67 nm and R_{pv} value of 952.0 nm, and PPyCl-Ti exhibited the least R_{rms} value among all other samples (Table 3-8).

Table 3-8. The average root-mean-square roughness (R_{rms}) and average peak-to-valley roughness (R_{pv}) of PPy drug-containing films as analyzed using AFM measurements. 'PPyCl-Ti' or 'PPy-Ti' is PPy films electrodeposited onto AuPd-Ti without drug, 'PPy[P/S]-Ti' is PPy films electrodeposited onto AuPd-Ti with penicillin/streptomycin (antibiotics), 'PPy[Dex]-Ti' is PPy films electrodeposited onto AuPd-Ti with dexamethasone (anti-inflammatory drugs), and 'PLGA-PPy[Dex]-Ti' is amine functionalized PPy films electroposited onto AuPd-Ti with dexamethasone, and further conjuagated with PLGA-NHS (activated PLGA-COOH).

Samples	R_{rms} (nm)	R_{pv} (nm)
PPyCl-Ti or PPy-Ti	35.87	349.0
PPy[P/S]-Ti	57.58	200.5
PPy[Dex]-Ti	100.04	495.5
PLGA-PPy[Dex]-Ti	198.67	952.0

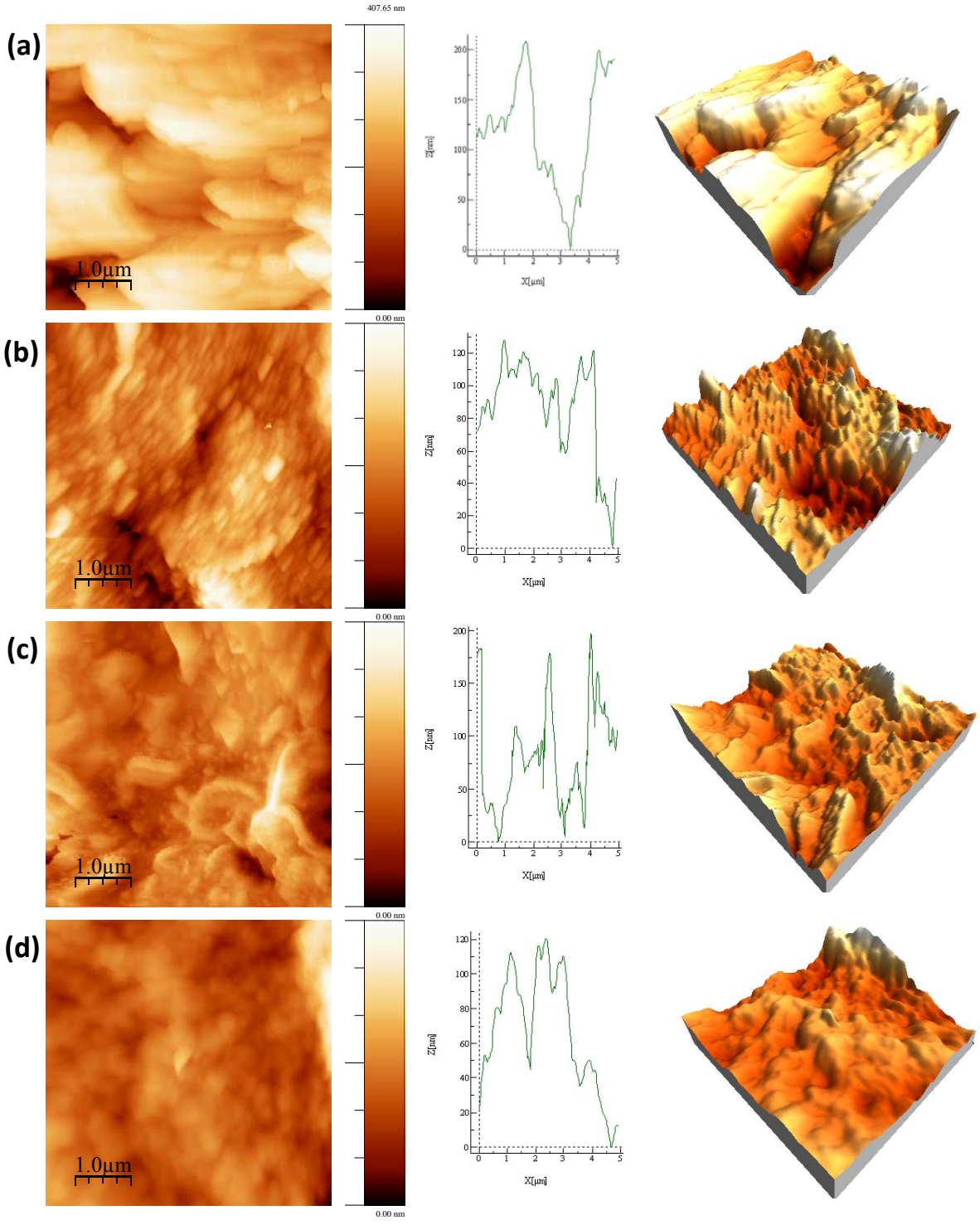

Figure 3-44. AFM micrographs demonstrated qualitatively and quantitatively the surface topography of the various PPy films created here: (a) PPyCl-Ti with a R_{rms} value of 35.87 nm and a R_{pv} value of 349.0 nm; (b) PPy[P/S]-Ti with a R_{rms} value of 57.58 nm and a R_{pv} value of 200.5 nm; (c) PPy[Dex]-Ti with a R_{rms} value of 100.04 nm and a R_{pv} value of 495.5 nm; and (d) PLGA-PPy[Dex]-Ti with a R_{rms} value of 198.67 nm and a R_{pv} value of 952.0 nm.

3.2.7.2 Chemical Analysis

3.2.7.2.1 X-ray Photoelectron Spectroscopy

XPS scans identified C 1*s*, N 1*s*, O 1*s*, and Cl 1*s* as the major chemical constituents in the substrates of interest to this study (Table 3-9). The presence of the P/S (chemical structure: $C_{37}H_{57}N_9O_{16}S$) dopant in PPy[P/S]-Ti after sputter cleaning for 2.5 minutes was confirmed by XPS analysis, which identified the presence of S 2*p* (Table 3-9). Although the F 1*s* peak of Dex ($C_{22}H_{29}FO_5$) in the PPy[Dex]-Ti cannot be identified by XPS survey spectra, the C–F bond of Dex was confirmed by high-resolution XPS analysis and curve-fitting for the C 1*s* spectra in PPy[Dex]-Ti and PPyNH_2[Dex]-Ti (Figure 3-45 and Table 3-10).

Table 3-9. XPS survey of the PPy films electrodeposited on AuPd-Ti. 'n/d' stands for not detected.

PPy coated on AuPd-Ti	Atomic %				
	C 1*s*	O 1*s*	N 1*s*	Cl 2*p*	S 2*p*
PPyCl	77.6, 92.0*	4.3, 2.5*	15.6, 3.2*	2.4, 2.3*	n/d, n/d*
PPy[P/S]	49.7, 82.1*	36.8, 7.0*	12.3, 8.9*	1.2, 0.6*	n/d, 1.4*
PPy[Dex]	67.5, 93.5*	16.7, 0.1*	11.2, 4.5*	4.7, 1.9*	n/d, 0*
PPyNH_2[Dex]	70.7, 87.4*	11.8, 2.9*	16.6, 8.4*	1.0, 1.3*	n/d, n/d*
PLGA-PPy[Dex]	59.5, 94.2*	40.5, <0.1*	<0.1, 4.9*	n/d, 0.9*	n/d, n/d*

* After sputter cleaning for 2.5 minutes.

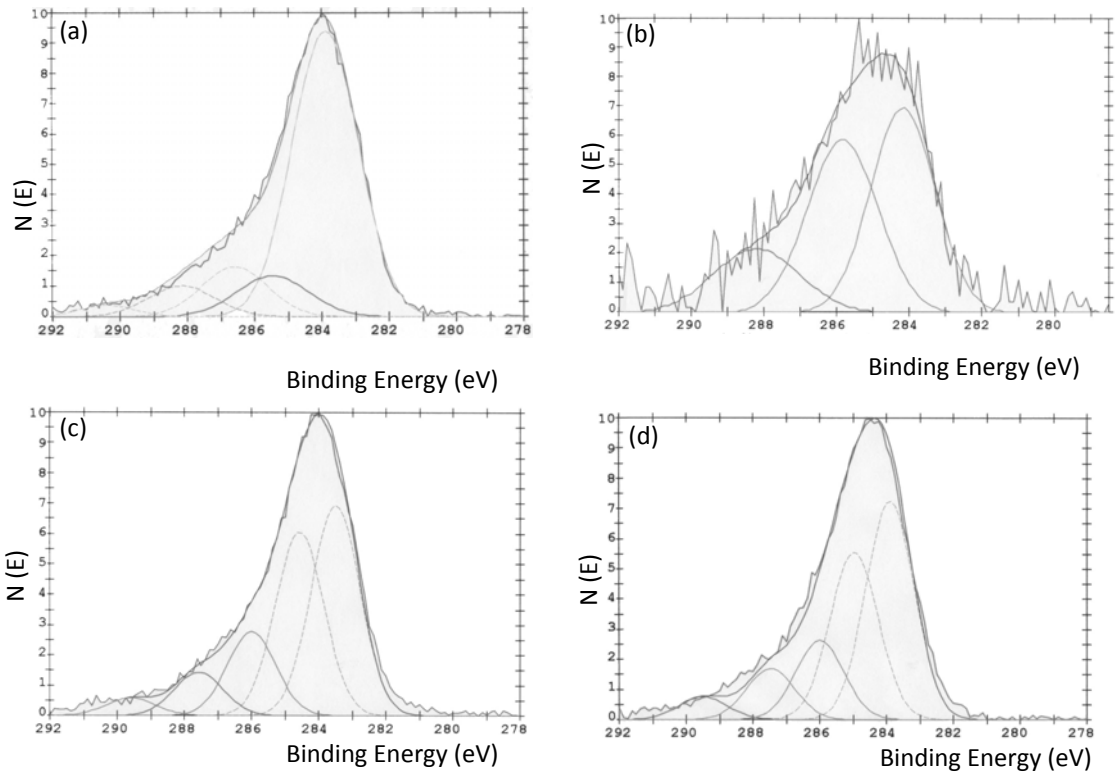

Figure 3-45. High resolution XPS analysis at C 1*s* by curve fitting: (a) PPy-Ti, (b) PPy[P/S]-Ti, (c) PPy[Dex]-Ti, and (d) PPy functionalized with NH_2 [Dex]-Ti (without further conjugation with PLGA-NHS). 'N(E)' is the number of free electrons from their atoms.

Table 3-10. High resolution XPS analysis for C 1*s* by curve fitting of the as the prepared PPy-Ti, PPy[P/S]-Ti, PPy[Dex]-Ti, and PPy functionalized with NH_2 [Dex]-Ti. 'BE' is binding energy (eV).

PPy[P/S]-Ti			PPy[Dex]-Ti			$PPyNH_2$[Dex]-Ti		
BE (ev)	% Area	Assignment	BE (ev)	% Area	Assignment	BE (ev)	% Area	Assignment
284.17	42.78	Pyrrole β	283.5	39	Pyrrole β	283.9	40.46	Pyrrole β
		Carbon			Carbon			Carbon
		C–C sp^2			C–C sp^2			C–C sp^2
285.83	39.45	Pyrrole α	284.57	34	Pyrrole α	284.97	31.11	Pyrrole α
		Carbon			Carbon			Carbon
		C–C sp^3			C–C sp^3			C–C sp^3
			286	15.6	C–OH	286	14.73	C–OH
288.2	17.78	C=O, $C–N^+$	287.57	8.09	C–F, $C–N^+$	287.47	9.47	C–F, $C–N^+$
			289.6	3.3	COOH	289.5	4.23	COOH

The curve fitting for the N 1*s* spectra of the PPy polymerized with different drug-anions clearly indicated the existence of three distinct nitrogen heteroatoms (Figure 3-46 and Table 3-11). The major peaks in the N 1*s* core spectra appeared at a binding energy of approximately 399 eV and were attributed to the neutral pyrrole nitrogen (−NH−), which was a result of the dehydrogenation of a pyrrolium nitrogen atom. The shoulder shift at the binding energy of approximately 400 eV was attributed to positively charged nitrogen ($-N^+-$) atoms. This shift results from their electrostatic interactions with anions. The lower binding energy shoulder shifted in the negative direction by about <2 eV for all samples, from the neutral pyrrole nitrogen (−NH−) to the imine nitrogen (−N=). Curve fitting at N 1*s* did not show bipolaron states ($C=N^+$) on PPy films of all samples, which typically shifts from the $C–N^+$ (polaron) peak at <2 eV [19], [20].

Because the diffusion rate for the recombination of polarons into bipolarons was limited by the diffusion of the accompanying anions (P/S or Dex), this phenomenon of semiconducting PPy was slow enough to be observed by UV-vis spectrophotometry (Figure 3-30). It was found that the bipolaron states, developed during *in situ* electrodeposition after applying 10 CV cycles, were not incorporated into PPy films because electrodeposition in this present study was accomplished by applying only 5 CV cycles. Therefore, more electrodeposition time was required to allow the bipolaron nitrogen to migration into the PPy films and XPS results showed only polarons appeared on PPy films in this study (Figure 3-46 and Table 3-11). Importantly as this study demonstrated, PPy films can control the charge density and wettability of PPy films can be controlled through electropolymerization based on the chosen drug, electrolyte solution, and applied voltage (or charge density).

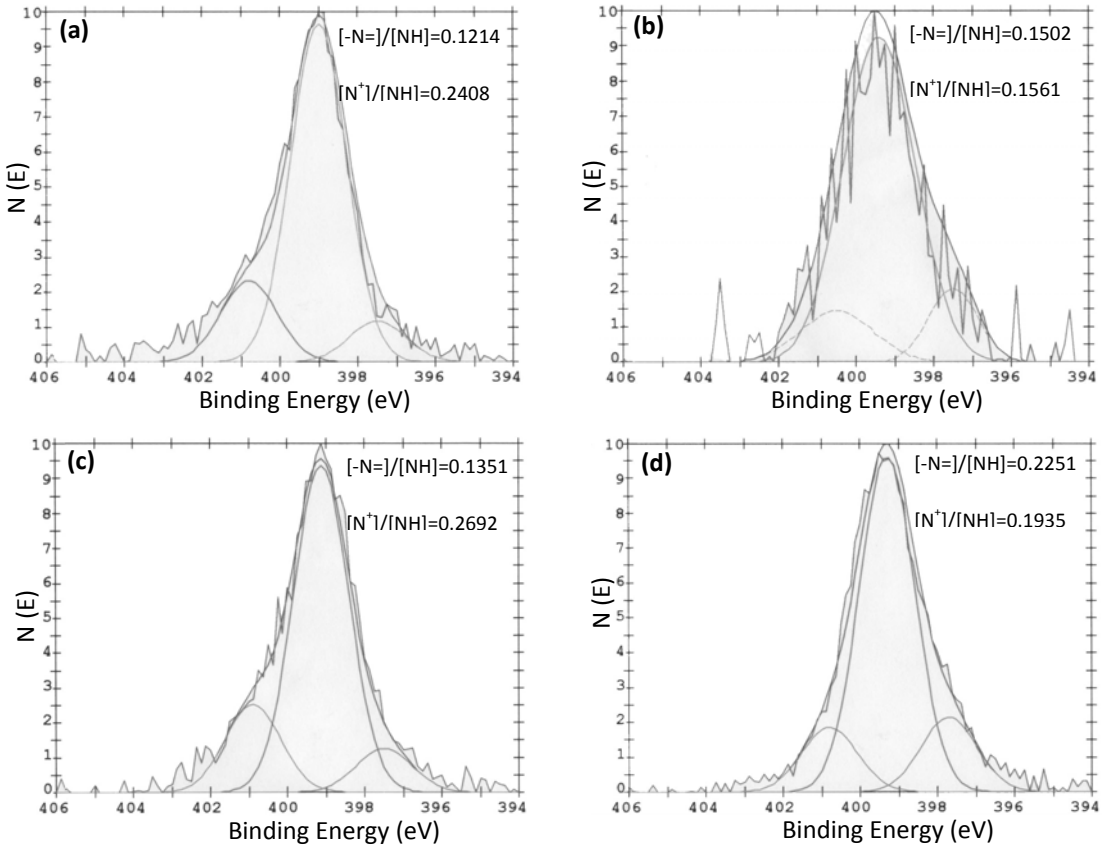

Figure 3-46. High resolution XPS analysis and curve fitting of the N 1*s* core spectra of: (a) PPy-Ti; (b) PPy[P/S]-Ti; (c) PPy[Dex]-Ti; and (d) PPy functionalized with NH_2 [Dex]-Ti (without further conjugating with PLGA-NHS). 'N(E)' is the number of free electrons from their atoms.

Table 3-11. High resolution XPS analysis and curve fitting for N 1*s* core spectra of the as-prepared PPy-Ti, PPy[P/S]-Ti, PPy[Dex]-Ti, and PPy functionalized with NH_2 [Dex]-Ti (without further conjugation with PLGA-NHS). 'BE' is binding energy (eV).

PPy-Ti		PPy[P/S]-Ti		PPy[Dex]-Ti		$PPyNH_2$[Dex]-Ti		Assignment
BE (ev)	% Area	BE (ev)	% Area	BE (ev)	% Area	BE (ev)	% Area	
397.5	8.91	397.5	11.5	397.5	9.62	397.7	15.87	Deprotonate pyrrole nitrogen (Imine-like) –N=
399	73.42	399.4	76.55	399.12	71.21	399.3	70.49	Neutral pyrrole nitrogen (Amine-like) –NH–
400.8	17.68	400.5	11.95	400.9	19.17	400.8	13.64	Positive pyrrole nitrogen $–N^+–$

The relative ratio of the imine-like (−N=) to amine-like (−NH−) components indicated a direct measure of the intrinsic oxidation state of PPy and the −N= represents the loss of conductivity or irreversible overoxidation of PPy [21]. As shown in Table 3-11, the complete deprotonation of the PPy produced a rise in the [−N=]/[−NH−] ratio, which was 0.1502 for PPy[P/S]-Ti, 0.1351 for PPy[Dex]-Ti, and 0.1214 for PPy-Ti. The amount of anodic drug loaded can be indicated by the $[-N^+-]/[-NH-]$ ratio [22]. Specifically, the $[-N^+-]/[-NH-]$ ratio was 0.1561 for PPy[P/S]-Ti, 0.2408 for PPy-Ti, and 0.2692 for PPy[Dex]-Ti. The XPS results showed that PPy[P/S]-Ti had a 0.1502 intrinsic oxidized surface (neutral) while PPy-Ti and PPy[Dex]-Ti were in a more reduced form (positively charged) than the PPy[P/S]-Ti. The relative intensities of N 1*s* to S 2*p* levels can also be used to determine the amount of P/S doping. The [S]/[N] ratio of PPy[P/S]-Ti samples was 0.1583 which was relatively similar to the $[-N^+-]/[-NH-]$ ratio of 0.1561. Because oxygen is in PLGA, the O 1*s* was predominantly found (at about 40.5 atomic %)

for PLGA-PPy[Dex]-Ti (Table 3-9). The presence of N 1*s* and C 1*s* (in PLGA-PPy[Dex]-Ti) increased after sputter cleaning for 2.5 min reaching the PPy layer, while the presence of O 1*s* was observed to decrease (Table 3-12). The curve fitting for the C 1*s* and O 1*s* spectra of the PLGA-PPy[Dex]-Ti clearly indicated the existence of carboxylic groups (−C=O−), as shown in Figure 3-47 and Table 3-13. Overall, XPS analysis from Table 3-10, Table 3-11, Table 3-13, and Figure 3-45 showed that the surface chemistry of PPy[Dex]-Ti and PPy[P/S]-Ti consisted of mostly −NH−, while PLGA-PPy[Dex]-Ti possessed −C=O− (carboxylic group) instead, and PPy[Dex]-Ti had a comparable amount of both compositions (−NH− and −C=O−(carboxylic)) on its surface.

Table 3-12. XPS survey of PLGA-PPy[Dex]-Ti, where 'SC' is sputter cleaned to drill the surface and 'AR' is as-received.

PLGA-PPy[Dex]-Ti	Atomic %				
	C 1*s*	O 1*s*	N 1*s*	Cl 1*s*	Ti 2*p*
AR	59.5	40.5	<0.1	0	0
SC for 12 sec	90.1	9.9	<0.1	<0.1	0
SC for 30 sec	94.1	5.2	<0.1	0.7	0
SC for 1.5 min	88.3	3.8	4.3	3.6	0
SC for 2.5 min	94.2	<0.1	4.9	0.9	0
SC for 3.0 min	88.6	2.4	4.2	3.4	1.4
SC for 4.5 min	30.8	2.4	<0.1	3.0	3.9

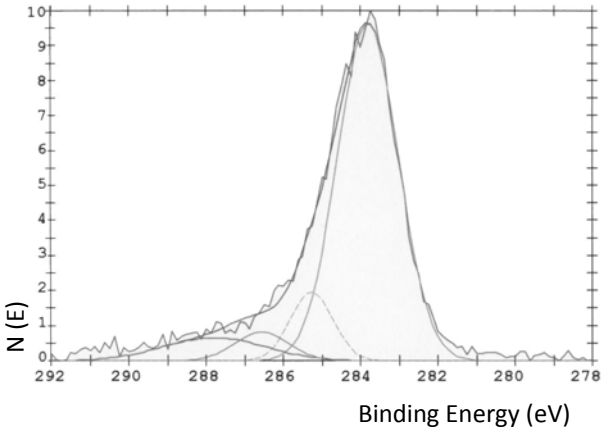

Figure 3-47. High resolution XPS analysis and curve fitting of PLGA-PPy[Dex]-Ti for C 1*s* (sputter cleaning for 2.6 minutes). 'N(E)' is the number of free electrons from their atoms.

Table 3-13. High resolution XPS analysis and curve fitting of PLGA-PPy[Dex]-Ti for C 1*s* (sputter cleaning for 2.6 minutes) and O 1*s* (sputter cleaning for 12 seconds) spectra. 'BE' is binding energy (eV).

PLGA-PPy[Dex]-Ti					
C 1s			O 1s		
BE (ev)	% Area	Assignment	BE (ev)	% Area	Assignment
283.81	75.21	C–H (Fullerenic)	530	23.17	O-C (Pluonics, carboxylic group)
285.27	10.62	C–C sp^2	531.92	47.39	O=C (carboxylic group)
286.56	5.61	C–O	533.8	29.43	O–C (ether group)
287.8	8.56	C=O			

3.2.7.2.2 Attenuated Total Reflection Fourier Transform Infrared Spectroscopy

The C 1*s* spectra with high-resolution XPS were not symmetric at high binding energies due to disorder effects (e.g. interchain links, side chains, or chain terminations) [23], as the peak assignment shown in Table 3-10. Thus, the surface chemistry of the PPy-drug films was also analyzed by using ATR-FTIR as shown in Figure 3-48. The peak assignments from ATR-FTIR spectra are shown in Table 3-14. The interchain links can occur with the 2,5-position (α-α'), observed in the present films by ATR-FTIR (Spectrum One FTIR with Zinc Selenide (ZnSe) Crystal; Perkin-Elmer) at 1561 cm^{-1} (PPy-Ti and PPy[P/S]-Ti) and 1653 cm^{-1} (PPy[Dex]-Ti). The peaks at 793, 901.5, and 1095.5 cm^{-1} were assigned to the 1,3,4 trisubstitution of pyrrole on PPy-Ti and PPy[P/S]-Ti, while the peaks at 793.5, 901.5, and 1072.5 cm^{-1} appeared on PPy[Dex]-Ti. The N-C stretching band was present at 1176.5 cm^{-1} for PPy-Ti and PPy[P/S]-Ti, but was present at 1098 cm^{-1} for PPy[Dex]-Ti. The PLGA-NHS showed -OH- peaks at 2988 cm^{-1} in the ATR-FITR spectra. This peak disappeared on PLGA-PPy[Dex]-Ti, confirming the cross-linking of $PPyNH_2$ and PLGA-NHS in the films created.

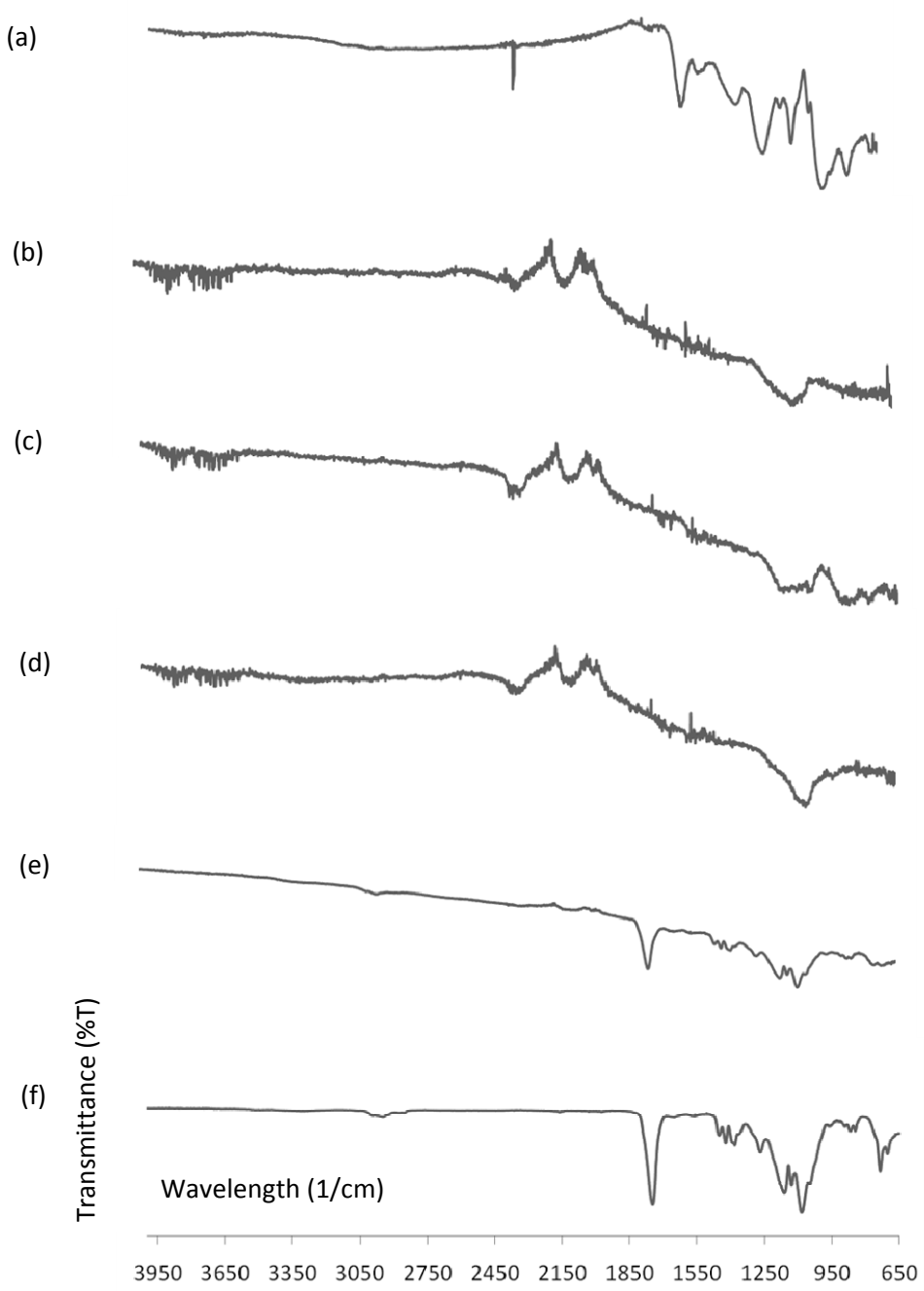

Figure 3-48. FTIR spectra of: (a) PPy functionalized with NH_2 (chemically synthesized with $FeCl_3$), (b) PPy-Ti, (c) PPy[P/S]-Ti, (d) PPy[Dex]-Ti, (e) PLGA-PPy[Dex]-Ti, and (f) PLGA-NHS.

Table 3-14. FTIR spectra of PPy functionalized with NH_2 (chemically synthesized with $FeCl_3$), PPy-Ti, PPy[P/S]-Ti, PPy[Dex]-Ti, PLGA-PPy[Dex]-Ti, and PLGA-NHS.

Materials	Bands (cm^{-1})	Assignments
PPy functionalized NH_2 (chemically	1558	2,5-substituted pyrrole
synthesized with $FeCl_3$)	1477.5	polyprrole ring vibration
	1317.5	=C-H in plane vibration
	1187.5	-N-C stretching
	797, 915.5, 1050	1,3,4 trisubstituted pyrrole
PPy-Ti	2331, 2123.5	-CH out-of-plane deformations in aromatics
	1561	2,5-substituted pyrrole
	793, 901.5, 1095.5	1,3,4 trisubstituted pyrrole
PPy[P/S]-Ti	2368.5, 2128	-CH out-of-plane deformations in aromatics
	1561	2,5-substituted pyrrole
	1176.5	-N-C stretching
	793.5, 901.5, 1095.5	1,3,4 trisubstituted pyrrole
PPy[Dex]	2367, 2124.5	-CH out-of-plane deformations in aromatics
	1098	-C-O stretching
	793.5, 901.5, 1072.5	Polymerized pyrrole
PLGA-PPy[Dex]-Ti	2971	-CH, $-CH_2$, $-CH_3$ stretching
	1752.5	-C=O stretching
	1653	$-CONH_2$ (amide)
	1173	-C-N stretching
	1096	-C-O stretching
	764.5, 891, 1067.5	1,3,4 trisubstituted pyrrole
PLGA-NHS	2988	-OH
	2899	-CH, $-CH_2$, $-CH_3$ stretching
	1753	-C=O stretching
	1170	-C-N stretching
	1089.5	-C-O stretching

3.2.8 Relative Shear Stress Testing

The relative ultimate shear stress (with collagen paper and 0.25 M polyethylene glycol MW=1000) of: commercially pure Ti was 5.7179 kPa, MWCNTs grown out of anodized Ti was 10.7260 kPa, MWCNTs grown out of anodized Ti and electrodeposited with PPy was 2.2977 kPa, MWCNTs grown out of unanodized Ti and electrodeposited with PPy was 0.9653 kPa, and PPy films electrodeposited without any drugs on AuPd-Ti was 1.6412 kPa. Results showed that the electrodeposited PPy significantly decreased the ultimate shear stress of MWCNT-Ti with collagen paper and polyethylene glycol about 79% as shown in Figure 3-49. Importantly, MWCNT-Ti increased the ultimate shear stress to about 187% when compared to the shear stress that was obtained from commercially pure Ti (Table 3-15).

Table 3-15. Relative ultimate shear stress (with collagen paper, 0.25 M and polyethylene glycol MW=1000) of commercially pure Ti, MWCNTs grown out of anodized Ti, PPy film electrodeposited without any drugs on AuPd-Ti, MWCNTs grown out of anodized Ti and electrodeposited with PPy, and MWCNTs grown out of unanodized Ti and electrodeposited with PPy.

Samples	Ultimate shear stress (kPa)
Commercially pure Ti	5.7179
MWCNTs grown out of anodized Ti	10.7260
PPy film electrodeposited without any drug on AuPd-Ti	1.6412
MWCNTs grown out of anodized Ti and electrodeposited with PPy	2.2977
MWCNTs grown out of unanodized Ti and electrodeposited with PPy	0.9653

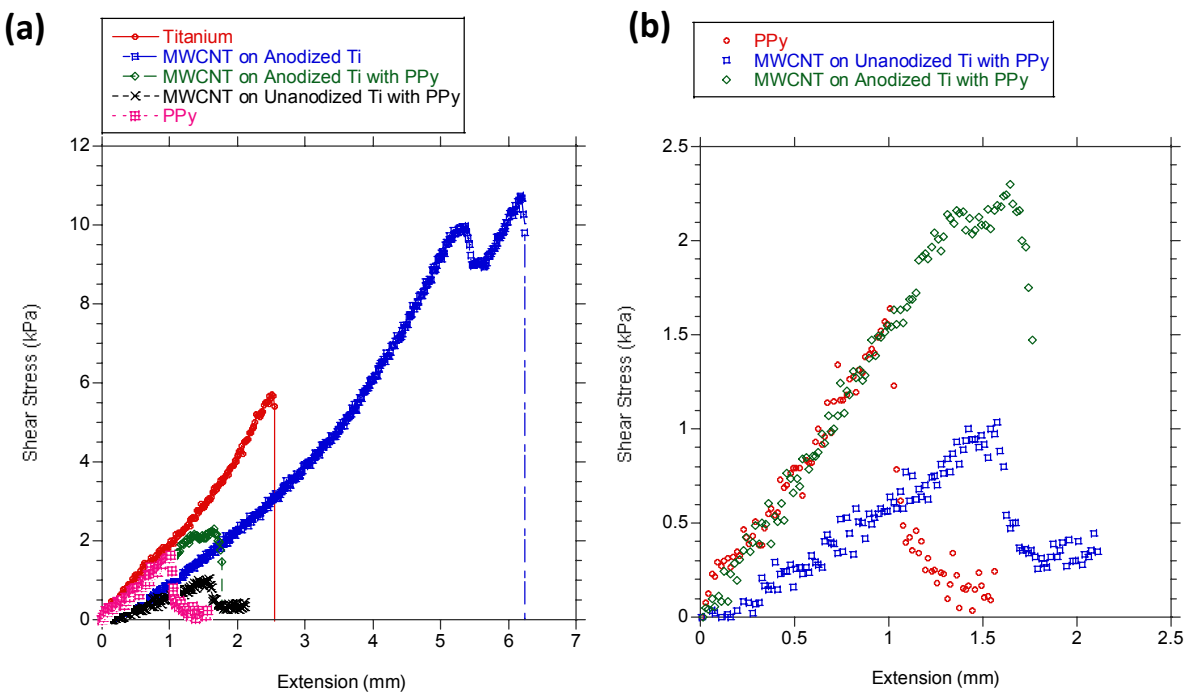

Figure 3-49. Relative shear stress testing between collagen paper-polyethylene glycol (MW=10,000; 0.25 M) and: commercially pure Ti, MWCNTs grown out of anodized Ti, PPy without any drug electrodeposited on AuPd-Ti, MWCNTs grown out of anodized nanotubular Ti and electrodeposited with PPy, and MWCNTs grown out of commercially pure (unanodized) Ti and electrodeposited with PPy. (b) is a larger magnification of (a), specifically, PPy without any drug electrodeposited on AuPd-Ti, MWCNTs grown out of anodized Ti and electrodeposited with PPy, and MWCNTs grown out of unanodized Ti and electrodeposited with PPy.

3.2.9 Drug Release Profiles

In this study, the anionic drugs were released using cyclic voltammetry during reduction, which were observed as the peaks in the cyclic voltammograms (current-voltage diagram, Figure 3-50a and Figure 3-50b). For the first five cycles, anionic molecules were observed to move in and out of the PPy thin film coating due to continuous oxidation and reduction. The reduction peaks of P/S release disappeared after 15 CV cycles. For Dex, the reduction peak was still observed after 25 CV cycles, but disappeared after 40 CV cycles. The overoxidation that occurred after 15 (for P/S) and 40 (for Dex) CV cycles contributed to the significant decrease in the area of cyclic voltammograms for both P/S and Dex. This result indicated that the PPy films lost their redox activity, and thus P/S or Dex had been released. The continuous electrical stimulation of PPy films caused them to lose electrochemical activity, electrical conductivity, and can become insulators, observed as a horizontal planula on cyclic voltammograms.

Moreover, the drug concentration was determined by ultraviolet-visible (UV-vis) spectrophotometry since each drug has a specific light absorbance (Figure 3-50d). The increase in the amount of P/S or Dex released after electrical excitation was significant until five cycles of sweep voltages. The cumulative P/S and Dex approached 80% of the drug release (Figure 3-50c) and became relatively stable. Importantly, the stability of the absorbance curve also corresponded to the disappearance of the reduction peaks in the CV. In addition, after soaking PPy membranes in PBS (pH 7.4) for 24 hours at room temperature and incubating in PBS (pH 7.2) for 144 hours at 37 °C, the films became swollen, but no P/S and Dex absorbance was detected by UV-vis spectrophotometry. Thus, without an applied voltage, there was no significant P/S and Dex release detected from the PPy films from this study.

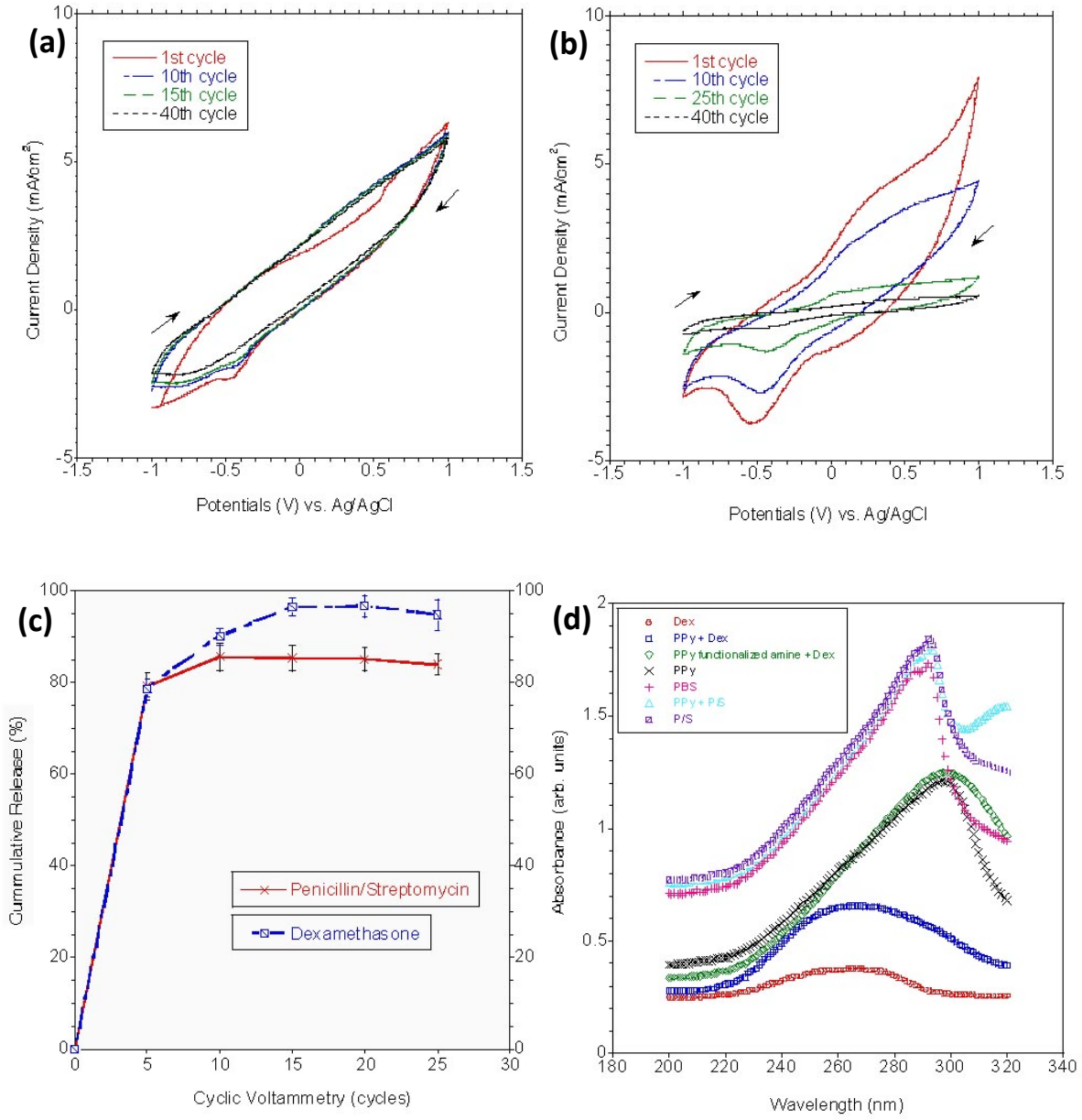

Figure 3-50. Cyclic voltammograms of drug release from PPy films: (a) PPy[P/S]-Ti and (b) PPy[Dex]-Ti. (c) The cumulative concentration of P/S and Dex release after electrical stimulation (scan rate = 100 mV/s from -1 V to 1 V). (d) The absorption spectra in the solution (diluted with PBS buffer at pH 7.2) of P/S, Dex, pyrrole monomers with P/S, pyrrole monomers with Dex, pyrrole monomers functionalized NH_2 with Dex, and pyrrole monomers. (d) The absorption spectra were obtained after electrical stimulation for the case of pyrrole monomers added.

3.4 Cell Responses

3.4.1 Osteoblast Responses

3.4.1.1 Multiwalled Carbon Nanotubes

3.4.1.1.1 Osteoblast Adhesion

Results of this study showed a similar number of osteoblasts adhererent after four hours on commercially pure Ti, anodized nanotubular Ti without MWCNTs and anodized nanotubular Ti with MWCNTs (Figure 3-51); all were greater than the carbon nanopaper. Osteoblasts on anodized Ti without MWCNTs were not observed to possess with cytoplasmic prolongations (Figure 3-52 and Figure 3-53). Although MWCNTs on anodized Ti showed less number of cells (Figure 3-51), osteoblasts were observed with cytoplasmic prolongations on the surfaces of MWCNTs grown out of anodized nanotubular Ti (Figure 3-54 and Figure 3-55), resulting in possible stronger adhesion (with a higher density of points of contact) [37].

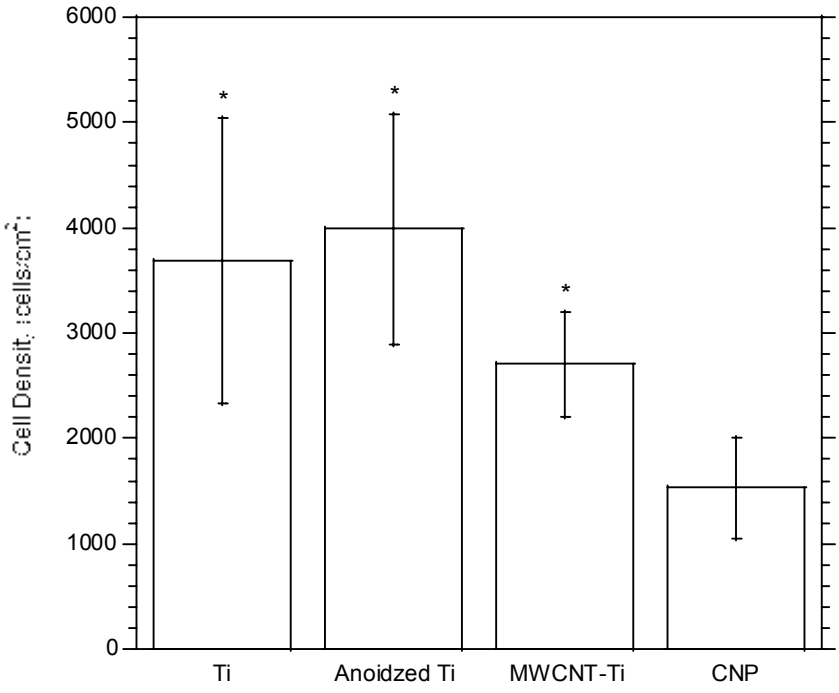

Figure 3-51. Osteoblast adhesion after four hours on commercially pure Ti, anodized Ti, MWCNT-Ti, and carbon nanopaper. Values are mean ±S.E.M., N=3, and * $p<0.05$ compared to carbon nanopaper (CNP).

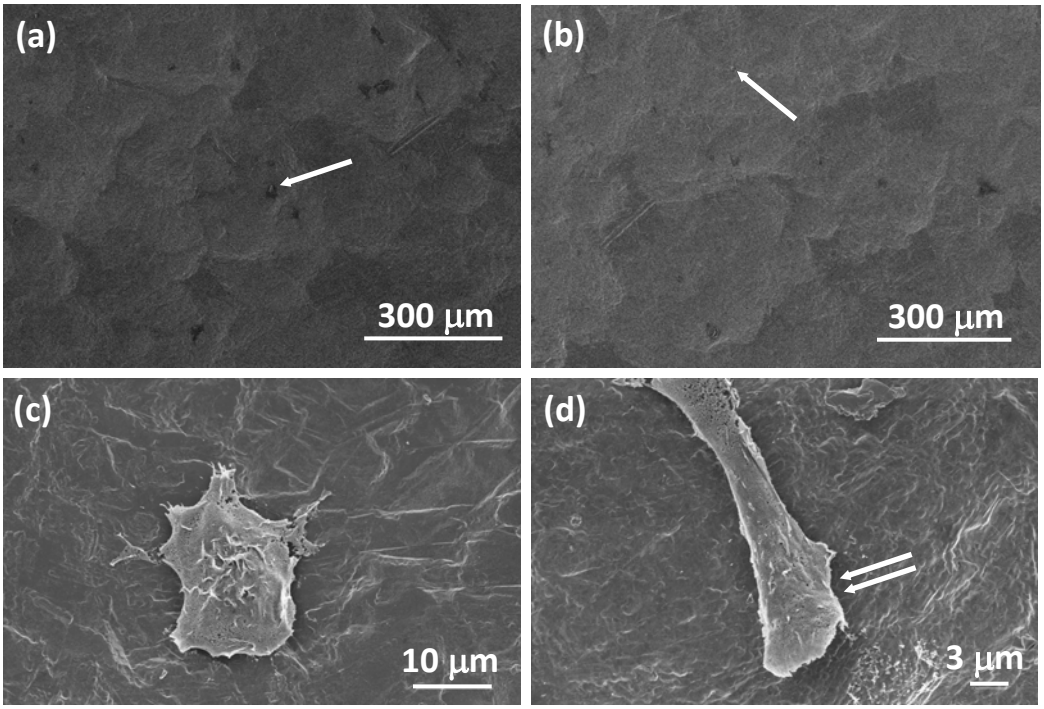

Figure 3-52. Osteoblast morphology after four hours of adhesion on commercially pure Ti. One arrow shows osteoblasts and double arrow shows the osteoblast membrane.

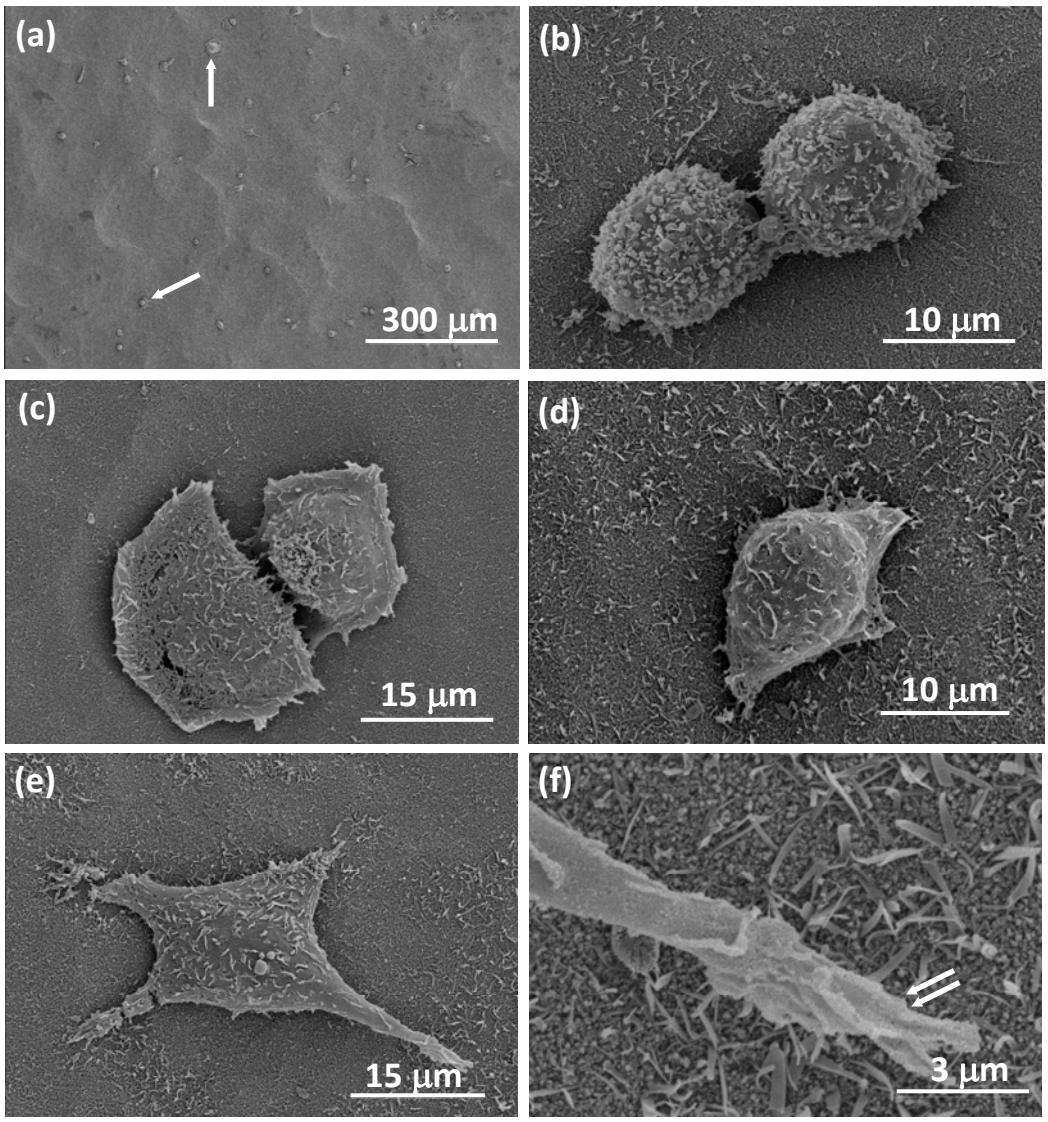

Figure 3-53. Osteoblast morphology after four hours of adhesion on anodized nanotubular Ti. One arrow shows an osteoblast and double arrows show osteoblast filopodia.

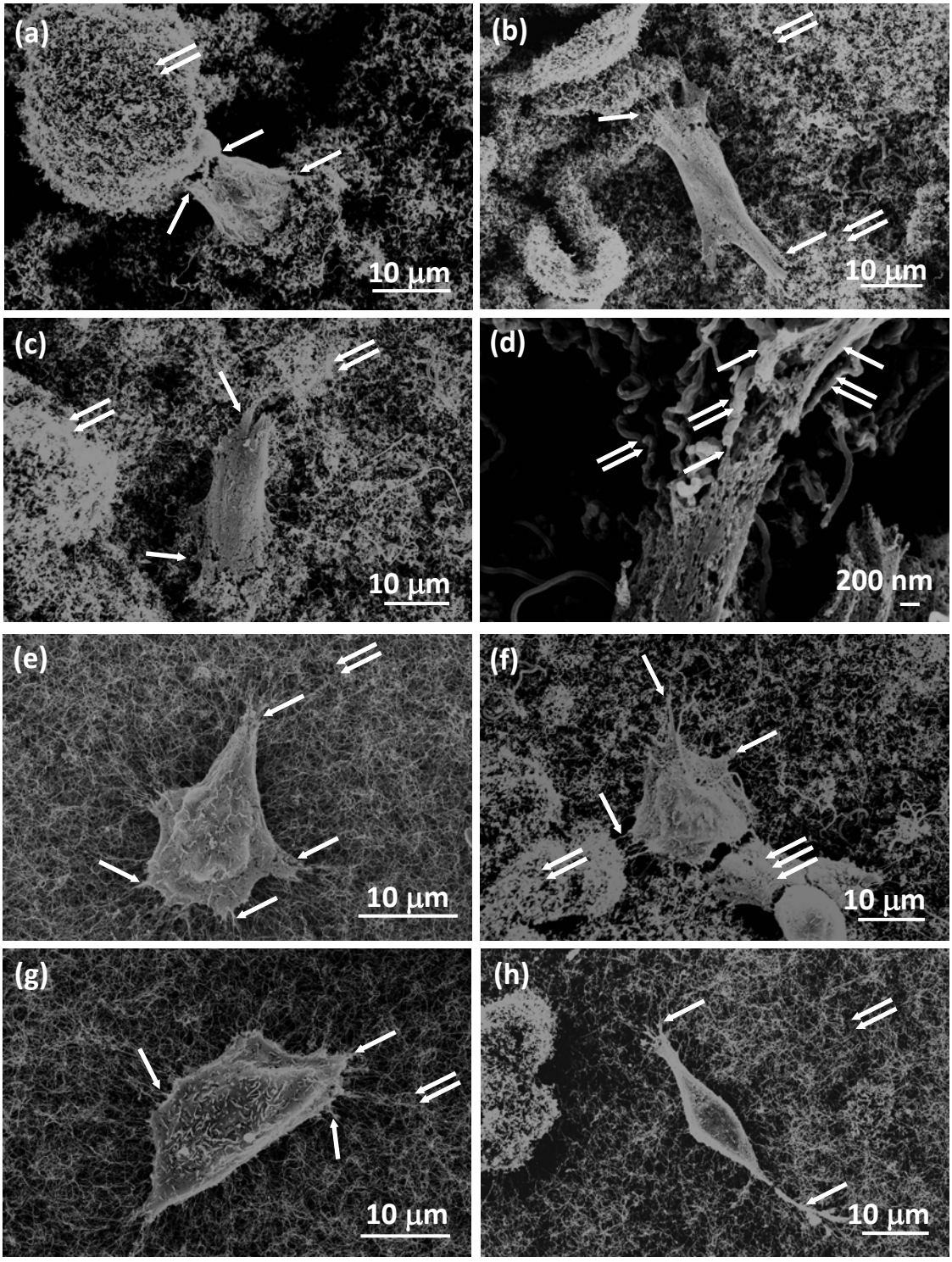

Figure 3-54. (a)-(h) Osteoblast morphology after four hours of adhesion on MWCNT-Ti. One-arrow shows osteoblasts cytoplasmic prolongation. Double-arrows show MWCNTs while triple-arrows show the osteoblast membrane.

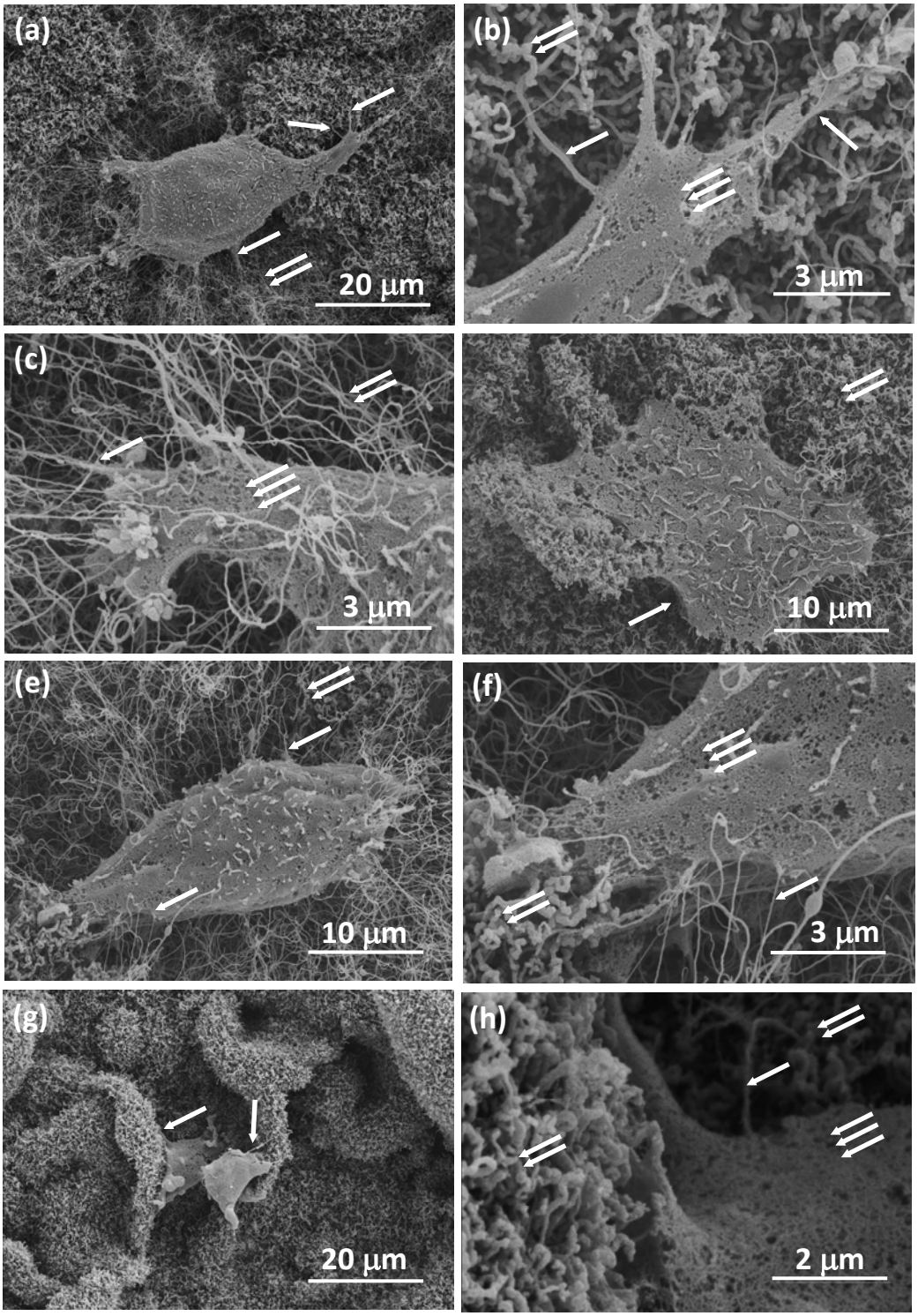

Figure 3-55. (a)-(h) Osteoblast morphology after four hours of adhesion on MWCNT-Ti. One-arrow shows osteoblast cytoplasmic prolongation. Double-arrows show MWCNTs while triple-arrows show the osteoblast membrane.

3.4.1.1.2 Osteoblast Differentiation

In vitro results after 21 days of culture showed that osteoblasts on MWCNTs grown from anodized nanotubular Ti secreted more alkaline phosphatase and deposited more calcium compared to anodized nanotubular Ti and commercially pure Ti (as shown in Figure 3-56 (a) alkaline phosphatase activity and (b) calcium deposition).

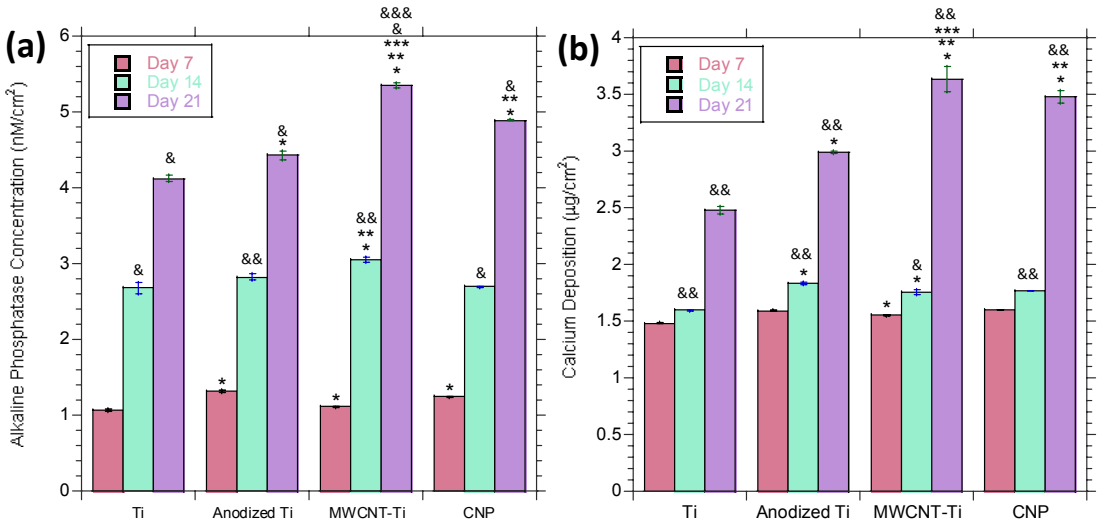

Figure 3-56. Osteoblast long term functions: (a) Alkaline phosphatase activity and (b) calcium deposition. Values are mean ± S.E.M; N=3; Student t-test; * $p<0.05$ compared to commercially pure Ti (Ti) at the respective time periods; ** $p<0.01$ compared to anodized Ti at the respective time periods; *** $p<0.01$ compared to carbon nanopaper (CNP) at the respective time periods; & $p<0.05$ compared to day 1; && $p<0.01$ compared to day 1; and &&& $p<0.05$ compared to day 3.

3.4.1.1.3 Osteoblast Extracellular Component Analysis

After osteoblasts were cultured for 21 days on the substrates of interest to this study, energy dispersive spectroscopy (EDS) performed on commercially pure Ti substrates revealed the

presence of various minerals indicating newly deposited bone. Figure 3-57 shows the peaks of numerous inorganic substances deposited, including magnesium (Mg), phosphorus (P), sulphur (S), potassium (K), and calcium (Ca). Result indicated that the Ca/P weight ratio of minerals deposited by osteoblasts on Ti (1.34) was less than that on MWCNT-Ti (1.52), while the natural Ca/P ratio of hydroxyapatite, the main calcium-phosphate crystallite in bone, was about 1.67 [24, 25]. Thus, this study demonstrated that the minerals deposited by osteoblasts on MWCNT-Ti were more similar to natural bone than the minerals deposited on Ti. X-ray diffraction (XRD) analysis also showed that hydroxyapatite was deposited on MWCNT-Ti than on both commercially pure Ti and anodized Ti after osteoblasts were cultured for 21 days, as shown Figure 3-58. In addition, the amount of calcium deposited by osteoblasts as determined by a calcium quantification assay kit was 1.481 $\mu g/cm^2$ after 7 days, 1.597 $\mu g/cm^2$ after 14 days, and 2.483 $\mu g/cm^2$ after 21 days on commercially pure Ti (Figure 3-37b). These results suggest a greater deposition of calcium by osteoblasts when cultured on MWCNT-Ti compared to commercially pure Ti, anodized nanotubular Ti, and carbon nanopaper.

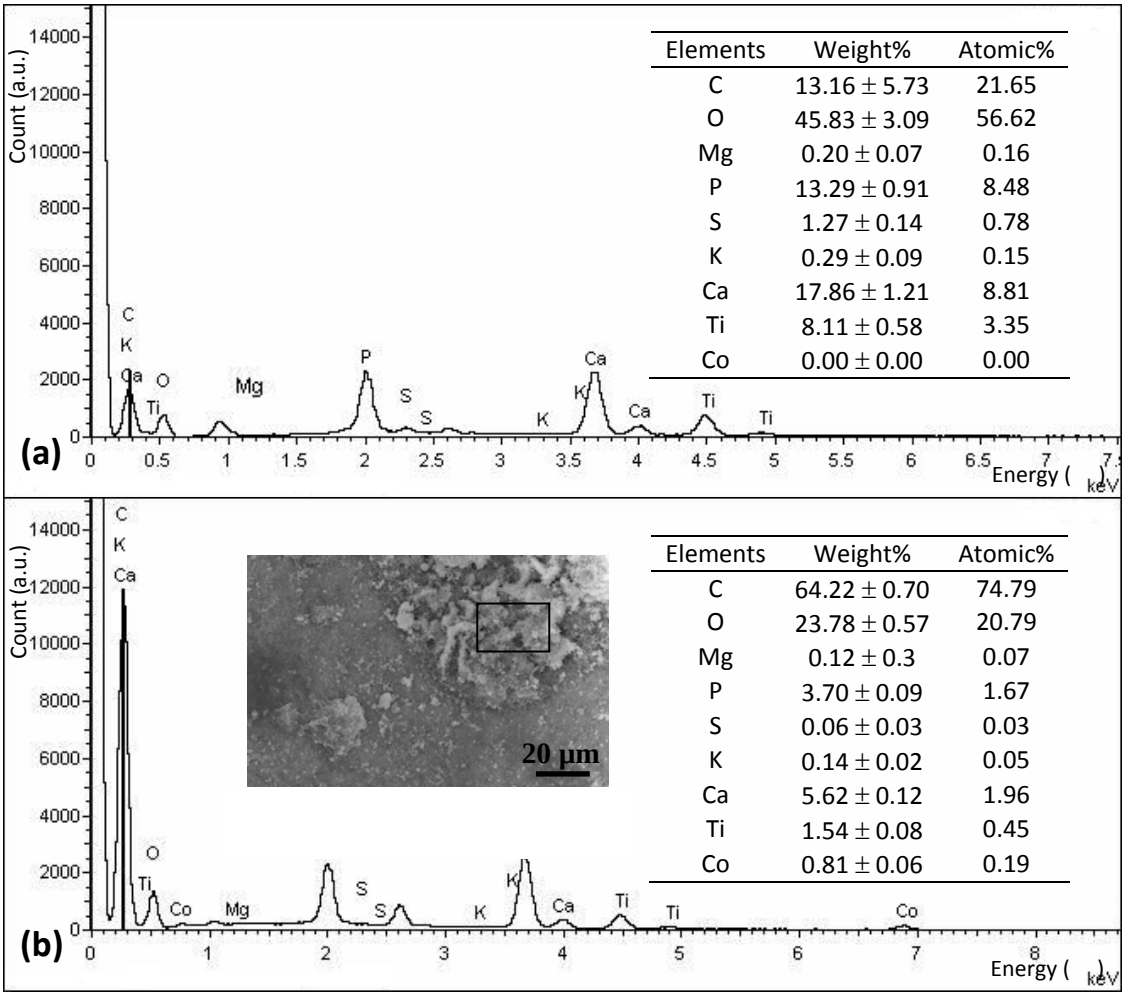

Elements	Weight%	Atomic%
C	13.16 ± 5.73	21.65
O	45.83 ± 3.09	56.62
Mg	0.20 ± 0.07	0.16
P	13.29 ± 0.91	8.48
S	1.27 ± 0.14	0.78
K	0.29 ± 0.09	0.15
Ca	17.86 ± 1.21	8.81
Ti	8.11 ± 0.58	3.35
Co	0.00 ± 0.00	0.00

Elements	Weight%	Atomic%
C	64.22 ± 0.70	74.79
O	23.78 ± 0.57	20.79
Mg	0.12 ± 0.3	0.07
P	3.70 ± 0.09	1.67
S	0.06 ± 0.03	0.03
K	0.14 ± 0.02	0.05
Ca	5.62 ± 0.12	1.96
Ti	1.54 ± 0.08	0.45
Co	0.81 ± 0.06	0.19

Figure 3-57. SEM-EDS analysis of osteoblasts cultured for 21 days on (a) commercially pure Ti and (b) MWCNT-Ti. SEM micrograph (inset (b)) shows the analyzed area. More Ca and P was deposited by osteoblasts on MWCNT-Ti. Tables in (a) and (b) show the composition of mineral deposits after osteoblasts were cultured for 21 days. The Ca/P weight ratio on commercially pure Ti was 1.32 while on MWCNT-Ti it was 1.52.

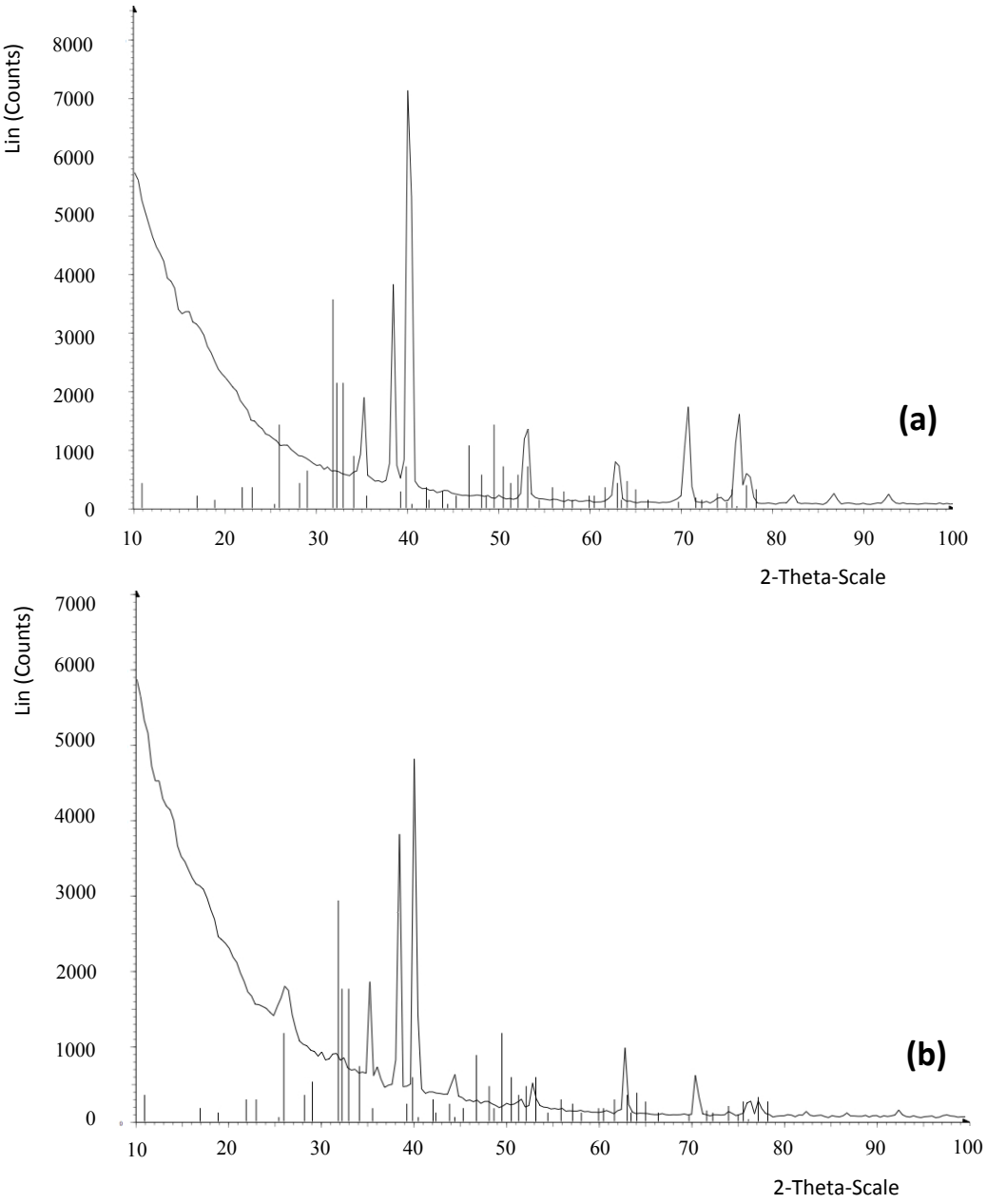

Figure 3-58. XRD analysis of hydroxyapatite deposited by osteoblasts (HA; $Ca_5(PO_4)_3OH$) on (a) commercially pure Ti and (b) MWCNT-Ti, after culture for 21 days. The micrographs show that the hydroxyapatite XRD spectra more closely matches that deposited on MWCNT-Ti than on commercially pure Ti.

3.4.1.2 Polypyrrole

3.4.1.2.1 Osteoblast Adhesion

The results of this study showed that osteoblasts adhered more on PPy[Dex]-Ti than on PPy[P/S]-Ti, PPy-Ti, and commercially pure Ti (Figure 3-59 and Figure 3-60). Osteoblast numbers on commercially pure Ti and PPy[P/S]-Ti were comparable, while osteoblasts adhered less on PPy-Ti (PPyCl) by about 29% when compared to commercially pure Ti and PPy[P/S]-Ti. Osteoblast density was more on PLGA-PPy[Dex]-Ti by about 44.7% when compared to commercially pure Ti, by about 21% when compared to PPy[Dex]-Ti, and by about 46.7% when compared to PPy[P/S]-Ti. However, osteoblasts were better spread on PPy-Ti than other samples (Figure 3-60). The presence of chloride anions in PPy-Ti down regulated osteoblast adhesion. Therefore, the choice of anionic drugs and electrolytes are extremely important in PPy electrodeposited films to mediate biological responses pertinent for orthopedic applications.

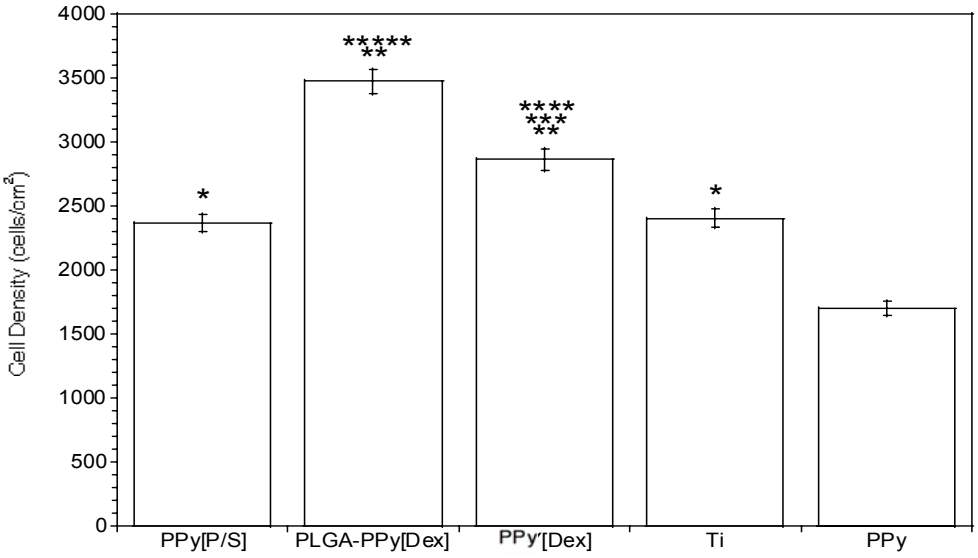

Figure 3-59. *In vitro* osteoblast adhesion after four hours of culture on PPy[P/S], PLGA-PPy[Dex], PPy[Dex], commercially pure Ti, and PPy. Values are mean ± S.E.M.; N=3; * $p<0.05$ when compared with PPy, ** $p<0.01$ when compared with PPy, *** $p<0.01$ when compared with PPy[P/S], **** $p<0.01$ when compared with Ti, and ***** $p<0.05$ when compared with PPy[Dex].

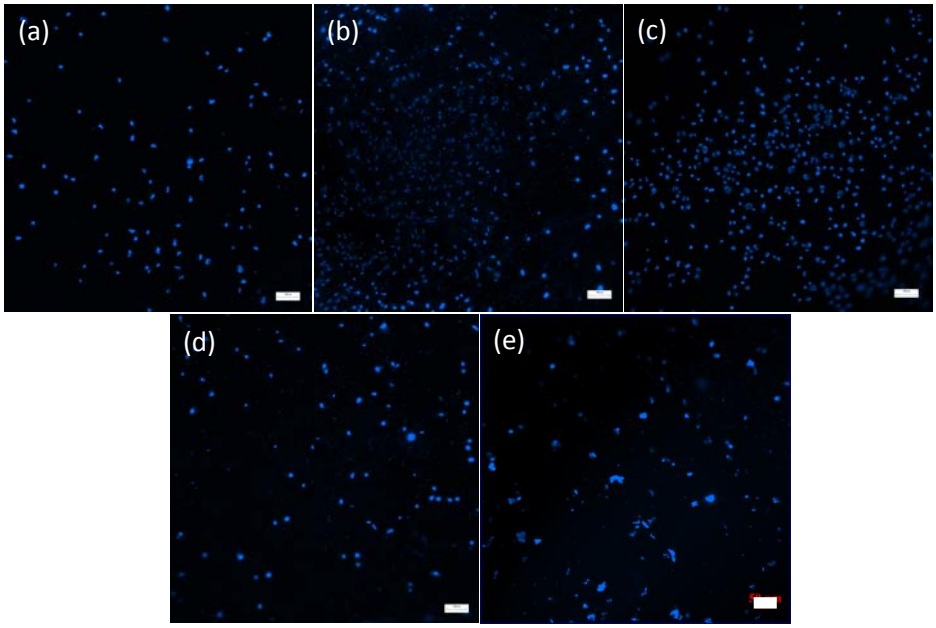

Figure 3-60. Fluorescent images of osteoblast adhesion, stained with DAPI, after four hours on: (a) PPy[P/S], (b) PLGA-PPy[Dex], (c) PPy[Dex], (d) commercially pure Ti, and (e) PPy. Scale bars are 50 μm.

3.4.1.2.2 Osteoblast Proliferation

After one day of osteoblast culture, cell density on PLGA-PPy[Dex]-Ti was significantly more than on PPy[P/S]-Ti and PPy-Ti, but not on PPy[Dex]-Ti and commercially pure Ti. There was no significant difference in cell numbers on PPy[P/S]-Ti, PPy[Dex]-Ti, PPy-Ti, and commercially pure Ti after three days of culture, while PLGA-PPy[Dex]-Ti still had the most osteoblasts compared to other samples for up to five days. On PPy[Dex]-Ti, there was significantly greater osteoblast density when compared to PPy-Ti, but not when compared to PPy[P/S]-Ti and commercially pure Ti after five days, as shown in Figure 3-61.

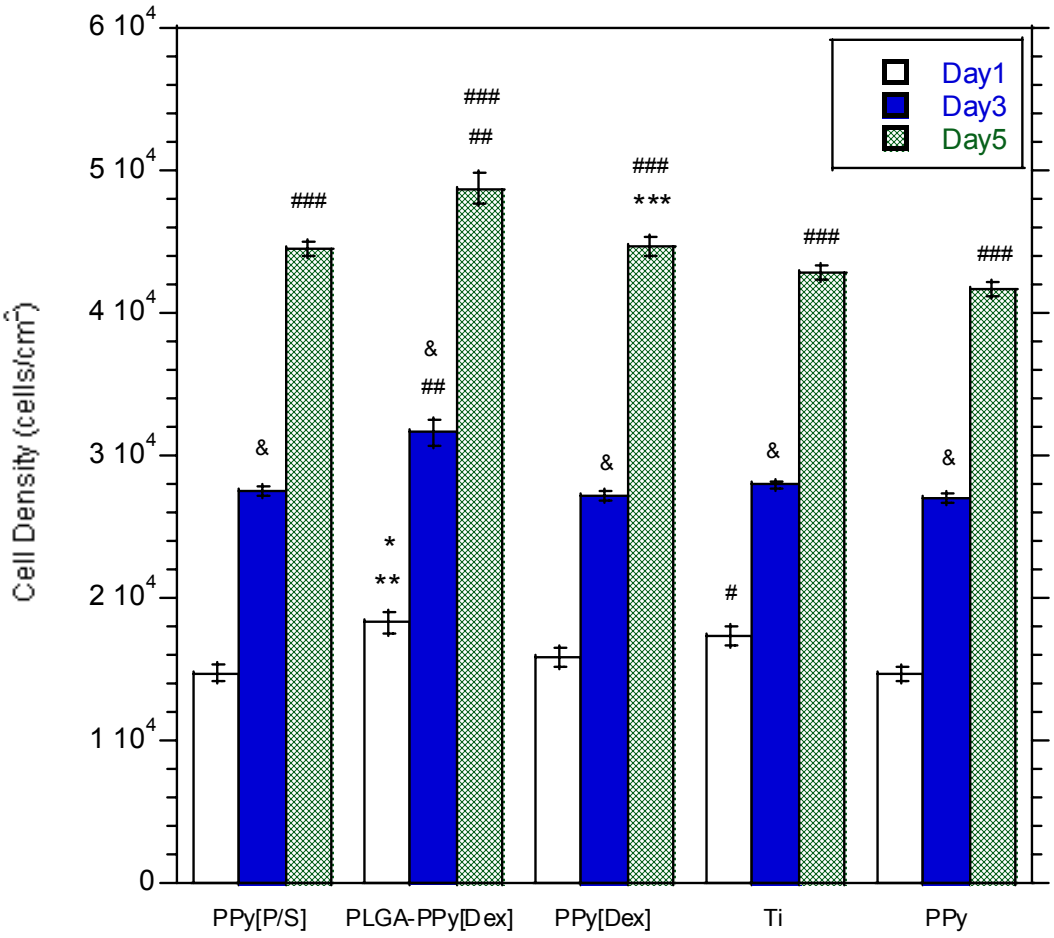

Figure 3-61. Osteoblast proliferation determined using the MTS assay on PPy[P/S]-Ti, PLGA-PPy[Dex]-Ti, PPy[Dex]-Ti, commercially pure Ti, and PPy-Ti. Values are mean ± S.E.M.; N=3; ANOVA, Tukey HSD test, with * $p<0.01$ when compared with PPy[P/S] and PPy at the same time period; ** $p<0.05$ when compared with PPy[Dex] at the same time period; # $p<0.05$ when compared with PPy[P/S] and PPy at the same time period; ## $p<0.01$ when compared with PPy[P/S], PPy[Dex], Ti, and PPy at the same time period; *** $p<0.05$ when compared with PPy at the same time period; ### $p<0.01$ when compared with day 1 and day 3 at the same time period; and & $p<0.01$ when compared with day 1 at the same time period.

3.4.2 Fibroblast Responses

3.4.2.1 Fibroblast Adhesion

The PPy-drug coatings on Ti decreased fibroblast (cells that synthesize soft fibrous tissue, not hard bony tissue) adhesion after four hours when compared to commercially pure Ti (Figure 3-62 and Figure 3-63). Fibroblasts density after four hours also decreased on PPy-Ti compared to PPy[Dex]-Ti (by 48%) and commercially pure Ti (by 70%). Figure 3-63 shows that fibroblasts spread more on PPy[P/S]-Ti and PPy-Ti when compared to PLGA-PPy[Dex]-Ti, PPy[Dex], and commercially pure Ti.

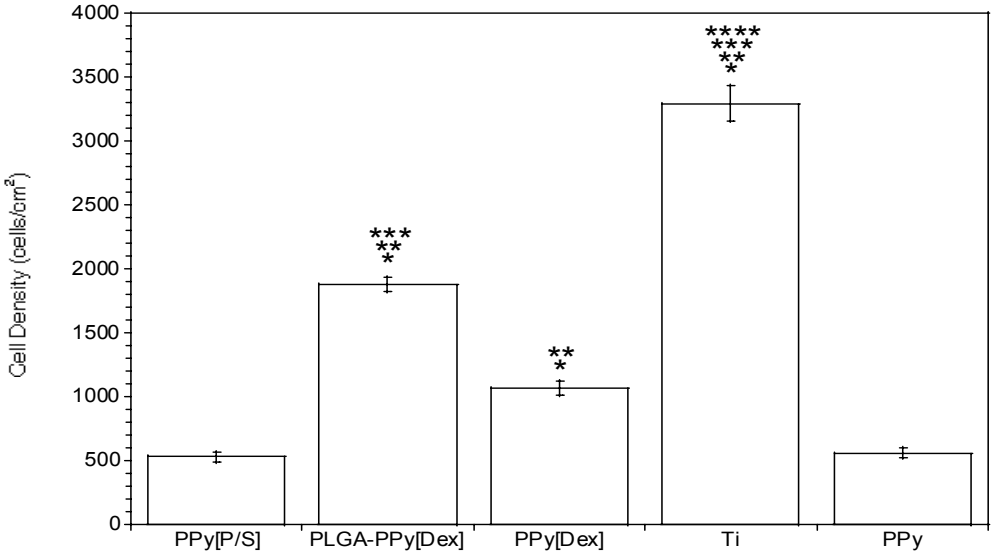

Figure 3-62. Fibroblast adhesion after four hours of *in vitro* culture on PPy[P/S]-Ti, PLGA-PPy[Dex]-Ti, PPy[Dex]-Ti, commercially pure Ti, and PPy-Ti. Values are mean ± S.E.M.; N=3; * $p<0.01$ when compared with PPy[P/S]-Ti, ** $p<0.01$ when compared with PPy, *** $p<0.01$ when compared with PPy[Dex]-Ti, and **** $p<0.05$ when compared with PLGA-PPy[Dex]-Ti.

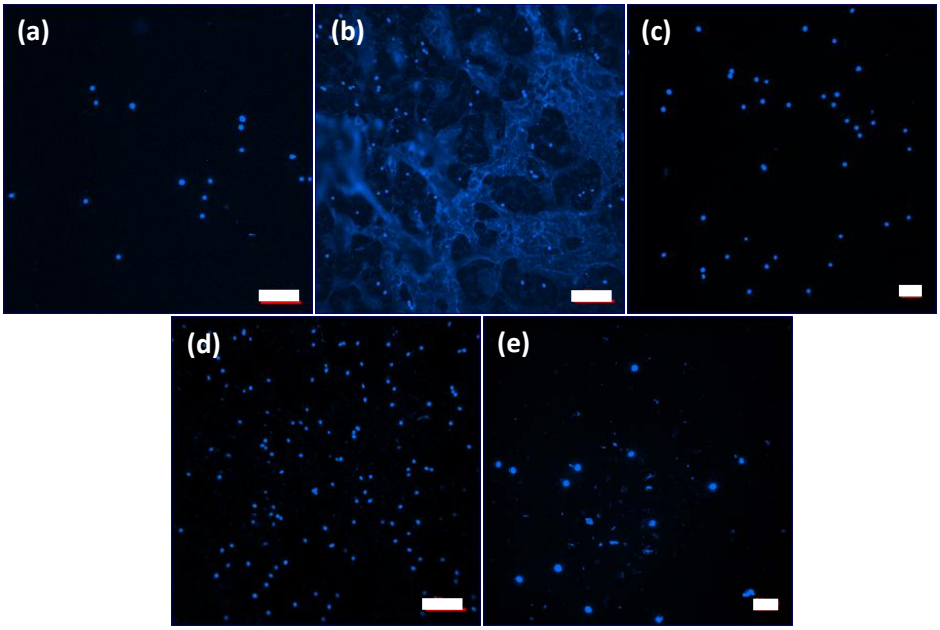

Figure 3-63. Fluorescent images of fibroblast adhesion (nuclei stain with DAPI) after four hours on: (a) PPy[P/S]-Ti, (b) PLGA-PPy[Dex]-Ti, (c) PPy[Dex]-Ti, (d) commercially pure Ti, and (e) PPy-Ti. Scale bars are 50 μm.

3.4.2.2 Fibroblast Proliferation

On commercially pure Ti, fibroblast density was significantly higher among all other samples (specifically, PPy[P/S]-Ti, PLGA-PPy[Dex]-Ti, PPy[Dex]-Ti, and PPy-Ti) after one, three, and five days, as shown in Figure 3-63. After one day of culture, fibroblasts proliferated more significantly on PLGA-PPy[Dex]-Ti than on PPy[P/S]-Ti and PPy-Ti. Lastly, fibroblast numbers on PPy-Ti were higher than on PPy[Dex]-Ti.

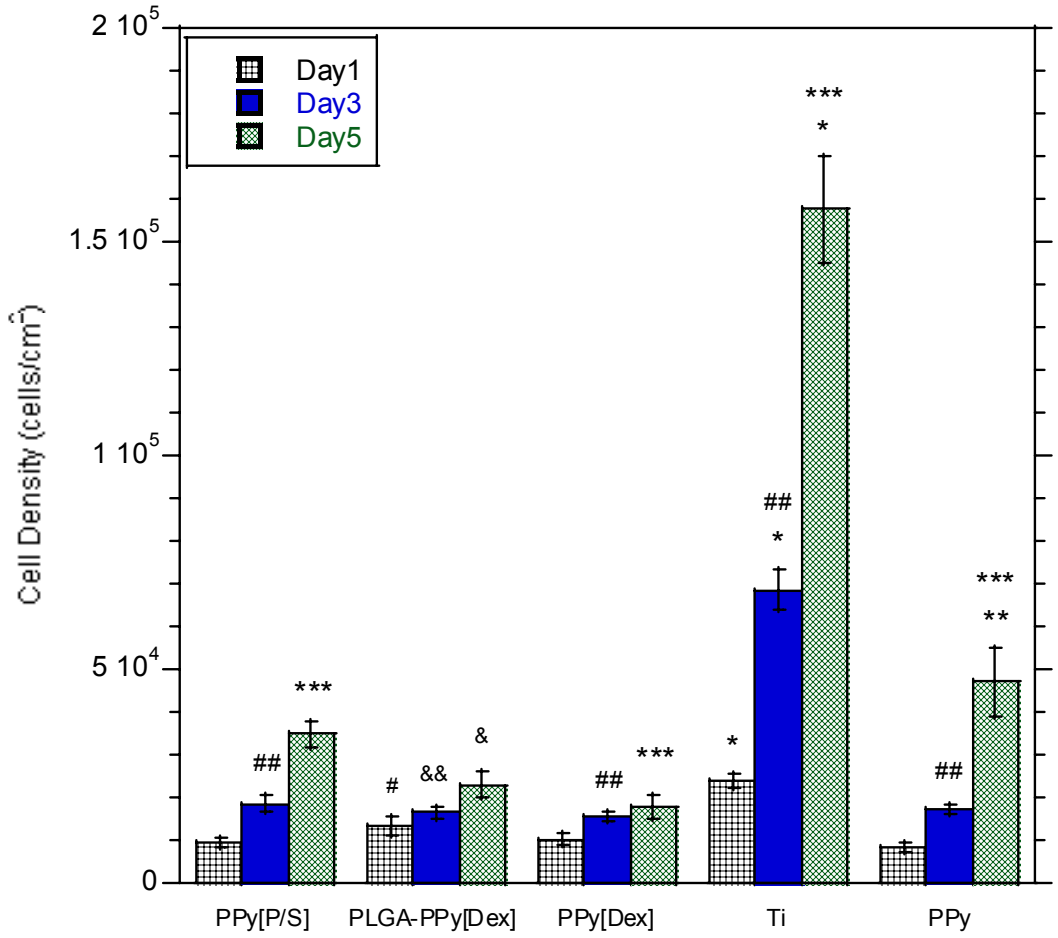

Figure 3-64. Fibroblast proliferation determined using the MTS assay on PPy[P/S]-Ti, PLGA-PPy[Dex]-Ti, PPy[Dex]-Ti, commercially pure Ti, and PPy-Ti. Values are mean ± S.E.M.; N=3; (ANOVA, Tukey HSD test), with * $p<0.01$ when compared with PPy[P/S]-Ti, PLGA-PPy[Dex]-Ti, PPy[Dex]-Ti, and PPy-Ti at the same time period of culture, # $p<0.05$ when compared with PPy[P/S]-Ti and PPy-Ti after one day of culture, ** $p<0.05$ when compared with PPy[Dex]-Ti after five days of culture; ## $p<0.01$ when compared with day 1; *** $p<0.01$ when compared with day 1 and day 3; && $p<0.01$ when compared with day 1; and && $p<0.05$ when compared with day 5.

3.4.3 Macrophage Responses

3.4.3.1 Macrophage Adhesion

Importantly, there was no significant difference in macrophage adhesion after four hours on PPy[Dex]-Ti and PPy-Ti, as shown in Figure 3-65 and Figure 3-66. However, PLGA-PPy[Dex]-Ti had the highest macrophage number among all other samples, and was significantly higher than PPy[Dex]-Ti (by 56%) and glass (by 40%). Moreover, macrophages adhered significantly less on PLGA-NHS than PPy-Ti (by 59%), PPy[Dex]-Ti (by 60%) and glass (by 70%). Figure 3-66 showed that macrophages spread more on glass, PPy-Ti, and PPy[Dex]-Ti than commercially pure Ti, PLGA-PPY[Dex]-Ti, and PLGA-NHS.

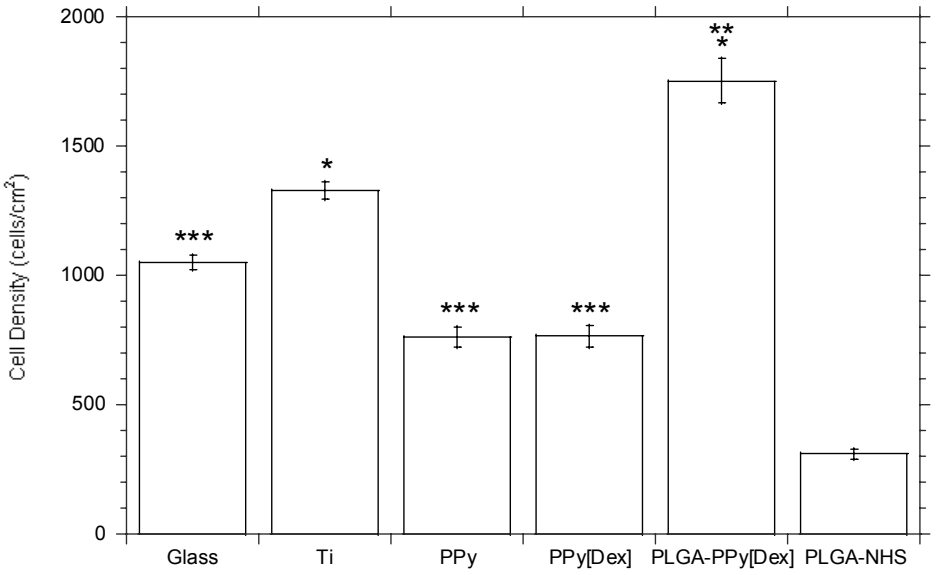

Figure 3-65. Macrophage adhesion after four hours on glass, commercially pure Ti, PPy-Ti, PPy[Dex]-Ti, PLGA-PPy[Dex]-Ti, and PLGA-NHS cast film on glass. Values are mean ± S.E.M.; N=3; (ANOVA, Tukey HSD test), * p<0.01 when compared with glass, ** p<0.01 when compared with PPy[Dex], PPy, PLGA-NHS, and Ti, and *** p<0.01 when compared with PLGA-NHS.

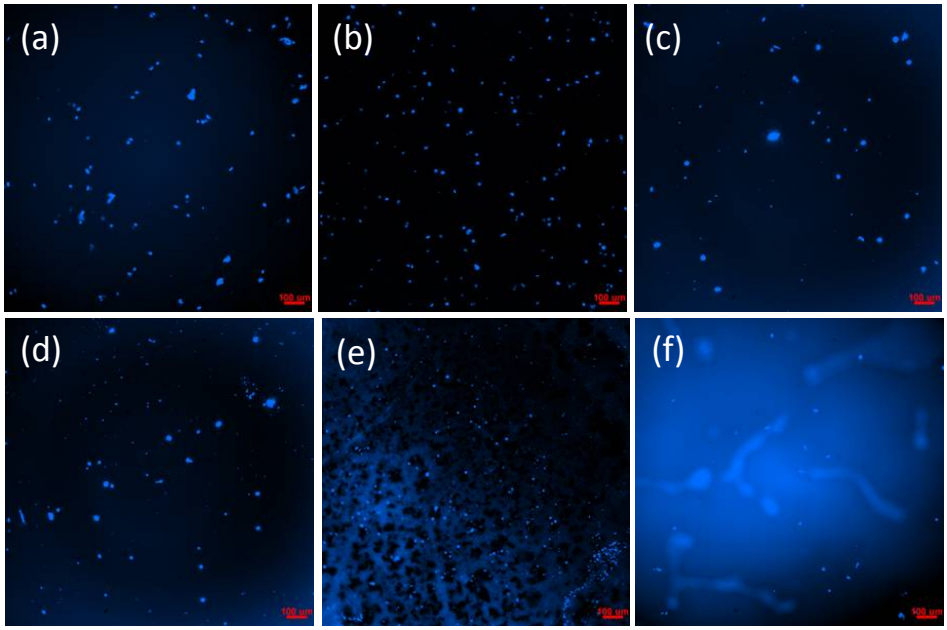

Figure 3-66. Fluorescent images of macrophages adherent after four hours on: (a) glass, (b) commercially pure Ti, (c) PPy-Ti, (d) PPy[Dex]-Ti, (e) PLGA-PPy[Dex]-Ti, and (f) PLGA-NHS.

3.4.3.2 Macrophage Adhesion in Response to Electrical Stimulation of Drug Release

After four hours of macrophage culture, electrical stimulation to stimulate Dex releases was used. Cyclic voltammetry was used to stimulate PPy[Dex]-Ti and PPy-Ti with a scan rate of 100 mV/s for 5 cycles from -1 V to 1 V. Importantly, macrophages adhered significantly less on PPy[Dex]-Ti when compared to PPy-Ti without electrical stimulation (about 33% for four hours and about 29% after nine hours), as shown in Figure 3-67. With electrical stimulation, cell density increased after an additional four hours to an additional nine hours about 28% for PPy-Ti and about 25% for PPy[Dex]-Ti. After electrical stimulation and an additional four hours, cell

density decreased about 59% for PPy-Ti and 51% for PPy[Dex]-Ti. Figure 3-68 and Figure 3-69 show macrophages adhered on PPy[Dex]-Ti and PPy-Ti, respectively, with and without electrical stimulation. After PPy[Dex]-Ti and PPy-Ti were subjected to electrical stimulation, the number of macrophages decreased significantly, however, there were macrophages adherent as shown in Figure 3-68 and Figure 3-69. After, an additional nine hours, macrophages proliferated and were more spreading on both PPy[Dex]-Ti and PPy-Ti.

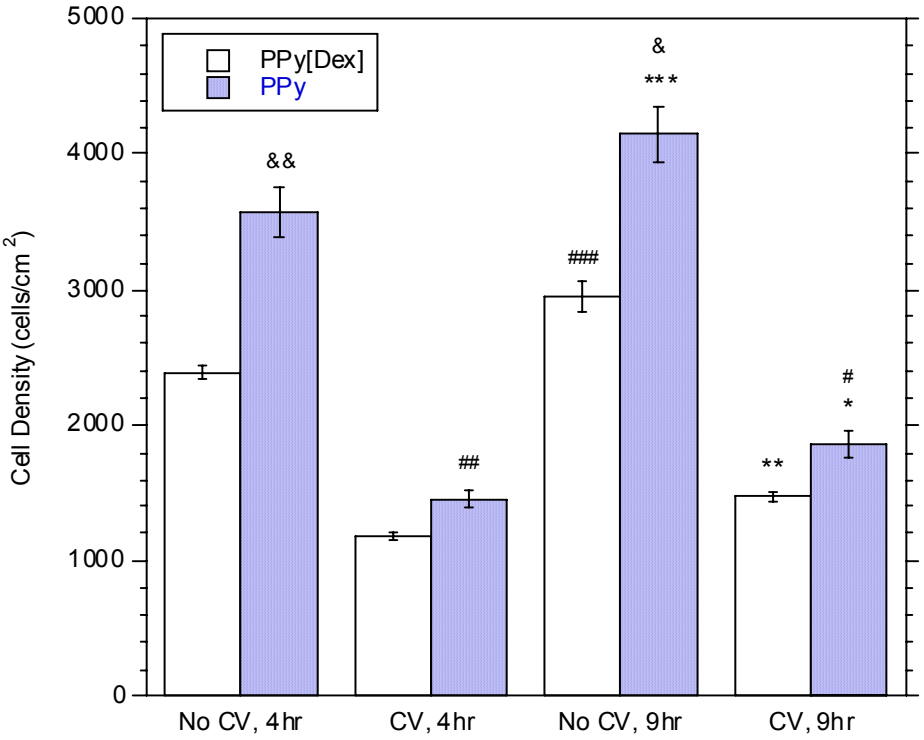

Figure 3-67. Macrophage adhesion on PPy-Ti and PPy[Dex]-Ti. Electrical stimulation using cyclic voltammetry was performed after four hours of culture with a scan rate of 100 mV/s from -1 V to 1V. Macrophages were further incubated for four and nine hours, and counted under a fluorescence microscope (Leica Microsystem). Values are mean ± S.E.M.; N=3; (ANOVA, Tukey HSD test), $p<0.01$: * when compared with PPy (CV, 4hr); ** when compared with PPy[Dex] (CV, 4hr); # when compared with PPy[Dex] (CV, 9hr); ## when compared with PPy[Dex] (CV, 4hr); *** when compared with PPy (no CV, 4hr); ### when compared with PPy[Dex] (no CV, 4hr); & when compared with PPy[Dex] (no CV, 9hr); and && when compared with PPy[Dex] (no CV, 4hr).

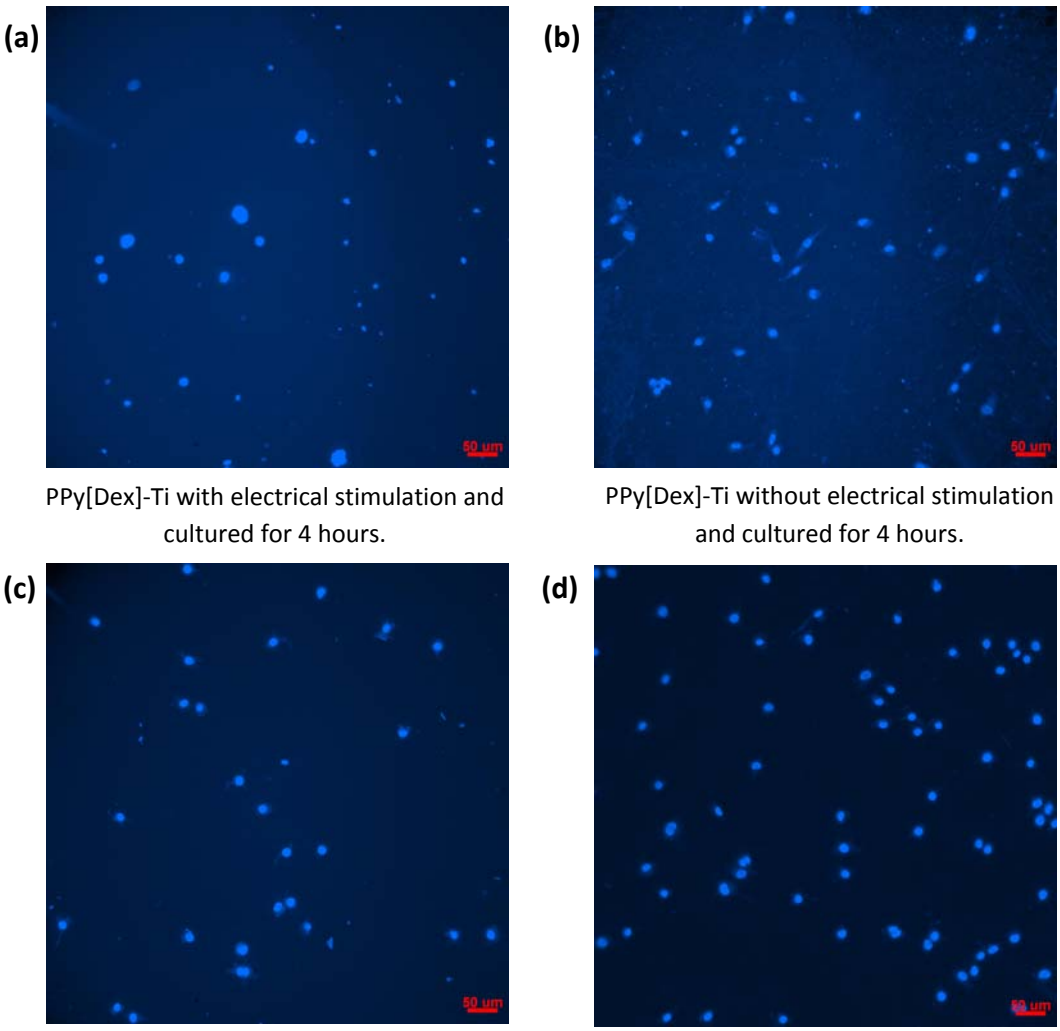

PPy[Dex]-Ti with electrical stimulation and cultured for 4 hours.

PPy[Dex]-Ti without electrical stimulation and cultured for 4 hours.

PPy[Dex]-Ti with electrical stimulation and cultured for 9 hours.

PPy[Dex]-Ti withot electrical stimulation and cultured for 9 hours.

Figure 3-68. Macrophage adhesion on PPy[Dex]-Ti after electrical stimulation for four and nine hours. Electrical stimulation using cyclic voltammetry was performed after four hours of culture with a scan rate of 100 mV/s from -1 V to 1 V. Macrophages were stained with DAPI and the images were captured by a fluorescence microscope at 20X magnification. Scale bars are 50 µm.

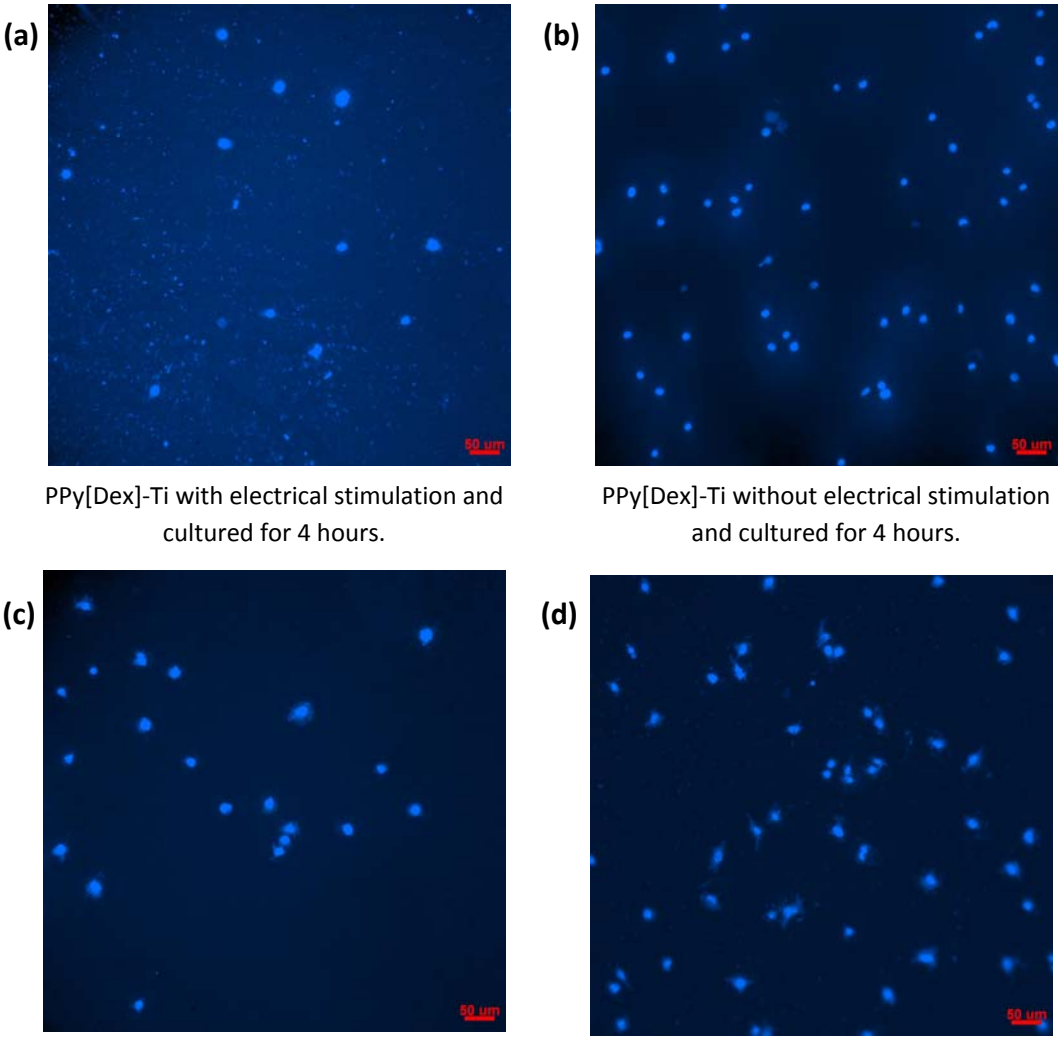

PPy[Dex]-Ti with electrical stimulation and cultured for 4 hours.

PPy[Dex]-Ti without electrical stimulation and cultured for 4 hours.

PPy[Dex]-Ti with electrical stimulation and cultured for 9 hours.

PPy[Dex]-Ti withot electrical stimulation and cultured for 9 hours.

Figure 3-69. Macrophage adhesion on PPy-Ti after electrical stimulation for four and nine hours. Electrical stimulation using cyclic voltammetry was performed after four hours of culture with a scan rate of 100 mV/s from -1 V to 1 V. Macrophages were stained with DAPI and the images were captured by a fluorescence microscope at 20X magnification. Scale bars are 50 μm.

3.4.4 Bacteria Responses

3.4.4.1 Bacteria Colony Formation

Staphylococcus epidermidis adhered the least on PPy[P/S]-Ti when compared to PPy-Ti, Ti, and glass after one hour (Figure 3-70). Importantly, the bacteria density on PPy[P/S]-Ti decreased by about 26% when compared with PPy-Ti and by about 47% when compared with commercially pure Ti. On PPy-Ti, bacteria numbers decreased by about 28% when compared with commercially pure Ti.

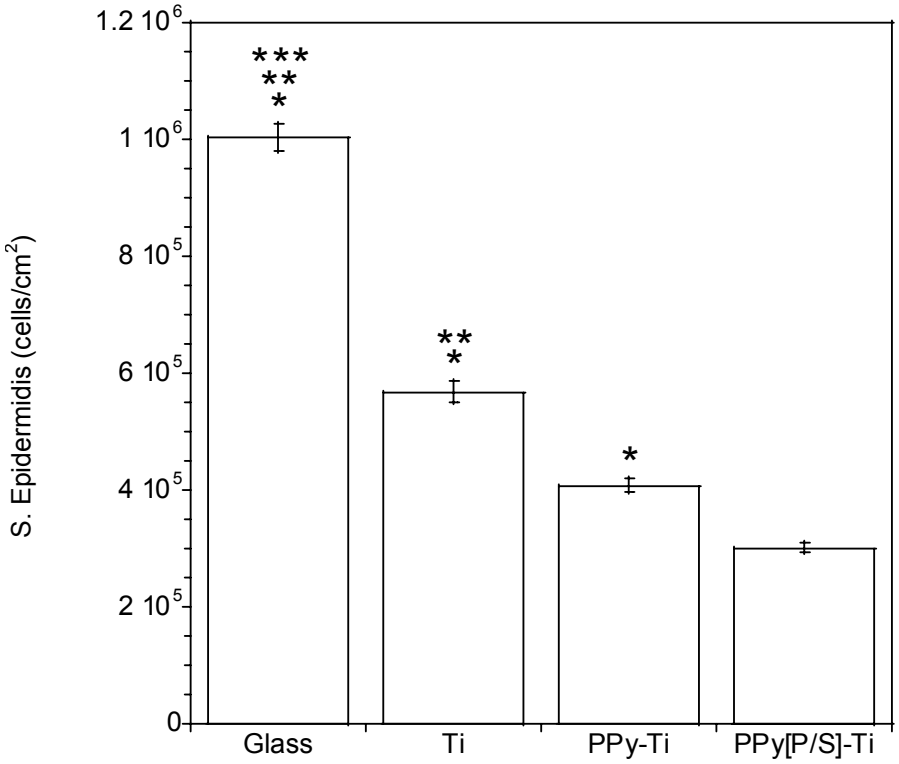

Figure 3-70. *Staphylococcus epidermidis* numbers after one hour. Values are mean ± S.E.M; N=3; (ANOVA, Tukey HSD test), * $p<0.01$ when compared with PPy[P/S]-Ti; ** $p<0.01$ when compared with PPy-Ti; and *** $p<0.01$ when compared with Ti.

3.4.4.2 Bacteria Colony Formation in Response to Electrical Stimulation of Drug Release

After electrical stimulation of PPy[P/S]-Ti by applying sweep voltages, *Staphylococcus epidermidis* numbers significantly decreased following an increasing number of applied voltage cycles, as shown in Figure 3-71 (after one hour) and Figure 3-72 (after 12 hours).

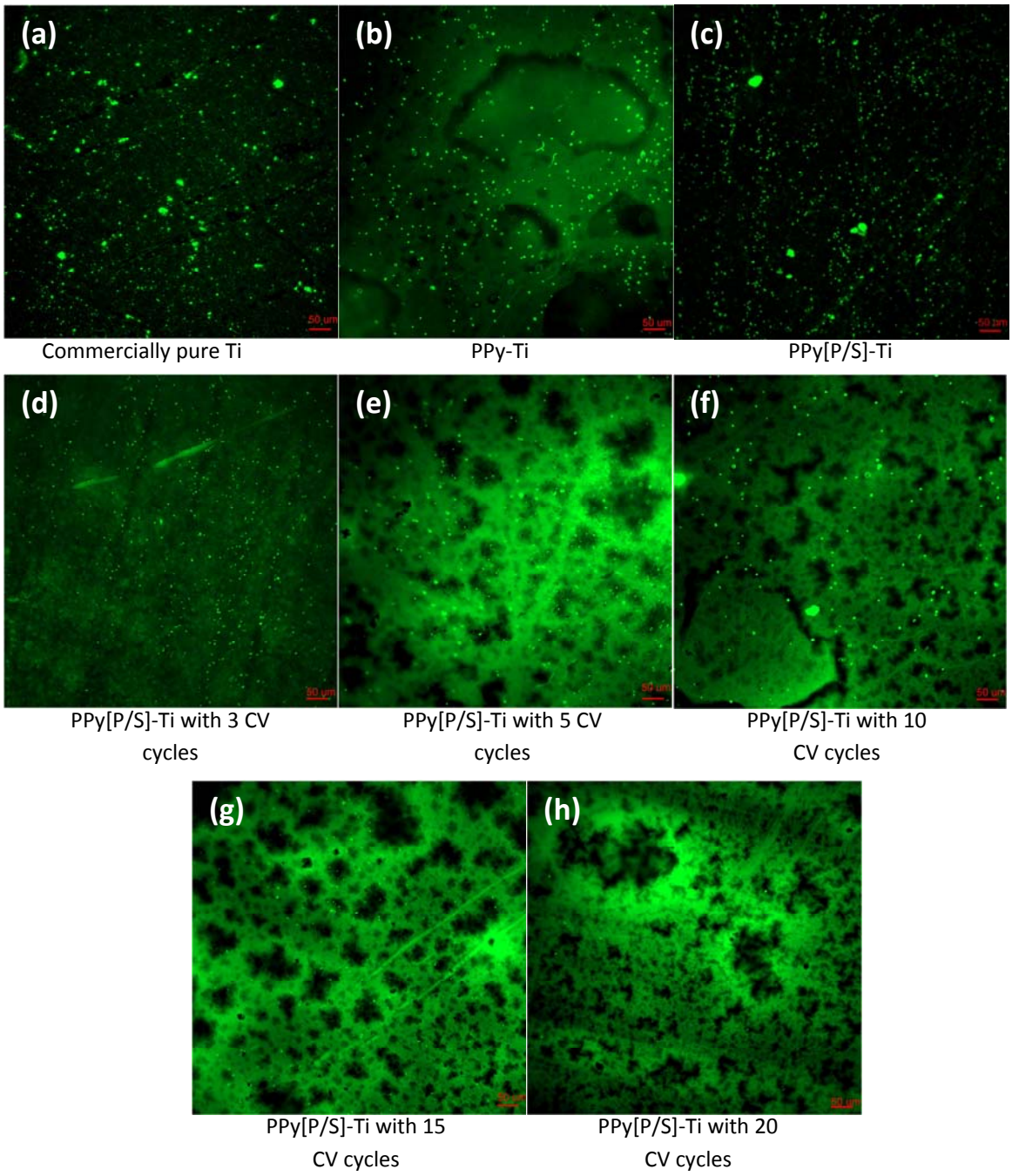

Figure 3-71. Green fluorescent images of bacteria colonies, after being cultured for one hour, stained using the Live/Dead BacLight Bacterial Viability kit (Molecular Probes) on: (a) Ti; (b) PPy-Ti; (c) PPy[PS]-Ti; PPy[P/S]-Ti after electrically-controlled release by electrical stimulation for (c) 3 cycles, (d) 5 cycles, (f) 10 cycles, (g) 15 cycles, and (h) 20 cycles. Cyclic voltammetry was used to trigger the release with 100 mV/s from -1 V to 1 V. Scale bars are 50 μm. Images were captured by a fluorescence microscopy (Leica Microsystem) at 20X magnification.

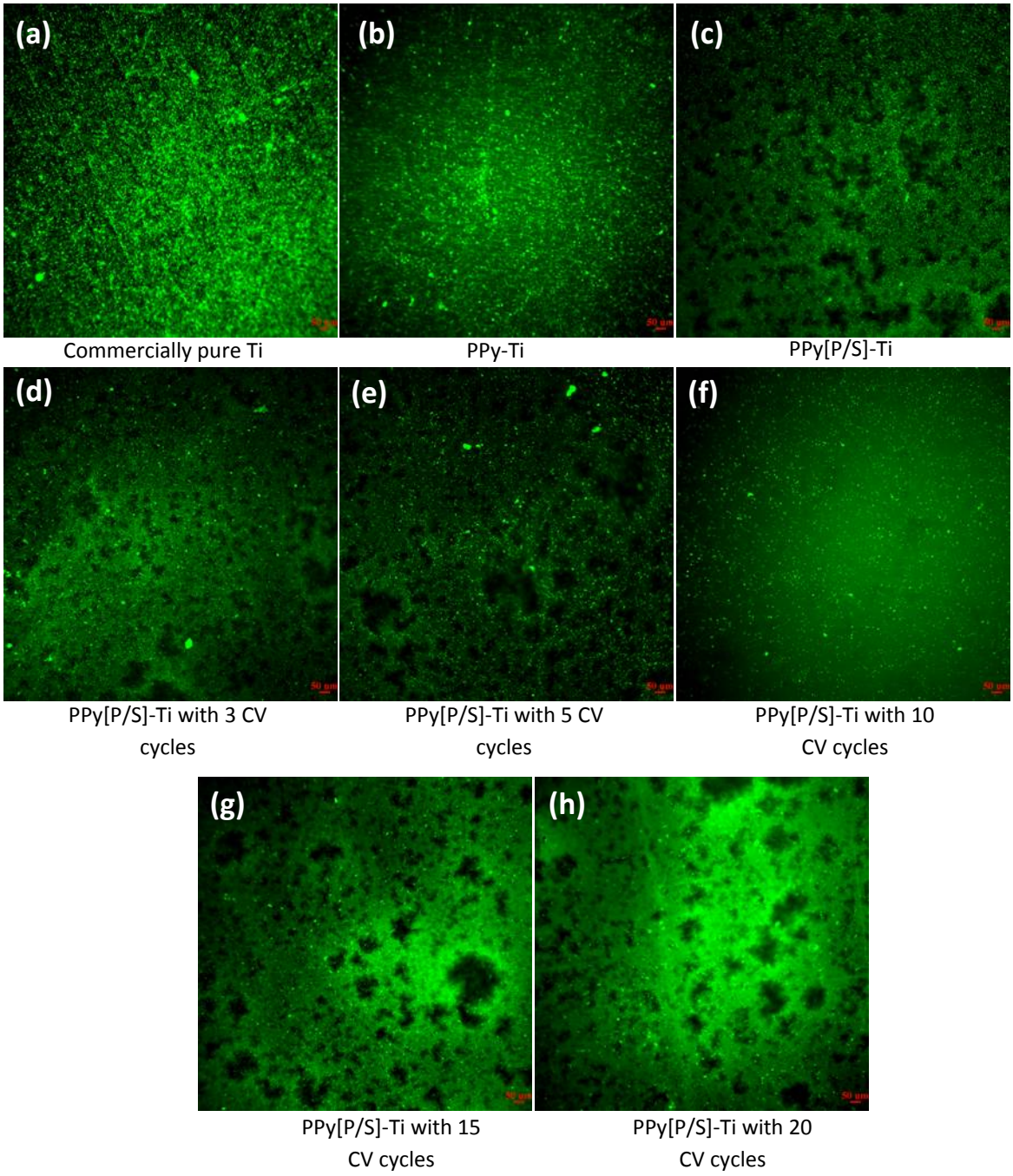

Figure 3-72. Green fluorescent images of bacteria colonies, after being cultured for 12 hours, stained using the Live/Dead BacLight Bacterial Viability kit (Molecular Probes) on: (a) Ti, (b) PPy-Ti, and (c) PPy[PS]-Ti, PPy[P/S]-Ti after controlled release by electrical stimulation for (c) 3 cycles, (d) 5 cycles, (f) 15 cycles, (g) 20 cycles, and (h) 25 cycles. Cyclic voltammetry was used to trigger the release with 100 mV/s from -1 V to 1V. Scale bars are 50 μm. Images were captured by a fluorescence microscopy (Leica Microsystem) at 10X magnification.

References

1. Yao C, Perla V, McKenzie JL, Slamovich EB, Webster TJ. Anodized Ti and Ti6Al4V Possessing Nanometer Surface Features Enhances Osteoblast Adhesion. Journal of Biomedical Nanotechnology 2005;1:68-73(66).

2. Yao C, Webster TJ. Anodization: A Promising Nano-Modification Technique of Titanium Implants for Orthopedic Applications. Journal of Nanoscience and Nanotechnology 2006 October 2006;6:2682-2692(2611).

3. Soneda Y, Duclaux L, Béguin Fo. Synthesis of high quality multi-walled carbon nanotubes from the decomposition of acetylene on iron-group metal catalysts supported on MgO. Carbon 2002 5;40(6):965-969.

4. Hofmann S, Cantoro M, Kleinsorge B, Casiraghi C, Parvez A, Robertson J, et al. Effects of catalyst film thickness on plasma-enhanced carbon nanotube growth. Journal of Applied Physics 2005;98(3):034308-034308.

5. Zolyomi V, Kurti J, Gruneis A, Kuzmany H. Origin of the Fine Structure of the Raman D Band in Single-Wall Carbon Nanotubes. Physical Review Letters 2003;90(15):157401-157404.

6. Kurti J, Zolyomi V, Gruneis A, Kuzmany H. Double resonant Raman phenomena enhanced by van Hove singularities in single-wall carbon nanotubes. Physical Review B (Condensed Matter and Materials Physics) 2002;65(16):165433-165439.

7. Doorn SK, Zheng L, O'Connell MJ, Zhu Y, Huang S, Liu J. Raman Spectroscopy and Imaging of Ultralong Carbon Nanotubes. J Phys Chem B 2005;109(9):3751-3758.

8. Ouyang Y, Cong LM, Chen L, Liu QX, Fang Y. Raman study on single-walled carbon nanotubes and multi-walled carbon nanotubes with different laser excitation energies. Physica E: Low-dimensional Systems and Nanostructures 2008;40(7):2386-2389.

9. Yan H, Li Q, Zhang J, Liu Z. Possible tactics to improve the growth of single-walled carbon nanotubes by chemical vapor deposition. Carbon 2002;40(14):2693-2698.

10. Ratner BD. Biomaterials science : an introduction to materials in medicine. Amsterdam; Boston: Elsevier Academic Press, 2004.

11. de Gennes P-G, Brochard-Wyart F, Quere D. Capillarity and wetting phenomena: Drops, Bubbles, Pearls, Waves. USA: Springer, 2003.

12. Yao C. Surface Modification of Titanium by Anodization for Orthopedic Applications: Purdue University; 2005.

13. Somasundaran P. Encyclopedia of surface and colloid science. 2 ed: CRC Press, 2006.

14. Pavia DL, Lampman GM, Kriz GS, Engel RG. Introduction to organic techniques: a microscale approach. 4 ed: Thomson Higher Education, 2007.

15. Zhang Y, Baer CD, Camaioni-Neto C, O'Brien P, Sweigart DA. Steady-state voltammetry with microelectrodes: determination of heterogeneous charge transfer rate constants for metalloporphyrin complexes. Inorganic Chemistry 1991;30(8):1682-1685.

16. Hrapovic S, Liu Y, Male KB, Luong JHT. Electrochemical Biosensing Platforms Using Platinum Nanoparticles and Carbon Nanotubes. Analytical Chemistry 2004;76(4):1083-1088.

17. Hrapovic S, Luong JHT. Picoamperometric Detection of Glucose at Ultrasmall Platinum-Based Biosensors: Preparation and Characterization. Analytical Chemistry 2003;75(14):3308-3315.

18. Eastell R, Baumann M, Hoyle N, Wieczorek L. Bone markers: biochemical and clinical perspectives: Informa Health Care, 2001.

19. De Giglio E, Cometa S, Calvano C-D, Sabbatini L, Zambonin P, Colucci S, et al. A new titanium biofunctionalized interface based on poly(pyrrole-3-acetic acid) coating: proliferation of

osteoblast-like cells and future perspectives. Journal of Materials Science: Materials in Medicine 2007;18(9):1781-1789.

20. Malitesta C, Losito I, Sabbatini L, Zambonin PG. New findings on polypyrrole chemical structure by XPS coupled to chemical derivatization labelling. Journal of Electron Spectroscopy and Related Phenomena 1995;76:629-634.

21. Wallace GG, Spinks GM, Teasdale PR. Conductive electroactive polymers intelligent materials systems. Lancaster, Pa.: Technomic Pub. Co., 1997.

22. Zhang X, Kang ET, Neoh KG, Tan KL, Kim DY, Kim CY. Surface studies of pristine and surface-modified polypyrrole films. Journal of Applied Polymer Science 1996;60(4):625-636.

23. Joo J, Lee JK, Baeck JS, Kim KH, Oh EJ, Epstein J. Electrical, magnetic, and structural properties of chemically and electrochemically synthesized polypyrroles. Synthetic Metals 2001;117(1-3):45-51.

24. Calafiori A, Di Marco G, Martino G, Marotta M. Preparation and characterization of calcium phosphate biomaterials. Journal of Materials Science: Materials in Medicine.

25. Wang H, Lee J-K, Moursi A, Lannutti JJ. Ca/P ratio effects on the degradation of hydroxyapatite in vitro. Journal of Biomedical Materials Research Part A 2003;67A(2):599-608.

CHAPTER 4

Discussion

4.1 Summary

Results of this thesis showed that MWCNT-Ti electrodes had the ability to determine new bone growth by detecting the redox reaction of osteoblast secreted extracellular matrix component. In addition, electrically-conducting PPy films were electrodeposited with antibiotic and anti-inflammatory drugs, specifically P/S and Dex, onto AuPd coated commercially pure Ti, widely used for orthopedic implants. Both P/S and Dex were released about 80% of their initial amounts by using cyclic voltammetry for 5 cycles (with scan rate of 100 mV/s from -1 V to 1 V). The MWCNT-Ti sensor and electrically-controlled drug release system from PPy can, thus, be used as novel nanomaterials to develop a closed-loop sensing and therapy for orthopedic applications (Figure 4-73).

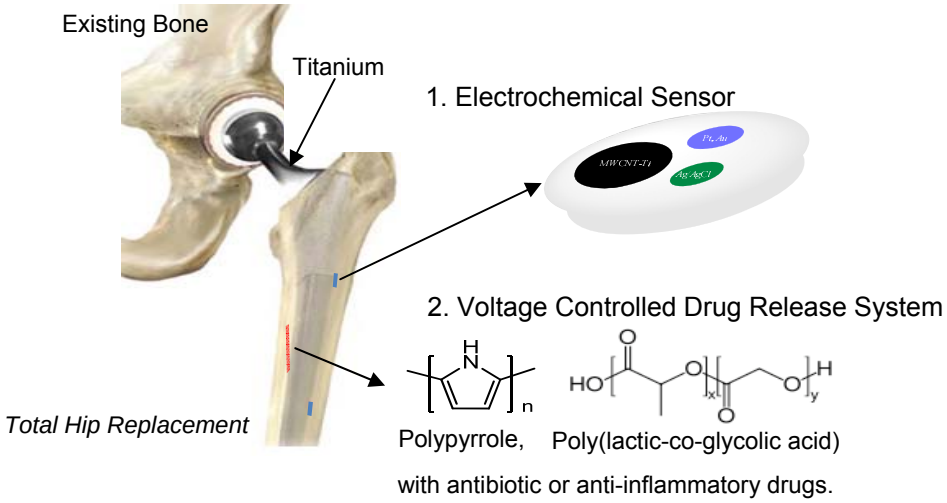

Figure 4-73. The proposed schematic of the presently designed sensor and associated components and the conductive polymer (PPy) coating along with a biodegradable polymer (PLGA) as a drug (P/S and/or Dex) carrier on the surface of a Ti total hip implant.

4.2 Anodized Nanotubular Titanium

As the first step towards making this sensor, commercially pure Ti was anodized to possess nanotubes. In the case of surface chemistry, oxidized layers of to oxide (TiO_2) are formed on Ti surfaces simply through their exposure to air and/or physiological fluids [1]. After implantation, oxidized Ti surfaces bind with structural water, forming $–O^-$ and $–OH^-$ sites which possess a weak negative charge at physiological pH. Therefore, this oxidized layer provides a kinetic barrier that prevents Ti from corroding and provides bone implant materials the ability to promote protein adsorption and cellular adhesion leading to osteoblast calcium phosphate crystal formation. However, the implantation of commercially pure Ti still has a high failure rate clinically due a lack of osseointegration or loosening of implants, and in order to increase their anti-corrosive

and biocompatibility properties, surface modification should be employed to further improve Ti for orthopedic applications [2, 3].

For example, the topography of Ti surfaces can be modified in order to increase biologically-inspired nanometer surface roughness for promoting select protein adsorption, osteoblast attachment, and eventual osseointegration [4]. Anodization is one of the surface modification techniques that can be used to create nanofeatures on Ti. Results by others from surface analysis by Raman scattering revealed that unanodized (commercially pure) Ti contains mainly anatase TiO_2, whereas anodized Ti mainly contains both anatase TiO_2 and Ti_2O_3 [3]. Osteoblast responses on anodized Ti were enhanced more than on unanodized Ti due to higher surface roughness, hydrophilicity, and vitronectin/fibronectin adsorption [5-7].

As recent research shows, nanometer surfaces on anodized Ti can be created by employing two-electrodes electrochemically in an acidic solution to enhance osteoblast adhesion [6]. In that study, Ti was anodized to create nanotube-like pores, in which Zhu et al. have shown that such anodized nanotubular Ti possesses higher surface energy and improved wettability compared to unanodized Ti [1]. Also, Huang et al. showed that the number of osteoblast-like U-2 OS cells adherent on a network-structured TiO_2/Ti_2O_3 layer (10-300 nm thickness) formed on Ti substrates by employing a three-electrode electrochemical technique in an alkaline solution, increased more than 1.4 times when compared to untreated Ti substrates [3]. Chiang et al. showed that anodized Ti (with nanopores 65±33 nm and 94±48 nm in diameter), created in a 5 M NaOH electrolyte solution and by varying the current, enhanced bone marrow stem cell growth after 28 days *in vivo* compared to unanodized Ti [8]. Histology highlighted the formation of osteocyte-like cells in bone marrow stem cell-formed tissues, and the presence of osteopontin (one of the makers for osteogenic differentiation) was confirmed

by immunofluorescent staining. In that study, bone marrow stem cells were modified to express a green fluorescent protein (GFP) by retroviral transduction. After 28 days *in vivo* with bone marrow stem cells, the GFP signal on anodized Ti in mice were much higher (indicating better cell growth) than on unanodized Ti (Figure 4-74).

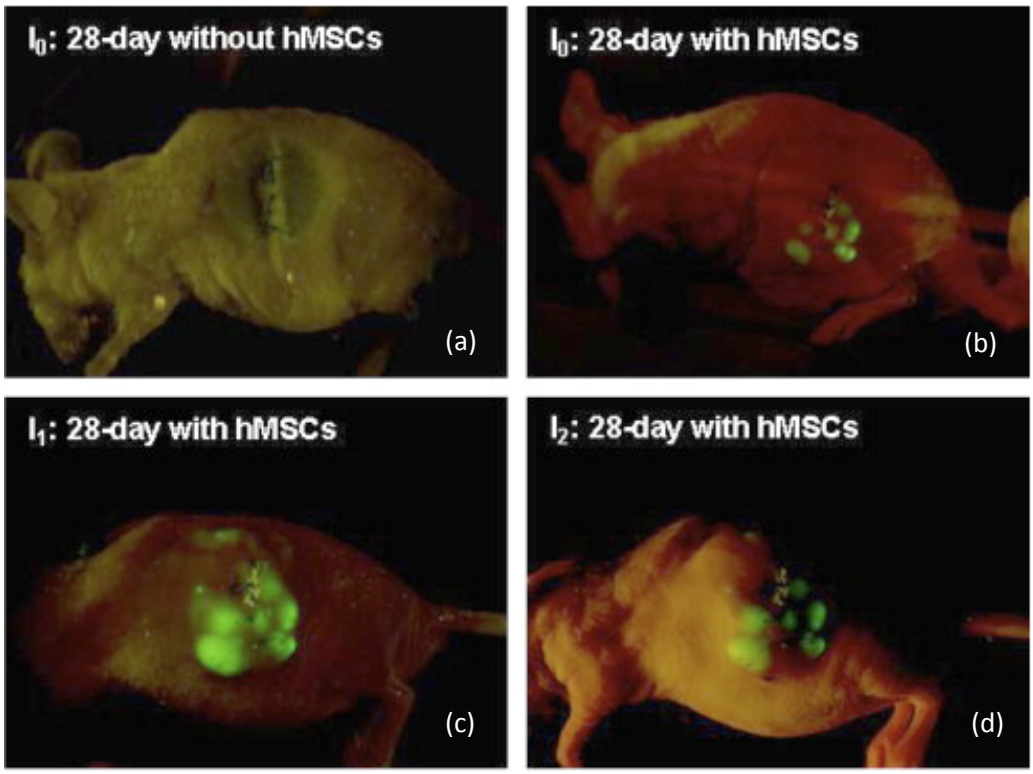

Figure 4-74. *In vivo* bone marrow stem cell growth (hMSCs) on: (a) Ti (without hMSCs), (b) Ti with hMSCs), (c) anodized Ti (with hMSCs) with a nanopore size of 65±33 nm, and (c) anodized Ti (with hMSCs) with a nanopore size of 94±48 nm, at a subcutaneous site under the back skin of nude mice after 28 days [8].

To fundamentally understand why bone formation is enhanced on anodized nanotubular Ti, Yao et al. demonstrated greater initial vitronectin and fibronectin adsorption from serum leading to greater osteoblast functions (such as alkaline phosphatase and calcium deposition) on anodized compared to unanodized Ti [6]. Since vitronectin and fibronectin are proteins which mediate osteoblast functions *in vitro* [9], different surface energetics between anodized and unanodized Ti which promotes optimal protein adsorption (vitronectin/fibronectin) are important for greater osteoblast functions [7].

Another advantage of anodized nanotubular Ti is for a drug eluting, providing a sustain release of drugs from nanotubes for local drug delivery to bone implants. Since delivering drugs on the interface of an implant is an effective way to deliver drugs (such as antibiotic or anti-inflammatory drugs), Popat et al. developed drug eluting protocols from anodized nanotubular Ti to release gentamicin (amino-glycoside antibiotic) [10]. In a loading step, gentamicin solution was pipetted onto the nanotubes surface and vacuum dried at room temperature for two hours, and repeated after obtain about 200, 400, and 600 μg of gentamicin in the nanotubes. Further, the osteoblast adhesion and proliferation on anodized nanotubular Ti with and without gentamicin were similar suggesting that the drug was not negatively influencing osteoblast interactions with the anodized Ti with gentamicin. The entire drug was eluted from nanotubes loaded with 400 μg of gentamicin within 90 minutes and 600 μg of gentamicin was released by almost 150 minutes.

4.3 Multiwalled Carbon Nanotubes

4.3.1 Biocompatibility and Toxicity

Researchers have further utilized the cytocompatibility properties of carbon nanofibers (CNFs with diameters less than 100 nm) by patterning to promote bone formation to match that of the natural anisotropic arrangement of collagen and hydroxyapatite in long bones of the body [11]. Such studies report higher adsorption of fibronectin and subsequently adhesion of osteoblasts on CNFs by approximately 300% compared to polyurethane surfaces without patterned CNFs. In addition, a novel adaptation of the standard surface-enhanced Raman Scattering technique provided additional evidence of increased unfolding of vitronectin (and, thus, exposure of cell adhesive epitopes) on nanoparticulate versus microparticulate ceramics (such as alumina), possibly promoting the availability of specific epitopes (such as Arginine-Glycine-Asparitc acid (RGD)) to increase osteoblast adhesion *in vitro* [12]. Thus, numerous studies have shown that nanomaterials, including CNFs, promote the adsorption and bioactivity of numberous proteins important for bone formation.

In this thesis, MWCNTs grown out of anodized nanotubular Ti were investigated for osteoblast adhesion and differentiation. The CVD process was used to grow MWCNTs out of anodized nanotubular Ti for an optimal time period (30 minutes) in the presence of C_2H_2 gas. After this process, the as grown-MWCNTs on anodized nanotubular Ti formed a flat surface at the microscale. The CVD growing time was extened to an hour to allow MWCNT growth to cover the anodized nanotubular Ti. However, there were some regions of the MWCNTs grown out of the anodized Ti substrates (for 30 minutes) that were not flat, leading to an observation that osteoblasts adhered after four hours, for example, on two different heights of MWCNTs (Figure

3-54 and Figure 3-55); this may have influenced results of this study. However, osteoblasts were observed at a higher cell density on MWCNT-Ti than unanodized Ti and anodized Ti after four hours of culture, as shown in Figure 3-52, Figure 3-53, Figure 3-54, and Figure 3-55. At this it is not clear which regions on the MWCNT-Ti samples were favorable or unfaborable for osteoblast adhesion. Importantly, though, Zanello et al. observed a thin neurite-like cytoplasmic protrusion from osteoblasts that reached nanotube bundles after cell culture for five days. Thus, the micro/nanotopography of MWCNTs can affect osteoblast responses in order to promote bone formation [13].

Clearly, measuring only cell densities is not enough to determine cytocompatible properties of bone implant materials. Alkaline phosphatase is a marker of early osteoblast differentiation, which is used to form a mineralized extracellular matrix (ECM) as a consequence of osteoblastic differentiation (Figure 4-75). Calcium mineral deposition measurements also help to determine osteoblast differentiation into calcium producing cells (Figure 4-75). The results of this study showed that the markers of osteoblast differentiation, alkaline phosphatase activity and calcium deposition, increased when osteoblast were cultured on MWCNTs grown from anodized nanotubular Ti compared to anodized nanotubular Ti without MWCNTs, unanodized Ti, and carbon nanopaper (control) after 21 days (Figure 3-56).

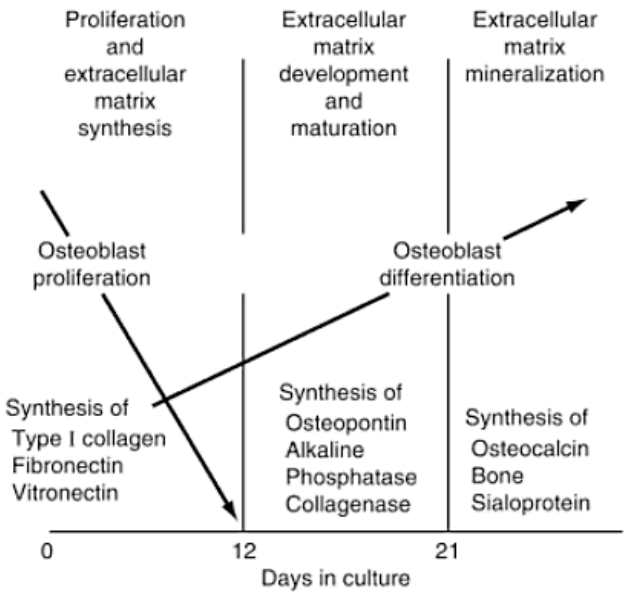

Figure 4-75. The differentiation stages that osteoblasts complete after adhesion to an implanted biomaterial. These stages are proliferation and extracellular matrix synthesis, extracellular matrix development and maturation, and extracellular matrix mineralization [14].

Moreover, chemical surface modifications were not conduct after growing MWCNTs on anodized nanotubular Ti via the CVD process. In this thesis, MWCNTs, nonfunctionalized or 'as-grown' (AG-) MWCNTs, were used in osteoblast cultures. Whereas in the study of Zanello et al., glass cover slips with positively and/or negatively charged functional groups (-NH_2 or -COOH) on SWCNTs were used for culturing osteoblasts. SWCNTs on glass formed a flat microtopography, whereas MWCNTs had a non-uniform microtopograhy which varied in length [15, 16]. It was observed that these surface modifications of electrically neutral SWCNTs functional with -PEG, nonfunctionalized AP (as-prepared)-SWCNTs, and nonfunctionalized AP-MWCNTs were more suitable for osteosacroma ROS 17/2.8 cell growth [16]. Nonfunctionalized AP-MWCNTs

sustained higher cell growth below 15% than functionalized MWCNTs. This work further supported the high cytocompatibility properties of MWCNTs.

In addition, Lovat et al. showed that CNTs also improve neural signal transfer and supported dendrite elongation and cell adhesion *in vitro* [17]. CNTs also have been shown to support smooth muscle cell [18] and fibroblast functions [19]. Smooth muscle cells were incorporated in collagen-CNT composites and cell viability was consistently above 85% after three and seven days of culture. However, after three days of culture, smooth muscle cell density was lower in collagen-CNT composites than pure collagen and statistically unchanged after seven days of culture [18]. Most of the fibroblasts had adhered to the MWCNT-based 3D network after one day of culture and most of the surface of the MWCNT-based 3D network was hidden beneath the cell layer after seven days of growth (Figure 4-76) [19].

Moreover, osteoblasts cultured on PLGA and CNTs composites demonstrated that the number of osteoblasts and calcium deposition by osteoblasts were increased after electrical stimulation (10 μA at 10Hz) for six hours a day. There was a 46% increase in osteoblast proliferation after two days, a 307% increase in the concentration of calcium deposition after 21 days, and an upregulation of mRNA expression for collagen type-I after one and 21 days when compared to PLGA alone [20].

Jia et al. found that increasing dosages of multiwalled CNTs led to the cytotoxicity of alveolar macrophages, which stand as the guardian of the alveolar-blood interface (serving as the front line of cellular defenses against respiratory pathogens), after six hours [21]. Ninety percent impurity of SWCNTs at a dosage of 3.06 $\mu g/cm^2$ led to necrosis and degeneration of macrophages *in vitro*, however, SWNTs significantly impaired phagocytosis of alveolar

macrophages at a low dosage of 0.38 μg/cm^2. Moreover, SWCNT particles have been reported to be toxic to human keratinocytes (which are stratified, squamous, epithelial cells that comprise skin and mucosa, and prevent the entry of toxic substances from the environment and the loss of important constituents from the host) since SWCNT particles activate NF-κB causing stress-related kinases (an enzyme that catalyzes the transfer of a phosphate group from ATP to a specified molecule) [22].

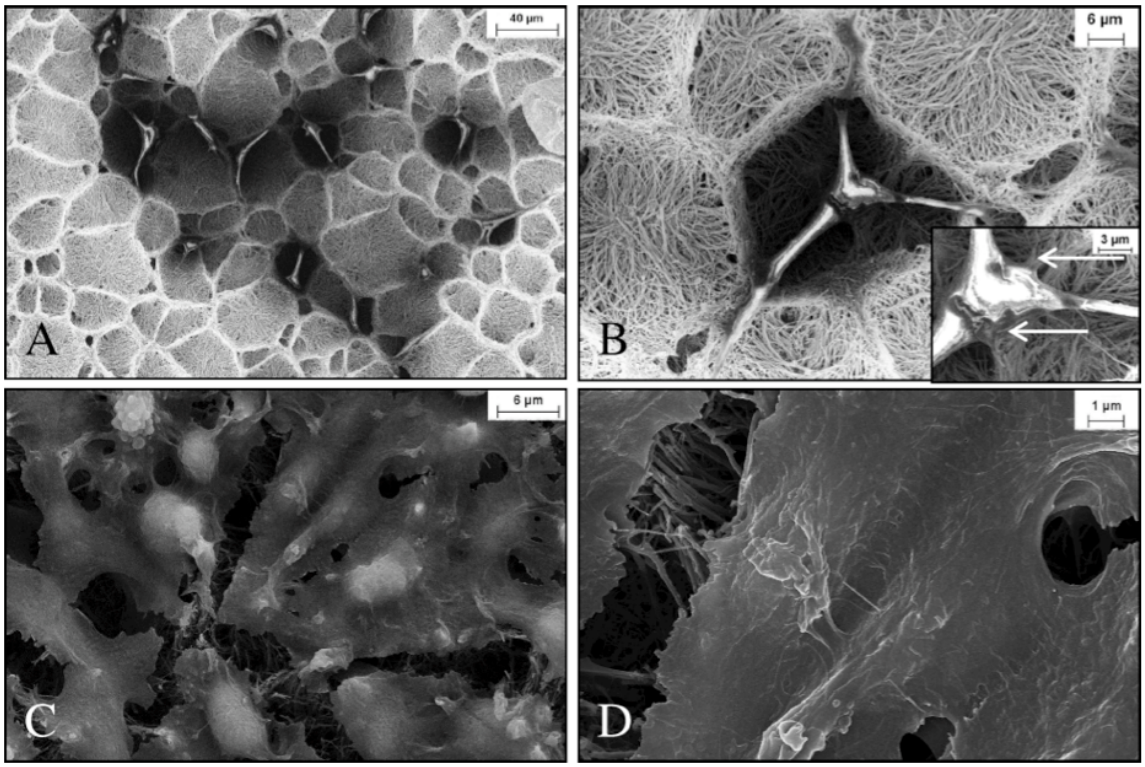

Figure 4-76. SEM of fibroblasts growing on a MWCNT-based 3D network: (a) and (b) after one day of culture, (c) and (d) after seven days of culture. (b) Isolated large stretched cells were found with elongated cytoplasm projections attached to the walls of the CNT-bundle cavities. The arrows indicate that cells appeared to attach to the bottom of the cavities by shorter projections

arising from their lower surfaces. (c) and (d) fibroblasts had formed a confluent layer covering the surface of the network [19]. Scale bar in (a) is 40 μm, in (b)-(c) is 6 μm, and (d) is 1 μm.

Although this present study used cobalt as a catalyst, osteoblasts cultured on MWCNT-Ti *in vitro* after 21 days increased calcium deposition and alkaline phosphatase activity compared to anodized Ti and commercially pure Ti. This is even though the cytotoxicity of cobalt ions *in vitro* has been reported showing that human MG-63 osteoblast numbers decreased in a time- and dose-dependent manner, with Co^{2+} more toxic than Cr^{3+} for a concentration of 0.01, 0.1, and 1 mg/ml [23]. Specifically, MG-63 proliferation decreased after 24 hours by 40% and 72 hours by 50% with 10 ppm of cobalt compared to without using cobalt. Another research project demonstrated that cobalt was toxic to both SaOS-2 and MG-63 osteoblasts, and inhibited the production of alkaline phosphatase at concentrations of 1.0 mg/ml after 24, 48, and 72 days [24]. However, cobalt at a concentration of 0.01, 0.1, 1 mg/ml most inhibited osteocalcin expression by culturing for 24, 48, and 72 days when compared to chromium and cobalt-chromium. Cobalt-chromium inhibited type-I collagen synthesis at a concentration of 0.01 (for SaOS-2) and 0.1 mg/ml (for MG-63), whereas, at a concentration at 1.0 mg/ml, cobalt-chromium inhibited osteocalcin expression by osteoblasts after 24, 48, and 72 days of culture.

4.3.2 Critical Surface Tension and Surface Energy

The critical surface tension is a useful quantity to characterize in possible bone implant materials because it is related to the degree of biological interaction of biomaterials and cells. In such models, relative biological interactions increase with a decrease in critical surface tension below

approximately 21 dynes/cm (Figure 4-77) [25]. In contrast, total surface energy usually depends on the properties of the liquid and the mathematic model being used. Following the Owens-Wendt method, this study showed that MWCNT-Ti and anodized nanotubular Ti had similar total surface energy (using only deionized water), even though the contact angles were different (Table 3-7 and Figure 3-32). Importantly, this is because the total surface energy of MWCNT-Ti contributed more to the dispersive surface energy (of carbon), while the majority of the total surface energy for anodized nanotubular Ti was due to the polar part (OH-groups). Coupled to the results of osteoblast proliferation and differentiation [26] (as measured by alkaline phosphatase acitivity and calcium mineral deposition) which was more on MWCNT-Ti than on anodized nanotubular Ti and commercially pure Ti after 21 days of cultures. Surface energy had a direct correlation to bone cell function here. Typically, proteins adsorb better on hydrophilic surfaces [27]. However, from the results of contact angle measurements, MWCNT-Ti was shown to be more hydrophobic (with double deionized water) than anodized nanotubular Ti and commercially pure Ti, or had more dispersive surface energy than anodized Ti and unanodized Ti according to the Owen-Wendt method. Therefore, total surface energy from a single probe liquid was not enough to predict cell responses on solid surfaces. Instead considering the Zisman method [28] (which uses several probe liquids with several liquid surface tensions) a prediction of cell responses on materials of interests can be improved. Another practical way to predict biological interaction is to measure protein (such as fibronectin) adsorption on high energy surfaces by an enzyme-linked immunosorbent assay to explain subsequent cell functions [29].

Importantly, cell adhesion led by surface energy, for example, it was found that 50% of osteoblasts adhered more on hydroxyapatile, which had surface energy of 44 mJ/m^2, than calcium apatite, which had surface energy of 9 mJ/m^2 [30]. However, decreased surface energy

can lead to the increased adhesion of competitive cells (such as fibroblasts). For example, Price et al. suggested that on polycarbonate urethane-carbon nanofiber composites, high surface energy played little role in the adhesion of osteoblasts after one hour, instead the increased surface roughness and changed surface chemistry between polycarbonate urethane-carbon nanofiber composites and polycarbonate urethane alone were more important for osteoblast adhesion [31]. In contrast, an increased surface energy of polycarbonate urethane-carbon nanofiber composites decreased fibroblast adhesion after one hour *in vitro* when compared to Ti6AlV and CoCrMo alloys.

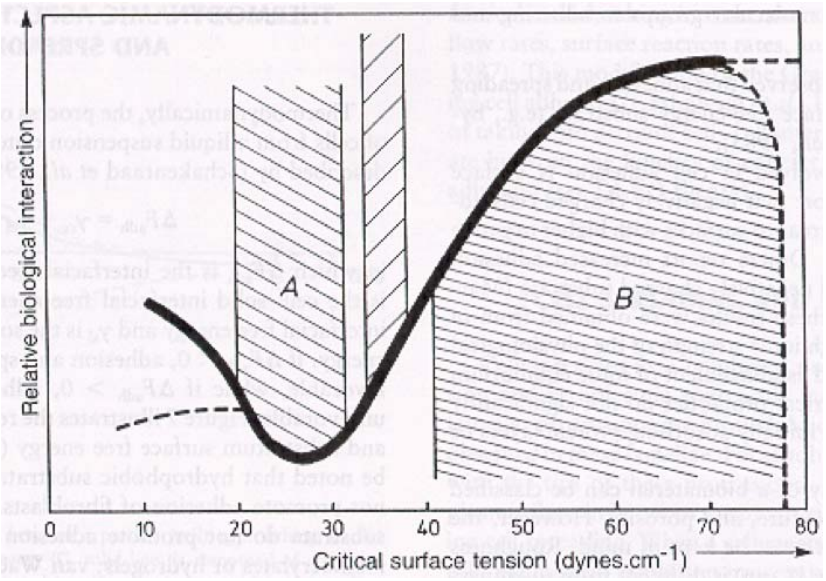

Figure 4-77. Relationship between the biological interactiveness and the critical surface tension of a biomaterial. Area "A" represents a non-adhesive zone between 20 and 30 mJ/m^2 (dynes/cm) of critical surface tension. The area marked as "B" represents biomaterials with good adhesive properties [27].

For the electrochemical perspective of carbon nanotubes (CNTs), a strong connection between CNTs and metallic substrates is needed for nanosensor applications [32]. In order to form a robust interconnection, CNTs were anchored into the pores of commercially pure Ti in this study. Moreover, CNTs have the capability of enhancing electron transfer for electrochemistry applications (such as biosensors [33]). A stronger connection will reduce resistance between the substrate and CNTs [34] leading to an increase in current passing through them which would utilize the electrochemical sensing capability of an electrode or transducer.

4.3.3 Electrochemical Behavior of the $Fe^{2+/3+}$ Redox Couple on Ti, Anodized Ti, and MWCNT-Ti

A goal of this study was to not only determine cell functions on the sensors developed, but also determine if they can sense bone growth. As a first step, the electrochemical behavior of the Fe^{2+}/Fe^{3+} redox couple was investigated. Since the $Fe(CN)_6^{4-/3-}$ redox system (with an exhibition of a heterogeneous one electron transfer (*n*=1)) is one of the most extensively studied redox couples in electrochemistry [35], it was tested here to determine the performance of MWCNT-Ti electrodes. Although the area of the working electrode was constant in the presence of MWCNTs, the overall surface area and the electroactivity of the surface increased [36]. MWCNTs acted as a nanobarrier between the titanium oxide layer, which was its growth template, and the electrolyte solution. The surface atoms or molecules of MWCNTs played an important role in determining its bulk properties due to their nanosize effects [37]. A large surface, corresponding to the greater electrocatalytic activity, confers the catalytic role on the MWCNTs in the chemical reaction. Well-defined and persistent redox peaks are shown in Figure

3-34c, confirming the increase of electron transfer and higher electrochemical activities at the MWCNT-Ti surface. Cyclic voltammetry was performed with a glassy carbon electrode (GCE; Bioanalytical) and a platinum electrode (PTE; Bioanalytical), and it also showed ΔE_p>59/n mV (Figure 3-38). Importantly, at the same scan rate, the CV of GCE and PTE showed the similar redox reactions but with more widely separated anodic and cathodic peaks, confirming the performance of the MWCNT-Ti electrode.

However, in Figure 3-34a and Figure 3-34b, the Ti and anodized Ti did not show any redox peaks. This is due to the inert inhibiting property of the titanium oxide with respect to electron transfer. Figure 3-34 shows that the commercially pure Ti has less capacitance than MWCNT-Ti. The capacitance relationship is derived from: $i = C\left(\frac{dv}{dt}\right)$, where $\frac{dv}{dt}$ is a scan rate [35]. Hence, the capacitance between the working and reference electrodes during cyclic voltammetry was calculated by dividing the current in CV with respect to the specific scan rate, as shown in Figure 3-34d and Figure 3-36d. In summary, the electrochemical response of the MWCNT-Ti electrode provides a higher charge transfer than the Ti and anodized Ti electrodes.

Other studies have shown promising results when using CNT-modified electrodes in biosensing, since MWCNTs have good electrochemical characteristics as electron mediators and adsorption matrices [38-51]. For example, Harrison et al. reported that CNTs offer a promising method to enhance the detection sensitivity because they have high signal-to-noise ratios [52]. The structure-dependent metallic character of CNTs should allow them to promote electron-transfer reactions for redox processes, which can provide the foundation for unique biochemical sensing systems at low over-potentials [33]. The electrolyte-electrode interface barriers are reduced by CNTs because they facilitate double-layer-effects [53]. Typically, when the

supporting electrolyte is in excess, at least a hundred-fold greater than the active electrolyte [54], the charge in the electrolyte solution causes the Debye layer (a charge layer around an electrode and next to a diffuse layer) to be more compact. Therefore, this compact layer can rapidly exchange electrons between electroactive proteins and the surface of a MWCNT-Ti electrode. This can be the reason sharpened cathodic and anodic peaks were observed in CV when using MWCNT-Ti electrode for electrochemical sensing appliactions, as shown in Figure 3-34c, Figure 3-35c, Figure 3-36b, and Figure 3-37a.

4.3.4 Sensing Bone Growth: Electrochemical Behavior of Osteoblast Secreted Protein Redox on Ti, Anodized Ti, and MWCNT-Ti

Since the result from the $Fe^{2+/3+}$ confirmed the utility of MWCNT-Ti as an electrode in order to detect a redox couple, different concentrations of calcium deposited by osteoblasts after 7, 14, and 21 days of culture were further tested on the novel sensor. In Figure 3-35c and Figure 3-36a, CV showed well-defined redox peaks from the contents of the osteoblast extracellular matrix. The more HA deposited and synthesized by osteoblasts, the higher the calcium and protein concentration. Therefore, it is likely that the supernatant after 21 days has higher protein concentrations than the solutions after 7 and 14 days, leading to stronger redox reactions and higher capacitance between the electrode surfaces. In addition, a measurement of the redox reactions when oxygen was dissolved in the electrolyte solution showed that the peak currents were negatively shifted.

The reduction of Ca^{2+} to Ca crystal (nucleation) typically is expected with the reduction current for a negative potential. However, a positive feedback IR compensation (IRC) is needed

to be applied in order to drive the oxidation current to dissolve the Ca crystal into Ca^{2+}. However, an overpotential more than -1 V (IRC = 0.771 Ω; melting temperature = 900°C; scan rate = 50 mV/S) is required [55]. Since IRC and such temperatures were not used in this study, thus, the diffusion-controlled behavior (which can occur to electrochemically deplete calcium cations near the electrode surface) was not achieved here. In addition, the reduction and oxidation of titanium oxides, which are the reaction counterparts of the calcium redox reaction, appeared at the positive potential between 0 and 0.25 V, respectively.

The PBS buffer contained phosphates were used in cyclic voltammetry for Ti, anodized Ti, and MWCNT-Ti electrodes. The metal orthophosphate ions exhibited high stability to reduce from P(V) (such as PO_4^{3-}, PO_4^{-}) to P(III) and further to P(I). However, there were not any peaks in the potential range of -1 to 1 V that corresponds to calcium or phosphate redox reaction (Figure 3-38 and Figure 3-39). This is because the redox reactions of either calcium ions or phosphate did not occur here due to the absence of these peaks. Thus, the redox peaks appeared when only using the MWCNT-Ti electrode maybe because of the reduction and oxidation of proteins from the osteoblast extracelluar matrix.

The shift of the redox current and potential may have also been influenced by the pH of the electrolyte solution and by the different amount of proteins dissolved from the extracelluar matrix deposited by osteoblasts. At the potential range between -1 to 1 V, cyclic voltammetry of the MWCNT-Ti electrode was performed in the dissolved extracelluar matrix solution, as a result of the H^+ reduction peak at the potential between -0.5 to -0.8 V, as shown in Figure 3-39. Moreover, the H^+ reduction peak still appeared after cyclic voltammetry decreased to -0.5 to 0.5 V and to -0.35 to 0 V.

However, when using the sweep voltage to -1 to 1 V, mixed redox peaks with two oxidation- and two reduction-peaks appeared (Figure 3-39). Since the process involved more than one electron transfer, more than one redox reaction can be observed in CV. Each peak from the redox couple was unequal in faradic current magnitude and potential. The second oxidation peak, as shown in Figure 3-39a and Figure 3-39b, was observed at 236 mV for MWCNT-Ti, 405 mV for GCE, and -33 mV for PTE, all with a scan rate of 100 mV/s. However, at the GCE and the PTE electrode, the second reduction did appear, while MWCNT-Ti showed two well-defined redox reactions. Thus, it can be concluded that the MWCNT-Ti electrode had a higher electron transfer than the GCE and the PTE. Therefore, it was hypothesized that the proteins secreted by osteoblasts were involved in these redox reactions.

The redox peaks were observed due to the fact that the MWCNT-Ti sensor promoted the electrochemical reactions. Typically, when the carbon bonds of proteins changed due to protein adsorption, irreversible organic redox couples occurred, whereas configurations of ions (such as Ca^{2+}, PO_4^{3-}, and OH^-) remained unchanged and promoted redox reactions [56]. However, the MWCNT-Ti electrode provided a relatively specific surface for proteins to bind reversibly (observed from cyclic voltammograms) by diffusion retaining its ability to repeatedly determine tissue growth. In addition, a negative shift of faradic potentials was observed when using MWCNT-Ti electrode, due to the acidic effect of HCl used to dissolve osteoblast extracellular matrix proteins. The protein redox reaction was also dependent on the pH of the electrolyte solution (acidic or basic) [57]. Thus, when using 0.6 N HCl with H_2O as a solvent effects protein structure dissolved in the electrolyte, leading to redox peak shifting into the negative potential, as shown in Figure 3-35b, Figure 3-36c, and Figure 3-37a. In summary, it is clear that the

proteins from the extracellular matrix can be detected with the electrochemical response of the MWCNT-Ti electrode.

The formation of bone matrix minerals first depends on achieving a critical concentration of calcium and phosphorus. Then, the aggregation of phospholipids, anionic proteins, as well as calcium and phosphorus occurs in nucleation pores that are in the 35 nm “hole-zones” between collagen molecules [58]. The addition of calcium, phosphate, and hydroxyl ions contributes to the growth of crystalline hydroxyapatite. However, the crystals are not pure since they also contain carbonate, sodium, potassium, citrate, and traces of other elements, such as strontium and lead. The imperfection of hydroxyapatite contributes to its solubility, which plays a role in the ability of osteoclasts to resorb the mineral phase. Although osteoblasts synthesize type I collagen, which is the predominant organic component of bone, type III/V/VI collagen also exists in bone. Collagens play a role in bone mineralization; the calcium crystals associate with the collagen fibrils in bone. Moreover, non-collagenous proteins in bone (such as growth factors, osteocalcin, osteopontin and osteonectin) and proteins in serum and other tissues (such as fibronectin, vitronectin, and laminin) absorb into the mineral component of bone during bone growth. These components are directly involved in the generation and maintenance of bone health. For example, osteonectin is glycoprotein in bone that binds calcium and is secreted by osteoblasts during bone formation, initiating mineralization and promoting mineral crystal formation [59]. Osteocalcin is a non-collagenous protein, secreted by osteoblasts, and is thought to play a role in the mineralization and calcium ion homeostasis. Osteopontin plays an important role in anchoring osteoclasts to the mineral matrix of bones. Thus, not only minerals, but also other non-collagenous proteins, are broken down after dissolution with hydrochloric acid (HCl) as was used here to dissolve calcium deposited by osteoblasts. As such, a number of

unspecified proteins from the ECM deposited by osteoblasts were used when cyclic voltammetry was performed on MWCNT-Ti which may have contributed to the observed redox process. On an electrode surface, the native conformation of a protein may be retained (reversible or diffusion-controlled) or distorted (irreversible or adsorption-controlled), depending on the extent of the interactions (such as the electrostatic or covalent bonds) between them.

Importantly, bone resorption and remodeling involve the secretion of HCl by osteoclasts in the body [60]. Osteoclasts dissolve bone mineral by isolating a region of the matrix and then secreting HCl and proteinases (enzymes that break peptide bonds) at the bone surface (Figure 4-78), resulting in the bone acting as a reservoir of Ca^{2+}, PO_4^{3-}, and OH^- [61]. This is the likely reason that HCl is frequently used in laboratories to dissolve calcium minerals deposited on substrates by osteoblasts *in vitro*. Thus, after dissolving calcium deposited by osteoblasts with 0.6 N HCl, Ca^{2+}, PO_4^{3-}, and OH^- are present in the solution.

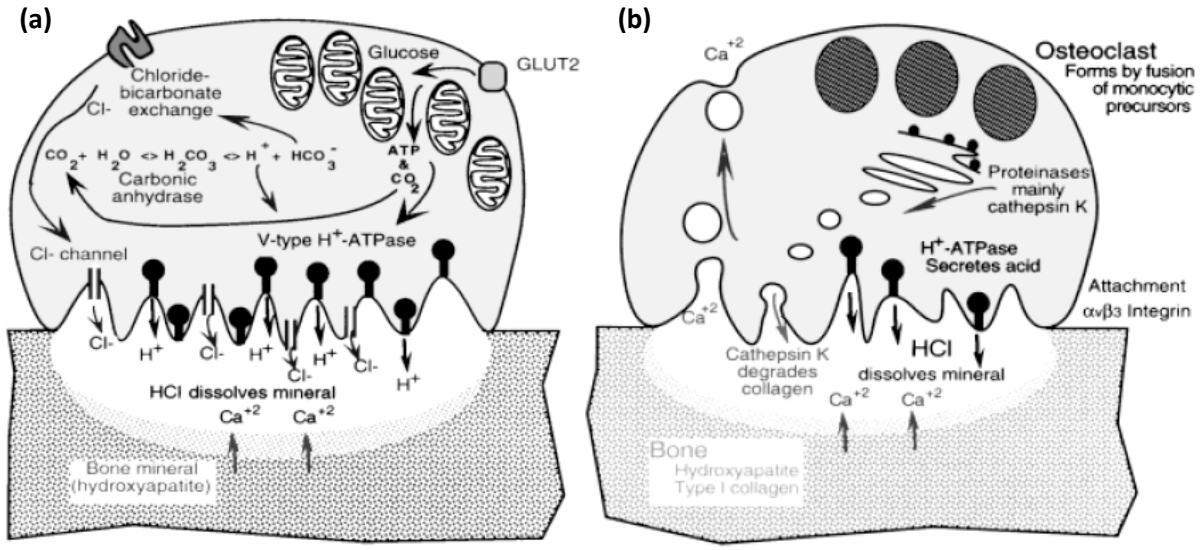

Figure 4-78. (a) The acid-transport pathway of the osteoclast. (b) Cellular specialization of the osteoclast. A multi-nucleated acid-secreting osteoclast is schematically represented as having three nuclei (shaded ovals) and a convoluted acid-secreting surface with vacuolar-type H+-ATPases. Osteoclast formation under some conditions requires contact with stromal cells, but there are exceptions. The integrin $\alpha_v\beta_3$ is required for the formation of the extracellular acid compartment. Synthesis and secretion of a novel thiol proteinase, cathepsin K, degrades bone collagen in an acid. Removal of degraded collagen and ionized calcium is by vesicular transcytosis [62].

In Figure 4-78, the osteoclast consumes large amounts of energy to drive HCl secretion, which produces calcium, water, and phosphate from the strongly basic calcium salt hydroxyapatite, $[Ca_3(PO_4)_2]_3CaOH_2$, that comprises bone mineral. The source of the energy is oxidative phosphorylation of glucose, taken up by a GLUT2 transporter, in mitochondria. Protons are derived from carbonic acid, a process facilitated by high expression of carbonic anhydrase II in osteoclasts. Proton secretion is by a massively expressed V-type H+-ATPase. This

electrogenic pump drives chloride co-secretion with cellular pH homeostasis by passive chloride-bicarbonate exchange at the contralateral surface coupled in turn to bicarbonate formation and chloride secretion[62].

The type of electrolyte used in sensor applications is important to the redox reaction because of the gained capacitance and the scan rate window are dependent on the electrolyte used [63]. Since electrolytes were not degassed with nitrogen or argon gas when performing cyclic voltammetry, the redox reactions in CV were related to the H_2O decomposition, which includes H^+ reduction and OH^- oxidation. The pH of the electrolyte also affects H_2O decomposition. In the case of an acidic 1 N HCl solution (without other electroactive molecules), the H^+ ions induced the formation of H_2 gas at -0.2 V as a result of the increased current during the reduction process [63]. It should be noted that in an alkaline 1 M KOH solution, OH^- ions resulted in the formation of O_2 gas at 0.7 V during the oxidation process. *In vivo* these decompositions may occur at the interface of the Ti implant due to the pH changes and the presence of H_2O and O_2.

4.4 Polypyrrole

4.4.1 Electrodeposition

To incorporate P/S or Dex into the PPy films, the electropolymerization or electrodeposition was performed using cyclic voltammetry with the scan rate of 100 mV/s from 0 to 1.1 V. Typically, the electrodeposition of PPy films occurs above 0.65 V, and the above increases voltage can affect the electrical conductivity and mechanical properties of PPy films. In this thesis, cyclic

voltammetry from 0 to 1.1 V was used to deposited PPy films on AuPd-Ti. In addition, MWCNTs were important in this study to allow for the electropolymerization of pyrrole on MWCNT-Ti; by contrast, commercially pure Ti required a thin conductive coating, in this case AuPd, to increase conductivity so that electrodeposition of PPy could occur. During electrodeposition, the charge of PPy was balanced by anions from the drugs (either P/S or Dex) added to the solution of 1 M PBS. The electropolymerization and doping reactions are shown in Figure 4-79.

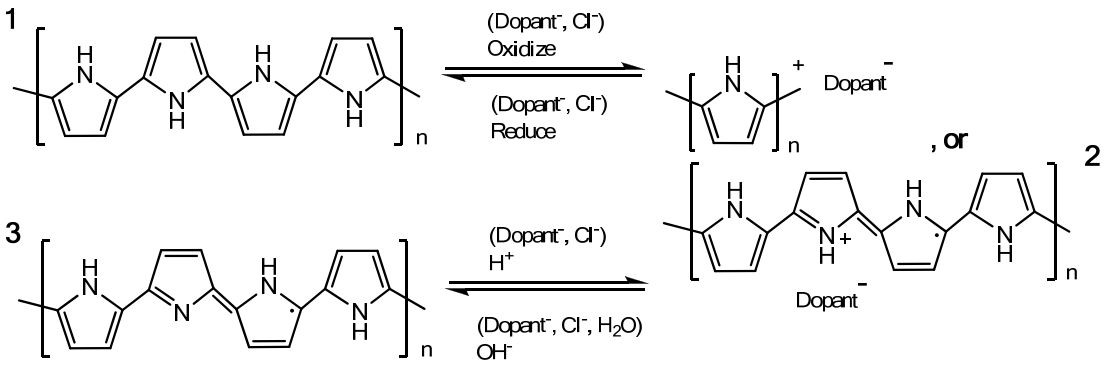

Figure 4-79. Reaction schemes proposed for: the redox mechanism between 1 (neutral reduced aromatic PPy) and 2 (oxidized polaronic PPy) and the acid-base mechanism between 1 and 3 (neutral deprotonated quinoidal PPy). The drug was either penicillin/streptomycin, or dexamethasone. Cl^- was contained in a PBS buffer at pH 7.2.

The electrodeposition of PPy by potentiodynamic (cyclic voltammetry) deposition had high electrochemical reactivity compared to potentiostatic deposition [64], and the necessary required redox peaks were attained with the cyclic voltammograms. The disordered effect obtained from the XPS experiments confirmed that the electrodeposited PPy can be considered as such a quasi network system. Moreover, the electrostatic interaction did not occur at specific

nitrogen sites but involved the whole pyrrole ring unit. This separation may be characteristic of two-dimensional PPy films, because of the inter- and intra-molecular interactions.

4.4.2 Mechanisms of Electropolymerization

In a deformable PPy chain, both polaron and bipolaron formation are possible on the polymer lattice. This change in the UV-vis spectra may indicate conformational changes in the PPy chains. The polarity of the solvent determines the arrangement of the PPy backbone, changing the absorption intensity and the peak shift after an applied sweep voltage and self-polymerization. PBS at pH 7.2 with anodic drugs exhibited some degree of polarity. As observed in Figure 3-30, the pyrrole monomers in PBS (without any drug) exhibited an absorption peak at 390 nm for 10 cycles of cyclic voltammetry, but no absorbance for 0 and 5 cycles. Furthermore, after 4 and 30 hours, the peak at 390 nm was still present without shifting. In the case of the PPy doped with P/S, the solution exhibited two characteristic absorption bands during electrical stimulation at 420 nm (polaron) and 585 nm (bipolaron). However, after allowing the stock solution to sit for 4 and 30 hours, the solution did not show any absorption peaks, which reflected the neutral state of PPy in the stock solution, and the absence of self-polymerization. In the case of the $PPyNH_2$ doped with Dex, the solution exhibited bands at 380 (polaron) and 540 nm (bipolaron) after 10 cycles of cyclic voltammetry. The PPy+Dex solution after 4 and 30 hours showed more intense absorbance than the solution which was measured immediately after electropolymerization. Peaks were found at approximately 415 nm for the polaron state and 580 nm for the bipolaron state in the stock solution (self-polymerization). Without electrical stimulation the process continued for 30 hours and appeared as a stronger polaron peak.

The intensity of absorption for the $PPyNH_2$+Dex solution was relatively low when compared with PPy+P/S. After only 5 cycles of cyclic voltammetry, the peak of absorbance for the polaron state was observed at 395 nm for PPy+P/S, but not for the $PPyNH_2$+Dex solution. After 10 cycles, bipolaron states were formed in both PPy+P/S and $PPyNH_2$+Dex stock solutions. The results from XPS analysis already showed, however, that the bipolaron states were not incorporated into PPy films because this study electrodeposited PPy films by applying only 5 cycles. The PPy+Dex after four hours showed peaks at 420 nm and 575 nm after 10 CV cycles, but only one peak at 585 nm after 5 CV cycles. After 30 hours, the PPy+Dex did not show any peaks after 10 CV cycles (the neutral polypyrrole), but the polaron peak was still apparent at 380 nm after 5 CV cycles. This suggests that the self-polymerization of pyrrole with Dex or P/S in PBS buffer cannot occur without an initial electrical stimulus. PPy doped with P/S or Dex needs initial energy to form the polymer structure. Furthermore, the presence of nitrogen bipolaron states in PPy films requires more electrodeposition time to allow the bipolaron nitrogens to integrate into the films in the present electrodepositing condition. Because the diffusion rate for recombination by the hopping of polarons into bipolarons was limited by the diffusion of the accompanying anion (P/S or Dex), this phenomenon of semiconducting PPy was slow enough to be observed by UV-vis spectrophotometry.

In summary, the results from UV-vis spectrophotometry showed that adding P/S during electropolymerization had a large influence, but that it did not affect self-polymerization. In contrast, Dex present in the PBS promoted self-polymerization, and the absorption peaks were mainly observed for the bipolaron state, while only the polaron state was observed at lower wavelengths during electropolymerization. Thus, PPy films can control the charge density and wettability through electropolymerization with the chosen drug and electrolyte solution.

4.4.3 Osteoblast and Fibroblast Responses

4.4.3.1 Surface Chemistry of Polypyrrole Films

Clearly, results of this study showed that the biological performance of PPy was dependent on its chemical characteristics (surface chemistry, charge density, etc.), its physical attributes (topography, roughness, etc.), the presence of bioactive factors, and mechanical properties (stiffness, etc.). In this study, the oxidative PPy[P/S]-Ti surface increased osteoblast and fibroblast adhesion more than neutral deprotonated PPy-Ti, which corresponded to a [−N=]/[−NH] ratio of PPy[P/S]-Ti being higher than that of the PPy-Ti. Wong et al. showed that applying -0.25 V (induced neutral state of PPy) to fibronectin-doped PPy films before endothelial culture decreased DNA synthesis in such endothelial cells and led to cell retraction [65]. Neutral PPy surfaces were reported to be less favorable to endothelial cells than oxidized PPy films [66]. Moreover, alginate-containing PPy enhanced arteriogenesis, specifically, increasing arteriole density within the infarct scar [67].

The results of this study showed that fibroblasts adhered more on commercially pure Ti than on PPy films containing −CO− groups, which were PPy[Dex]-Ti and PLGA-PPy[Dex]-Ti, than on PPy containing −NH− groups, which were PPy[P/S]-Ti and PPy-Ti. Moreover, fibroblast density was less on PPy[Dex]-Ti than PLGA-PPy[Dex]-Ti, because both had compositions of −NH− and −COOH− on PPy[Dex]. Functional groups like NH_2 and COOH can modulate fibrobalst adhesions. Faucheux et al. showed that human fibroblasts plated on COOH formed matrix fibrils significantly better because cell segregation of focal contact components (αv integrin subunits, phosphotyrosine proteins) and fibrillar adhesions (α5 integrin subunits, tensin) on COOH containing surfaces while the majority of fibroblasts on NH_2 did not [68].

In addition, surface chemistry and textured nanostructured surfaces can highly regulate fibroblast (soft tissue forming cells) adhesion. For example, Harris et al. showed that fibroblasts on proprietary anodized Ti were only seen closely to smooth areas [76]. Ungersböck et al. showed that anodized Ti with coarse surfaces had the thinnest soft tissue layer, and electropolished stainless steel plates induced statistically significant thicker soft tissue layers after implantation *in vivo* for three months [69]. Fibrous tissue formation in the gap between bone and the implant can loosen the implant. Therefore, the increased roughness of PPy films when compared to Ti could inhibit fibroblast adhesion. In this study, the results showed that fibroblasts adhered the most on commercially pure Ti when compared to PPy films, but not for osteoblasts. Moreover, cell adhesions can also affect from mechanical properties of biomaterials, since both cells have a different sensitivity towards surface stiffness [70]. PPy films were softer than commercial pure Ti, thus, the stiffness can also be influenced the fibroblasts and osteoblasts adhesion in this study.

For this study, the PLGA-PPy[Dex]-Ti had the highest osteoblast and fibroblast density among all other PPy films. XPS results showed that the −CO-contained groups, which were mainly present on PPy[Dex]-Ti and PLGA-PPy[Dex]-Ti, favored osteoblast and fibroblast adhesion. Therefore, osteoblasts and fibroblasts adhered more on the –CO– (carboxylic) containing surfaces, PPyDex-Ti and PLGA-PPy[Dex]-Ti (Figure 3-45, Figure 3-47 and Table 3-10). It is intriguing to wonder why. AFM analysis showed that among all samples, greater cell adhesion corresponded to higher PPy film roughness at the nanometer level (Figure 3-44). The roughness of both PPy-Ti and PPy[P/S]-Ti were not significantly different, and the number of fibroblast and osteoblast adhesion on both surfaces were comparable.

4.4.3.2 Bioactivity of Drugs

Not only are cells on biomaterials truly responsive to surface roughness, topography, chemistry, and mechanical properties, but also the bioactivity of a potentially released drug influences cell behavior. The results showed that P/S in PPy[P/S]-Ti had low cytotoxicity for osteoblasts; in other words, osteoblast density was not significantly different when compared to commercially pure Ti (p-value < 0.2). For other antibiotics, it was found that the cytotoxicity of vancomycin towards osteoblasts was lower than cefazolin, and aminoglycosides had good compatibility with vital tissue [71, 72]. Salzmann et al. demonstrated that at low cefuroxime concentrations (<250 μg/ml) there were no inhibiting effects towards human osteoblasts [73]. Moreover, osteoblast viability was not significantly different among gentamicin, fosfomycin, imipenem, and amphotericin loaded into hydroxyapatite composites (such as hydroxyapatite, plaster of Paris, and chitosan), as well as controls (without any antibiotic) [74]. Therefore, low antibiotics amount can be used for local delivery to provide enough bactericidal activity and show a possibility of a low cytotoxicity against osteoblasts or surrounding tissues. Moreover, the results here showed that PPy[Dex]-Ti promoted osteoblast adhesion and proliferation when compared to PPy-Ti and commercially pure Ti. As electrochemically-fabricated in the present study, local delivery of Dex from the implant surface not only decreased systemic toxicity of drugs, but it also promoted osteoblast function (adhesion and proliferation), as was seen from this study.

4.4.4 Electrically-Controlled Drug Releases: Influenced by Multiwalled Carbon Nanotubes

PPy can be electrodeposited with MWCNTs to improve a sensor conductivity, increase an electrode sensitivity, and prolong a drug release. Although it was found that PPy can be overoxidized and lose its electroactivity at higher potentials or when voltages are applied for long time periods [75, 76], CNTs can maintain and prolong the electroactivity of PPy due to their excellent conductivity properties. For example, Li et al. showed that MWCNT and overoxidized PPy composites exhibited excellent electrocatalytic properties when coated on glassy carbon electrodes, maintained electrode conductivity, and reserved stability [76]. Green et al. showed that by creating a composite polymer (PPy) layered with MWCNTs, electrochemical stability was improved by up to 50% in poorly performing films when subjected to CV for 400 cycles [77]. Even though cumulative drug releases from PPy-drug electrodeposited on AuPd-Ti were mainly investigated in this study, a step or constant voltage may apply to PPy-MWCNT-Ti to trigger drug release through the reduction of PPy (applying negative voltages).

The present study did not describe the electrochemical behavior, electrical conductivity, drug release profiles, and cell responses from PPy-MWCNT-Ti; this would be the focus of future studies. This study also demonstrated the electrodeposition of PPy on MWCNTs. However, it has been shown that the incorporation of PPy and MWCNTs produced high surface area, electrical conductivity, and electrochemical stability for neuronal interface implant electrodes [78]. A nanobiocomposite film consisting of PPy, functionalized MWCNTs, and glucose oxidase were electrochemical polymerized and used as glucose-sensing electrodes [79]. Also, in this study, MWCNT-Ti were cytocompatible with osteoblasts after 21 days of cultures *in vitro* [80].

4.5 Applications and Limitations

4.5.1 Multiwalled Carbon Nanotubes Grown Out of Anodized Nanotubular Titanium

The electrochemical experiments were performed without degassing with bubble nitrogen gas, which may result in an apparent background signal of current-voltage curves (CV). The redox reaction at MWCNT-Ti electrodes can depend on various ion sources, including reversible protein adsorption, dissolved oxygen, and HCl. However, the redox reactions of iron (II/III) and the osteoblast extracellular components occurred when using MWCNT-Ti, but not when using Ti or anodized Ti. Importantly, MWCNTs performed as the electrocatalysts for the oxidation and reduction of iron (II/III) and the extracellular components, which included various proteins and inorganic substances synthesized and deposited by osteoblasts. Moreover, MWCNTs have been used to modify electrodes to enhance the redox reactions of other biomolecules, such as DNA. Specifically, SWNCT with single-stranded DNA, used as a chemical sensor (DNA as the chemical recognition site and SWCNT field effect transistor as the electronic read-out component), were able to detect a variety of gases with consistent responses and fast recovery times [81].

The growth of MWCNTs from nanoporous metals and its surface modification can enhance many applications. For example, MWCNTs functionalized with thiol groups have been used for sensing aliphatic hydrocarbons (such as methanol and ethanol), forming unique electrical identifiers [47]. MWCNTs grown on silicon substrates with enhanced ionic conductivity were integrated with an unmodified plant cellulose as a film, and used as a supercapacitor with bioelectrolytes (such as biological fluid and blood) [82]. Such a MWCNTs-based device might also work here if used as a dry-body implant, such as to determine bone growth by the

detection of ionic movements *in vivo*. That is, after a hip implant insertion, blood and body fluids surround the Ti implant, creating a specific capacitance for Ti. Within one month, osteoblasts may deposit calcium, then the capacitance of the implant and bone tissue increases since the deposited calcium may surround the implant. Cell membranes also have electrical potential and perform redox processes [83, 84], and after 14 days *in vitro* the redox processes at the surface of Ti electrodes increased, thus it is likely that *in vivo* the electroactive surface of Ti is enhanced after bone tissue is formed. Moreover, this film can serve as a cathode electrode in a lithium ion battery. Interestingly, the supercapacitor and battery, derived from a MWCNTs-nanocomposite film, can be combined together to build a hybrid, or dual-storage battery-in-supercapacitor device [82]. The cytocompatible MWCNTs-device may be useful to combine with an orthopedic-implanted biosensor as passive energy storage.

Not only can an electronic circuit be powered by an implant battery (fabricated or self-integrated) within the implant material, but it also can be induced by an external power supply. For orthopedic application, telemetric devices started in 1966 and became imperative as a telemetric orthopedic implant in order to transmit a signal to an external device [85-90]. For example, Graichen et al. (2007) developed a new 9-channel telemetry transmitter used for *in vivo* load measurements in three patients with shoulder Ti endoprostheses [91]. The low radio frequency (RF) of the externally inductive power source generates power transmission through the implanted metal. At the end of the Ti implant, the pacemaker feedthrough rounds a single loop antenna to transmit the pulse interval signal, which is modulated at a higher RF by the microcontroller, to an external device. Then, the RF receiver of the external device synchronizes with the modulated pulse interval to recover the data stream and reports to a clinician. Either an implanted battery (electrical potentials or a telemetry system (RF was sent to activate the

electrical power) can supply the electrical power to a calcium-detectable chip inside the orthopedic implant for clinical use. An energy source energizes a telemetric-implanted circuit and allows it to transmit data to an external receiver to determine bone growth. The automatical-sensing concept for bone growth juxtaposed to orthopedic implants can also be applied to fight infection and scar tissue formation. The electrochemical biosensor may reduce the complexity of imaging techniques and patient difficulties to improve orthopedic implant efficacy.

4.5.2 Polypyrrole as a Drug Delivery System

Since PPy is a conducting polymer, PPy films can be used as drug eluting vehicles and electrically controling drug releases from PPy films on demand to obtain desirable drug bioavalibility. Electrochemical switching of PPy is accompanied by the movement of charged molecules in and out of the films allowing for the conduction of an applied electrical stimulus [78]. Therefore, conducting PPy can be exploited to develop an electrically-controlled drug delivery. PPy can be doped not only with antibiotics (P/S) and anti-inflammatory drugs (Dex), which was demonstrated in this thesis, but various biomolecules (e.g., growth factors, peptides, enzymes, antibodies, proteins, other drugs, etc.) to alter its biological, physical, chemical, and electrical properties to design controlled release for various biomedical applications [65, 92-99]. In addition, PPy can be coated on electrodes or integrated with implantable chips to introduce an electrical signal into the biological environment, or allow the preloading of drugs to obtain clinically controllable and predictable doses.

Typically an implant surgery is followed by series of drug therapies to prevent either infection of inflammation, and to induce appropriate integration of the implant with the natural tissue in the body [10]. The system toxicity and low bioavailability often is a result of the oral or intravenous delivery of antibiotic and anti-inflammatory drugs, requiring a series of medications in high doses. Drug delivery using PPy may be able to offer sequential drug releases with different regions of PPy-drug coatings and the degree of current passing through PPy films to control the type of drug release (Figure 4-80).

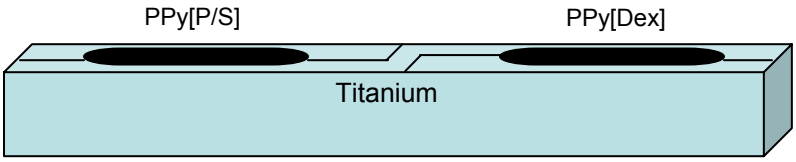

Figure 4-80. The drug delivery diagram proposed through the use of a conductive polymer (polypyrrole, PPy) embedded with penicillin/streptomycin (P/S) and dexamethasone (Dex).

After electrical stimulation, cracks and holes throughout the surfaces of the PPy films were observed in this study. The release of P/S and Dex was accelerated when the voltage triggered diffusion from PPy, causing swelling and contracting, which was observed as delaminating and brittle fracturing of the films. This poor mechanical stability in the long-term biological performance still needs to be evaluated but was addressed in this thesis. Some thoughts on how to deal with this are below.

Since the PPy film can be brittle and become difficult to mechanically manipulate, conjugation of $PPyNH_2$ with activated PLGA via EDC/NHS (via covalent bonds) may enhance the coating stability of the PPy film. The conducting $PPyNH_2$ backbone doped with Dex (inner layer) was bonded covalently with the PLGA-NHS (outer layer), trapping Dex within these two polymer layers. When the voltage was applied, the electrical force created pressure in the PPy layers, expelling the negatively charged drugs through the PLGA layer, and caused expulsion of PLGA degradation products, as observed in the PBS buffer. The degradability of PLGA-PPy[Dex]-Ti was not fully explored in this study, however, PLGA which undergoes hydrolysis (degradable via ester bonds) under physiological conditions may result in the biodegradability of the PPy. The erodible

forms of PPy have been developed to increase the scope of biomedical applications including neuron scaffolds and polymeric devices [100-102].

4.6 Closed-Loop Sensing System for Biomedical Applications

PPy can, thus, be doped not only with P/S and Dex, allowing for the preloading of drugs to obtain clinically controllable and predictable doses, but also various other biomolecules (e.g., growth factors, peptides, enzymes, antibodies, proteins, etc.) to alter its biological, physical, chemical, and electrical properties to design a controlled released system for biomedical applications [65, 92-98]. In addition, PPy can be coated on electrodes or integrated with implantable chips to introduce an electrical signal into the biological environment. This study showed that MWCNTs enhanced direct electron transfer to promote redox reactions of proteins (synthesized by osteoblasts *in vitro*) and ferri-ferro cyanide [103]. MWCNT-Ti sensors may determine whether healthy bone, infection, or inflammation is occurring on a Ti implant by generating distinct current-voltage profiles. Moreover, MWCNT-Ti enhanced osteoblast differentiation by increasing the alkaline phosphatase activity and calcium mineral deposition after 21 days of culture *in vitro* [80]. These results lay the foundation for developing intelligent orthopedic drug-delivery technologies that can utilize a closed-loop sensing and drug administration process based on that sensing information. Both MWCNT-based sensors and controllable drug delivery systems could be an excellent way to improve the lifetime of orthopedic implants, allowing implants to be free from bacteria, and reducing the susceptibility of implants to prolonged inflammatory responses.

References

1. Zhu X, Chen J, Scheideler L, Reichl R, Geis-Gerstorfer J. Effects of topography and composition of titanium surface oxides on osteoblast responses. Biomaterials 2004 Aug;25(18):4087-4103.

2. Webster TJ, Ejiofor JU. Increased osteoblast adhesion on nanophase metals: Ti, Ti6Al4V, and CoCrMo. Biomaterials 2004 8;25(19):4731-4739.

3. Huang H-H, Pan S-J, Lai Y-L, Lee T-H, Chen C-C, Lu F-H. Osteoblast-like cell initial adhesion onto a network-structured titanium oxide layer. Scripta Materialia 2004 11;51(11):1017-1021.

4. Liu H, Webster TJ. Nanomedicine for implants: A review of studies and necessary experimental tools. Cellular and Molecular Biology Techniques for Biomaterials Evaluation 2007 1;28(2):354-369.

5. Yao C. Surface Modification of Titanium by Anodization for Orthopedic Applications: Purdue University; 2005.

6. Yao C, Perla V, McKenzie JL, Slamovich EB, Webster TJ. Anodized Ti and Ti6Al4V Possessing Nanometer Surface Features Enhances Osteoblast Adhesion. Journal of Biomedical Nanotechnology 2005;1:68-73(66).

7. Yao C, Webster TJ. Anodization: A Promising Nano-Modification Technique of Titanium Implants for Orthopedic Applications. Journal of Nanoscience and Nanotechnology 2006 October 2006;6:2682-2692(2611).

8. Chiang C-Y, Chiou S-H, Yang W-E, Hsu M-L, Yung M-C, Tsai M-L, et al. Formation of TiO_2 nano-network on titanium surface increases the human cell growth. Dental Materials 2009;In Press, Corrected Proof.

9. Anselme K. Osteoblast adhesion on biomaterials. Biomaterials 2000 4;21(7):667-681.

10. Popat KC, Eltgroth M, LaTempa TJ, Grimes CA, Desai TA. Decreased Staphylococcus epidermis adhesion and increased osteoblast functionality on antibiotic-loaded titania nanotubes. Biomaterials 2007;28(32):4880-4888.

11. Dongwoo K, Michiko S, Rachel LP, Alexander ER, Thomas JW. Selective adhesion and mineral deposition by osteoblasts on carbon nanofiber patterns. 2006;1(1):65-72.

12. Christenson EM, Anseth KS, van den Beucken JJ, Chan CK, Ercan B, Jansen JA, et al. Nanobiomaterial applications in orthopedics. Journal of orthopaedic research : official publication of the Orthopaedic Research Society 2007 Jan;25(1):11-22.

13. Taton TA. Nanotechnology: Boning up on biology. Nature 2001 08/02;412(6846):491-492.

14. Laurencin CT, Nair L. Nanotechnology and Tissue Engineering: The scaffold: CRC Press, 2008.

15. Zanello LP. Electrical properties of osteoblasts cultured on carbon nanotubes. Micro & Nano Letters 2006 July 2006;1(1):19-22.

16. Zanello LP, Zhao B, Hu H, Haddon RC. Bone Cell Proliferation on Carbon Nanotubes. Nano Letters 2006;6(3):562-567.

17. Lovat V, Pantarotto D, Lagostena L, Cacciari B, Grandolfo M, Righi M, et al. Carbon Nanotube Substrates Boost Neuronal Electrical Signaling. Nano Letters 2005;5(6):1107-1110.

18. MacDonald RA, Laurenzi BF, Viswanathan G, Ajayan PM, Stegemann JP. Collagen-carbon nanotube composite materials as scaffolds in tissue engineering. Journal of biomedical materials researchPart A 2005 Sep 1;74(3):489-496.

19. Correa-Duarte MA, Wagner N, Rojas-Chapana J, Morsczeck C, Thie M, Giersig M. Fabrication and Biocompatibility of Carbon Nanotube-Based 3D Networks as Scaffolds for Cell Seeding and Growth. Nano Letters 2004;4(11):2233-2236.

20. Supronowicz PR, Ajayan PM, Ullmann KR, Arulanandam BP, Metzger DW, Bizios R. Novel current-conducting composite substrates for exposing osteoblasts to alternating current stimulation. Journal of Biomedical Materials Research 2002 Mar 5;59(3):499-506.

21. Jia G, Wang H, Yan L, Wang X, Pei R, Yan T, et al. Cytotoxicity of Carbon Nanomaterials: Single-Wall Nanotube, Multi-Wall Nanotube, and Fullerene. Environmental Science & Technology 2005;39(5):1378-1383.

22. Manna SK, Sarkar S, Barr J, Wise K, Barrera EV, Jejelowo O, et al. Single-Walled Carbon Nanotube Induces Oxidative Stress and Activates Nuclear Transcription Factor-B in Human Keratinocytes. Nano Letters 2005;5(9):1676-1684.

23. Fleury C, Petit A, Mwale F, Antoniou J, Zukor DJ, Tabrizian M, et al. Effect of cobalt and chromium ions on human MG-63 osteoblasts in vitro: Morphology, cytotoxicity, and oxidative stress. Biomaterials 2006 6;27(18):3351-3360.

24. Allen MJ, Myer BJ, Millett PJ, Rushton N. The effects of particulate cobalt, chromium and cobalt-chromium alloy on human osteoblast-like cells in vitro. Journal of Bone and Joint Surgery - British Volume 1997 May 1;79-B(3):475-482.

25. Ratner BD. Biomaterials science : an introduction to materials in medicine: Amsterdam ; Boston : Elsevier Academic Press, Edition: 2nd ed; 2004.

26. Sirivisoot S, Yao C, Xiao X, Sheldon B, Webster T. Greater osteoblast functions on multiwalled carbon nanotubes grown from anodized nanotubular titanium for orthopedic applications. Nanotechnology 2007;18(36):365102.

27. Ratner BD. Biomaterials science : an introduction to materials in medicine. Amsterdam; Boston: Elsevier Academic Press, 2004.

28. Fox HW, Zisman WA. The spreading of liquids on low-energy surfaces, .2. Modified tetrafluoroethylene polymers. Journal of Colloid Science (US) Changed to J Colloid Interface Sci; Vol: 7 1952:Pages: 109-121.

29. Zhang L, Rakotondradany F, Myles AJ, Fenniri H, Webster TJ. Arginine-glycine-aspartic acid modified rosette nanotube-hydrogel composites for bone tissue engineering. Biomaterials 2009;30(7):1309-1320.

30. Baèáková L, Vorèik V, Rybka V, Mièek I, Hnatowicz V, Lisá V, et al. Adhesion and proliferation of cultured human aortic smooth muscle cells on polystyrene implanted with N^+, F^+, and Ar^+ ions: correlation with polymer surface polarity and carbonization. Biomaterials 1996;17(11):1121-1126.

31. Price RL, Waid MC, Haberstroh KM, Webster TJ. Selective bone cell adhesion on formulations containing carbon nanofibers. Biomaterials 2003;24(11):1877-1887.

32. Talapatra S, Kar S, Pal SK, Vajtai R, Ci L, Victor P, et al. Direct growth of aligned carbon nanotubes on bulk metals. Nat Nano 2006 Nov;1:112-116.

33. Roy S, Vedala H, Choi W. Vertically aligned carbon nanotube probes for monitoring blood cholesterol. Nanotechnology 2006;17(4):S14-S18.

34. Ngo Q, Petranovic D, Krishnan S, Cassell AM, Ye Q, Li J, et al. Electron transport through metal-multiwall carbon nanotube interfaces. Nanotechnology, IEEE Transactions on 2004;3:311-317.

35. Tamir G, Moti B-D, Itshak K, Raya S, Ze'ev RA, Eshel B-J, et al. Electro-chemical and biological properties of carbon nanotube based multi-electrode arrays. Nanotechnology 2007(3):035201.

36. Bard AJ, Faulkner LR. Electrochemical Methods: Fundamentals and Applications: Wiley, 2000.

37. Cao G. Nanostructures & nanomaterials : synthesis, properties & applications. London: Imperial College Press, 2004.

38. Besteman K, Lee J-O, Wiertz FGM, Heering HA, Dekker C. Enzyme-Coated Carbon Nanotubes as Single-Molecule Biosensors. Nano Letters 2003;3(6):727-730.

39. Cui X, Li CM, Zang J, Yu S. Highly sensitive lactate biosensor by engineering chitosan/PVI-Os/CNT/LOD network nanocomposite. Biosensors and Bioelectronics;In Press, Corrected Proof:1755-1755.

40. He P, Xu Y, Fang Y. Applications of Carbon Nanotubes in Electrochemical DNA Biosensors. Microchimica Acta 2006;152(3):175-186.

41. Hrapovic S, Liu Y, Male KB, Luong JHT. Electrochemical Biosensing Platforms Using Platinum Nanoparticles and Carbon Nanotubes. Analytical Chemistry 2004;76(4):1083-1088.

42. Lin Y, Lu F, Tu Y, Ren Z. Glucose Biosensors Based on Carbon Nanotube Nanoelectrode Ensembles. Nano Letters 2004;4(2):191-195.

43. Lin Y, Yantasee W, Wang J. Carbon nanotubes (CNTs) for the development of electrochemical biosensors. Frontiers in bioscience : a journal and virtual library 2005 Jan 1;10:492-505.

44. Liu Q, Lu X, Li J, Yao X, Li J. Direct electrochemistry of glucose oxidase and electrochemical biosensing of glucose on quantum dots/carbon nanotubes electrodes. Biosensors & bioelectronics 2007 Mar 1.

45. Liu S, Lin B, Yang X, Zhang Q. Carbon-Nanotube-Enhanced Direct Electron-Transfer Reactivity of Hemoglobin Immobilized on Polyurethane Elastomer Film. Journal of Physical Chemistry B 2007;111(5):1182-1188.

46. Liu Y, Wang M, Zhao F, Xu Z, Dong S. The direct electron transfer of glucose oxidase and glucose biosensor based on carbon nanotubes/chitosan matrix. Biosensors and Bioelectronics 2005 12/15;21(6):984-988.

47. Padigi SK, Reddy RKK, Prasad S. Carbon nanotube based aliphatic hydrocarbon sensor. Biosensors and Bioelectronics 2007 1/15;22(6):829-837.

48. Qu F, Yang M, Shen G, Yu R. Electrochemical biosensing utilizing synergic action of carbon nanotubes and platinum nanowires prepared by template synthesis. Biosensors and Bioelectronics 2007 3/15;22(8):1749-1755.

49. Siew PS, Loh KP, Poh WC, Zhang H. Biosensing properties of nanocrystalline diamond film grown on polycrystalline diamond electrodes. Diamond and Related Materials 2005;14(3-7):426-431.

50. Sotiropoulou S, Gavalas V, Vamvakaki V, Chaniotakis NA. Novel carbon materials in biosensor systems. Biosensors and Bioelectronics 2003 3;18(2-3):211-215.

51. Vamvakaki V, Chaniotakis NA. Carbon nanostructures as transducers in biosensors. Sensors and Actuators B: Chemical;In Press, Corrected Proof:63-63.

52. Harrison BS, Atala A. Carbon nanotube applications for tissue engineering. Cellular and Molecular Biology Techniques for Biomaterials Evaluation 2007 1;28(2):344-353.

53. Fang WC, Sun CL, Huang JH, Chen LC, Chyan O, Chen KH, et al. Enhanced electrochemical properties of arrayed CNx nanotubes directly grown on Ti-buffered silicon substrates. Electrochemical and Solid State Letters 2006;9(3):A175-A178.

54. Christian GD. Analytical Chemistry. New York: John Wiley & Sons, 1980.

55. Chen GZ, Fray DJ. Voltammetric Studies of the Oxygen-Titanium Binary System in Molten Calcium Chloride. Journal of the Electrochemical Society 2002;149(11):E455-E467.

56. Schüring J. Redox : fundamentals, processes, and applications. New York: Springer, 2002.

57. Battistuzzi G, Loschi L, Borsari M, Sola M. Effects of nonspecific ion-protein interactions on the redox chemistry of cytochrome c. Journal of Biological Inorganic Chemistry 1999;4(5):601-607.

58. Bronner F, Farach-Carson MC. Bone formation. New York: Springer, 2003.

59. Eastell R, Baumann M, Hoyle N, Wieczorek L. Bone markers: biochemical and clinical perspectives: Informa Health Care, 2001.

60. Zaidi M, Moonga BS, Huang CL-H. Calcium sensing and cell signaling processes in the local regulation of osteoclastic bone resorption. Biological Reviews 2004;79(01):79-100.

61. Blair HC, Zaidi M, Schlesinger PH. Mechanisms balancing skeletal matrix synthesis and degradation. Biochem J 2002 Jun 1, 2002;364(2):329-341.

62. Blair HC. How the osteoclast degrades bone. BioEssay 1998;20(10):837-846.

63. Hong MS, Lee SH, Kim SW. Use of KCl Aqueous Electrolyte for 2 V Manganese Oxide/Activated Carbon Hybrid Capacitor. Electrochemical and Solid-State Letters 2002;5(10):A227-A230.

64. Li CM, Sun CQ, Chen W, Pan L. Electrochemical thin film deposition of polypyrrole on different substrates. Surface and Coatings Technology 2005;198(1-3):474-477.

65. Wong JY, Langer R, Ingber DE. Electrically conducting polymers can noninvasively control the shape and growth of mammalian cells. Proceedings of the National Academy of Sciences of the United States of America 1994 April 12, 1994;91(8):3201-3204.

66. Garner B, Georgevich A, Hodgson AJ, Liu L, Wallace GG. Polypyrrole-heparin composites as stimulus-responsive substrates for endothelial cell growth. Journal of Biomedical Materials Research 1999;44(2):121-129.

67. Mihardja SS, Sievers RE, Lee RJ. The effect of polypyrrole on arteriogenesis in an acute rat infarct model. Biomaterials 2008;29(31):4205-4210.

68. Faucheux N, Tzoneva R, Nagel M-D, Groth T. The dependence of fibrillar adhesions in human fibroblasts on substratum chemistry. Biomaterials 2006;27(2):234-245.

69. Ungersböck A, Pohler OEM, Perren SM. Evaluation of soft tissue reactions at the interface of titanium limited contact dynamic compression plate implants with different surface treatments: an experimental sheep study. Biomaterials 1996;17(8):797-806.

70. Solon J, Levental I, Sengupta K, Georges PC, Janmey PA. Fibroblast Adaptation and Stiffness Matching to Soft Elastic Substrates. Biophysical Journal 2007;93(12):4453-4461.

71. Edin ML, Miclau T, Lester GE, Lindsey RW, Dahners LE. Effect of cefazolin and vancomycin on osteoblasts in vitro. Clin Orthop Relat Res 1996 Dec(333):245-251.

72. Winkler H, Kaudela K, Stoiber A, Menschik F. Bone grafts impregnated with antibiotics as a tool for treating infected implants in orthopedic surgery – one stage revision results. Cell and Tissue Banking 2006;7(4):319-323.

73. Salzmann GM, Naal FD, von Knoch F, Tuebel J, Gradinger R, Imhoff AB, et al. Effects of cefuroxime on human osteoblasts *in vitro*. Journal of Biomedical Materials Research Part A 2007;82A(2):462-468.

74. Krisanapiboon A, Buranapanitkit B, Oungbho K. Biocompatability of hydroxyapatite composite as a local drug delivery system. J Orthop Surg (Hong Kong) 2006 Dec;14(3):315-318.

75. Wallace GG, Spinks GM, Teasdale PR. Conductive electroactive polymers intelligent materials systems. Lancaster, Pa.: Technomic Pub. Co., 1997.

76. Li Y, Wang P, Wang L, Lin X. Overoxidized polypyrrole film directed single-walled carbon nanotubes immobilization on glassy carbon electrode and its sensing applications. Biosensors and Bioelectronics 2007;22(12):3120-3125.

77. Green RA, Williams CM, Lovell NH, Poole-Warren LA. Novel neural interface for implant electrodes: improving electroactivity of polypyrrole through MWNT incorporation. J Mater Sci Mater Med 2008 Apr;19(4):1625-1629.

78. Green RA, Lovell NH, Wallace GG, Poole-Warren LA. Conducting polymers for neural interfaces: Challenges in developing an effective long-term implant. Biomaterials 2008;29(24-25):3393-3399.

79. Tsai Y-C, Li S-C, Liao S-W. Electrodeposition of polypyrrole-multiwalled carbon nanotube-glucose oxidase nanobiocomposite film for the detection of glucose. Biosensors and Bioelectronics 2006;22(4):495-500.

80. Sirivisoot S, Yao C, Xiao X, Sheldon BW, Webster TJ. Greater osteoblast functions on multiwalled carbon nanotubes grown from anodized nanotubular titanium for orthopedic applications. Nanotechnology 2007;18(36):365102.

81. Staii C, Johnson AT, Chen M, Gelperin A. DNA-Decorated Carbon Nanotubes for Chemical Sensing. Nano Letters 2005;5(9):1774-1778.

82. Pushparaj V, Shaijumon M, Kumar A, Murugesan S, Ci L, Vajtai R, et al. Flexible energy storage devices based on nanocomposite paper. Proceedings of the National Academy of Sciences 2007 August 21;104(34):13574-13577.

83. Jeansonne BG, Feagin FF, McMinn RW, Shoemaker RL, Rehm WS. Cell-to-cell communication of osteoblasts. Journal of dental research 1979 Apr;58(4):1415-1423.

84. Jeansonne BG, Feagin FF, Shoemaker RL, Rehm WS. Transmembrane potentials of osteoblasts. Journal of Dental Research 1978 February 1;57(2):361-364.

85. Kaufman K, Kovacevic N, Irby S, Colwell C. Instrumented implant for measuring tibiofemoral forces. Journal of Biomechanics 1996 5;29(5):667-671.

86. Bergmann G, Deuretzbacher G, Heller M, Graichen F, Rohlmann A, Strauss J, et al. Hip contact forces and gait patterns from routine activities. Journal of Biomechanics 2001 7;34(7):859-871.

87. Bergmann G, Graichen F, Rohlmann A, Verdonschot N, van Lenthe GH. Frictional heating of total hip implants. Part 1: measurements in patients. Journal of Biomechanics 2001 Apr;34(4):421-428.

88. Graichen F, Bergmann G. Four-channel telemetry system for in vivo measurement of hip joint forces. Journal of Biomedical Engineering 1991 9;13(5):370-374.

89. Graichen F, Bergmann G, Rohlmann A. Hip endoprosthesis for in vivo measurement of joint force and temperature. Journal of Biomechanics 1999 10;32(10):1113-1117.

90. D'Lima DD, Townsend CP, Arms SW, Morris BA, Colwell CW. An implantable telemetry device to measure intra-articular tibial forces. Journal of Biomechanics 2005;38(2):299-304.

91. Graichen F, Arnold R, Rohlmann A, Bergmann G. Implantable 9-channel telemetry system for in vivo load measurements with orthopedic implants. IEEE transactions on bio-medical engineering 2007 Feb;54(2):253-261.

92. Thompson BC, Moulton SE, Ding J, Richardson R, Cameron A, O'Leary S, et al. Optimising the incorporation and release of a neurotrophic factor using conducting polypyrrole. Journal of Controlled Release 2006 12/1;116(3):285-294.

93. Gomez N, Schmidt CE. Nerve growth factor-immobilized polypyrrole: bioactive electrically conducting polymer for enhanced neurite extension. J Biomed Mater Res A 2007 Apr;81(1):135-149.

94. Ramanavicius A, Kausaite A, Ramanaviciene A, Acaite J, Malinauskas A. Redox enzyme - glucose oxidase - initiated synthesis of polypyrrole. Synthetic Metals 2006;156(5-6):409-413.

95. Song HK, Palmore GTR. Conductive Polypyrrole via Enzyme Catalysis. J Phys Chem B 2005;109(41):19278-19287.

96. Wadhwa R, Lagenaur CF, Cui XT. Electrochemically controlled release of dexamethasone from conducting polymer polypyrrole coated electrode. Journal of Controlled Release 2006 2/21;110(3):531-541.

97. Wang X, Gu X, Yuan C, Chen S, Zhang P, Zhang T, et al. Evaluation of biocompatibility of polypyrrole in vitro and in vivo. Journal of Biomedical Materials Research Part A 2004;68A(3):411-422.

98. Wang Z, Roberge C, Dao LH, Wan Y, Shi G, Rouabhia M, et al. In vivo evaluation of a novel electrically conductive polypyrrole/poly(D,L-lactide) composite and polypyrrole-coated poly(D,L-lactide-co-glycolide) membranes. Journal of Biomedical Materials Research Part A 2004;70A(1):28-38.

99. Wang Z, Roberge C, Wan Y, Dao LH, Guidoin R, Zhang Z. A biodegradable electrical bioconductor made of polypyrrole nanoparticle/poly(D,L-lactide) composite: A preliminary in vitro biostability study. Journal of Biomedical Materials Research Part A 2003;66A(4):738-746.

100. George PM, Lyckman AW, LaVan DA, Hegde A, Leung Y, Avasare R, et al. Fabrication and biocompatibility of polypyrrole implants suitable for neural prosthetics. Biomaterials 2005;26(17):3511-3519.

101. Kotwal A, Schmidt CE. Electrical stimulation alters protein adsorption and nerve cell interactions with electrically conducting biomaterials. Biomaterials 2001;22(10):1055-1064.

102. Christine ES, Venkatram RS, Joseph PV, Robert L. Stimulation of neurite outgrowth using an electrically conductingâ€‰polymer. Proceedings of the National Academy of Sciences of the United States of America 1997 August 19, 1997;94(17):8948-8953.

103. Sirivisoot S, Webster TJ. Multiwalled carbon nanotubes enhance electrochemical properties of titanium to determine in situ bone formation. Nanotechnology 2008(29):295101.

Chapter 5

Conclusions

This thesis contributed to the field of orthopedics and bone tissue engineering by developing for the first time nano-biomaterials as orthopedic biosensors, which can be placed on the surface of an implant to ensure efficacy and allow voltage-controlled drug release. The results concluded that:

5.1 Fabrication of Orthopedic Implant Sensors

- The capability of titanium (Ti) to function as an electrochemical electrode remarkably increases by growing multiwalled carbon nanotubes out of anodized Ti nanopores (MWCNT-Ti).
- MWCNTs improved the sensitivity of a commercially pure Ti electrode for sensing bone growth *in situ* as observed via redox peaks in cyclic voltammograms.
- MWCNTs enhanced direct electron transfer from ferri/ferrocyanide redox couples and the osteoblast extracellular matrix through anodized nanotubes on commercially pure Ti.
- MWCNT-Ti can serve as an electrochemical electrode with great electrocatalytic properties due to increased surface area and conductivity.

- MWCNTs promoted redox reactions by enhancing direct electron transfer through MWCNT-Ti when surrounded by an ionic solution, which contained the electroactive species, specifically ferri/ferrocyanide and the extracellular components from osteoblasts.

- The redox reaction of proteins in the osteoblast extracellular matrix (as osteoblasts synthesize bone) can be detected on MWCNT-Ti electrodes, whereas it cannot on anodized Ti or commercially pure Ti without MWCNTs.

- MWCNT-Ti produced by the cobalt-catalyzed chemical vapor deposition (CVD) technique exhibited excellent electrochemical properties.

- MWCNT-Ti can be used as an electrochemical electrode to determine new bone growth *in situ* surrounding an orthopedic implant.

- The ability of MWCNT-Ti to sense osteoblast extracellular components by detecting their redox reaction profiles in specific concentrations may improve the diagnosis of orthopedic implant success or failure, and thus, improve clinical efficacy.

- MWCNT-Ti can be used as a biosensing material to generate electrical signals, which can be designed to indicate bone ingrowth, inflammation, or biofilm formation for biomedical applications.

5.2 Cytocompatible Properties of Orthopedic Sensors

- MWCNT-Ti enhanced osteoblast (bone-forming cell) functions with greater alkaline phosphatase activity and calcium mineral deposition after 21 days of cultures *in vitro* (with

cell densities of 40,000 cells/cm^2) compared to commercially pure Ti and anodized nanotubular Ti.

- MWCNT-Ti have similar total surface energy when compared to anodized nanotubular Ti, but the former contributed more to the dispersive component of total surface energy (in the Owens-Wendt approach), while the latter contributed more to the polar surface energy when using deionized water as a probe liquid following the Owen-Wendt method.

- The critical surface tension according to the Zisman method (with at least three probe liquids) can be used to predict the biological interactiveness of the MWCNT-Ti and can be more informative than using the Owen-Wendt method alone for total surface energy.

5.3 Drug Release from Orthopedic Sensors

- Drugs were immobilized successfully inside conducting PPy films, which can be electrodeposited on AuPd-Ti and MWNT-Ti.

- PPy films were created to be diffusion-controlled release devices to improve osteoblast adhesion and decrease fibroblast adhesion.

- The use of PPy to deliver penicillin/streptomycin (P/S), the antibiotics used to treat gram-positive and -negative bacteria, respectively, was demonstrated.

- The use of PPy to deliver dexamethasone (Dex), a glucocorticoid used clinically as an anti-inflammatory and immunosuppressive agent, was evaluated.

- Both drugs (P/S and Dex) were confirmed to be anionic by zeta potential results.

- The PPy-drug films enhanced osteoblast adhesion to form bone, *in vitro*, whereas they inhibited fibroblast adhesion and scar tissue formation, when compared to Ti.

- Potentiodynamic methods (cyclic voltammetry) can control the P/S and Dex releases out of PPy films.

- The results revealed a controllable, reliable, typical biphasic release profile for both P/S and Dex upon voltage application.

- The cumulative P/S and Dex released into the PBS buffer were about 80% of the total amount of drug loading after 5 CV cycles of applied sweep voltages, and the PPy lost its electroactivity after a continuing electrical stimulus.

- The electrodeposition method can control the thickness of PPy films, the amount of drugs immobilized, and the implant surface charge, chemistry, topography, and roughness.

- For four hours, the –COOH functional groups of PPy films favored osteoblast adhesion and proliferation when compared to the $–NH_2$ functional groups and commercially pure Ti, while they favored fibroblast adhesion when compared to PPy functionalized NH_2.

- The PPy films decreased fibroblast adhesion when compared to commercially pure Ti.

- The PLGA-NHS, representing the activated PLGA-COOH, inhibited macrophage adhesion for four hours *in vitro*.

- The number of *Staphylococcus epidermidis* on PPy[P/S] was significantly less than on PPyCl films.

- After repeated electrical stimulation using cyclic voltammetry, a decrease of *Staphylococcus epidermidis* adhesion for one and 12 hours, on PPy[P/S] films was observed.

- Both the PPyCl and PPy[P/S] films decreased the *Staphylococcus epidermidis* adhesion after one hour when compared with glass and commercially pure Ti.

- The macrophage adhesion on the PPy[Dex] and PPyCl films were similar after four hours of culture.

- PPy functionalized with NH_2 and oxidized with Dex conjugated with 50:50 poly(d,l-lactic-co-glycolic acid) with acidic end groups (PLGA-PPy[Dex]), as well as PPyCl, PPy[PS], and PPy[Dex], were each tested on AuPd-Ti, and all possessed nanometer scale roughness important for promoting osteoblast adhesion and proliferation, and decreasing fibroblast adhesion and proliferation.

- The surface topography, roughness, and charge of the PPy films can be controlled by the type of drug, electrolyte solution, applied voltage/current, or current density.

- The use of conducting PPy coatings for electrically controlled orthopedic drug-delivery systems was developed and evaluated.

5.2 Future Directions

From the findings that MWCNT-Ti can determine new bone growth by detecting the redox reaction of osteoblast proteins *in situ*, and that the release of antibiotic and anti-inflammatory drugs from PPy can be electrically controlled, possible future directions of this research include:

- Integrating an MWCNT-Ti sensor and a PPy-drug film to form a closed-loop diagnosis and therapeutic system for orthopedic applications.

- Developing MWCNT-Ti as a biosensor or chip by micro- or nano-fabrication to allow communication from inside the body to the outside.

- Using MWCNT-Ti as an electrode or sensor, it is possible to detect in *vivo* infection (bacteria or biofilm formed) and inflammation (cytokine released) by considering current-voltage behaviors.

- Since MWCNT-Ti was found to "sense" the type of tissue growing on its surface, the applications of MWCNT-Ti sensors fabricated by lithography can be further studied for detecting other specific biological entities.

- Determining how changes in the atomic-level structure of CNTs affect their surface chemistry and their electrochemical properties.

- Electrodepositing PPy on MWCNT-Ti to detect organic and inorganic redox couples.

- Functionalizing PPy films with $-NH_2$ and with -COOH to optimize osteoblast adhesion and decrease fibroblast adhesion.

- Electrodepositing PPy films with several drugs in specific areas of commercially pure Ti implants or biosensors.

- Combining PPy-drugs on MWCNT-Ti and investigating them further by applying a constant voltage or current for a long period of time.

- Developing systems to deliver multiple, consecutive, electrically released drugs using PPy.

- Conjugating PLGA with amine functionalized PPy to sequentially release drugs by applied voltages. Especially, in the case of infection, which usually precedes chronic inflammation, such multifunctional devices can be designed to release antibiotics before anti-inflammatory drugs.

- The degree and pattern of the applied voltage or current can be further studied to control the amount of drugs releases.

- Self-polymerization of PPy and growth factors can be further investigated in order to develop PPy-growth factor nanoparticles. These particles can be used with electrospun fibers to create a conducting scaffold for nerve regeneration.

- The electrodeposition method can integrate biological entities with PPy films in order to develop sensors to detect antibodies, enzymes, glucose, and other biological agents.

Appendix A

Nanotechnology **2008(29):295101**

Multiwalled Carbon Nanotubes Enhance Electrochemical Properties of Titanium to Determine *in situ* Bone Formation

Sirinrath Sirivisoot and Thomas J Webster*

Division of Engineering, Brown University, Providence, RI 02912, USA

* Contact Author

Thomas J. Webster

Associate Professor

Divisions of Engineering and Orthopaedics

Brown University

Providence, RI 02912 USA

E-mail: Thomas_Webster@Brown.edu

Abstract

Multiwalled carbon nanotubes (MWCNTs) are cytocompatible with osteoblasts (bone-forming cells) and enhance osteoblast calcium deposition, and, thus, bone formation. In this study, MWCNTs were grown out of nanopores of anodized titanium (MWCNT-Ti), which has a surface layer of titanium oxide–a popular chemistry for orthopedic implants. The electrochemical responses of MWCNT-Ti were investigated in an attempt to ascertain if MWCNT-Ti can serve as novel *in situ* sensors of bone formation. MWCNT-Ti was subjected to the ferri/ferrocyanide redox couple, and its electrochemical behavior was measured. Cyclic voltammograms (CV) showed the enhanced redox potentials of the MWCNT-Ti. These redox signals were superior to that obtained by bare Ti, which did not sense either oxidation or reduction peaks in CV. The main objective of this study was to investigate the redox reactions of MWCNT-Ti in a solution of extracellular components, which was synthesized by osteoblasts *in vitro*. We found that MWCNT-Ti also exhibited well-defined and persistent CV, similar to the ferri/ferrocyanide redox reaction. The higher electrodic performance and electrocatalytic activity of the MWCNT-Ti compared to the bare Ti that were observed are likely because of the fact that MWCNTs enhance direct electron transfer and facilitate double layer effects, leading to a strong redox signal. These results may encourage further study and modification of MWCNT-Ti to sense new bone growth *in situ* next to implants and perhaps to monitor other events such as infection and/or scar tissue formation to improve current clinical diagnosis of orthopedic implant success or failure.

Keywords: osteoblasts, titanium, multiwalled carbon nanotubes, biosensing

1. Introduction

Osteoblasts and osteoclasts are located in bone, a natural nanostructure-mineralized organic matrix. While osteoblasts make bone, osteoclasts decompose bone by releasing acid that degrades calcium phosphate-based apatite minerals into an aqueous environment. Synthesis, deposition, and mineralization of this organic matrix, in which osteoblasts proliferate and mineralize (that is, deposit calcium), require the ordered expression of a number of osteoblast genes. Bone has the ability to self-repair or remodel routinely. However, osteoporosis (unbalanced bone remodeling) and other joint diseases (such as osteoarthritis, rheumatoid arthritis, or traumatic arthritis) can lead to bone fractures. These disabilities associated with bone all lead to difficulties in performing common activities and may require an orthopedic implant. However, the average functional lifetime of, for example, a hip implant (usually composed of titanium) is only 10 to 15 years. A lack of fixation into surrounding bone eventually loosens the implant and is the most common cause of hip replacement failure.

Approximately 200,000 total, 100,000 partial, and 36,000 hip replacement revisions were performed in the United States in 2003 [1]. Unfortunately, only limited techniques, such as insensitive imaging (through X-rays or bone scans), exist to determine if sufficient bone growth is occurring next to a titanium implant after surgery. Thus, techniques used in orthopedic diagnostics need to more accurately identify musculoskeletal injuries and conditions after implantation. Although there have been improvements in implants to increase bone formation, the clinical diagnosis of new bone growth surrounding implants remains problematic, sometimes significantly increasing patients' hospital stays and decreasing the ability of doctors to quickly prescribe a change in action if new bone growth is insufficient.

Currently, a physical examination (e.g., palpation, or laboratory testing) might be completed before imaging techniques are used to inform a clinician about a patient's health. Although advanced imaging techniques, such as bone scans, computer tomography scans, and radiographs (X-rays) are important in medical diagnosis, each has its own limitations and difficulties. A bone scan is used to identify areas of abnormal active bone formation, such as arthritis, infection, or bone cancer. However, bone scans require an injection of a radioactive substance (e.g., technetium) and a prolonged delay for absorbance before performing the scan. Computer tomography combines X-rays with computer technology to produce a two dimensional cross-sectional image of a body on the computer screen. Although this technique produces more detail than an X-ray, in some cases (e.g., severe trauma to the chest, abdomen, pelvis or spinal cord), a dye (e.g., barium sulfate) must be injected in order to improve the clarity of the image. This often causes pain to the patient. Another technique, called electromyography, has been used to analyze/diagnose nerve functions inside body conditions. Thin electrodes are placed in soft tissues to help analyze and record electrical activity in the muscles. However, this electrode technique leads to pain and discomfort for the patient. When the needles are removed, soreness and bruising can occur.

Electrochemical biosensors on the implant itself show promise for medical diagnostics *in situ* to possibly determine new bone growth surrounding the implant. Yet, this technology has not been fully explored. Incorporation of such electrochemical biosensors into current bone implants may be possible through nanotechnology; different types of nanoscale biomaterials have varying abilities to enhance *in vitro/vivo* bone formation. Carbon nanotubes (CNTs) are macromolecules of carbon, classified either as singlewalled carbon nanotubes (SWCNTs) with diameters of 0.4–2 nm or multiwalled carbon nanotubes (MWCNTs) with diameters of 2-100 nm

[2-3]. Due to their unique electrical, mechanical, chemical, and biological properties [4-11], CNTs have shown promise for bone implantation. For example, nanocomposites of polylactic acid and MWCNTs increased osteoblast proliferation by 46% and calcium production by greater than 300% when an alternating current was applied *in vitro* [12-13]. In addition, combining MWCNTs with precusor powders improves the mechanical properties of as-aligned hydroxyapatite (HA) composite coatings [9]. MWCNTs, reinforced with HA coatings, promoted human osteoblast proliferation *in vitro*, as observed in the appearance of cells near MWCNT regions [8]. Osteoblasts extended in all directions within the CNT scaffold that formed on polycarbonate membranes [14]. Osteoblasts significantly enhanced their adhesion on vertically aligned MWCNT arrays, according to Giannona et al. by recognizing nanoscaled features [15]. In addition, Zanello et al. (2006a) showed that CNTs are suitable for proliferation of osteosarcoma ROS 17/2.8 cells on single and multiwalled carbon nanotubes scaffolds [6]. Human osteoblast-like (Saos2) cells grown on the MWCNT scaffold showed a higher cell density and transforming growth factor-β1 concentration compared with those grown on polystyrene and polycarbonate scaffolds [16].

Our previous studies have shown greater osteoblast differentiation on MWCNT-Ti than on Ti alone [17]. Moreover, MWCNTs are a promising material for electrochemical biosensors because they also possess relatively well-characterized behavior in terms of electron transport [18-21]. Coating CNTs on Ti electrodes also increases the active surface area and enhances direct-electron-transfer [22-23]. These studies encourage the use of MWCNTs to modify currently used Ti for orthopedic implants. CNTs can be produced by the laser furnace arc and chemical vapor deposition (CVD) methods. Unlike the laser furnace arc, CVD is a scalable and controllable method of obtaining a high purity of CNTs [24]. A strong mechanical connection

between CNTs and the metal is needed for nanosensor applications [25], and the reduced resistance between the Ti and CNTs [26] leads to increased current passage. For example, Sato et al. showed potential for using CNTs in electrochemical biosensors by using CVD to grow MWCNTs, with Ti biometallic particles and cobalt (Co) as a catalyst. They revealed that Co has the ability to combine with Ti [27] to form a strong electrical contact between metal Ti and MWCNTs.

In order to form a more robust interconnection, CNTs were anchored in the pores of anodized nanotubular Ti in this study. Then, MWCNTs were grown, using CVD techniques, out of anodized Ti nanotubes (with diameters of 50-60 nm and depths of 200 nm) as a template.

In vivo, many cell processes rely on the redox reactions of various biomolecules and ions. The mechanisms of electron transfer reaction and the role of proteins in aiding the electron transfer of redox processes can be examined by electrochemical analysis. In electronic theory, when two different materials come in contact with each other, electron transfer will occur in an attempt to balance Fermi levels, causing the formation of a double layer of electrical charge at the interface [28]. Because, the formation of electric contact between the redox proteins and the electrode surface is the fundamental challenge of electrochemical biosensor devices, in this study, we investigated the redox reactions of iron (II/III) and the osteoblast extracellular components at the surface of Ti, anodized Ti, and MWCNT-Ti.

2. Materials and Methods

2.1. Ti-based Electrodes

Commercially pure titanium (Ti; Alfa Aesar), anodized Ti, and MWCNT-Ti were used as working electrodes with geometric areas of 1 mm^2 and 1 cm^2. Ti was prepared by anodization techniques [17]. Briefly, 1 cm^2 of Ti was etched with a solution of 1.5% by weight nitric acid and 0.5% by weight hydrofluoric acid (HF) for 10 seconds. A potential of 20 volts was applied between a Ti and platinum (Pt; Alfa Aesar) sheet electrode for 10 minutes in the presence of 1.5% by weight HF in order to create uniform nanopores. Afterward, anodized Ti was modified by growing MWCNTs out of the nanopores via chemical vapor deposition (CVD) [17]. The dense and entangled MWCNTs formed a three-dimensional structure on the Ti surface with exceptional electric conductivity and surface area.

2.2. Osteoblast Culture and Extracellular Component Solutions

Human osteoblasts (hFOB 1.19; CRL-11372; ATCC; population number = 5-12) were cultured in Dulbecco's Modified Eagle Medium (DMEM; Gibco) supplemented with 10% fetal bovine serum (FBS; Hyclone), 1% penicillin/streptomycin (P/S; Hyclone), 50 nM β-glycerophosphate (Sigma), and 50 μg/ml ascorbic acid (Sigma) for 7, 14, and 21 days on commercially pure Ti with an initial cell density of 40,000 cells/cm^2 under standard cell culture conditions (a humidified, 5% CO_2, and 95% air environment at 37° C). After each time period, and three freeze-thaw cycles with distilled water to lyse the cells, Ti was soaked in 0.6 N HCl (Sigma) for 24 hours to dissolve the extracellular components of the osteoblasts. A calcium quantification kit (Sigma) was used to determine the amount of calcium deposited by osteoblasts. The light absorbance of calcium in

the supernatants was measured by a spectrophotometer (SpectraMAX 340PC[384]; Molecular Devices) at 570 nm. The chemical composition on the surfaces of the Ti substrates after osteoblast culture for 21 days was also evaluated by energy dispersive spectroscopy (SEM-EDS; Leo 1530VP FE-4800).

2.3. Electrochemical Measurements

An epsilon EC electrochemical workstation and Digisim software (Bioanalytical) performed the cyclic voltammetry experiments in this study. The Ti, anodized Ti, and MWCNT-Ti substrates were used as the working electrodes. A silver/silver chloride (Ag/AgCl; MW-2052; Bioanalytical) and a platinum (MW-1032; Bioanalytical) wire were used as reference and counter electrodes, respectively. Before the measurements, all electrodes were cleaned with deionized water. All electrodes were connected to the electrochemical workstation and immersed in an electrolyte solution. The electrolytes were a 10 mM $K_3Fe(CN)_6$ (potassium ferricyanide) solution with 1 M KNO_3, and the solution of 0.6 N HCl dissolved the extracellular components from the commercially pure Ti that had been cultured for 7, 14, and 21 days. The cyclic voltammograms (CV) were generated by applying a linear sweep potential at several scan rates. The electrochemical responses at the three types of working electrodes were compared with CV in both electrolyte solutions. All measurements were carried out at room temperature and in oxygen-containing electrolyte solutions.

3. Results and Discussion

3.1. Electrode Topography

The commercially pure Ti surface, shown in Figure 1 (a), exhibits a smooth Ti oxide. After anodization, the nanopores of Ti oxide were formed on the Ti surface uniformly with diameters of 50-60 nm and depths of 200 nm, as shown in Figure 1 (b). After CVD treatment, MWCNTs covered the anodized Ti templates as shown in Figure 1 (c) side view and (d) top view.

3.2. Osteoblast Extracellular Component Analysis

After osteoblasts were cultured for 21 days, results from energy dispersive spectroscopy (EDS) performed on commercial Ti substrates revealed the presence of various minerals of newly formed bone. Figure 2 shows the peaks of many inorganic substances, consisting of magnesium (Mg), phosphorus (P), sulphur (S), potassium (K), and calcium (Ca). The Ca/P weight ratio of minerals deposited by osteoblasts on Ti (1.34) was less than that on MWCNT-Ti (1.52) in this study. However, the Ca/P ratio of hydroxyapatite (HA), the main calcium-phosphate crystallite in bone, is typically about 1.67 [29-30]. This study demonstrated that the minerals deposited by osteoblasts on MWCNT-Ti were more similar to natural bone than the minerals deposited on Ti. X-ray diffraction (XRD) analysis also showed that more hydroxyapatite was deposited on MWCNT-Ti than on both commercially pure and anodized Ti after osteoblasts were deposited the minerals for 21 days, as shown in Figure 3. In addition, the amount of calcium deposited by osteoblasts as determined by a calcium quantification assay kit was 1.481 $\mu g/cm^2$ for 7 days, 1.597 $\mu g/cm^2$ for 14 days, and 2.483 $\mu g/cm^2$ for 21 days on commercially pure Ti, as shown in Figure 7 (b). These results imply a greater deposition of calcium by osteoblasts on MWCNT-Ti.

Bone resorption and remodeling involve a secretion of hydrochloric acid (HCl) by osteoclasts [31]. Osteoclasts dissolve bone mineral by isolating a region of the matrix and then secreting HCl and proteinases at the bone surface, resulting in the bone acting as a reservoir of Ca^{2+}, PO_4^{3-}, and OH^- [32]. This is likely the reason that HCl is so prevalent in laboratories to dissolve calcium minerals deposited on substrates by osteoblasts *in vitro* as the supernatant to further use in calcium deposition assay. Thus, after dissolving with 0.6 N HCl, it is likely that Ca^{2+}, PO_4^{3-}, and OH^- are contained in the solution of the osteoblast extracellular components.

The formation of bone matrix minerals first depends on achieving a critical concentration of calcium and phosphorus. Then phospholipids, anionic proteins, as well as calcium and phosphorus aggregate in nucleation pores that are in the 35 nm “hole-zone” between collagen molecules [33]. The addition of calcium, phosphate, and hydroxyl ions contributes to the growth of crystal hydroxyapatite. However, the crystals are not pure since they also contain carbonate, sodium, potassium, citrate, and traces of other elements, such as strontium and lead. The imperfection of the hydroxyapatite contributes to its minerals’ solubility, which plays a role in the ability of osteoclasts to resorb the mineral phases. Although osteoblasts synthesize type I collagens, which are the predominant organic components of bone, type III/V/VI collagens also exist in bone. Moreover, non-collagen proteins of bone (such as growth factors, osteocalcin, osteopontin and osteonectin) and proteins in serum and other tissues (such as fibronectin, vitronectin, and laminin) are absorbed into the mineral component during bone growth. These components are directly involved in the genesis and maintenance of bone. Thus, not only minerals, but also other non-collagen proteins, are broken down after dissolution with HCl. As such, unspecific proteins in the supernatant when the cyclic

voltammetry is performed with MWCNT-Ti may contribute to the observed redox process in CV here. On an electrode surface, the native conformation of a protein may be retained (reversible or diffusion-controlled) or distorted (irreversible or adsorption-controlled), depending on the extent of the interactions (such as the electrostatic or covalent bonds) between them.

The type of electrolyte is important to the redox reaction because the gained capacitance and scan rate window are dependent on it [34]. Since we did not degas with nitrogen or argon when we performed the cyclic voltammetry, the redox reactions in CV were related to the H_2O decomposition, which includes H^+ reduction and OH^- oxidation. The pH of the electrolyte also affects the H_2O decomposition. In the case of acid 1 N HCl solution (without other electroactive molecules), the H^+ ions induced the formation of H_2 gas at -0.2 V as a result of the increased reduction current [34]. In the alkaline 1 M KOH solution, OH^- ions resulted in the formation of O_2 gas at 0.7 V by the oxidation process. This fact should be noted because *in vivo*, these decompositions may occur at the interface of the Ti implant due to pH changes and the presence of H_2O and O_2 around the implant.

3.3. Electrochemical Behavior of $Fe^{2+/3+}$ Redox Couple at Ti, anodized Ti, and MWCNT-Ti

The $\mathrm{Fe(CN)_6^{4-/3-}}$ redox system with an exhibition of heterogeneous one electron transfer (n=1) is one of the most extensively studied redox couples in electrochemistry [35]. We performed the cyclic voltammetry experiments of the $\mathrm{Fe^{2+/3+}}$ redox couple by placing MWCNT-Ti in an electrolyte solution of 10 mM $K_3Fe(CN)_6$ and 1 M KNO_3. In potassium ferricyanide ($K_3Fe(CN)_6$), the reduction process is Fe^{3+} ($\mathrm{Fe(CN)_6^{3-} + e^- \rightarrow Fe(CN)_6^{4-}}$) followed by the oxidation of Fe^{2+}

($Fe(CN)_6^{4-} \rightarrow Fe(CN)_6^{3-} + e^-$) under a sweeping voltage. The iron (II/III) redox couple did not exhibit any observable peaks for bare Ti or anodized Ti electrodes, as shown in Figure 4 (a) and (b). This implies that the electrochemical reaction is slow on both these electrodes. However, the highly direct electron transfers at the MWCNT-Ti electrode were observed as redox peaks, shown in Figure 4 (c). At a scan rate of 100 mV/s in Figure 4 (c), a well-defined redox peak appears with the anodic (E_{pa}) and cathodic (E_{pc}) potentials at 175 mV and 345 mV, respectively. Moreover, on the inner set of Figure 4 (c), the relationship is linear between the anodic and cathodic peak currents versus the square root of the scan rate, while the ratio of I_{pa}/I_{pc} is about 1, corresponding to the Randles-Sevcik equation (1). Because the root scan rate has this linear relation with the peak currents, the mass transport in this process must be by diffusion. Zhang et al. found that the heterogeneous charge-transfer rate constant (k) of $Fe(CN)_6^{4-/3-}$ complex with H_2O as a solvent is 0.05 cm/s [36]. Since the k value is in the range of 10^{-4} to 10^{-1} cm/s and $\Delta E_p > 59/n$ mV (in this case n=1 and ΔE_p~170 mV), this process is quasi-reversible.

To analyze the electrochemical behavior at the surface of the MWCNT-Ti electrode, we use the Randles-Sevcik equation for quasi-reversible processes, equation (1). Hence, the peak current (I_p) is given by:

$$I_p = 2.99 \times 10^5 A D^{1/2} n (n_a \gamma)^{1/2} C \qquad (1)$$

where n is the number of electrons participating in the redox process, n_a is the number of electrons participating in the charge-transfer step, A is the area of the working electrode (cm^2), D is the diffusion coefficient of the molecules in the electrolyte solution (cm^2/s), C is the concentration of the probe molecule in the bulk solution (molar), and γ is the scan rate of the sweep potential (V/s). When the $Fe(CN)_6^{4-/3-}$ redox system exhibits heterogeneous one-

electron transfer ($n=n_a=1$) and the concentration C is equal to 10 mM, the diffusion coefficient D is equal to $6.7 \pm 0.02 \times 10^{-6}$ cm^2/s [37-38]. Hence, the quasi-reversible redox of iron (II/III) is truly enhanced by MWCNTs.

Other studies have shown promising results when using CNT-modified electrodes in biosensing. Since MWCNTs have good electrochemical characteristics as electron mediators and adsorption matrices [39], they may further enhance applications in biosensor systems. For example, Harrison et al. showed that CNTs offer a promising method to enhance detection sensitivity because they have high signal-to-noise ratios [11]. The structure-dependent metallic character of CNTs should allow them to promote electron-transfer reactions for redox processes, which can provide the foundation for unique biochemical sensing systems at low over-potentials [19]. The electrolyte-electrode interface barriers are reduced by CNTs because they facilitate double-layer-effects [40]. Typically, when the supporting electrolyte is at least a hundred-fold greater than the active electrolyte [41], the charge in the electrolyte solution causes the Debye layer to be more compact. Therefore, this compact layer can rapidly exchange electrons between electroactive proteins and the surface of an MWCNT-Ti electrode. This is likely the reason we observe the sharpened cathodic and anodic peaks in CV, as shown in Figures 4 (c), 5 (c), 6 (b), and 7 (a).

Although the area of the working electrode iss constant in the presence of MWCNTs, the overall surface area and the electroactivity of the surface are increased [42]. The MWCNTs act as a nanobarrier between the titanium oxide layer, which was its growth template, and the electrolyte solution. The surface atoms or molecules of MWCNTs play an important role in determining its bulk properties due to their nanosize effects [43]. A large surface, corresponding to the greater electrocatalytic activity, confers the catalytic role on the MWCNTs in the chemical

reaction. Well-defined and persistent redox peaks are shown in Figure 4 (c), confirming the increases of electron transfers and higher electrochemical activities at the MWCNT-Ti surface. Cyclic voltammetry was also performed with a glassy carbon electrode (GCE; Bioanalytical) and a platinum electrode (PTE; Bioanalytical), and it also showed ΔE_p>59/n mV (data not shown). Importantly, for the same scan rate, CV of GCE and PTE showed the redox reactions with similar but more widely separated anodic and cathodic peaks, confirming the performance of the MWCNT-Ti electrode.

However, in Figures 4 (a) and (b), the Ti and anodized Ti did not show any redox peaks. This is likely due to the inert inhibiting property of the titanium oxide on electron transfer through them. Figures 4 (a) and (b) show that bare Ti has less capacitance than MWCNT-Ti. The capacitance relation is derived from: $i = C\left(\frac{dv}{dt}\right)$, where $\frac{dv}{dt}$ is a scan rate [35]. Hence, the capacitance between the working and reference electrodes during cyclic voltammetry was calculated by dividing the current in CV with respect to the specific scan rate, as shown in Figures 4 (d) and 6 (d). In sum, the electrochemical response of the MWCNT-Ti electrode promoted a higher charge transfer than the Ti and anodized Ti electrodes.

3.4 Electrochemical Behavior at Ti, Anodized Ti, and MWCNT-Ti in the Solution of Osteoblast Extracellular Components

The result from the previous section showed the utility of MWCNT-Ti as an electrode for detecting $\mathrm{Fe}^{2+/3+}$ redox couples. For biological applications, it is also necessary to show that MWCNT-Ti can detect redox reactions associated with osteoblast differentiation. We used

extracellular components from osteoblasts in an HCl solution to mimic the biological environment around an orthopedic implant. Figures 5 (a) and (b) show the bare Ti and anodized Ti electrodes cannot detect any redox process. While, the results in Figure 5 (c) confirmed that MWCNTs enhance the direct electron transfer through Ti by adding the high conductivity surface of the MWCNTs.

After decreasing the surface area of the MWCNT-Ti electrode from 1 cm^2 to 1 mm^2, the redox potentials were also decreased as shown in Figures 5 (c) and 6 (b). The faradic current of the oxidation process dropped approximately ten times with respect to decrease in surface area *A*, corresponding to equation (1). Corresponding with the Randles-Sevcik equation, the peak current was linearly proportional to the area. When plotting the anodic (I_{pa}) and cathodic peak (I_{pc}) currents of MWCNT-Ti, a linear relationship to the square root of the scan rates was observed, as shown in Figure 6 (c).

CV showed well-defined redox peaks in the osteoblast supernatants at all concentrations. The peaks detected in the solution at the calcium concentrations of 1.481 $\mu g/cm^2$ (after 7 days), and 1.597 $\mu g/cm^2$ (after 14 days) have less faradic current and I-V graph area than the concentration of 2.48 $\mu g/cm^2$ (after 21 days), as shown in Figures 7 (a) and (b). Typically, the more HA deposited and synthesized by osteoblasts, the higher the calcium and protein concentrations is. Therefore, it is likely that the supernatant of 21 days had higher protein concentrations than the solutions of 7 and 14 days, leading to the stronger redox reactions and higher capacitance between the electrode surfaces.

In addition interpretation of CV results must consider other factors. In particular, a measurement of the redox reactions when oxygen was dissolved in the electrolyte solution

showed that the peak currents were shifted toward the negative. Furthermore, a change in the pH of the electrolyte solution and the presence of water may also shift the current and affect the potential of the redox peaks. Thus, cyclic voltammetry with the potential range between -1 to 1 V of MWCNT-Ti was performed in a pure solution of 0.6 N HCl without other proteins or ions. An H^+ reduction peak at a potential between -0.5 to -0.8 V was found (data not shown). Moreover, the H^+ reduction peak still appeared when window ranges from -5 to 5 V and from -0.35 to 0 V were used, confirming the H_2O decomposition occurred in our CV experiments.

The MWCNT-Ti electrodes showed the potential for better performance than commercially available electrodes, such as GCE and PTE. When using the sweep voltage from -1 to 1 V, a set of mixed redox peaks with two oxidations and two reductions appeared (data not shown). These two redox peaks in the CV, indicate that the process likely involved more than one electron transfer. For each couple, the amplitude and position of the oxidation peak in CV was unequal to those of the reduction peak. The second oxidation peak (omitted from Figures 5 (c) or 6 (b)) was observed at 236 mV for the MWCNT-Ti electrode, 405 mV for the GCE, and -33 mV for the PTE, all with the scan rate of 100 mV/s. However, for the GCE and the PTE electrodes, a second reduction did not appear, while the MWCNT-Ti showed two complete and well-defined redox reactions. These two peaks reflect that more than one electron transfers are involved. Since one occur at positive potential and one at negative in the CV. Further, the current amplitude for the MWCNT-Ti peaks was noticeably larger than that for GCE and PTE. Thus, it can be concluded that the MWCNT-Ti electrode has higher electron transfer as well.

At first we hypothesized that these redox reactions happened due to redox of inorganics such as Ca or P. In the case of Ca, the reduction of Ca^{2+} to Ca crystal (nucleation) typically is expected with the reduction current for a highly negative potential. A positive feedback IR

compensation (IRC) needs to be applied to the cyclic voltammetry in order to drive the oxidation current to dissolve the Ca crystal into Ca^{2+}. For example, an overpotential of more than -1 V, IRC of 0.771 Ω, melting temperature of 900 °C, and scan rate of 50 mV/S were required [44]. Due to without apply IRC in this study, diffusion-controlled behavior, which electrochemically depletes calcium cation near the electrode surface, was impossible to achieve here. In addition, the reduction and oxidation of titanium oxides, which are the reaction counterparts of calcium redox, appeared at a positive potential between 0 and 0.25 V, respectively, which do not appear in our CV. In the case of P, the cyclic voltammetry experiments were performed further in this phosphate buffered saline (PBS). A final concentration of 1 M PBS, which was prepared in-house, had 137 mM NaCl, 10 mM phosphate, 2.7 mM KCl, and a pH of 7.4. The metal orthophosphate ions exhibit the high stability to reduce from P(V) (such as PO_4^{3-}, PO_4^{-}) to P(III), or further to P(I). However, no redox peaks appeared in the potential range of -1 to 1 V (data not shown). It is therefore likely that neither the redox reactions of calcium ions nor phosphate occurred here due to the absence of the peaks. Instead, we hypothesized that the appearance of the redox peaks when using an MWCNT-Ti electrode is likely because of the reduction and oxidation of proteins from the osteoblast supernatant.

The observed quasi-reversible redox reaction here reflected the fact that MWCNT-Ti promotes the electrochemical reactions. However, an irreversible process can occur at the interface of an electrode due to a denaturation of protein, or ion reduction. Typically, when the carbon bonds of proteins are changed, irreversible organic reduction or oxidation happens only [45]. While, the configurations of ions (Ca^{2+}, PO_4^{3-}, OH^{-}) which remain unchanged also can lead the irreversible process due to only its reduction or oxidation. Importantly, without MWCNTs on the Ti surface, non-specific protein adsorption may readily occur, leading to an

electrochemically insulating surface layer. Nevertheless, the redox at MWCNT-Ti did not decrease its oxidation and reduction currents after applying the sweep voltage for some time, so protein adsorption did not occur apparently significantly at the MWCNT-Ti electrode. Indeed, in the osteoblast supernatant, the MWCNT-Ti electrode provides a relatively specific surface to which the proteins can bind reversibly by diffusion while retaining their function. The protein redox is also dependent on the pH of the electrolyte solution (acidic or basic) [46]. This shift appears due to the influence of 0.6 N HCl with H_2O as a solvent influences the proteins, leading the peak shift into the negative potential, as shown in Figures 5 (b), 6 (c), and 7 (a).

We hypothesized that the proteins were involved in these redox reactions at the surface of MWCNT-Ti in the solution of osteoblast extracelluar components. If those proteins maintain their function and are detected by the MWCNT-Ti electrode, the excellent electrochemical behavior observed here may show MWCNT-Ti as a superior candidate for biosensor applications. However, investigating types and sizes of acidic resistant proteins are still in progress.

3.5. Applications and Limitations

As shown here, the electrodic performance of the MWCNT-Ti electrode, but not the bare Ti, provided excellent redox reactions. However, some specific condition used in this study has to be in concerned due to effect to CV resulted. As mentioned, the electrochemical experiments were performed without degassing by bubble nitrogen gas. This omission may have resulted in an apparent background signal, which was mixed and appeared in our current-voltage curves (CV). Moreover, the redox reaction at MWCNT-Ti electrode in this study may

depend on various ion sources, including reversible protein adsorption, dissolved oxygen, and acidic nature of HCl. However, the redox reactions of iron (II/III) and the osteoblast extracellular components still occurred only when using MWCNT-Ti, and not when using Ti or anodized Ti. Importantly, we showed that MWCNTs performed as the electrocatalysts for the oxidation and reduction of iron (II/III) and of extracellular components, which included various proteins and inorganic substances which were synthesized and deposited by osteoblasts.

The electrolyte solution of osteoblast extracellular components was composed of inorganic and organic substances. We did not classify the types of molecules in the solution, but rather, all components were dissolved together the acidic solution and used in all cyclic voltammetry in this study. One of future works is classification the type of proteins in our osteoblast supernatant.

However, it is likely that *in vivo* the capacitance and the electroactive surface of Ti will be enhanced after bone tissue is formed without presence of MWCNTs. After a hip implant insertion, blood and body fluids surround the Ti implant, creating a specific capacitance for Ti electrode in the beginning. Within one month, as osteoblasts deposit calcium around the implant, the capacitance of the implant and bone tissue increases. Cell membranes also have electric potentials and perform redox processes [47-48], and we found that after 14 days *in vitro* these redox processes at the surface of bare Ti were increased (data not shown).

In vitro, nevertheless, MWCNTs have been used to modify the electrodes to detect other biomolecules and enhance their redox reactions, such as NADH [49], hydrogen peroxide [21,49], glucose [22], putrescine [50], and DNA [51]. Specifically, the growth of MWCNTs from nanoporous metals electrodes can enhance many diverse sensor applications. For example,

MWCNTs functionalized with thiol groups have been used for sensing aliphatic hydrocarbons (such as methanol and ethanol), forming unique electrical identifiers [18]. Moreover, MWCNTs grown on silicon substrates that enhanced ionic conductivity were integrated with unmodified plant cellulose as a film, and used as a cathode electrode in a lithium ion battery, or as a supercapacitor with bioelectrolytes (such as biological fluid and blood) [52]. Interestingly, both supercapacitor and battery, derived from a MWCNTs-nanocomposite film, can be integrated together to build a hybrid, or dual-storage battery-in-supercapacitor device. The cytocompatible MWCNTs-device may be useful to integrate with an orthopedic-implanted biosensor as passive energy storage.

Not only can an implanted electronics circuit be powered by an implant battery (fabricated or self-integrated) within the implant material, but also it can be induced by an external power supply. For orthopedic application, telemetric devices started in 1966 and became imperative as a telemetric orthopedic implant in order to transmit a signal to an external device [53-58]. For example, Graichen et al. (2007) developed a new 9-channel telemetry transmitter used for *in vivo* load measurements in three patients with shoulder Ti endoprostheses [59]. The low radio frequency (RF) of the externally inductive power source generates power transmission through the implanted metal. At the end of the Ti implant, the pacemaker feedthrough rounds a single loop antenna to transmit the pulse interval signal, which is modulated at a higher RF by the microcontroller, to an external device. Then, the RF receiver of the external device synchronizes with the modulated pulse interval to recover the data stream and report to a clinician. Thus, either an implanted battery or a telemetry system can supply the electric power to a calcium-detectable chip inside the orthopedic implants for clinical use.

The automatically-sensing concept for bone growth juxtaposed orthopedic implants also can apply with the infection and scar tissue formation. An energy source energizes a telemetric-implanted circuit, and allows it to transmit data to an external receiver to determine bone growth. Indeed, the electrochemical biosensor may reduce the complexity of imaging techniques and patient difficulties.

4. Conclusions

The capabilities of titanium (Ti) as an electrochemical electrode were increased remarkably by growing multiwalled carbon nanotubes out of anodized Ti nanopores (MWCNT-Ti). MWCNTs improved the sensitivity of the bare Ti electrode displaying redox peaks in cyclic voltammograms and interestingly high capacitance. These results provide evidence that MWCNT-Ti can serve as a novel electrochemical electrode with great electrocatalytic properties due to increased surface area and conductivity. Moreover, MWCNTs were shown to be more highly electroactive in chemical transformations than the metallic (Ti) surface, which typically undergoes electrochemical oxidation or dissolution of metal oxides, but is chemically susceptible to corrosion. MWCNTs promoted a redox reaction by enhancing the direct electron transfer through their electrically conductive surface surrounded by ionic solutions, which contained the electroactive species, herein ferri/ferricyanide and the extracellular components from osteoblasts. Moreover, MWCNTs are cytocompatible, promoted osteoblast differentiation after 21 days, and can be integrated into a supercapacitor or battery to enhance the functionalities of biosensing systems *in vivo*. Therefore, MWCNT-Ti constitutes an exceptional candidate as an electrochemical electrode to determine *in situ* new bone growth surrounding an orthopedic

implant. Further, the ability of MWCNT-Ti to sense the osteoblast extracellular components by detecting their redox reaction profiles in specific concentrations may improve the diagnosis of orthopedic implant success or failure, and thus improve clinical efficacy.

5. Acknowledgments

The authors would like to thank the Coulter Foundation for funding; Professor Brian W. Sheldon for the chemical vapor deposition (CVD) facility; Anthony W. McCormick and Geoffrey Williams for their help with the scanning electron microscope; and Maryam Jouzi for her help with an electrochemical workstation.

6. Figures

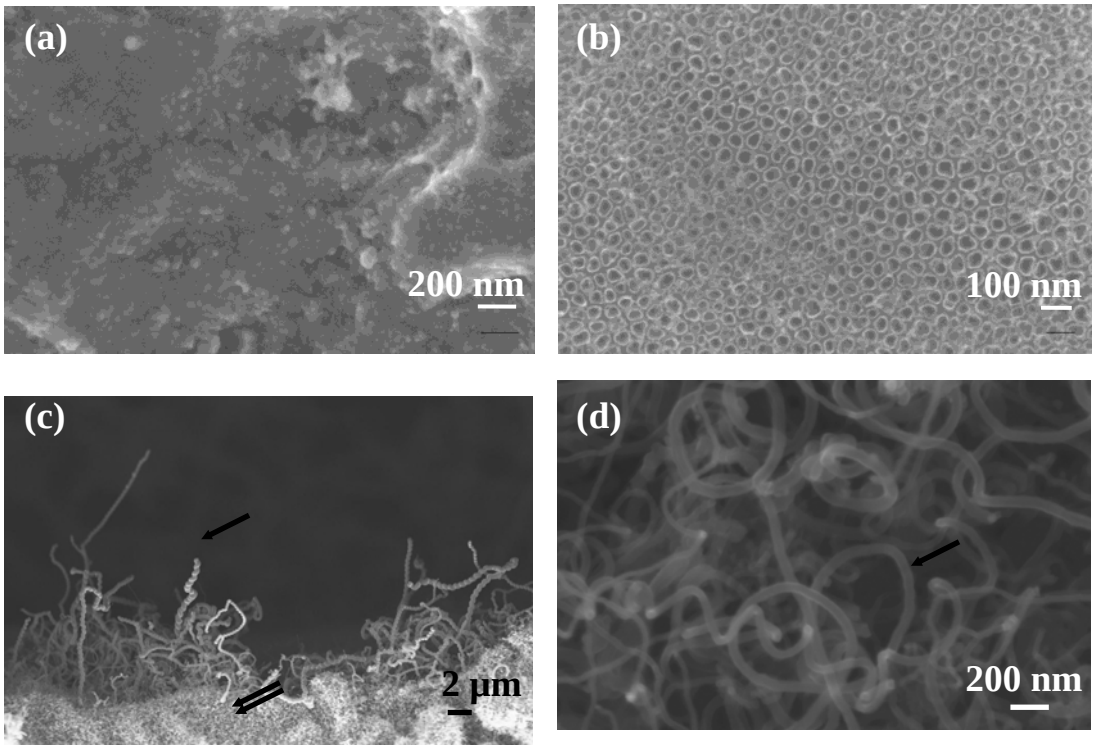

Figure 1. SEM micrographs of the electrode surfaces: (a) commercially pure Ti; (b) anodized Ti; and (c) side view and (d) top view of MWCNT-Ti. Single arrow shows MWCNTs, whereas the double arrows show the anodized Ti template.

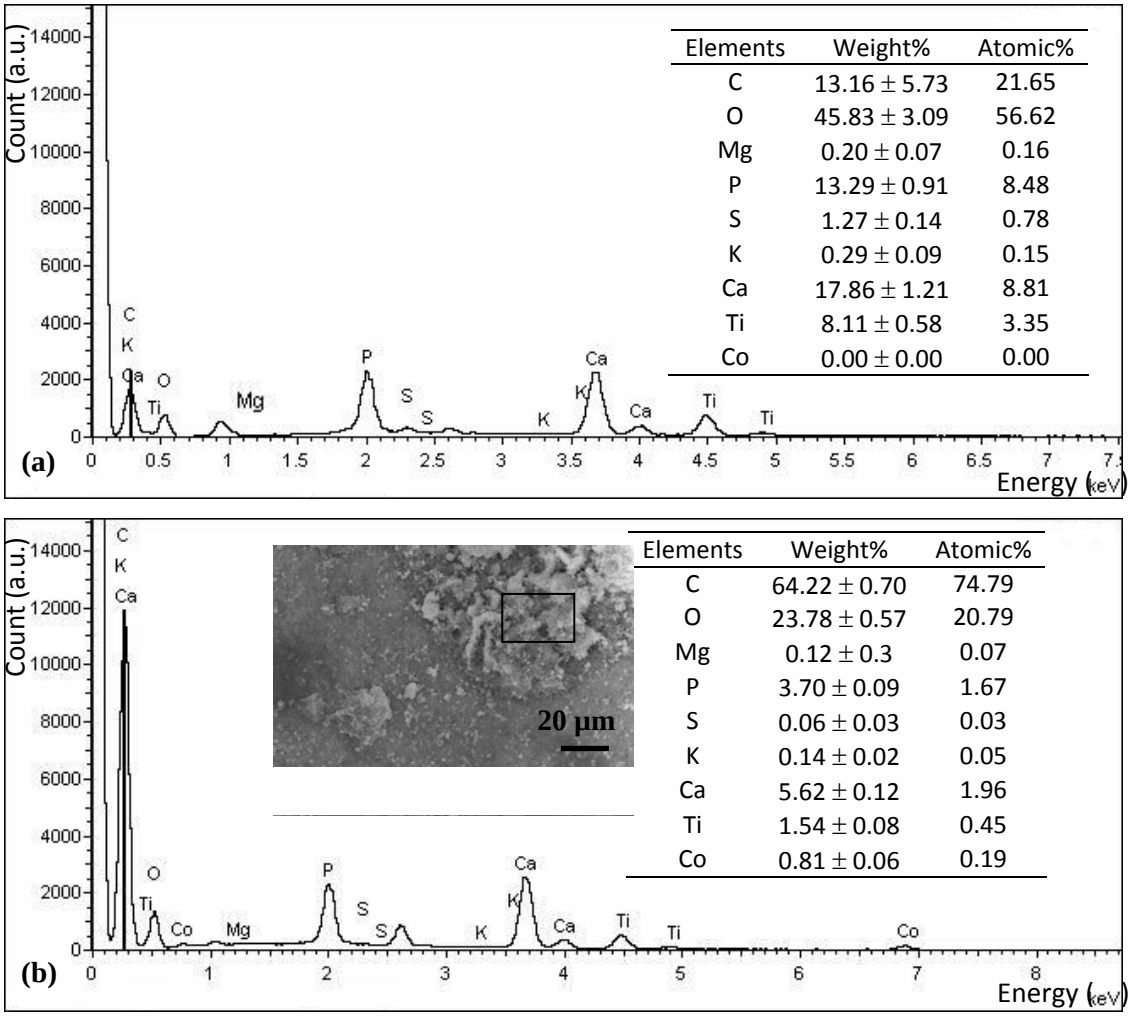

Figure 2. EDS analysis of osteoblasts cultured for 21 days on (a) Ti and (b) MWCNT-Ti. SEM micrograph of inset (b) shows the analyzed area. For the MWCNT-Ti, more Ca and P deposited by osteoblasts were observed. Tables in (a) and (b) show the composition of the mineral deposits after osteoblasts were cultured for 21 days. The Ca/P weight ratio on bare Ti was 1.32 and on MWCNT-Ti was 1.52.

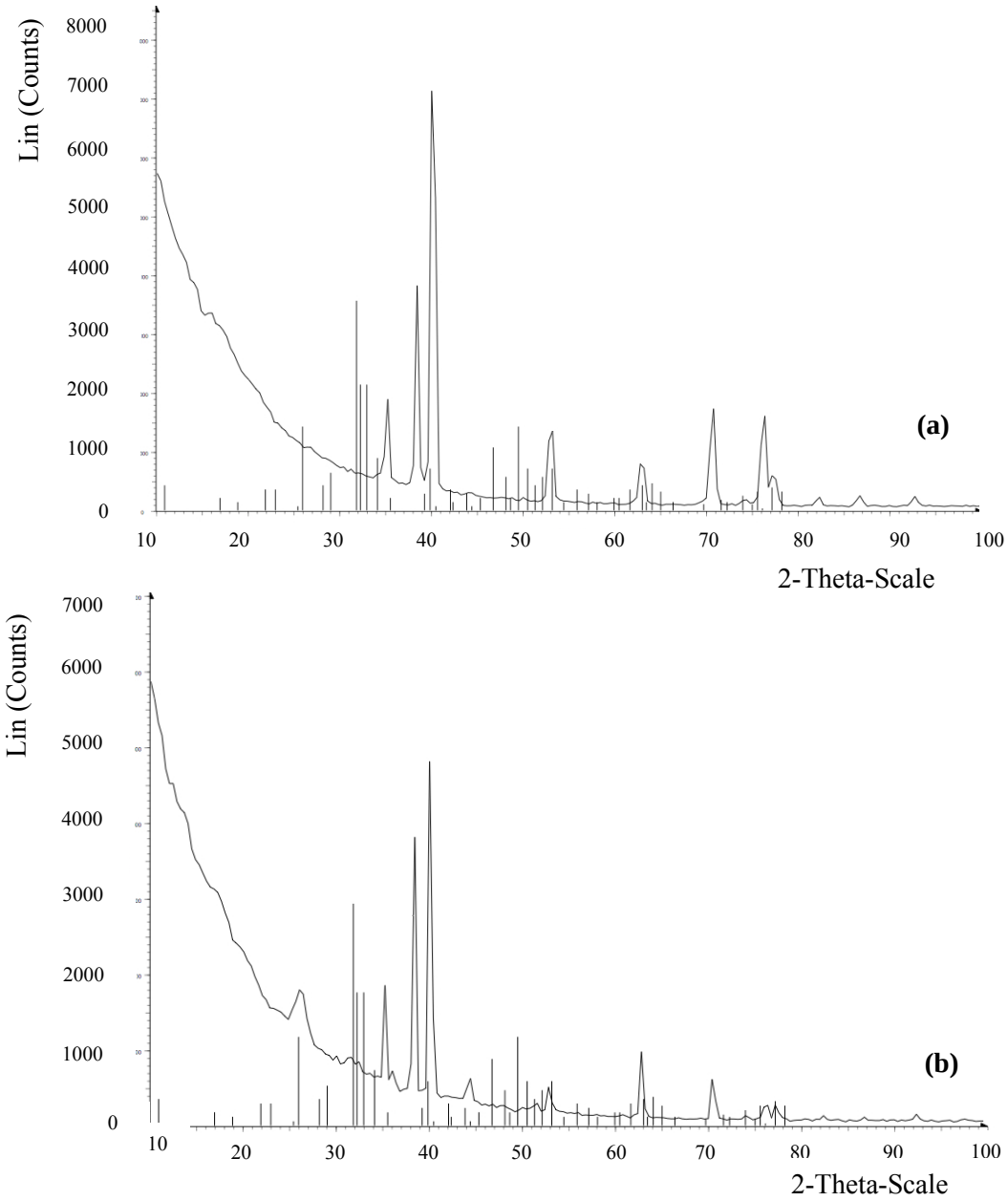

Figure 3. XRD analysis of hydroxyapatite-like (HA; $Ca_5(PO_4)_3OH$) deposited minerals after osteoblasts were cultured for 21 days on (a) Ti and (b) MWCNT-Ti. The micrographs show that the peak pattern of HA more closely matches that of the mineral deposited by osteoblasts when cultured on MWCNT-Ti than Ti.

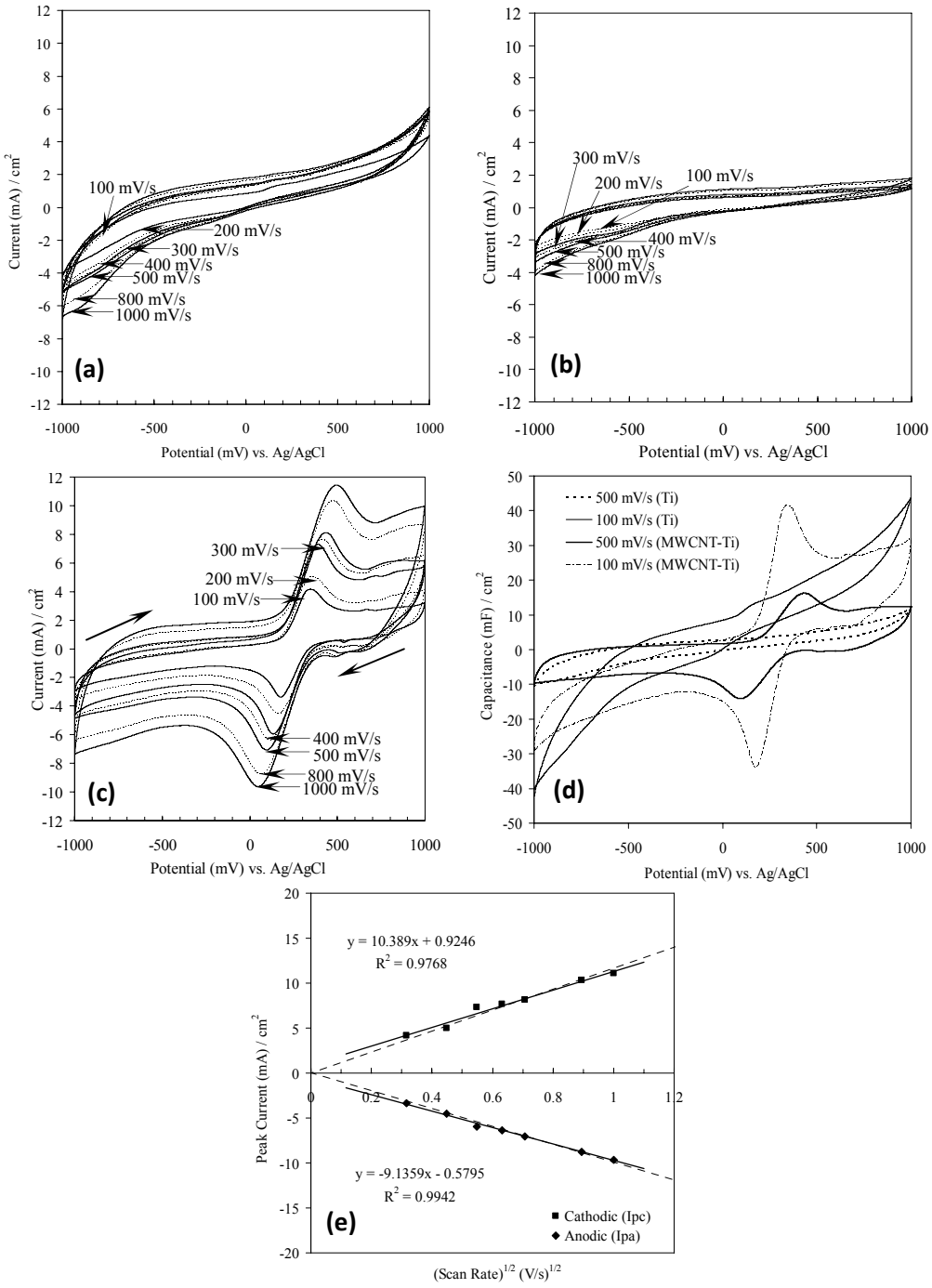

Figure 4. Cyclic voltammograms with an electrolyte solution of 10 mM $K_3Fe(CN)_6$ in 1 M KNO_3 for: (a) commercially pure Ti; (b) anodized Ti; and (c) MWCNT-Ti. (d) The capacitance of all the electrodes in comparison. (e) The plot of the square root of scan rates with anodic peak currents (I_{pa}) and cathodic peak currents (I_{pc}).

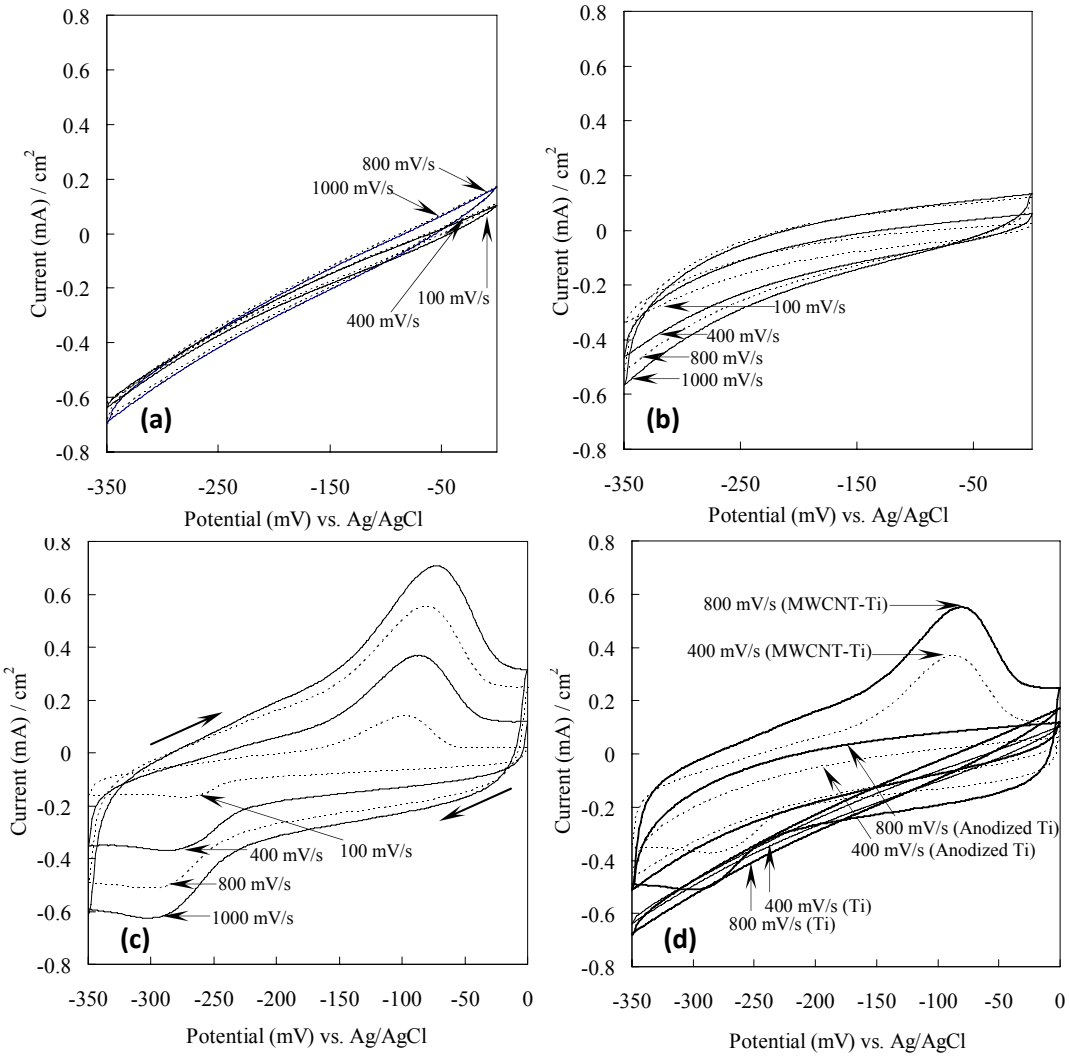

Figure 5. Cyclic voltammmograms with an electrolyte solution of the extracellular matrix secreted by osteoblasts after 21 days of culture for: (a) commercially pure Ti; (b) anodized Ti; and (c) MWCNT-Ti with a working area of 1 cm^2. (d) CV of all three electrodes in comparison. Only MWCNT-Ti possessed the quasi-reversible redox potential, while commercially pure Ti and anodized Ti did not.

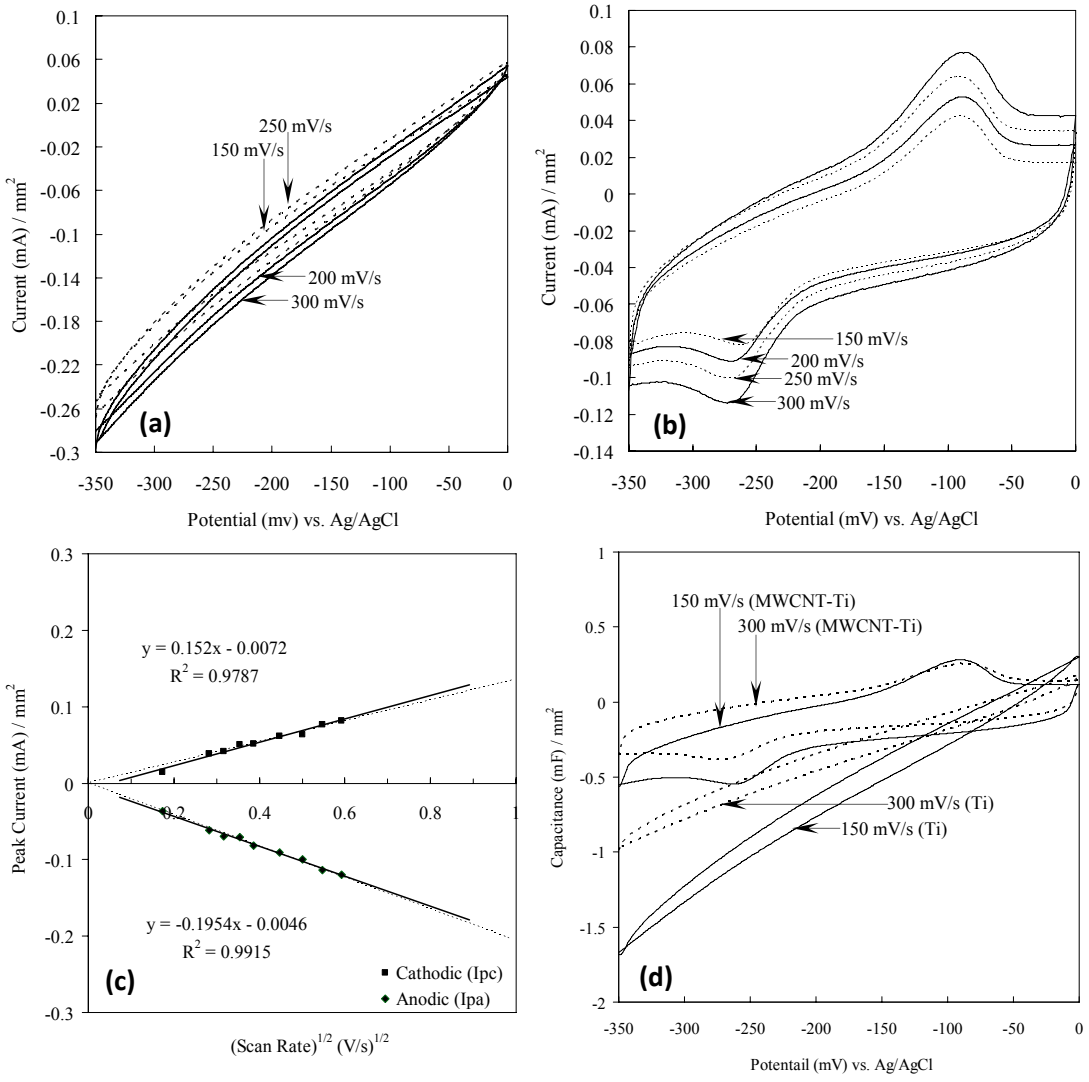

Figure 6. Cyclic voltammmograms with an electrolyte solution of the extracellular matrix secreted by osteoblasts after 21 days of culture for (a) commercially pure Ti and (b) MWCNT-Ti with a working area of 1 mm^2. (c) Plot of the experimental cathodic and anodic peak currents, obtained from (b), versus the square root of the scan rates; and (d) the compared capacitance of MWCNT-Ti and Ti.

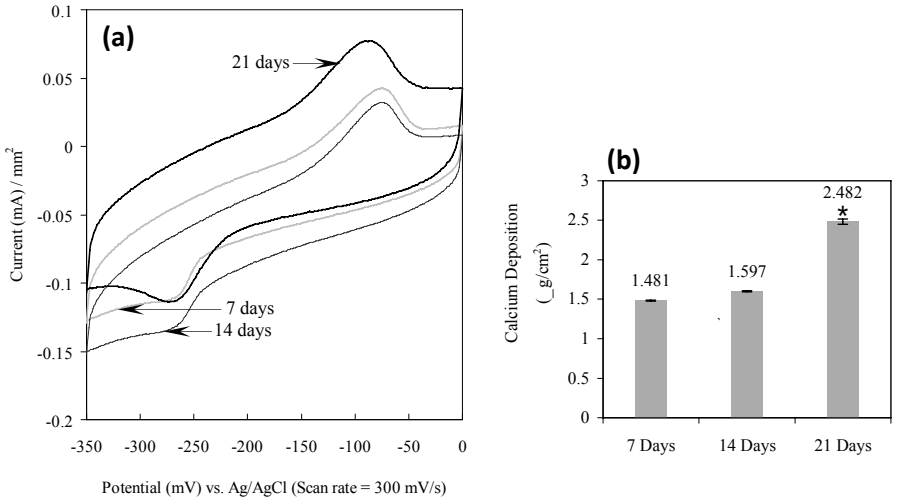

Figure 7. (a) Cyclic voltammograms of MWCNT-Ti electrodes in an electrolyte solution of the extracellular matrix secreted by osteoblasts cultured on commercially pure Ti after 21 days. (b) Results from calcium deposition assay determined the calcium concentrations in an electrolyte solution of the extracellular matrix secreted by osteoblasts on commercially pure Ti after 7, 14, and 21 days of culture. Data = mean ± S.E.M; n=3; *p<0.01 (compared to 7 and 14 days).

References:

[1] Zhan C, Kaczmarek R, Loyo-Berrios N, Sangl J and Bright R A 2007 Incidence and Short-Term Outcomes of Primary and Revision Hip Replacement in the United States *J. Bone Joint Surg. Am.* **89** 526-3

[2] Iijima S 1991 Helical microtubules of graphitic carbon *Nature* **354** 56-8

[3] L Lin Y, Taylor S, Li H, Fernando K A S, Qu L, Wang W, Gu L, Zhou B and Sun Y-P 2004 Advances toward bioapplications of carbon nanotubes *J. Mater. Chem.* **14** 527-41

[4] Webster T J, Waid M C, McKenzie J L, Price R L and Ejiofor J U 2004 Nano-biotechnology: carbon nanofibres as improved neural and orthopaedic implants *Nanotechnology* **15** 48-54

[5] Smart S K, Cassady A I, Lu G Q and Martin D J 2006 The biocompatibility of carbon nanotubes *Carbon* **44** 1034-47

[6] Zanello L P, Zhao B, Hu H and Haddon R C 2006a Bone Cell Proliferation on Carbon Nanotubes *Nano Lett.* **6** 562-7

[7] Zanello L P 2006b Electrical properties of osteoblasts cultured on carbon nanotubes *Micro & Nano Lett.* **1** 19-22

[8] Balani K, Anderson R, Laha T, Andara M, Tercero J, Crumpler E and Agarwal A 2007 Plasma-sprayed carbon nanotube reinforced hydroxyapatite coatings and their interaction with human osteoblasts in vitro *Biomaterials* **28** 618-24

[9] Chen Y, Zhang T H, Gan C H and Yu G 2007 Wear studies of hydroxyapatite composite coating reinforced by carbon nanotubes *Carbon* **45** 998-1004

[10] Wei W, Sethuraman A, Jin C, Monteiro-Riviere N A and Narayan R J 2007 Biological Properties of Carbon Nanotubes *J. Nanosci. Nanotechnol.* **7** 1284-97(14)

[11] Harrison B S and Atala A 2007 Carbon nanotube applications for tissue engineering *Biomaterials* **28** 344-53

[12] Supronowicz P R, Ajayan P M, Ullmann K R, Arulanandam B P, Metzger D W and Bizios R 2002 Novel current-conducting composite substrates for exposing osteoblasts to alternating current stimulation *J. Biomed. Mater. Res.* **59** 499-506

[13] Ciombor D M and Aaron R K 2005 The Role of Electrical Stimulation in Bone Repair *Orthobiologics* **10** 579-93

[14] Aoki N, Yokoyama A, Nodasaka Y, Akasaka T, Uo M, Sato Y, Tohji K and Watari F 2005 Cell Culture on a Carbon Nanotube Scaffold *J. Biomed. Nanotechnol.* **1** 402-5(4)

[15] Giannona S, Firkowska I, Rojas-Chapana J and Giersig M 2007 Vertically Aligned Carbon Nanotubes as Cytocompatible Material for Enhanced Adhesion and Proliferation of Osteoblast-Like Cells *J. Nanosci. Nanotechnol.* **7** 1679-83(5)

[16] Tsuchiya N, Sato Y, Aoki N, Yokoyama A, Watari F, Motomiya K, Jeyadevan B and Tohji K 2007 Evaluation of Multi-Walled Carbon Nanotube Scaffolds for Osteoblast Growth. ed K Tohji*, et al.*: AIP) pp 166-9

[17] Sirinrath S, Chang Y, Xingcheng X, Brian W S and Thomas J W 2007 Greater osteoblast functions on multiwalled carbon nanotubes grown from anodized nanotubular titanium for orthopedic applications *Nanotechnology* **18** 365102

[18] Padigi S K, Reddy R K K and Prasad S 2007 Carbon nanotube based aliphatic hydrocarbon sensor *Biosens. Bioelectron.* **22** 829-37

[19] Somenath R, Harindra V and Wonbong C 2006 Vertically aligned carbon nanotube probes for monitoring blood cholesterol *Nanotechnology* **17** S14

[20] Tang H, Chen J H, Huang Z P, Wang D Z, Ren Z F, Nie L H, Kuang Y F and Yao S Z 2004 High dispersion and electrocatalytic properties of platinum on well-aligned carbon nanotube arrays *Carbon* **42** 191-7

[21] Kurusu F, Koide S, Karube I and Gotoh M 2006 Electrocatalytic Activity of Bamboo-Structured Carbon Nanotubes Paste Electrode Toward Hydrogen Peroxide *Anal. Lett.* **39** 903-911(5)

[22] Liu Y, Wang M, Zhao F, Xu Z and Dong S 2005 The direct electron transfer of glucose oxidase and glucose biosensor based on carbon nanotubes/chitosan matrix *Biosens. Bioelectron.* **21** 984-8

[23] Liu S, Lin B, Yang X and Zhang Q 2007 Carbon-Nanotube-Enhanced Direct Electron-Transfer Reactivity of Hemoglobin Immobilized on Polyurethane Elastomer Film *J. Phys. Chem. B* **111** 1182-8

[24] Robertson J 2004 Realistic applications of CNTs *Mater. Today* **7** 46-52

[25] TalapatraS, KarS, Pal S K, VajtaiR, CiL, VictorP, Shaijumon M M, KaurS, NalamasuO and Ajayan P M 2006 Direct growth of aligned carbon nanotubes on bulk metals *Nat. Nano.* **1** 112-6

[26] Quoc N, Petranovic D, Krishnan S, Cassell A M A C A M, Qi Ye A Q Y, Jun Li A J L, Meyyappan M A M M and Yang C Y A Y C Y 2004 Electron transport through metal-multiwall carbon nanotube interfaces *IEEE Trans. Nanotechnology* **3** 311-7

[27] Sato S, Kawabata A, Kondo D, Nihei M and Awano Y 2005 Carbon nanotube growth from titanium,Äìcobalt bimetallic particles as a catalyst *Chem. Phys. Lett.* **402** 149-54

[28] Mathiowitz E and Knovel (Firm) 1999 Encyclopedia of controlled drug delivery. (New York: John Wiley & Sons) p 1120

[29] Calafiori A, Di Marco G, Martino G and Marotta M 2007 Preparation and characterization of calcium phosphate biomaterials *J. Mater. Sci.-Mater. Med.* **18** 2331-8

[30] Wang H, Lee J-K, Moursi A and Lannutti J J 2003 Ca/P ratio effects on the degradation of hydroxyapatite *in vitro J. Biomed. Mater. Res. Part A* **67A** 599-608

[31] Zaidi M, Moonga B S and Huang C L H 2004 Calcium sensing and cell signaling processes in the local regulation of osteoclastic bone resorption *Biol. Rev.* **79** 79-100

[32] Blair H C, Zaidi M, Schlesinger P H 2002 Mechanisms balancing skeletal matrix synthesis and degradation *Biochem. J.* **364** 329-41

[33] Bronner F and Farach-Carson M 2004 *Bone formation* (London; New York: Springer)

[34] Myoung Shin H, Seok Hyun L and Sun Wook K 2002 Use of KCl Aqueous Electrolyte for 2 V Manganese Oxide/Activated Carbon Hybrid Capacitor *Electrochemical and Solid-State Letters* **5** A227-A30

[35] Tamir G, Moti B-D, Itshak K, Raya S, Ze'ev R A, Eshel B-J and Yael H 2007 Electro-chemical and biological properties of carbon nanotube based multi-electrode arrays *Nanotechnology* **18** 035201

[36] Zhang Y, Baer C D, Camaioni-Neto C, O'Brien P and Sweigart D A 1991 Steady-state voltammetry with microelectrodes: determination of heterogeneous charge transfer rate constants for metalloporphyrin complexes *Inorg. Chem.* **30** 1682-5

[37] Hrapovic S, Liu Y, Male K B and Luong J H T 2004 Electrochemical Biosensing Platforms Using Platinum Nanoparticles and Carbon Nanotubes *Anal. Chem.* **76** 1083-8

[38] Hrapovic S and Luong J H T 2003 Picoamperometric Detection of Glucose at Ultrasmall Platinum-Based Biosensors: Preparation and Characterization *Anal. Chem.* **75** 3308-15

[39] Sotiropoulou S, Gavalas V, Vamvakaki V and Chaniotakis N A 2003 Novel carbon materials in biosensor systems B*iosens. and Bioelectron.* **18** 211-5

[40] Fang W-C, Sun C-L, Huang J-H, Chen L-C, Chyan O, Chen K-H and Papakonstantinou P 2006 Enhanced Electrochemical Properties of Arrayed CN_x Nanotubes Directly Grown on Ti-Buffered Silicon Substrates *Electrochem. Solid-State Lett.* **9** A175-A8

[41] Christian G D 1986 *Analytical chemistry* (New York: Wiley)

[42] Bard A J and Faulkner L R 2001 *Electrochemical methods fundamentals and applications* (New York: Wiley)

[43] Cao G 2004 *Nanostructures & nanomaterials synthesis, properties & applications* (London: Imperial College Press)

[44] George Z C and Derek J F 2002 Voltammetric Studies of the Oxygen-Titanium Binary System in Molten Calcium Chloride *Journal of The Electrochemical Society* **149** E455-E67

[45] Schuring J 2000 *Redox fundamentals, processes, and applications* (Berlin; New York: Springer)

[46] Battistuzzi G, Loschi L, Borsari M and Sola M 1999 Effects of nonspecific ion-protein interactions on the redox chemistry of cytochrome c *Journal of Biological Inorganic Chemistry* **4** 601-7

[47] Jeansonne B G, Feagin F F, Shoemaker R L and Rehm W S 1978 Transmembrane potentials of osteoblasts *J Dent Res* **57** 361-4

[48] Jeansonne B G, Feagin F F, McMinn R W, Shoemaker R L and Rehm W S 1979 Cell-to-cell communication of osteoblasts *J Dent Res* **58** 1415-23

[49] Lin Y, Yantasee W and Wang J 2005 Carbon nanotubes (CNTs) for the development of electrochemical biosensors *Front. Biosci.* **10** 492-505A

[50] John H. T. Luong S H D W 2005 Multiwall Carbon Nanotube (MWCNT) Based Electrochemical Biosensors for Mediatorless Detection of Putrescine *Electroanalysis* **17** 47-53

[51] He P, Xu Y and Fang Y 2006 Applications of Carbon Nanotubes in Electrochemical DNA Biosensors *Microchimica. Acta.* **152** 175-86

[52] Pushparaj V L, Shaijumon M M, Kumar A, Murugesan S, Ci L, Vajtai R, Linhardt R J, Nalamasu O and Ajayan P M 2007 Flexible energy storage devices based on nanocomposite paper *Proceedings of the National Academy of Sciences* **104** 13574-7

[53] Kaufman K R, Kovacevic N, Irby S E and Colwell C W 1996 Instrumented implant for measuring tibia femoral forces *J. Biomech.* **29** 667-71

[54] D'Lima D D, Townsend C P, Arms S W, Morris B A and Colwell C W 2005 An implantable telemetry device to measure intra-articular tibial forces *J. Biomech.* **38** 299-304

[55] Bergmann G, Deuretzbacher G, Heller M, Graichen F, Rohlmann A, Strauss J and Duda G N 2001 Hip contact forces and gait patterns from routine activities *J. Biomech.* **34** 859-71

[56] Bergmann G, Graichen F, Rohlmann A, Verdonschot N and van Lenthe G H 2001 Frictional heating of total hip implants, Part 1: measurements in patients *J. Biomech.* **34** 421-8

[57] Graichen F, Bergmann G and Rohlmann A 1999 Hip endoprosthesis for in vivo measurement of joint force and temperature *J. Biomech.* **32** 1113-7

[58] Graichen F and Bergmann G 1991 Four-channel telemetry system for in vivo measurement of hip joint forces *J. Biomed. Eng.* **13** 370-4

[59] Graichen F, Arnold R, Rohlmann A, Bergmann G and Bergmann A G 2007 Implantable 9-Channel Telemetry System for *In Vivo* Load Measurements With Orthopedic Implants*, IEEE Trans. Biomed. Eng.* **54** 253-61

Appendix B

Nanotechnology **2007;18(36):365102.**

Greater Osteoblast Functions on Multiwalled Carbon Nanotubes Grown on Anodized Titanium for Orthopedic Applications

Sirinrath Sirivisoot, Chang Yao, Xingcheng Xiao, Brian W. Sheldon, and

Thomas J. Webster*

Division of Engineering, Brown University, Providence, RI 02912, USA

* Contact Author

Thomas J. Webster

Associate Professor

Divisions of Engineering and Orthopaedics

Brown University

Providence, RI 02912 USA

E-mail: Thomas_Webster@Brown.edu

Abstract

Since titanium (Ti) is the most widely implanted orthopedic material, in this study, Ti surfaces were modified as anodized nanoporous Ti. Because of the unique electrical and chemical properties of multiwalled carbon nanotubes (MWCNTs), surface modification of Ti with MWCNTs can change the surface characteristics of the implants. Human osteoblasts (CRL-11372; ATCC) was determined their cytocompatibility *in vitro* on Ti and MWCNTs composites. Anodized Ti was prepared in 1.5 wt.% hydrofluoric acid resulting in nanopores of 50-60 nm in diameter on surface. The anodized surface was coated with cobaltous nitrate (catalyst) and MWCNTs were grown on the nanopores by a chemical vapor deposition process. The results of this study provided evidence that osteoblast (bone forming cell) functions (specifically, alkaline phosphatase activity and calcium deposition) were significantly greater on MWCNTs fuctionalized the anodized Ti substrates compared to anodized Ti without MWCNTs and unanodized Ti substrates for up to 21 days. In summary this study showed that bone growth can be enhanced in orthopedic applications on currently-used Ti with protruding MWCNTs and they can be further studied for orthopedic applications.

Keywords: osteoblasts, anodized titanium, multiwalled carbon nanotubes

1. Introduction

Bone matrices are mineral phase consisting of calcium phosphate-based apatite mineral (inorganic) and roughtly ~90% by weight of nanostructured fibrillar type-I collagen (organic) [1-4]. Osteoblasts form the nanostructured organic matrix of bone and produce alkaline phosphatase as well as other proteins, which play critical roles in the mineralization process. After osteoblasts proliferate into multilayer foci after confluence, these foci will form nodule which minerizalize and resemble woven bone ultrastructurally and biochemically both *in vitro/vivo* [5-6]. Undoubtedly, orthopedic implants require the functions of osteoblasts to create new bone on their surfaces; the lack of sufficient new bone growth on current materials have contributed in part to current average hip implant lifetimes of less than 15 years [7]. In fact, although due to numerous psychological and physical reasons, a recent University of Maryland Medical School study reported that up to 25% of patients receiving a hip implant die in the following surgery from hip fractures approximately 340,000 among U.S. population in 2000 [8]. Such data clearly indicate that much is needed to improve current bone implants.

Surprisingly, no gold standard material exists for orthopedic applications; titanium (Ti), CoCrMo, and Ti6Al4V are common variants each with varying degrees of success towards promoting new bone growth [9-11]. Ti is well-known for its high strength-to-weight ratio, low toxicity, and consequently is the most widely utilized material in orthopedic and maxillofacial replacements [12-13]. Not only are the mechanical properties of Ti (such as stiffness, high load resistance, fatigue resistance and ductility) sufficient for physiological loading, but its biocompatibility properties are also attractive for orthopedic applications. Critical in the design of successful implants is the ability of such materials to control protein adsorption and consequently osteoblast adhesion after they are implanted. The degree to which proteins

adsorb on implant surfaces depends on biomaterial properties, such as their chemistry, charge, wettability, and topography [14].

In the case of surface chemistry, oxidized layers of titanium oxide (TiO_2), favorable biological properties, are formed on Ti surfaces simply through their exposure to air and/or physical fluids [15]. After implantation, oxidized Ti surfaces bind with structural water, forming $–O^-$ and $–OH^-$ sites which possess a weak negative charge at physiological pH. Therefore, this oxidized layer provides a kinetic barrier that prevents Ti from corroding and provides bone implant material that promotes calcium phosphate crystal, protein, and cellular bonding. However, unanodized Ti implantation still has a high failure rate clinically [16], in order to increase their anti-corrosive and biocompatibility, the surface modification can further improve Ti its application in orthopedic field. [11] [16]. For example, topography of Ti surfaces can be modified in order to increase biologically-inspired nanometer surface roughness for better protein adsorption, osteoblast attachment, and eventual osseointegration [4]. Anodization is one of the surface modification techniques to create nanofeatures on Ti. The results of a surface analysis by Raman scattering spectrometer revealed that unanodized Ti contained mainly anatase TiO_2, whereas anodized Ti mainly contained both anatase TiO_2 and Ti_2O_3 [16]. As recent research shows, nanometer surfaces of anodized Ti can be created to enhance osteoblast adhesion by two-electrodes electrochemically in an acidic solution [13]. In that study, Ti was anodized to create nanotube-like pores, in which Zhu *et al.* have shown, possess higher surface energy and improved wettability compared to unanodized Ti [15]. Also, Huang *et al.* showed that the number of osteoblast-like U-2 OS cells adhered on network-structured TiO_2/Ti_2O_3 layer (10-300 nm), formed on Ti substrates by three-electrodes electrochemical technique in an alkaline solution, increases more than 1.4 times when compared to untreated Ti substrates [16].

Carbon nanotubes (CNTs) are macromolecules of carbon [17], classified as singlewalled carbon nanotubes (SWCNTs), diameter 0.4–2 nm, and multiwalled carbon nanotubes (MWCNTs), diameter 2-100 nm [18]. Due to their unique electrical, mechanical, chemical, and biological properties [19-26], CNTs have shown promise for bone implantation. For example, nanocomposites of polylactic acid and MWCNTs have been shown to increase osteoblast proliferation by 46% and calcium production by greater than 300% when an alternating current was applied to the substrate *in vitro* [27-28]. SWCNTs, functionalized with phosphoates and poly(aminobenzene sulfonic acid), can substitute as a collagen to direct the anisotropic crystallization of hydroxyapatite reaching a thickness of 3 mm after 14 days of mineralization, resulting in composites that can be used as a supporting scaffold for orthopedic applications [29]. Combining MWCNTs with the precusor materials' powder improves the mechanical properites of the as-aligned HA composites coatings [24]. MWCNTs, reinforced with hydroxyapatile coating, promote human osteoblast hFOB 1.19 proliferations *in vitro*, as observed in cell appearances near MWCNTs regions [23]. The nanophase PLGA cast of CNFs (diameter = 60 nm) compact poses a higher degree of surface roughness at approximately 50%, and promotes osteoblast adhesion after 1 h when compared with the cast of carbon conventional fiber (diameter = 200nm) compact [30]. Also, the number of human osteoblasts adhered more on carbon nanofibers' (CNFs) micro-pattern than polycarbonate urethane (PCU) [7]. Osteoblasts mophology extended in all directions within the CNT scaffold that formed on polycarbonate membranes [31]. Osteoblasts significantly enhanced their adhesion on vertically aligned MWCNT arrays with their potential sensing the nanoscaled feature [32]. Moreover, Zanello *et al.* showed that CNTs are suitable for osteoblast proliferation and bone formation by culturing osteosarcoma ROS 17/2.8 cells on single/multiwalled CNT scaffolds with/without surface modifications [21]. Human osteoblast-like (Saos2) cells grown on the MWCNT scaffold

showed a higher cell density and transforming growth factor-β1 concentration compared with polystryrene and polycarbonate scaffolds [33]. The currently used Ti for orthopedic implants can be modified with carbon nanotubes (CNTs). It can be produced by the laser furnace, arc, and chemical vapor deposition (CVD). However, CVD is a scalable and controllable method of obtaining the purity of CNTs [34]. Moreover, Sato *et al.* showed a potential growing MWCNTs by CVD with biometallic particle Ti and Co as a catalyst, and they revealed that Co can extend their catalystic ability by combining with Ti [35]. In this study, MWCNTs will be grown, using the CVD technique, out of anodized Ti nanotubes as a template, in order to form a strong contact between metal Ti and MWCNTs, with Co (catalyst support), which are employed for synthesis MWCNTs. The objective of the present *in vitro* study was to determine osteoblast cytocompatibility properties of nonfunctionalized MWCNTs grown from anodized nanotubular Ti; in doing so, an exciting new nanomaterial for promoting osteoblast functions was elucidated with biologically quantitative assays and osteoblast morphology/number analysis.

2. Materials and Methods

2.1 Anodization

In order to create nanotubes on Ti for subsequent MWCNTs growth, an anodization technique was adapted from Yao *et al.* [13]. Briefly, 99.2% pure Ti sheets (Alfa Aesar) were cut into 1x1 cm^2 squares and cleaned with acetone, 70% ethanol with a sonication for 10 minutes each, and followed by deionized H_2O. Then, these samples were etched for 10 seconds with a solution of 1.5% by weight nitric acid and 0.5% by weight hydrofluoric acid to remove the oxidized layer on Ti surfaces. Cleaned Ti samples were used as an anode, while a high purity platinum sheet (Alfa Aesar) served as a cathode. Both were immersed in an electrolyte solution consisting of 1.5% by

weight hydrofluoric acid, diluted by deionized H_2O, in a Teflon beaker. The surface of the etched Ti was placed next to the platinum sheet at a distance of around 1 cm. In this configuration, DC 20 volts (3645A; Circuit Specialists) were applied for 10 minutes to create nanotubes on the surfaces of currently used Ti for orthopedic implants.

2.2 Chemical Vapor Deposition

A chemical vapor deposition (CVD) system (Applied Science & Technology Inc.) was used to grow MWCNTs in Ti nanopores, which were created during anodization. The catalyst for CNT growth was cobaltous nitrate (Allied Chemical), diluted with methanol to a 5% by weight solution. The nanoporous anodized Ti samples were dipped in this solution for 5 minutes, prior to CVD. Next, the samples were rinsed with distilled water and dried with compressed air. The samples were then placed in the CVD chamber (Figure 2) and the air was pumped out to a base pressure below 10 mTorr. The samples were then heated to 700 ^{o}C in a flow of 100 standard cubic centimeters per minute (sccm) hydrogen gas for 20 minutes. To grow the MWCNTs, the gas composition was changed to 40 sccm H_2 and 160 sccm C_2H_2 (acetylene) for 30 minutes. Finally, the samples were cooled in a 100 sccm Ar flow. All samples were examined by scanning electron microscopy (SEM; Leo 1530VP FE-4800).

2.3 Cell Culture and Morphology

In vitro osteoblast cytocompatibility assays were determined on four types of samples in the present study including pure Ti, anodized nanotubular Ti, CNTs grown from anodized

nanotubular Ti, and carbon nanopaper (Buckypaper; NanoLab). For the CNTs grown from anodized Ti, all samples used in cell assays employed the cobaltous nitrate catalyst. Human osteoblasts (CRL-11372; American Type Culture Collection, population numbers 5-12) adhesion and differentiation from non-calcium to calcium depositing cells were determined on each substrate. First, all substrates were sterilized by ultraviolet (UV) light exposure for 4 hours on each side. Substrates were then immediately rinsed with phosphate buffered saline (PBS; 8 g NaCl, 0.2 g KCl, 1.5 g Na_2PO_4, and 0.2 g KH_2PO_4 in 1000 ml DI water adjusted to a pH of 7.4; Sigma-Aldrich) three times and placed in 12 well plates. For adhesion assays, 3,500 osteoblasts/cm^2 were seeded in Dulbecco's Modified Eagle Medium (DMEM; Gibco) supplemented with 10% fetal bovine serum (FBS; Hyclone), and 1% penicillin/streptomycin (P/S; Hyclone) onto the substrates under standard incubator conditions (a humidified, 5% CO_2, and 95% air environment at 37° C) for 4 hours, then washed with PBS three times to remove nonadherent cells. Afterward, remaining osteoblasts were fixed with acetate buffer containing 10% formalin (Fisher) for 10 min, stained with fluorescent stain, 4',6-diamidino-2-phenylindole (DAPI; Sigma), diluted as 300 nM, and counted the number of cell adhesion under fluorescence microscope (Zeiss Axiovert 200M). Five random fields were counted per substrate. Cell adhesion testing was repeated three different times. Whereas, the initial adhesion for 4 hours of osteoblasts on the anodized Ti surfaces with and without MWCNTs was evaluated by scanning electron microscopes (SEM; Hitachi 2700). Before SEM analysis, all samples were fixed with acetate buffer containing 10% formalin (Fisher) for 10 min, dehydrated with the series of ethanol (30%, 50%, 70%, 90%, and 100%; 20 min each), were critical point dried by LADD Research CPD, and finally coated with thin layer of gold. The set of samples for evaluation the cell density and their morphology were different.

2.4 Cellular Assays

In order to evaluate the osteoblast differentiation, 40,000 cells/cm^2 were seeded onto the substrates of interest and were cultured in DMEM supplemented with 10% FBS, 1% P/S, 50 nM β-glycerophosphate (Sigma), and 50 μg/ml ascorbic acid (Sigma) under standard incubator conditions for 7, 14, and 21 days. The culture medium was changed every other day. At the end of the prescribed time period, an alkaline/acid phosphatase assay kit (Upstate) was used to determine the concentration of alkaline phosphatase in cell lysates. Cell lysates were prepared by first rinsing all samples with Tris-buffered saline (TBS; 42 mM Tris-HCl, 8 mM Tris Base and 0.15 M NaCl; pH of 7.4; Sigma-Aldrich) three times and then subjecting the cells to three freeze-thaw cycles using distilled water. A calcium quantification kit (Sigma) was also used to determine the amount of calcium deposited by osteoblasts cultured on each substrate. An acidic supernatant solution for this assay was prepared by incubating all the samples with 0.6 N HCl (Sigma) overnight. The light absorbance was measured by a spectrophotometer (SpectoMAX; Molecular Devices) at 650 nm for alkaline phosphatase activity and 570 nm for calcium deposition. Long-term cytocompatible testing was conducted in triplicate and was repeated three different times. Numerical data was analyzed using the standard student t-test.

3. Results

3.1 Material Surface Topography

As expected, small pores were distributed uniformly on the Ti surface after anodization (as shown in Figure 3b). An unanodized Ti surface is shown in Figure 3a in comparison. The uniform pores, as observed by SEM, have diameters of 50-60 nm and a depth of 200 nm [13]. MWCNTs

successfully grew out of these anodized nanopores in the anodic oxide (Figure 3 c, d, and e) when the samples were pretreated with the catalyst solution (cobaltous nitrate) (Figure 3 e and f). When the catalyst pretreatment was not used, the same deposition conditions produced amorphous carbon instead of MWCNTs (Figure 3 c and d). The growth time in the C_2H_2 gas also influenced the MWCNTs, with more substantialMWCNTs coverage observed with an increase from 20 to 30 minutes with similarly observed MWCNTs diameter. However, the presence of C_2H_2 gas for an hour in the chamber is controlling the amount of disorganized carbon coating and MWCNTs diameter (SEM micrographs not shown). Using more than 5% wt. of the 5M cobaltous nitrate also increased amorphous carbon formation (SEM micrographs not shown), due to apparent Co poisoning effects [36]. Although the topography of anodized nanoporous Ti with MWCNTs varied between each sample, they were significantly rougher at the nanometer level than both the unanodized and anodized nanoporous Ti surfaces without MWCNTs.

3.2 Osteoblast Responses

Results of this study showed similar number of osteoblasts adhered after 4 hours on unanodized Ti, anodized nanotubular Ti without MWCNTs and anodized nanotubular Ti with MWCNTs (Figure 4); all were greater than the carbon nanopaper. Although MWCNTs on anodized Ti showed less the number of cells adhesion, osteoblasts were observed their cytoplasmatic prolongation on the surfaces of MWCNTs grown out of anodized nanotubular Ti (Figure 5 c and d), resulting the stronger adhesion (more density of the points of contact) [37]. While osteoblast on anodized Ti without MWCNTs does not be observed the cytoplasmic prolongation (Figure 5 a and b). As well as, Zanello *et al.* has been observed a thin neurite-like cytoplasmic

prolonagation of osteoblasts that reach the nanotube bundles after cell culture for 5 days. Lower osteoblasts growth in Figure 4 may be in part of losing MWCNTs while fixing and staining osteoblasts process. More importantly, results of the present study showed for the first time that the biological qualification, which is alkaline phosphatase activity and calcium deposition by osteoblasts, increased on MWCNTs grown from anodized nanotubular Ti compared to anodized nanotubular Ti without MWCNTs, unanodized Ti, and carbon nanopaper after 21 days (Figure 6).

4. Discussion

The different sterilization techniques for implant biomaterials may induce the different surface chemical modifications [1]. The effect of UV sterilization might effect to subsequent osteoblasts adhesion *in vitro*. Althought the conventional stream sterilization has been generally used, in this study, UV sterilization for 4 hours were performed right before MWCNTs samples were cultured, while other types of samples were autoclaved for 45 minutes. Due to different sterlizations between these samples might effect to cell adhesion and differentiation in this study. Moreover, the chemical surface modifications were not futher performed after CVD process. In this study, MWCNTs, also namely nonfunctionalized 'as-grown' (AG-) MWCNTs, grown on anodized Ti substrate were cultured with human osteoblasts. Whereas, the sutdy of Zanello *et al.* used the glass cover slip with covering the positive and/or negative of the functional groups of SWCNTs for culturing osteoblastic cells. It has been reported that the surface modification of electrically neutral SWCNTs (-PEG), nonfunctionalized AP (as-prepared)-SWCNTs, and nonfunctionalized AP-MWCNTs are more suitable for osteosacroma ROS 17/2.8 cells growth [21]. Nonfunctionalized AP-MWCNTs sustained higher cell growth than

functionallized MWCNTs, below 15% (data not shown) has been reported. CNTs are nanomaterials, while the bundles of them can observed in a microscale. Both micro/nanotopography of biomaterial affect to osteoblast responses in order to oraganize bone [38]. SWCNTs on glass form flat microtopography, whereas MWCNTs has non-uniformed microtopograhy varied in length [21-22]. In this study, after CVD process for the optimal time (30 min) in the introduce C_2H_2 gas, AG-MWCNTs on Ti form quite flat surface in microscale. The growing time was extened to an hour, we observed a longer MWCNTs and a rougher surface. However, there are some region of MWCNTs grown on the anodized Ti substrate (for 30 min) that do not flat, leading an observation osteoblasts overlied, for example, on two different heights of MWCNTs after 4 hours adhesion (SEM micrograph not show). Zanello *et al.* provide the results of chloride/calcium channels activities, cells density, SEM analysis, Von Kossa stainning, etc. However, this present study further supports MWCNTs biocompatibility by the biological quanlifications, which are alkaline phosphatase activity and calcium deposition testing.

The present results also confirmed previous studies which have demonstrated greater osteoblast functions (such as alkaline phosphatase and calcium deposition) on anodized compared to unanodized Ti [13]. Upon further investigation of why, researchers have shown greater initial vitronectin and fibronectin adsorption. Since vitronectin and fibronectin are proteins which mediate osteoblast functions *in vitro* [1], different surface energetics between anodized and unanodized Ti which promotes optimal protein adsorption (vitronectin/fibronectin) important for greater osteoblast functions [39]. Since, researchers have further utilized the cytocompatibility properties of CNFs (diameter = 100 nm) to direct bone formation to match that of the natural anisotropic arrangement of collagen and hydroxyapatite

in long bones of the body by patterning CNFs [7]. They observed the higher interactions of fibronectin and osteoblasts on CNFs as approximately 300% than PU surfaces without CNFs. In addition, a novel adaptation of the standard surface-enhanced Raman Scattering technique provided additional evidence of increased unfolding of vitronectin (and, thus, exposure of cell adhesive epitopes) on such nanoparticulate versus microparticulate ceramic, possibly promoting availability of specfic epitopes, such as Arginine-Glycine-Asparitc acid (RGD), which increase osteoblast adhesion *in vitro* [14].

5. Conclusions

Growing MWCNTs by chemical vapor deposition out of nanotubular Ti surfaces, anodized in electrochemical technique to create Ti nanopores around 50-60 nm in diameter. This study provided evidence *in vitro* that human osteoblasts synthesize more alkaline phosphatase and calcium on the surfaces when compared with anodized nanotubular Ti without MWCNTs and currently-used unanodized commercial Ti. Also, the cytoplasmatic prolongation of osteoblasts adhered for 4 hours on MWCNTs was observed, but not on anodized Ti. MWCNTs on anodized Ti were studied in short and long terms *in vitro*, resulting the enhancement the osteogenesis by osteoblasts. In the future work, their electrical property of Ti after growing MWCNTs out of their anodized nanotubes will be studied. Detecting calcium concentrations (synthesized by human osteoblasts) by those MWCNTs on anodized Ti electrodes will be also further investigated *in vitro* for ultimate goal in monitoring and controlling new bone growth around the orthopedic implant.

6. Acknowledgements

The authors would like to thank the Coulter Foundation for funding and Abhishek Kothari for assistance with growing multiwalled carbon nanotubes through chemical vapor deposition. Also, Geoffrey Williams and Anthony W. McCormick for electron microscope facility.

7. Figures

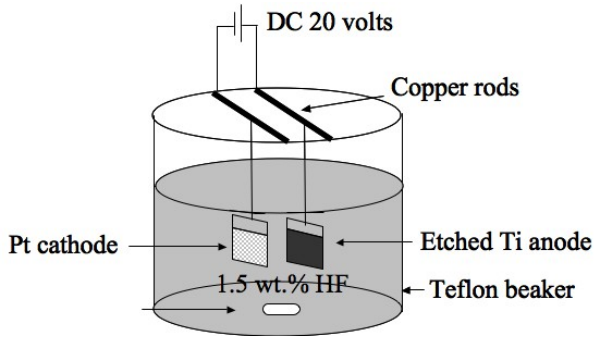

Figure 1. Anodization treatment: DC 20 volts was applied for 10 minutes to modify Ti surface as nanopores in 1.5% by weight hydrofluoric acid diluted with deionized water.

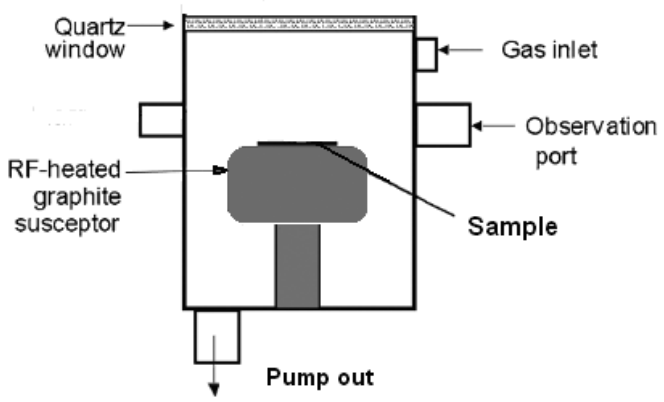

Figure 2. Chemical vapor deposition (CVD) system used to grow MWCNTs on Ti surfaces which were anodized as Ti nanotubes by using cobaltous nitrate as a catalyst, and acetylene gas as a carbon source.

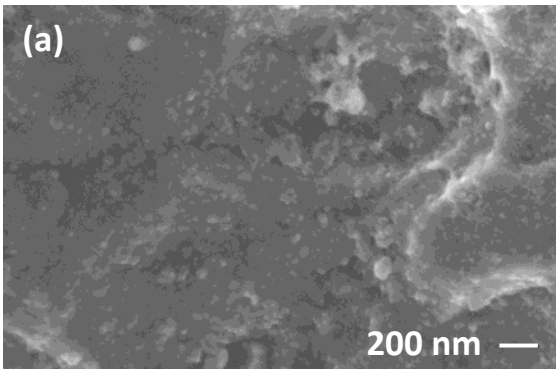

(a) Unanodized Ti.

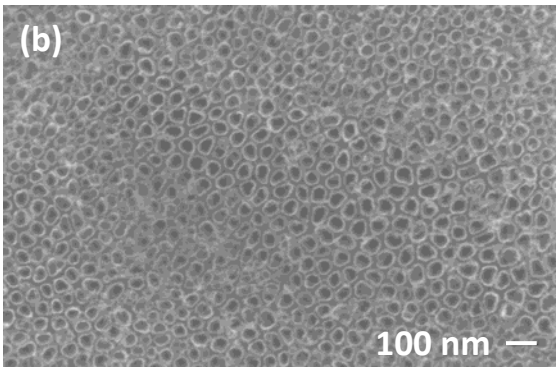

(b) Anodized Ti.

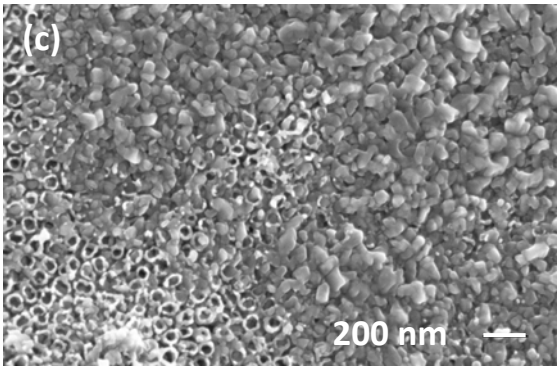

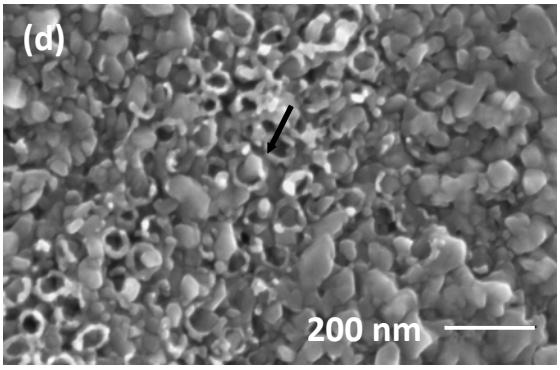

(c), (d) "MWCNTs grown on Anodized Ti" *without* Co catalyst for 20 minutes.

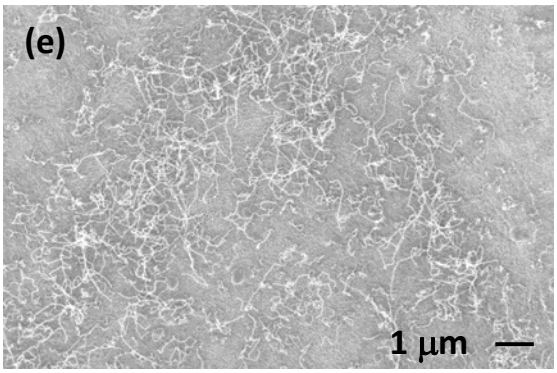

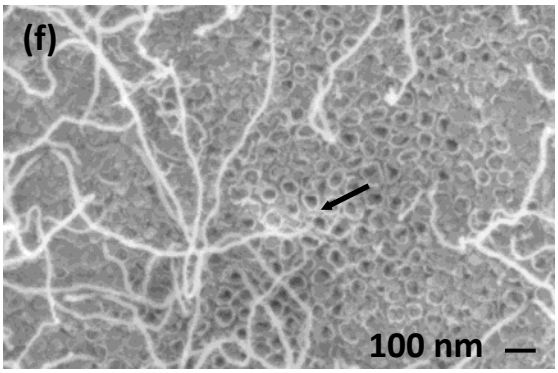

(e), (f) "MWCNTs grown on Anodized Ti" *with* Co catalyst for 20 minutes.

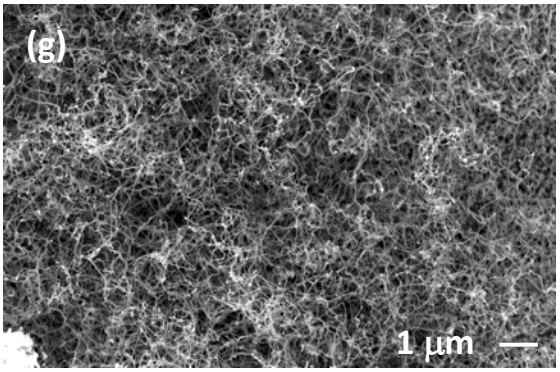

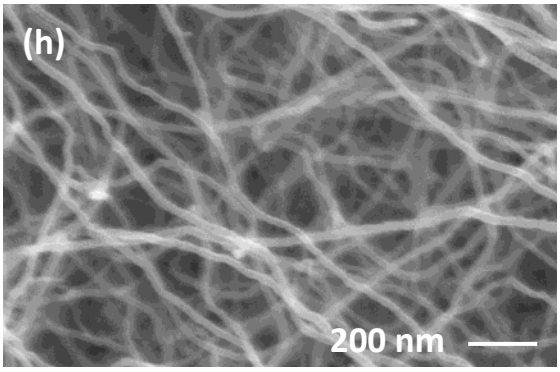

(g), (h) "MWCNTs grown on Anodized Ti" *without* Co catalyst for 30 minutes.

Figure 3. SEM micrographs: (a) Unanodized Ti; (b) Anodized Ti without MWCNTs; (c), (d) "MWCNTs grown on Anodized Ti" *without* a Co catalyst for 20 minutes; (e), (f) *with* a Co catalyst; (g), (h) "MWCNTs grown on Anodized Ti" *without* a Co catalyst for 30 minutes. The arrows show MWCNTs coming out of the nanopores.

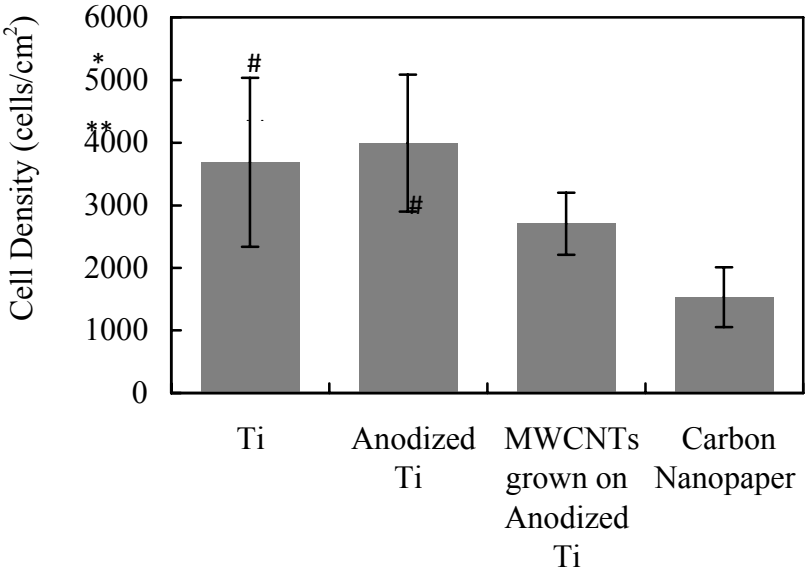

Figure 4. Osteoblast adhesion for 4 hours on Ti, Anodized Ti, "MWCNTs grown on Anodized Ti", and Carbon Nanopaper. Values are mean ±S.E.M; n=3; * $p<0.1$ compared to Carbon Nanopaper; ** $p<0.05$ compared to Carbon Nanopaper; # $p<0.05$ compared to "MWCNTs grown on Anodized Ti"

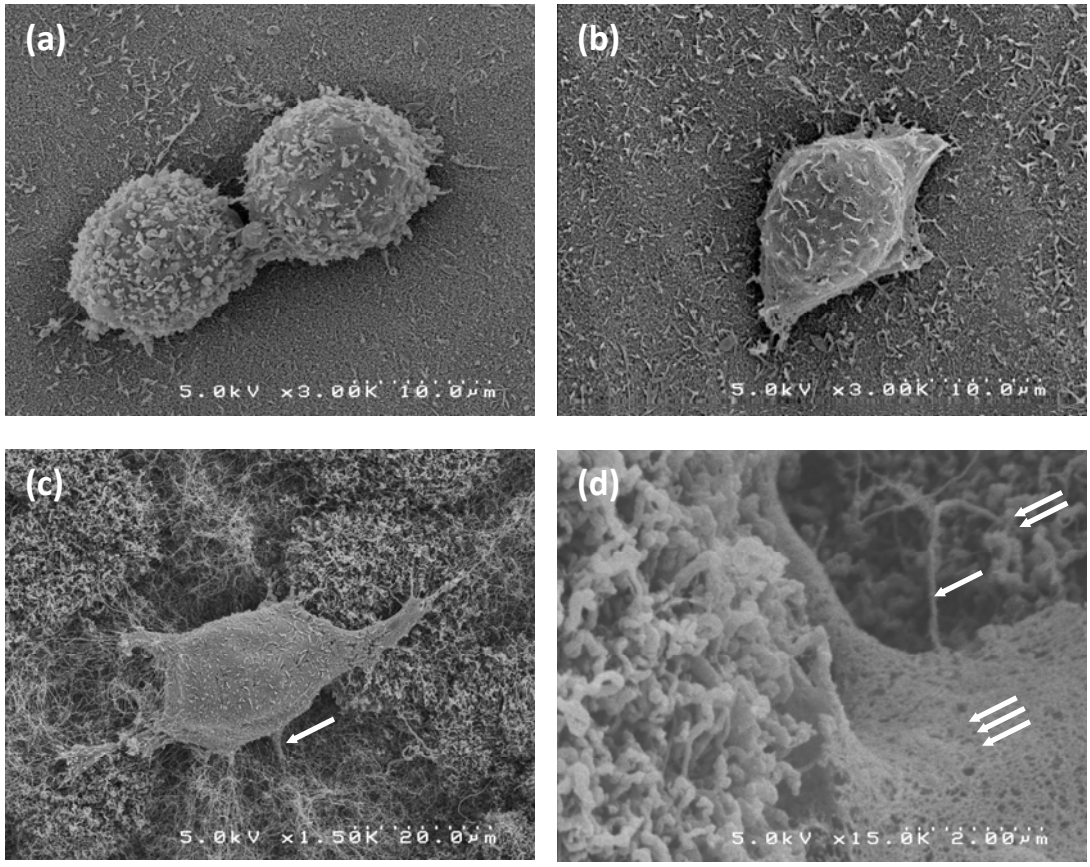

Figure 5. Osteoblast morphology after 4 hours adhesion on: (a), (b) Anodized Ti (Scale bars = 10 μm). Round-shaped osteoblasts are on the anodize Ti substrate without MWCNTs; and (c), (d) "MWCNTs grown on anodized Ti" (Scale bars = 20 μm left and 2 μm right). One-arrow shows the cytoplamatic prolongations of osteoblasts to MWCNTs. Double-arrows shows MWCNTs, while Triple-arrows shows the osteoblast membrane.

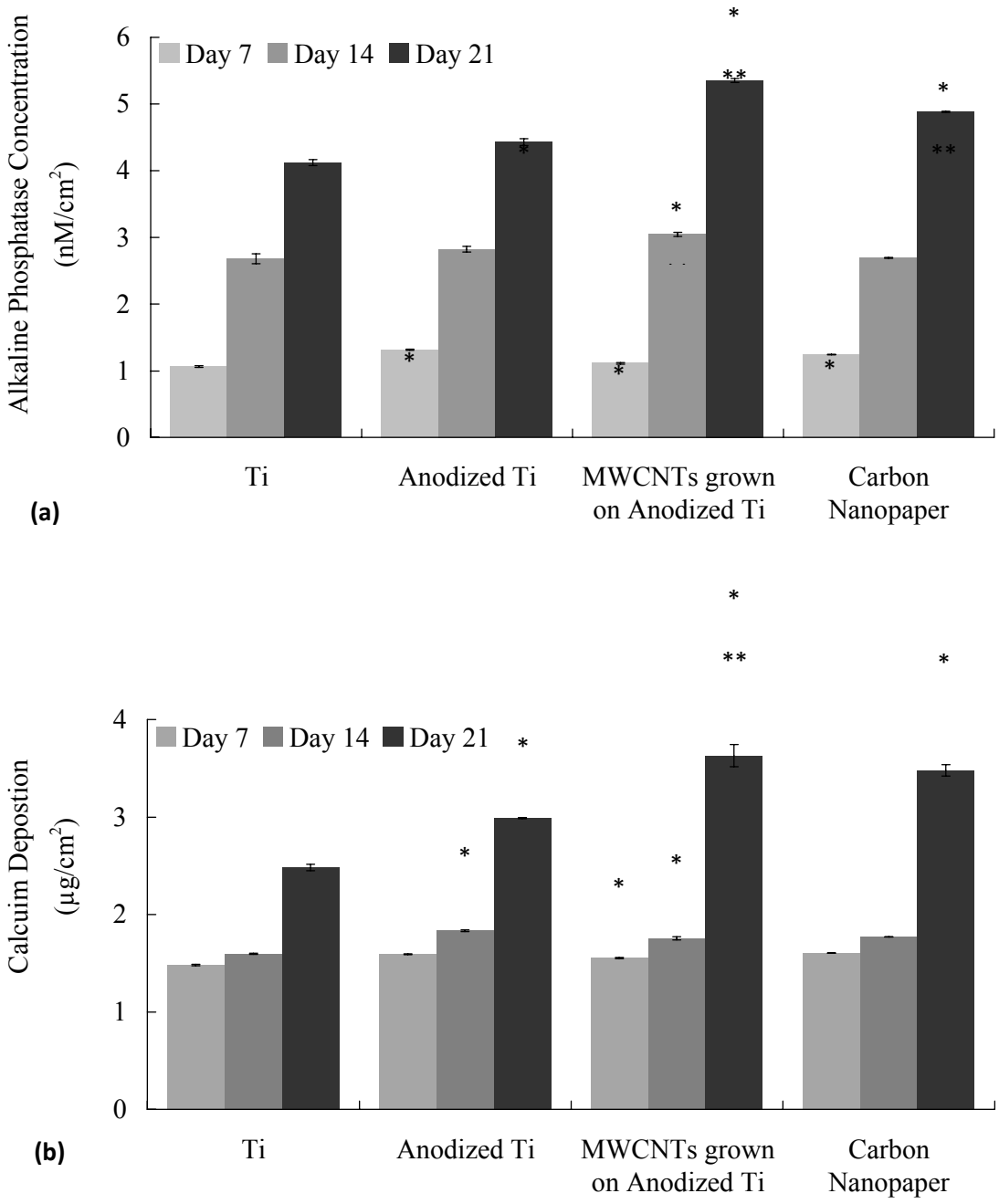

Figure 6. Osteoblasts long term functions: (a) Alkaline phosphatase activity; Values are mean ± S.E.M; n=3; * $p<0.05$ compared to Ti; ** $p<0.1$ compared to Anodized Ti; and # $p<0.1$ compared to Carbon Nanopaper and (b) Calcium deposition; Values are mean ± S.E.M; n=3; * $p<0.1$ compared to Ti; ** $p<0.1$ compared to Anodized Ti; and # $p<0.05$ compared to Carbon Nanopaper.

References:

[1] Anselme K 2000 Osteoblast adhesion on biomaterials *Biomaterials* **21** 667-81

[2] Ager, III, Balooch G and Ritchie R O 2006 Fracture, aging, and disease in bone *Journal of Materials Research* **21** 1878-92

[3] Ward B C and Webster T J 2006 The effect of nanotopography on calcium and phosphorus deposition on metallic materials in vitro *Biomaterials* **27** 3064-74

[4] Liu H and Webster T J 2007 Nanomedicine for implants: A review of studies and necessary experimental tools *Cellular and Molecular Biology Techniques for Biomaterials Evaluation* **28** 354-69

[5] Ahmad M, McCarthy M and Gronowicz G 1999 An in vitro model for mineralization of human osteoblast-like cells on implant materials *Biomaterials* **20** 211-20

[6] Dimitriou R, Tsiridis E and Giannoudis P V 2005 Current concepts of molecular aspects of bone healing *Injury* **36** 1392-404

[7] Dongwoo K, Michiko S, Rachel L P, Alexander E R and Thomas J W 2006 Selective adhesion and mineral deposition by osteoblasts on carbon nanofiber patterns **1** 65-72

[8] Orosz G M, L Hannan E, Magaziner J, Koval K, Gilbert M, Aufses A, Straus E, Vespe E and Siu A L 2002 Hip Fracture in the Older Patient: Reasons for Delay in Hospitalization and Timing of Surgical Repair *Journal of the American Geriatrics Society* **50** 1336-40

[9] Disegi J A 2000 Titanium alloys for fracture fixation implants *Injury* **31** 14-7(4)

[10] Morra M, Cassinelli C, Cascardo G, Cahalan P, Cahalan L, Fini M and Giardino R 2003 Surface engineering of titanium by collagen immobilization. Surface characterization and in vitro and in vivo studies *Biomaterials* **24** 4639-54

[11] Webster T J and Ejiofor J U 2004 Increased osteoblast adhesion on nanophase metals: Ti, Ti6Al4V, and CoCrMo *Biomaterials* **25** 4731-9

[12] Long M and Rack H J 1998 Titanium alloys in total joint replacement-materials science perspective *Biomaterials* **19** 1621-39

[13] Yao C, Perla V, McKenzie J L, Slamovich E B and Webster T J 2005 Anodized Ti and Ti6Al4V Possessing Nanometer Surface Features Enhances Osteoblast Adhesion *Journal of Biomedical Nanotechnology* **1** 68-73(6)

[14] Christenson E M, Anseth K S, van den Beucken J J, Chan C K, Ercan B, Jansen J A, Laurencin C T, Li W J, Murugan R, Nair L S, Ramakrishna S, Tuan R S, Webster T J and Mikos A G 2007 Nanobiomaterial applications in orthopedics *Journal of orthopaedic research: official publication of the Orthopaedic Research Society* **25** 11-22

[15] Zhu X, Chen J, Scheideler L, Reichl R and Geis-Gerstorfer J 2004 Effects of topography and composition of titanium surface oxides on osteoblast responses *Biomaterials* **25** 4087-103

[16] Huang H-H, Pan S-J, Lai Y-L, Lee T-H, Chen C-C and Lu F-H 2004 Osteoblast-like cell initial adhesion onto a network-structured titanium oxide layer *Scripta Materialia* **51** 1017-21

[17] Iijima S 1991 Helical microtubules of graphitic carbon *Nature* **354** 56-8

[18] Lin Y, Taylor S, Li H, Fernando K A S, Qu L, Wang W, Gu L, Zhou B and Sun Y-P 2004 Advances toward bioapplications of carbon nanotubes *Journal of Materials Chemistry* **14** 527-41

[19] Webster T J, Waid M C, McKenzie J L, Price R L and Ejiofor J U 2004 Nano-biotechnology: carbon nanofibres as improved neural and orthopaedic implants *Nanotechnology* **15** 48-54

[20] Smart S K, Cassady A I, Lu G Q and Martin D J 2006 The biocompatibility of carbon nanotubes *Toxicology of Carbon Nanomaterials* **44** 1034-47

[21] Zanello L P, Zhao B, Hu H and Haddon R C 2006 Bone Cell Proliferation on Carbon Nanotubes *Nano Letters* **6** 562-7

[22] Zanello L P 2006 Electrical properties of osteoblasts cultured on carbon nanotubes *Micro & Nano Letters* **1** 19-22

[23] Balani K, Anderson R, Laha T, Andara M, Tercero J, Crumpler E and Agarwal A 2007 Plasma-sprayed carbon nanotube reinforced hydroxyapatite coatings and their interaction with human osteoblasts in vitro *Biomaterials* **28** 618-24

[24] Chen Y, Zhang T H, Gan C H and Yu G 2007 Wear studies of hydroxyapatite composite coating reinforced by carbon nanotubes *Carbon* **45** 998-1004

[25] Wei W, Sethuraman A, Jin C, Monteiro-Riviere N A and Narayan R J Biological Properties of Carbon Nanotubes *Journal of Nanoscience and Nanotechnology* **7** 1284-97(14)

[26] Harrison B S and Atala A 2007 Carbon nanotube applications for tissue engineering *Cellular and Molecular Biology Techniques for Biomaterials Evaluation* **28** 344-53

[27] Supronowicz P R, Ajayan P M, Ullmann K R, Arulanandam B P, Metzger D W and Bizios R 2002 Novel current-conducting composite substrates for exposing osteoblasts to alternating current stimulation *Journal of Biomedical Materials Research* **59** 499-506

[28] Ciombor D M and Aaron R K 2005 The Role of Electrical Stimulation in Bone Repair *Orthobiologics* **10** 579-93

[29] Zhao B, Hu H, Mandal S K and Haddon R C 2005 A Bone Mimic Based on the Self-Assembly of Hydroxyapatite on Chemically Functionalized Single-Walled Carbon Nanotubes *Chemistry of Materials* **17** 3235-41

[30] Price R L, Ellison K, Haberstroh K M and Webster T J 2004 Nanometer surface roughness increases select osteoblast adhesion on carbon nanofiber compacts *Journal of biomedical materials research.Part A* **70** 129-38

[31] Aoki N, Yokoyama A, Nodasaka Y, Akasaka T, Uo M, Sato Y, Tohji K and Watari F 2005 Cell Culture on a Carbon Nanotube Scaffold *Journal of Biomedical Nanotechnology* **1** 402-5(4)

[32] Giannona S, Firkowska I, Rojas-Chapana J and Giersig M Vertically Aligned Carbon Nanotubes as Cytocompatible Material for Enhanced Adhesion and Proliferation of Osteoblast-Like Cells *Journal of Nanoscience and Nanotechnology* **7** 1679-83(5)

[33] Tsuchiya N, Sato Y, Aoki N, Yokoyama A, Watari F, Motomiya K, Jeyadevan B and Tohji K 2007 Evaluation of Multi-Walled Carbon Nanotube Scaffolds for Osteoblast Growth *AIP Conference Proceeding* **898** 166-9

[34] Robertson J 2004 Realistic applications of CNTs *Materials Today* **7** 46-52

[35] Sato S, Kawabata A, Kondo D, Nihei M and Awano Y 2005 Carbon nanotube growth from titanium-cobalt bimetallic particles as a catalyst *Chemical Physics Letters* **402** 149-54

[36] Soneda Y, Duclaux L and Béguin F 2002 Synthesis of high quality multi-walled carbon nanotubes from the decomposition of acetylene on iron-group metal catalysts supported on MgO *Carbon* **40** 965-9

[37] Zinger O, Zhao G, Schwartz Z, Simpson J, Wieland M, Landolt D and Boyan B 2005 Differential regulation of osteoblasts by substrate microstructural features *Biomaterials* **26** 1837-47

[38] Taton T A 2001 Nanotechnology: Boning up on biology *Nature* **412** 491-2

[39] Yao C and Webster T J Anodization: A Promising Nano-Modification Technique of Titanium Implants for Orthopedic Applications *Journal of Nanoscience and Nanotechnology* **6** 2682-92(11)